5-2010

Using fluid inclusions to trace formative fluid evolution at the Verde and Pancho porphyry Au deposits of the Refugio District, Chile

Brian Joshua Aillaud
University of Nevada Las Vegas

USING FLUID INCLUSIONS TO TRACE FORMATIVE FLUID EVOLUTION AT THE VERDE AND PANCHO PORPHYRY AU DEPOSITS OF THE REFUGIO DISTRICT, CHILE

by

Brian Joshua Aillaud

Bachelor of Science
New Mexico Institute of Mining and Technology
2005

A thesis submitted in partial fulfillment
of the requirements for the

Master of Science in Geoscience
Department of Geoscience
College of Sciences

Graduate College
University of Nevada, Las Vegas
May 2010

UNIVERSITY OF NEVADA LAS VEGAS

THE GRADUATE COLLEGE

We recommend the thesis prepared under our supervision by

Brian Joshua Aillaud

entitled

Using Fluid Inclusions to Trace Formative Fluid Evolution at the Verde and Pancho Porphyry Au Deposits of the Refugio District, Chile

be accepted in partial fulfillment of the requirements for the degree of

Master of Science in Geoscience

Adam Simon, Committee Chair

John Muntean, Committee Member

Jean Cline, Committee Member

Rodney Metcalf, Committee Member

Barbara Luke, Graduate Faculty Representative

Ronald Smith, Ph. D., Vice President for Research and Graduate Studies
and Dean of the Graduate College

May 2010

ABSTRACT

Using Fluid Inclusions to Trace Formative Fluid Evolution at the Verde and Pancho Porphyry Au Deposits of the Refugio District, Chile

by

Brian Joshua Aillaud

Dr. Adam Simon, Examination Committee Chair
Assistant Professor
University of Nevada, Las Vegas

Evolution of magmatically-derived formative fluids, and the processes that control the ratio of ore metals in porphyry and high-sulfidation epithermal deposits remain enigmatic. The Refugio district in the Maricunga Belt of Northern Chile hosts the temporally and spatially related Pancho and Verde porphyry gold deposits. Vein types at Pancho include A-veins, transitional veins, banded veins, D-veins and quartz-alunite ledges that formed by replacement. Verde East and West lack A-veins, and show an earliest vein type with transitional characteristics of A- to banded veins, banded veins and D-veins. Fluid inclusions and quartz textures were characterized by using optical microscopy and cathodoluminesence (CL). Microthermometry, and analyses using laser ablation inductively coupled plasma mass spectrometry (LA-ICP-MS) were used to constrain fluid chemistries at discrete stages in time and space, documenting the chemical evolution of the Pancho and Verde deposits.

Fluid inclusions were grouped by vein type and inclusion characteristics. A-vein liquid+vapor+daughter mineral(s) (LVD) inclusions had vapor bubbles

that comprised 10-40% with a mode of 20% of the inclusion volume by visual estimation, a halite daughter, and possible small (≤5%) opaques. Eight A-vein LVD inclusions were analyzed microthermometrically, and 12 by LA-ICP-MS. This inclusion type had salinities ranging from 34-38 wt.% NaCl eq. and homogenization temperatures of 430-510ºC. A-vein, banded vein and post-flashing banded vein liquid+vapor (LV) inclusions typically had a vapor bubble comprising 15-30% of the inclusion volume. Microthermometrically, 43 inclusions were analyzed, and 12 inclusions were analyzed by using LA-ICP-MS. LV inclusions in A-veins, banded veins and post-flashing banded veins have salinities of 3-6, 8-13 and 3-6 wt.% NaCl eq., respectively, and homogenization temperatures of 290±3ºC, 177-362ºC and 285ºC (for all inclusions except one with a Th of 278ºC), respectively. Cathodoluminesence and petrographic observations revealed no textural differences between quartz that hosted LV and LVD inclusions in A-veins. Single phase vapor inclusions (V) analyzed in banded veins have an average Cu/Au ratio of 7E3. A-vein LVD and LV inclusions have average Cu/Au ratios of 4E4 and 6E3, respectively. This is low when compared to the Cu/Au ratio of 1.5E5 for the bulk ore of porphyry Cu deposits.

Fluid inclusion data suggest that the low Cu/Au ratio in fluid inclusions is the result of a low Cu/Au ratio in the formative fluids, although the data are not inconsistent with Cu being retained in the vapor phase. This interpretation implies that the fluid chemistry was controlled by processes in the magma plumbing system prior to degassing, while vein evolution was controlled by the

pressure and temperature conditions of the country rock. Fractionation of a Cu-Fe-S phase(s) during magmatic differentiation may have preferentially sequestered Cu from the melt, resulting in a low Cu/Au ratio of the melt prior to volatile saturation.

TABLE OF CONTENTS

LIST OF TABLES

LIST OF FIGURES

CHAPTER 1

INTRODUCTION AND BACKGROUND

Introduction

Porphyry type ore deposits account for 57% of all discovered Cu, 9% of all discovered Au, and 13% of all discovered Ag (Singer, 1995). Epithermal deposits, including both low- and high-sulfidation, host 6% of all discovered Au, and 17% of all discovered Ag (Singer, 1995). Despite the significant contribution to global metal discoveries, the relationship between porphyry and high-sulfidation epithermal deposits, and the controls on ore metal grades are not well understood.

Porphyry and high-sulfidation epithermal deposits form from ore-metal-bearing aqueous magmatic-hydrothermal fluids that evolve from upper crustal magma chambers (Fig. 1). The magmatic-hydrothermal fluids rise into overlying country rock where ore metals precipitate owing to water-rock reaction, changes in oxygen and/or sulfur fugacities, cooling and/or decompression (cf., Audetat et al., 2008). Porphyry Cu deposits generally form at 1-6 km depth and temperatures from 300 to 600°C. Murakami et al. (2009) review and discuss geologically plausible processes responsible for the observed variation in metal ratios in porphyry deposits. They suggest that Au grade is controlled by magmatic processes, fluid phase separation and precipitation efficiency, noting that decreasing depth of formation generally leads to increased Au grades, and thus reduced Cu/Au ratios. High-sulfidation epithermal deposits generally form

closer to the surface at depths ≤1.5 km and at temperatures on the order of 200 to 300° C (Figure 2; Hendenquist and Lowenstern, 1994). Porphyry and high-sulfidation epithermal deposits form in belts of coeval igneous rocks associated with volcanic arcs (Richards, 2003). Processes at the slab-mantle wedge interface create melt that rises into the crust. At various levels in the mantle wedge and crust, the magma likely pools, melting and assimilating country rock, and fractionating through partial crystallization. Once the magma intrudes at a shallow level, cooling of the magma chamber and volatile saturation of the melt occurs (Burnham 1979). The exsolved fluid rises to the top of the magma chamber owing to its much lower density relative to the bulk magma. The fluid coalesces and ponds at the top of the chamber and owing to fluid expansion ($P\Delta V$), the local pressure at the top of the chamber exceeds the lithostatic pressure, and the pressure difference ($P\Delta V$) results in the fluid shattering the magma carapace (Burnham, 1979). Following on the conclusions of Burnham (1979), Candela (1991) modeled the physics of this fluid-release process which supported the conclusion that this process can occur multiple times as the magma solidification front propagates progressively toward the center of the chamber owing to irreversible heat loss. Fluid-release processes may create secondary inclusions in previously formed veins.

The physical and chemical relationship between shallow-level magmatic intrusions (i.e., 1 to 8 km depth of emplacement) and overlying Cu- and Au-bearing porphyry and high-sulfidation epithermal ore deposits has long been a

subject of debate (cf., Hedenquist and Lowenstern, 1994). Studies of the Lepanto epithermal and Far South East (FSE) porphyry systems in the Philippines have provided evidence for a genetic link between high-sulfidation epithermal and porphyry ore deposits. In the Lepanto-FSE deposits, the geometries, close spatial proximity and geochronologic constraints, are consistent with a single magmatic-hydrothermal system having formed the two deposits as a continuum (Arribas et al. 1995). Another important example of a link between high-sulfidation epithermal and porphyry deposits has been described in detail by Muntean (1998) and Muntean and Einaudi (2000, 2001) wherein they demonstrated a temporal and spatial link between several high-sulfidation epithermal and porphyry deposits located in the Refugio, Aldebaran and La Pepa mining districts of the Maricunga Belt, Northern Chile (Fig. 2). In this study, I examined high level deposits to further understand the evolution of these systems.

Background

Subduction of the Nazca plate beneath South America has created the Andes Mountains, marked by significant volcanism that is the Andean arc (Gill, 1981). The Maricunga Belt of Northern Chile marks the location of a segment of the Andean arc that was volcanically active during the Miocene, and is host to a large number of epithermal and porphyry mineral deposits that are grouped into multiple mining districts (Vila and Sillitoe, 1991; Fig. 2).

The deposits of the Maricunga Belt, with the exception of Casale Hill, have lower Cu/Au ratios than most porphyry Cu-Au deposits and are classified as Au-porphyry deposits (Fig. 3; Vila and Sillitoe, 1991; Muntean, 1998; Muntean and Einaudi 2000, 2001). For example, at Verde the Cu/Au ratio is 3E2, and Pancho is 1E3, compared with an average Cu/Au ratio for porphyry of 1E4 (Muntean, 1998).

The Verde and Pancho deposits are located approximately 1 km apart within the Refugio mining district, and are differentiated from other porphyry Cu deposits in vein assemblages and depth of formation. Au mineralization at Refugio is most prevalent in the banded veins that are not generally associated with mineralization in porphyry deposits, likely lowering the Cu/Au ratio for the bulk ore. Pancho and Verde formed at shallow paleodepths of <1 km compared to the 1-6 km depth of most Cu-porphyries (Muntean and Einaudi, 2000).

Detailed field mapping by Muntean (1998) established the spatial relationships between the deposits within the Refugio District of the Maricunga Belt (Fig. 4), as well as the locations of intrusions and vein types within the deposit, vein relationships, alteration characteristics and mineral paragenesis. Muntean (1998) also provides $^{40}Ar/^{39}Ar$ dates (±2σ) for Pancho of 23.22±0.06 Ma, Verde East of 23.28±0.02 Ma, and 23.27±0.06 Ma of Verde West, providing compelling evidence for a temporal link between the Pancho and Verde deposits (Table 1).

While the Pancho and Verde deposits are contemporaneous and spatially

associated, their geometry and observable vein types are distinct from one another. Vein types will be discussed in detail in a later section. Pancho is vertically telescoped (i.e., resembling a cone), with spatially overlapping zones of vein types and alteration. A-veins are the earliest observed vein type deep in the Pancho system. Verde is not as telescoped and A-veins have not been identified to date. While A-veins at Verde may be present at depth, transitional veins are the earliest and deepest vein type at the Verde deposit (Muntean, personal communication, 2009).

In addition to being telescoped, the Pancho deposit has a significant cross-sectional exposure (Fig. 5). The upper 400m of the Pancho deposit are exposed on a hillside. Collared near the bottom of the hillside, a deep (600m) drill hole has been drilled, hole P-8-C in Figure 5, providing approximately one kilometer of vertical exposure through the deposit. Increased cross-sectional exposure provides a wide range of environments to study how the magmatic-hydrothermal fluids evolved as they rose through the system.

Given the very low Cu/Au ratios in the Maricunga Belt (Fig. 3),the close temporal and spatial connection between the apparently different Pancho and Verde porphyry deposits, and the close spatial and temporal connection of porphyry mineralization and weak high-sulfidation eipithermal mineralization in the Refugio district, this study aimed to trace the fluid evolution from the earliest to latest magmatic-hydrothermal fluids and to document a chemical link between the porphyry and high-sulfidation epithermal styles of mineralization. Further, this

study sought to test two working hypotheses that potentially explain the low Cu/Au ratio of the deposit. The first hypothesis, proposed by Muntean and Einaudi (2000), suggested that Cu did not precipitate during a flashing event owing to the loss of S to the vapor phase. The second hypothesis proposes that a magma exsolved a fluid with an initially low Cu/Au ratio. The low Cu/Au ratio in the formative magmatic-hydrothermal fluid was primarily responsible for forming a deposit with a low Cu/Au ratio. The mechanisms for both of these hypotheses, including flashing and possible magmatic controls will be discussed in later sections.

Vein Types

Veins form as the result of hydrothermal fluids moving through fractures in country rock. Mineral precipitation occurs as a result of changes in pressure (P), temperature (T) and/or fluid composition (X). Changes in P-T-X occur owing to the upward migration of the fluid from the magma chamber, or deep crust, and interaction with the host rock (i.e., water-rock reaction). Veins are the result of specific P-T-X conditions at a specific point in time and space, and reflect precipitation of minerals into fluid-filled space. By mapping the locations of different vein types within a deposit and documenting cross-cutting relationships, the formation of various vein types in time and space can be established. The characteristics of veins, including fluid inclusions that may be contained within the veins, can place constraints on the P-T-X conditions at the time of vein formation. Combining these data from the different vein types in a single deposit

may allow one to track how P-T-X conditions of the formative fluids evolved through time and space.

Vein types in the Refugio district have been named using the Gustafson and Hunt (1975) classification scheme as reported and described in Muntean (1998) and Muntean and Einaudi (2000). Table 2 summarizes the nomenclature and vein descriptions. Gustafson and Hunt (1975) described the porphyry-Cu ore deposit at El Salvador, Chile, including the intrusions and the veining. Their description of veins at El Salvador has been used to describe the veining in many other porphyries, as vein types are broadly consistent between porphyry deposits. Using previously published nomenclature for the veins observed in the Refugio District (Muntean (1998, 2006) and Muntean and Einaudi (2000,2001)), the veins described in this study have been classified as A-veins, transitional veins, banded veins, D-veins and quartz-alunite ledges.

A-veins

A-veins (Fig. 6) in the Refugio District were divided into early and late subtypes by Muntean and Einaudi (2000). Early veinlets are generally thin (<0.2cm), wispy, have alteration halos and irregular vein walls. These are subsequently cross-cut by more continuous, straighter, thicker (up to 2 cm) A-veins that lack alteration halos, and occur with magnetite and/or minor chalcopyrite. No surface exposure, mining exposure or drill core has led to identification of A-veins at Verde East or West.

Transitional Veins

The deepest veins at Verde studied to date have been described as transitional veins (Fig. 7; John Muntean, personal communication, 2009), who described them as follows. These veins resemble A-veins, but they contain the characteristic dark quartz associated with banded vein-types, described below, in discontinuous streaks and zones, rather than continuous bands. They lack alteration halos, and the vein walls are slightly wavy. Transitional veins at Verde could very well represent a vein type that is a transition between the vertical zonations of deeper A-veins, and shallower banded veins, described below. Quartz in transitional veins appears subhedral, but does not elongate towards vein center. Transitional veins were originally described and exist at Pancho (Muntean, 2006). Pancho transitional veins were not studied herein as a separate vein category.

Banded Veins

Banded veins (Fig. 8) have straight to rarely slightly irregular walls, lack alteration halos and contain botryoidal dark bands that run parallel to sub-parallel to vein walls. Banded veins cut and offset A-veins and transitional veins. This vein type contains locally vuggy vein centers, a clear difference from A-veins. Banded veins may also have been reopened by later banded veins, where repeated banding events occurred.

Banded veins constitute most of the ore at Refugio and represent the mineralization from subeconomic porphyry Cu-Au deposits to economic porphyry

Au deposits (Muntean, 2000). While “banded vein” can also describe the more common banded veins in low-sulfidation epithermal deposits that form by flashing at much lower temperatures (e.g., Henley and Hughes, 2000), the term is used herein to describe specifically the ore stage veins of the deposits of the Refugio District.

D-Veins

D-veins (Fig. 6) cut A- and banded-veins as well as intrusions, and are composed dominantly of pyrite with other sulfides (Muntean and Einaudi, 2000) and anhydrite (Gustafson and Hunt, 1975). Pyrite, other sulfides and anhydrite were all observed in D-veins in this study. Phyllic alteration halos, zones of feldspar destructive (Gufstafson and Hunt, 1975) or quartz-sericite-pyrite (Muntean and Einaudi, 2000) wallrock alteration surrounding the veins, are visible around D-veins. Due to the late timing of D-veins, and the sudden appearance of abundant sulfide, these veins may represent the transition from porphyry to epithermal mineralization (Muntean and Einaudi, 2001).

Quartz-Alunite Ledges

The last “vein type” at Refugio is the quartz-alunite ledges (Muntean and Einaudi, 2000, 2001, Fig. 9) which in fact are not veins, but formed as a result of wallrock alteration and silicification (Jean Cline, personal communication 2010). Quartz-alunite ledges result from the mixing of magmatic and meteoric waters in the near surface environment, are steeply dipping, and contain quartz, alunite, pyrite and rutile (Muntean and Einaudi, 2000).

Fluid Inclusions

Roedder (1984) defines fluid inclusions as aliquots of fluid trapped during crystal growth or fracture healing. Fluid inclusions as observed in the modern sample may be filled with matter in the gas, liquid or solid state, or a mixture of different phases, provided that at the time of entrapment the matter was a fluid.

In order for the P-T-X conditions recorded by a fluid inclusion to be useful, the relative timing of trapping, specifically with respect to the crystal hosting the inclusion, must be determined. Three fluid inclusion origins are recognized; primary, secondary and pseudo-secondary. Primary inclusions were trapped during crystal growth. Thus, an inclusion of primary origin is an aliquot of the fluid from which the host crystal surrounding the inclusion formed. Secondary inclusions are fluids trapped in healed fractures. Unlike primary inclusions, secondary inclusions do not necessarily represent a fluid that was present during crystal growth, but rather a fluid that bathed the fracture after the crystal had formed. Pseudo-secondary inclusions form in a healing fracture that terminates at a growth zone. Pseudo-secondary inclusions are thus constrained to time of formation of the terminating growth zone, but are not concurrent with the host crystal that surrounds the inclusion. If the origin of the fluid inclusion cannot be determined, it is of unknown origin. Unknown inclusions must be of primary, secondary or pseudo-secondary origin, but the textural features are not sufficient to constrain the inclusion's origin.

Criteria must be established in order to properly identify the origin of each

fluid inclusion. Roedder (1984) presents detailed permissive criteria for determining the origin of fluid inclusions. Goldstein and Reynolds (1994) present compelling criteria for the determination of fluid inclusion origin that reduce ambiguity of inclusion origin. They observe and discuss the potentially complex geometry of a single fracture (e.g., curved fractures in minerals that fracture conchoidally), fractures that trace cleavage planes, many generations of fractures, and the migration of inclusions after formation as complications to determining origin. Goldstein and Reynolds (1994) also point out that inclusionists often do not precisely describe their criteria used in a given study.

Inclusions were categorized as primary, primary(?), psuedo-secondary, secondary, secondary(?) and unknown (Roedder, 1984, Jean Cline, personal communication). Primary fluid inclusions are interpreted to represent aliquots of the fluid(s) from which the host mineral precipitated (Roedder, 1984). Secondary inclusions are inclusions that were formed after the formation of the host crystal; e.g., along a healed fracture. In this study, primary(?) and secondary(?) inclusions have textural evidence suggesting the inclusions are primary or secondary inclusions, but the textures are not compelling. Primary(?) inclusions are those with a seemingly random three dimensional distribution that are spatially related within a zone of the host crystal, but cannot be demonstrated to be trapped in a growth zone; i.e., they do not appear confined to any observable fracture plane. The goal of this thesis was to characterize inclusions that could be genetically related to the ore-forming events and, thus, I focused on primary

or primary(?) fluid inclusions. While secondary inclusions can be useful, they were not characterized in this study. Therefore, lack of discussion of secondary inclusions should not be interpreted as an indication of their absence.

Fluid inclusions that were trapped at the same time, from the same fluid, are classified as a fluid inclusion assemblage (FIA; Goldstein and Reynolds, 1994). A FIA will contain fluid inclusions that have similar phase ratios, unless the FIA formed during a boiling event, or if the inclusions have undergone necking or leaking after formation. A boiling assemblage will contain vapor-rich and liquid-rich inclusions, with or without daughter mineral(s) (Roedder and Bodnar, 1980). These inclusions formed at the same time, during boiling or immiscibility, when two immiscible fluid phases were forming from a single parental fluid. Necking is a process whereby the shape of the fluid inclusion changes as a result of the recrystallization of the host mineral, to effect a reduction of the surface area of the inclusion (Roedder, 1984). This may result in the separation of one inclusion into two, inclusions which may have differing phase ratios. If a group of inclusions exhibit the same phase ratios, or is a boiling assemblage, the arrangement of the inclusions in a quartz crystal may allow one to characterize the inclusions, and thus the assemblage, as primary, secondary, etc. The classification scheme for determining inclusion origin in this study is based on Roedder (1984) and, for the purpose of clarity is discussed below.

Muntean (1998) studied fluid inclusions from the deposits of the Maricunga

Belt. His study was petrographic and microthermometric in scope and aimed to determine the depth of formation of the deposits, and compare the salinities and trapping temperatures of A- and banded veins in the Maricunga Belt, to deposits outside the Maricunga Belt. Muntean (1998) used a classification scheme based on Nash (1976), and Goldstein and Reynolds (1994), where he describes three-dimensional random arrays found in A-veins as unknown inclusions of likely secondary origin. This classification is consistent with Roedder (1971). Muntean (1998) studied groups of inclusions where fluid inclusion assemblage origins could not be determined. Muntean (1998) studied over 1000 samples, approximately 250 of which were studied petrographically as thin sections. His sample descriptions are contained in an appendix of his dissertation and an unpublished lab notebook. From these samples, he reported microthermometry from nine samples from the Maricunga Belt, three samples from Verde, two samples from Pancho, three from Casale Hill and one from Cavancha. The three samples from Verde were RV027, RV041 and DD-25 84-86m, representing only banded veins. Samples LYR-2 33.9m and LYR-2 45.7m from Pancho targeted A-veins. Samples ALC-1 292.8m, ASC024 and ALC-1 19.9m, all from Casale Hill, targeted A-veins, banded veins and polymetallic veins, respectively. Microthermometric results from Muntean (1998) are presented in Table 3. Salinity and temperature of homogenization (Th) data in Muntean (1998) can vary widely within groups, indicating that FIAs from different fluids may have been lumped into single groups. He addresses the variation in his dissertation;

see Muntean (1998) for a complete description of the variation in Th in his samples. Muntean (1998) reports that in A-veins, Th values have a range of at least 450ºC in the one group of fluid inclusions from Casale Hill in which microthermometry was done, though the halite dissolution temperature was tightly constrained. In the group from sample LYR-2 33.9m, five inclusions, reported as being of secondary origin, have a range of Th values from 230-270ºC. In this group, Muntean (1998) reported salinities as 31.9 wt.% NaCl eq. for 2 inclusions with Th values of 230 and 245ºC. One inclusion in this group had a Th of 250ºC and yielded a salinity of 33.5 wt.% NaCl eq. The remaining two inclusions homogenized at 255 and 270ºC, but salinities were not reported. The one inclusion group from sample LYR-2 45.7m, a Pancho A-vein sample, contained only two inclusions that did not homogenize at or below 700ºC; the highest temperature achieved by the fluid inclusion stage in the Muntean (1998) study. The inclusions had reported salinities of 78.3 and 84.5 wt.% NaCl eq., determined by halite dissolution.

Muntean (1998) and Muntean and Einaudi (2000, 2001) characterize banded veins as having dark bands of inclusion rich quartz within quartz veinlets. These studies conclude that the dark bands represent an important event in the formation of mineralization at Refugio, particularly at Verde, and the authors postulate that the banded veins may be a key element in understanding the evolution of magmatic-hydrothermal fluids in these systems. A discussion of the background of the inclusions, both mineral and fluid, in the banded veins requires

some introduction to the hypotheses of Muntean and Einaudi (2000) regarding the formation of these veins, and the precipitation of the mineral phases found within the dark bands.

Banded veins likely formed from a flashing event; i.e., a sudden drop in pressure from lithostatic to hydrostatic, resulting in the sudden immiscibility of the fluid (Muntean 1998). Banded vein fluid flashing would cause a significant decrease in the ability of the fluid to contain dissolved solids, resulting in the sudden precipitation of many of the elements dissolved in the fluid. The flashing event is manifested as vapor-rich fluid inclusions and micron- to submicron-sized grains of magnetite and gold that occur in continuous botryoidal bands that cut across grain boundaries of quartz crystals (Muntean and Einaudi, 2000) (Fig. 11). Muntean and Einaudi (2000) hypothesized that a fluid which experienced flashing would precipitate Fe and Au as non-sulfide phases; i.e., Fe as magnetite, and Au as native Au or as Au hosted within magnetite. Copper, however would remain in the low-density magmatic-hydrothermal fluid owing to the volatility of and preference for S to remain in the low-density vapor (Drummond and Ohmoto, 1985) as a Cu-S complex (cf., Heinrich et al., 1999); i.e., the magmatic-hydrothermal fluid did not saturate in a Cu-bearing sulfide such as chalcopyrite. Silica in solution would precipitate as a silica gel, later recrystallizing to quartz.

A challenge to the study of fluid inclusions in banded veins arises from the fact that the fluid inclusions within banded veins were initially trapped within the silica gel, and may not record the conditions of the flashing event (Muntean 1998,

Muntean and Einaudi 2000), i.e., the inclusions are primary to the quartz crystalization, but not to the silica gel precipitation. Muntean and Einaudi (2000) detail the flashing event where silica gel is precipitated, along with native gold, magnetite, but only trace amounts of sulfides. Upon cooling, the vapor-charged silica gel would have recrystallized to quartz and would have eventually intersected the liquid saturation curve and condensed a liquid. This process may account for the wide range of salinities of the fluid inclusions. Given the changing temperature, liquid condensation, and variable salinities of the liquid, it it is quite possible that the silica gel may have been unable to preserve the chemical composition of the flashed fluid.

Despite difficulties in interpreting the inclusions found within the banded veins, both the current study and Muntean (1998) analyzed fluid inclusions in banded veins. The results of the Muntean (1998) microthermometry study are contained in Table 3. Values from Casale Hill are contained in Table 3, but will not be discussed in detail, as this study looked only at Verde and Pancho, not Casale Hill. The Th and salinity data reported by Muntean (1998) for Verde samples are 215->400ºC and 3.4-37.4 wt.% NaCl eq. Excluding one group of inclusions from RV027, the Th for inclusion groups generally cluster fairly closely, with ranges for inclusion groups of secondary origin no greater than 50ºC. Primary inclusion groups generally show a greater spread of Th values within groups ranging from 25ºC to 185ºC (reported as ≥185ºC). The salinity of the inclusions generally clusters much more closely. In Group 1 from RV027 the

salinity values range from 31.9 – 37.4 wt.% NaCl eq. Muntean (1998) interpreted each of the FIAs in the Verde and Pancho samples as boiling assemblages, and explained the range of Th values to be the result of heterogeneous trapping.

Muntean (1998) also reports Th values for polymetallic veins at Casale Hill that are analogous to the D-veins. Homogenization temperatures of fluid inclusions (n=14) in these veins range from 120-200ºC, with most inclusions (n=9) homogenizing between 170-190ºC in the two inclusion groups studied at Casale Hill. The low Th suggests a lower trapping temperature than the inclusions found in A- and banded veins, which led Muntean (1998) and Muntean and Einaudi (2001) to suggest that these veins occurred late in the system when temperatures had significantly cooled.

Fluid inclusions in quartz-alunite ledges were not analyzed by microthermometry by Muntean (1998) owing to the insufficient size for observation in a heating/freezing stage. While some of the quartz-alunite ledges do contain small inclusions that lack daughter minerals in vug filling quartz that post-date the initial mineralization of the ledge, these are somewhat rare. These inclusions may contain fluids that represent the very last fluids associated with the deposit. Conversely, they may also only contain meteoric waters that were trapped after cessation of magmatic-hydrothermal processes that were responsible for the formation of the ore body. No such inclusions were found in samples used for this study, or studied in previous work.

CHAPTER 2

METHODS

Methods

Sample Selection

Samples were selected from the sample collection described in Muntean (1998), and by John Muntean during subsequent consulting trips he did for Kinross Gold Corp. in 2005 and 2006. Dissertation samples are described in Muntean (1998). Descriptions of core samples from 2005 and 2006 are contained in unpublished consulting reports by Muntean; however, no previous thin section descriptions exist for the deep samples. A detailed review of Muntean (1998) and published literature, as well as a petrographic review of 256 thin sections from the Maricunga Belt which resulted in the selection of 12 samples for detailed study in this project, based on the following criteria. Thin sections were made for the samples that had not previously been described. These samples included deep samples from new core, and one shallow sample from a quartz-alunite ledge. Refugio thin sections were evaluated based on sample location and cross-cutting relationships that provided space-time constraints within deposit formation. One hundred sixty-eight thin sections from the Refugio District were studied using standard petrography to identify samples with the most promising fluid inclusion and vein assemblages. Samples P-8-C 600 (Pancho, A- and D-veins), P-8-C 539_1 (Pancho, A-veins), P-8-C 539_2 (Pancho A-veins), P-8-C 539_3 (Pancho, A-veins), P-8-C 486 (Pancho, A- and D-

veins), RP028 (Pancho, quartz-alunite ledge), RP054 (Pancho, banded veins), RP058 (Pancho, banded veins), V6.5NWC 342.4 (Verde, transitional veins), DD25 84-86m (Verde, banded veins), DD35 148-150m (Verde, banded veins), and RV027 (Verde, banded veins) were selected for detailed analysis. Doubly polished fluid inclusion plates were prepared by Spectrum Petrographics and Burnham Petrographics.

The 12 samples came from both surface and drill core samples (Fig. 4). Four locations at Pancho provide 8 samples, five of which are from drill hole P-8-C (Fig. 5). Verde East and West provided two sample locations each, with one sample from each location.

Geologic Setting of Samples

Pancho

The Pancho deposit is mainly hosted by a quartz diorite porphryry stock, associated intrusive breccias, and overlying andesite flows and breccias. (Muntean and Einaudi 2000). Alteration and vein-types at Pancho are similar to those characteristic of porphyry-Cu deposits, with a potassically altered core that is overlain and cut by pyrite-albite-clay alteration (Muntean and Einaudi, 2000). Four vein-types have been characterized in the porphyry environment at Pancho, which are, from earliest to latest, A-veins, transitional veins, banded veins and D-veins. Banded veins are present throughout but are most abundant in the upper levels of the intrusive rocks near the contact with the overlying volcanic rocks. The banded veins cut the A-veins. The highest Au grades (>1 ppm) are

associated with banded veins. Zones of A-veins and potassic alteration in the deeper parts of Pancho typically grade grades of 0.5-1 ppm Au and 0.05 to 2% Cu.

Verde

The Verde deposit is mainly hosted by intrusive breccias and dacite porphyry intrusions, and is composed of 2 distinct zones, Verde West and Verde East. Surface exposure at Verde East, at time of discovery, was limited by overlying, post-mineralization volcanic rocks. Both Verde West and Verde East lack potassic alteration are centered on late intra-mineral quartz diorite porphyry stocks that truncate much of the ore. Verde is characterized by abundant banded veins with some transitional veins present in the deepest core holes. Gold grades are closely associated with the banded veins at Verde (Muntean and Einaudi, 2000).

Petrography

Thin section petrography was performed on a Nikon microscope with an attached Nikon Cool Pix 4500 camera and a Nikon microscope with a Nikon D50 digital single lens reflex camera. Fluid inclusion assemblages, as well as quartz that showed textural evidence of paragenesis or processes of formation, were photographed and labeled for identification in later analyses. Volume percent estimations were made of each phase present in an inclusion by visual estimation. A broad sampling of photomicrographs obtained from this process is available in the Appendix titled Photomicrographs.

Cathodoluminescence

When quartz precipitates from an aqueous fluid, the incorporation of certain trace elements into the quartz lattice (e.g., Ti, Al) may result in luminescence of quartz when stimulated by an electron beam. If quartz overgrowths form from successive, compositionally distinct fluids, cathodoluminescence (CL) may allow one to visually differentiate discrete growth zones. The CL technique has shown great promise in studies of poly-generational fluid inclusions at other porphyry deposits (e.g., Redmond et al., 2004; Rusk et al., 2006, 2008b; Pudack et al., 2009). In the current study, CL was used in an attempt to differentiate quartz growth zones and, thus, potentially different fluid inclusion assemblages. Growth zones in quartz within a single crystal were generally identifiable as distinct bands. Growth zones, in this study, represent small events occurring during the growth of a crystal that likely changed the trace element content of the quartz crystal only slightly. Different quartz generations reflect formation under different conditions that may include differences in temperature, pressure, chemistry, rate of crystallization, etc. Distinct quartz generations appear as zones within veins under CL where two or more generations of quartz occur throughout the veins.

Cathodoluminescence (CL) analysis was performed by using a JEOL JXA-8900R wavelength dispersive X-ray spectrometer and energy dispersive X-ray spectrometer electron probe microanalyzer (EPMA) equipped with an Oxford Mini CL detector to highlight growth zones and generations of quartz contained

within single crystals and within veins. EPMA settings were 20 kV and 30 nA, and images were acquired with two-pass beam scans for a total acquisition time of 2 minutes.

Each CL image required optimization of equipment settings to observe identifiable bands of grey within the field of view. Growth zones generally appeared as thin laminae that were difficult or impossible to correlate with surrounding quartz owing to strong changes in the appearance of growth zones between crystals. To highlight generations of quartz across veins, mosaics of CL maps had to be created. To stitch the mosaic, each image of the mosaic had to be adjusted by standardizing each generation of quartz to a standard grey. This was done using the GNU Image Manipulating Program, beginning with an image showing well defined quartz generations with distinct greys for each, then manipulating the levels of an adjacent image to match the first. This process was then repeated using the previously adjusted image as the “standard” for the next image. Mosaics allowed another look at various quartz generations, thus allowing quartz generations within a single vein to be visible. Further, mosaics allowed cross-cutting relationships to be studied that would otherwise be cryptic (Fig. 12, Fig. 13; a larger selection of CL images is contained in the appendix Cathodoluminesence). While this process removed the semi-quantitative nature of this technique, making it somewhat subjective, it allowed determination of the paragenesis of the quartz veins.

Microthermometry

Microthermometry was performed by using a Linkham THMSG-600 stage on an Olympus microscope for freezing point depression measurements, and heating measurements to 300º C. Homogenization temperatures above 300º C were measured by using a USGS Heating/cooling stage on a Nikon microscope. The stage was calibrated using synthetic fluid inclusions at -56.6º C and 374.1º C, and an ice water bath at 0.0º C.

Two useful microthermometric measurements may be obtained from liquid-vapor-daughter crystal (LVD) inclusions; halite dissolution temperature (TmH) and homogenization temperature (Th). Final homogenization may be observed as one of two phase changes; either halite dissolution, or liquid-vapor homogenization to the liquid. In this study, final homogenization was observed only as liquid-vapor homogenization to the liquid. The halite dissolution temperature is recorded and used to calculate the salinity of the fluid inclusion. Liquid-vapor (LV) inclusions require two microthermometric measurements, the temperature of final ice melting (Tm) and homogenization of the liquid and vapor phases. The LV inclusions in this study homogenized to liquid by vapor bubble disappearance. Vapor (V) inclusions could not be analyzed using microthermometry because only a single vapor phase was visible in the inclusions.

For LV and LVD inclusions, the equations of Bodnar and Vityk (1994) were used to convert measured Tm and Td into salinity. To calculate salinity from

measured Tm in LV inclusions, the freezing point depression (fpd) is obtained by taking the absolute value of the negative temperature (fpd=|Tm|), and then entering it into the equation:

$$\text{salinity} = 1.78(\text{fpd})-4.42\text{E-}2(\text{fpd})^2+5.57\text{E-}4(\text{fpd})^3$$

To obtain the salinity of LVD inclusions, the equation

$$\text{salinity}=26.242+0.4928\Psi+1.42\Psi^2-0.223\Psi^3+4.129\text{E-}2\Psi^4+6.295\text{E-}3\Psi^5$$
$$-1.967\text{E-}3\Psi^6+1.1112\text{E-}4\Psi^7$$

is used, where $\Psi=\text{Td}(^{o}\text{C})/100$ (Bodnar and Vityk 1994). These equations yield NaCl weight percent equivalence values (wt.% NaCl eq.) for the fluid in the inclusion. This value may be used as an internal standard for LA-ICP-MS work.

Laser Ablation Inductively Coupled Plasma Mass Spectrometry

Laser ablation inductively coupled plasma mass spectromety (LA-ICP-MS) was performed by using an Agilent 7500ce ICP-MS coupled to a GeoLas LA system by using a He-Ar carrier gas at the Virginia Polytechnic Institute and State University (VPI) Fluid Inclusion Laboratory. The instrument was calibrated by using the National Institute for Standards and Technology 610 synthetic glass standard. The laser pulse rate was set at 5 Hz, and the beam energy was set at 150 mJ. An initial analyte menu of 16 elements (Na, Mg, Al, Si, K, Ca, Ti, Fe, Cu, Zn, As, Ag, Sb, Ba, Au and Pb) was used with a dwell time of 10 ms per element. This analyte menu consistently returned results for Au below the limit of detection (LOD). In an attempt to decrease the LOD for Au, the dwell time for Au was increased to 30 ms. By increasing the dwell time for elements with lower

concentrations that are of particular value to the study, one may be able to quantify the concentration of that element, without sacrificing the number of elements in the analyte menu. Increasing the dwell time for Au failed to produce the desired effect; however, increasing the dwell time and reducing the analyte menu produced promising results, as analyzing for fewer elements allows more sweeps per element per analysis (cf. Heinrich et al., 2003). The analyte menu was reduced to 8 elements (Na, Si, Fe, Cu, Zn, As, Sb and Au), and the dwell time for Au was increased to 50 ms. Using the eight element menu reduced significantly the LOD for Au and allowed quantification of Au in fluid inclusions; e.g., one calculated LOD for Au with the 16 element menu and 10 ms dwell time on all elements was 1.1E-2 Au/Na compared to 7.0E-7 Au/Na for the 8 element menu and 50 ms dwell time on Au. It should be noted that analyte menu length and dwell time did not guarantee a high or low LOD, but simply increased the likelihood of having a high or low LOD, i.e., some analyses using the 16 element analyte menu achieved a low LOD, and some 8 element analyses had a high LOD, but in general, less elements with longer dwell times achieved lower LODs.

Since identifying FIAs is paramount to the study of fluid inclusions, all or several inclusions from the same assemblage would ideally be analyzed by LA-ICP-MS. However, individual inclusions within an FIA are often spatially tightly constrained. This presents significant challenges when analyzing an FIA by using LA-ICP-MS. The host quartz frequently can withstand the analysis of only one or two inclusions within an FIA before fracturing and leaking the other

inclusions within the FIA. Quartz may also become shrouded by debris from previous ablation runs. Separation between inclusions generally needed to exceed approximately 5+ times the diameter of the laser, which was set, at a minimum, to the maximum diameter of the inclusion. While analysis of an entire FIA is ideal, unfortunately single inclusions must frequently be quantified by LA-ICP-MS without the data from the rest of the assemblage.

To analyze fluid inclusions, the diameter of the laser beam was set slightly greater than the maximum diameter of each fluid inclusion such that the entire fluid inclusion was ablated together with a minimal volume of surrounding matrix quartz. The transient signal was deconvoluted and processed by using the Signal Integration for Laboratory Laser Systems (SILLS) MATLAB based program to remove the addition of elements present in the host from the fluid inclusion signal interval such that the reported composition of the fluid inclusion represents only those elements contained in the fluid inclusion with no contribution from the host (cf. Heinrich et al., 2003). Absolute concentrations of Na in each fluid inclusion are determined by correcting the microthermometrically-determined wt.% NaCl eq. for the presence of other metal-chlorides via the equation $NaCl_{true}=NaCl_{equiv}-0.5\bullet\sum C_{nCl}$, where n is all major cations. This equation assumes that all major cations in the fluid inclusion were present as chloride salts (Heinrich et al., 2003). The use of Na as an internal standard has been evaluated previously (Heinrich et al., 2003; Simon et al., 2007). The LA-ICP-MS raw data are in units of counts per second (cps). By

converting all element values to ratios against the applicable internal standard, one may calculate the absolute concentrations of each element. Since microthermometric data were limited for the inclusions analyzed, element "concentrations" are reported as ratios relative to the Na cps. The low density of a gas phase compared to a liquid phase means that V inclusions have a lower atomic density compared to LV and LVD inclusions. Further, the low mass makes V inclusions generally difficult to detect the abundance of elements present in low concentration via LA-ICP-MS. V fluid inclusions are of most interest in the banded veins where they occur as primary inclusions that may record metal ratios from gold deposition, and where they are most likely to have sufficient mass, due to larger volumes. Ratios of individual elements for fluid inclusions are given as the unitless ratio cps/cps, where the numerator is the element of interest (e.g., Au or Cu) and the denominator is Na. Comparing two elements may be accomplished by taking the ratios of the ratios against the internal standard (i.e. Na). Thus, the absolute ratio of Cu/Au may be obtained by canceling the Na from the ratio [Cu(cps)/Na(cps)]/[Au(cps)/Na(cps)]. The concentrations simply remain unknown. The use of internal standard ratios has been used by Seo et al. (2009). The benefits of using ratios is discussed by Klemm (2005), wherein he argues that ratios are a better way to examine the data from fluid inclusion analyses, as it eliminates error, rather than compounds it. That is, when LA-ICP-MS data is converted into absolute concentrations by use of microthermometric data, the errors from both LA-ICP-MS and

microthermometry are propagated into the concentration. However, when element ratios are used error only arises from LA-ICP-MS.

In addition to analyzing fluid inclusions by using LA-ICP-MS, spot analyses of quartz were performed by using the same instrument settings. Beam spot size was changed based on the quartz that was being ablated; i.e. where quartz generations or growth zones were tightly spaced, small beam sizes were used, and when entire crystals, or multiple crystals, were analyzed, large beam sizes were used. Silicon was chosen as the internal standard to deconvolute transient signals from quartz as this removes beam spot size weighting owing to increased mass ablated using large spot diameters.

CHAPTER 3

RESULTS

Results

A-Veins from Pancho

Petrography

A-vein descriptions are contained in Table 2. A-vein quartz was a poor fluid inclusion host, owing to small grain sizes. This caused difficulty in grouping inclusions as FIA, and determining origin. Most FIAs studied in A-veins were of primary(?) origin. This designation was given to groups of inclusions that shared the same phase ratios and were randomly three-dimensionally distributed throughout the host crystal. No primary or primary(?) FIAs were observed containing inclusions that represented fluid immiscibility. Using phase ratios as a tool for recognizing assemblages also aided in eliminating FIAs that contained inclusions that are necked. Goldstein and Reynolds (1994) cover several criteria to distinguish necked inclusion including all liquid inclusions and irregular inclusion shapes. No all liquid inclusions were used in this study. A summary of fluid inclusion petrographic observation is contained in Table 4. LVD inclusions (Fig. 14) contained a vapor bubble comprising 10-40 volume% of the inclusion, with a mode of 20%. LVD inclusions hosted a halite daughter crystal that comprised 5-25% of the inclusion volume, and opaques that constituted ≤5 volume %. LV inclusions (Fig. 15) were also observed in A-veins as primary(?) inclusions. These inclusions typically contained a vapor bubble that comprised

15-30 volume % of the inclusion. No primary or primary(?) V inclusions were observed in the A-veins. Many trails of secondary V inclusions are present in A-veins; these are generally small (~1 micron) inclusions (Fig. 16). Secondary assemblages were not the focus of the study, so exact characteristics were not recorded. However, the relationship between the phase ratios, size and location of secondary FIAs is useful to determine the origin of potentially unrelated inclusions that may be of primary origin. Trails of secondary inclusion FIAs were observed to locally cross three-dimensional groups of much larger (~5 micron) LVD inclusions. Since these two inclusion groups show very different phases, different sizes and different distributions throughout the crystal, these were interpreted as different FIAs, not boiling assemblages. Muntean (1998) reported boiling assemblages in shallower A-veins relative to those described in the current study. I did not observe boiling FIAs of any origin in the drill hole P-8-C A-vein samples studied. I observed V inclusions as unknown inclusions or as secondary FIAs in the deep A-veins, but V inclusions were not observed coexisting with liquid-rich or brine inclusions representative of an immiscible assemblage.

Microthermometry

Only LV and LVD inclusions contained sufficient liquid to facilitate the observation of Tm and Th, and were considered to be of potential primary origin (Sample P-8-C 539_2, Table 5). Thus, no microthermometric data were obtained from V inclusions in A-veins.

Microthermetric analyses of A-vein LVD inclusions from Pancho (n=8, 3 FIA) yielded salinities ranging from 36.0-38.4 wt.% NaCl eq. and final homogenization temperatures of 430-510ºC (Table 5). The individual FIAs have Th ranges of 430-510ºC for FIA 3, 470-510ºC for FIA 4 and 460 for FIA 4.5.

Pancho A-vein-hosted LV inclusions have ice-melting temperatures (Tm, n=2, 1 FIA) of -5.6 and -2.7 ºC, and homogenization temperatures (Th) (n=2, 1 FIA) of 290 and 287ºC. The Tm data correspond to salinities of 8.7 and 4.5 wt.% NaCl eq. based on freezing point depression measurements and using the equations of Bodnar and Vityk (1994, Table 5).

LVD inclusions in A-veins have an average Th of 479 ±32 ºC, and an average salinity of 37±1.4 wt.% NaCl eq., calculated using the equations of Bodnar and Vityk (1994). The highest measured Th is 510ºC in an LVD inclusion. Table 5 contains microthermometric data, and all microthermometrically-determined salinities and Th are presented graphically in Figure 17. Inclusion salinity and Th are also plotted as histograms for LV and LVD inclusions in Figure 18.

Cathodoluminesence

CL and petrographic observations revealed no textural differences between quartz that hosted LV and LVD Inclusions. However, some differences between quartz generations and quartz growth zones were seen in A-veins (Fig. 12). The CL differences observed in A-veins were visible as growth zones when acquisition conditions were optimized for individual crystals. Comparison

between crystals was not reasonable, as the grey levels had to be modified in an image processing software, and could be adjusted to match any growth zones by changing the adjustment. Quartz generations observed in CL were useful to identify cross-cutting relationships where veins appeared to truncate at vein intersections. With continuous features, i.e., a cross-cutting vein, standard greys could be maintained across mosaics.

Laser Ablation Inductively Coupled Plasma Mass Spectrometry

A-vein LVD (n=12) and LV (n=9) inclusions have average Cu/Au ratios (± the standard deviation of the mean ($1\,\sigma_{\bar{x}}$)) of 4E4±2E4 and 7E3±2E3, Cu/Na ratios of 0.1±0.05 and 0.1±0.06, and Au/Na ratios of 5E-5±3E-5 and 5E-5±3E-5, respectively (Table 6). Inclusions analyzed by LA-ICP-MS may not have been analyzed by microthermometry. LA-ICP-MS data for fluid inclusions are contained in Table 7. Average elemental ratios in fluid inclusions are plotted in Figure 19.

Quartz in A-veins ("spot analyses," n=18) have average Cu/Si, Au/Si and Cu/Au values ($\pm 1\,\sigma_{\bar{x}}$) of 1.5E-3 ± 7.6E-4, 7.9E-7 ± 4.6E-7, 6.6E3 ± 2.2E3, respectively (Table 9). Bulk quartz analyses are given as silicon ratios (Table 8). A summary of the Cu, Au and Cu/Au values for all quartz analyses is contained within Table 9. Average elemental concentrations in quartz are plotted in Figure 19.

Banded Veins From Pancho and Verde

Petrography

Descriptions of banded veins are in Table 2. Banded veins contain dark botryoidal bands that cut quartz grain boundaries. The dark bands owe their color to dense populations of inclusions, both mineral and fluid. The fluid and mineral inclusions in dark bands are generally sub-micron, and impart a dark color visible in hand sample comparable to the white color imparted by fluid inclusions in bull quartz. In some cases, individual crystals contain growth zones that appear similar to the banded nature of the vein, exhibiting an inclusion-rich core, an inclusion-free rim, and possibly a repeating pattern of inclusion-rich quartz, followed by inclusion free-quartz (Fig. 20). The inclusion-rich zones are referred to as “dark quartz,” and inclusion-free or inclusion-poor quartz is referred to as “clear quartz” (Fig. 20). These terms refer to the dark color of the band when observed in hand sample and thin section. Large fluid inclusions exist in banded veins both inside and outside the dark bands. V inclusions larger than 1 micron were only found as primary inclusions in the banded veins.

LV inclusions were also found in growth zones as primary inclusions in the vug-filling quartz at vein centers of the banded veins. These inclusions were deemed post-flashing owing to their location in a euhedral, vug-filling crystal at vein center. Vug-filling quartz showed much greater clarity than the quartz typically found in banded veins, suggesting that they were deposited through a different process than that of the predominant quartz found in banded veins.

Post-flashing LV inclusions typically had a vapor bubble that comprised 15-30 volume% by visual estimation.

Figure 20 shows the different types of V inclusions within a single quartz crystal located in a dark band within a banded vein. Of the large V inclusions observed in single crystals and banded veins, several subtypes are worth noting based on inclusion shape. Most V inclusions were contained within dark quartz at crystal cores, or within growth zones. Inclusions found in the dark quartz have a range of shapes (Fig. 20), but can be generally described as wavy, elongated in one direction, with a larger head at one end. These inclusions are generally found as clusters. The second V inclusion sub-type are cigar inclusions. Some of these cigar inclusions may contain trace quantities of liquid, but visual estimation suggests that this vapor occupies nearly 100% of the inclusion. Like the wavy inclusions, these inclusions are elongated perpendicular to the C-axis, which indicates they are crystallographically oriented and means they are primary. They differ from the wavy inclusions in that they have straight walls, occur in clear quartz, and are generally isolated spatially from one another and other inclusions. The last V inclusion sub-type are sub-equant, loosely definable as having a negative quartz crystal shape. This more regular inclusion shape was the most uncommon shape for V inclusions.

A second quartz texture was observed in banded veins did not host fluid inclusions. This fine grained quartz was anhedral and similar to the late quartz found in quartz-alunite ledges.

Microthermometry

Inclusions in banded veins were divided by deposit and inclusion type. Fluid inclusion data are presented in Table 5. All microthermometrically-determined salinities and Th are presented graphically in Figure 17. Only LV and LVD inclusions contained sufficient liquid to facilitate determination of Tm and Th; however no banded vein LVD inclusions were determined to be of primary origin.

LV inclusions that formed during flashing, i.e., contained within dark bands, at Verde (n=31, 7 FIA) had an average Tm of -8±4ºC, Th of 240±47ºC and an average salinity of 11±5 wt.% NaCl eq. (Table 5), calculated using the equations of Bodnar and Vityk (1994). Primary LV inclusions in a growth zone in vug-filling quartz in the center of a banded vein from sample RV027 (Verde, n=9, 1 FIA) have salinities, calculated using the equations of Bodnar and Vityk (1994), of 3-6 wt.% NaCl eq. and average Th of 286±6ºC. This assemblage in RV027 represents a post flashing fluid, and is interpreted as a post-ore assemblage. With the exception of a single higher salinity inclusion, the FIA from RV027 have low salinity and Th <300ºC. One LV inclusion at Pancho had a Tm of -8ºC, a Th of 253ºC and salinity of 20 wt.% NaCl eq., calculated using the equations from Bodnar and Vityk (1994).

Sample DD25 84-86m from Verde contains inclusions with the largest range of measured Th. DD25 84-86m inclusions, particularly large inclusions with complex shapes, were prone to decrepitation during homogenization. The complex shape of these inclusions is the result of minimum reequilibration to

more equant forms following inclusion trapping. Inclusions that decrepitated while being heated always did so within 5ºC after homogenization. Th values for decrepitated inclusions in sample DD25 84-86m ranged from 177ºC to 245ºC. All of the decrepitated inclusions had salinities, calculated using the equations of Bodnar and Vityk (1994), of approximately 12 wt.% NaCl eq. The tightest clusters of all of the DD25 84-86m fluid inclusion microthermometry data occur between 200 and 250ºC (Table 5; Fig. 18).

Cathodoluminescence

Cathodoluminescence was performed on banded veins. The results of the CL imaging showed generations of quartz that have distinctive luminescence differences that exactly correspond to the banding visible in hand sample and petrographic observations. Clear quartz at the vein walls can be identified as a first generation, followed by a second generation of CL-dark quartz, and a third generation of clear quartz between the bands (Fig. 13). Due to the ease of identifying quartz generations by using hand sample and thin section petrography, CL was not chosen as the primary indicator for quartz generations in banded veins. The quartz generations that were analyzed by using LA-ICP-MS either by bulk quartz, or through fluid inclusions will be discussed in the LA-ICP-MS section that follows in regards to the petrographic evidence used to divide the analyses by quartz generations.

Laser Ablation Inductively Coupled Plasma Mass Spectrometry

Deconvoluted LA-ICP-MS data in cps for fluid inclusions are contained in

Table 7. Average elemental ratios of fluid inclusions are plotted in Figure 19. Ideally, a large number of vapor inclusions would have been analyzed successfully. However, owing to the low mass in the vapor inclusions, only two cigar inclusions and one more equant shaped vapor inclusion showed a Na peak to differentiate the inclusion from the quartz host. Thus, in the banded veins, primary inclusions analyzed by LA-ICP-MS included two LV inclusions, and three V inclusions. One post-flashing banded vein LV inclusion was successfully analyzed by using LA-ICP-MS. The post-flashing inclusion had Cu/Na, Au/Na and Cu/Au ratios of 1.4E-3, 6.0E-6 and 2.3E2, respectively. One LV inclusion from a Pancho banded vein was successfully analyzed using LA-ICP-MS returning Cu/Na, Au/Na and Cu/Au ratios of 3.7E-2, 2.9E-5 and 1.3E3, respectively (Table 6). Single phase vapor inclusions analyzed in a banded vein sample from Verde (RV027) have average Cu/Na, Au/Na and Cu/Au ratios (±1 $\sigma_{\bar{x}}$) of 0.67±0.3, 1.8E-4±1.5E-4 and 7.3E3±2.6E3, respectively (Table 6). Average LA-ICP-MS values are contained in Table 6, and values obtained from LA-ICP-MS analyses of fluid inclusions are contained in Table 7.

Bulk quartz LA-ICP-MS data are presented in Table 8. A summary of the Cu, Au and Cu/Au values is contained within Table 9. Average elemental ratios of quartz are plotted in Figure 19. Banded veins have average Cu/Si, Au/Si and Cu/Au ratios (±1 $\sigma_{\bar{x}}$) of 1.4E-3 ±8E-4, 5.2E-6 ±3E-6, and 5.0E2 ±2E2, respectively (Table 9).

Transitional Veins at Verde

Petrography

The name “transitional vein” was given to veins at Pancho by Muntean (personal communication, 2009) that show similarities to both A- and banded veins, suggesting the possibility of a transition from processes controlling A-vein formation to processes that created banded veins. In hand sample, the transitional veins at Verde from sample V6.5NWC 342.4 have irregular walls, similar to very early, wispy A-veins, but are up to approximately 1 cm thick. In thin section, the quartz texture is similar to that of late A-veins, with sub-equant to equant grains with potentially poorly defined, irregular grain boundaries. Transitional veins do contain dark quartz in zones within the veins, but lack the banding of dark quartz and vuggy vein centers that are characteristic of the banded veins.

Cathodoluminesence

Cathodoluminesence of transitional veins indicated that transitional quartz is CL-dark (Fig. 21). Since this vein type lacked both FIAs and CL activity, CL could not be used to distinguish different generations of quartz, nor to demonstrate contemporaneity of FIAs throughout the vein type.

Laser Ablation Inductively Coupled Plasma Mass Spectrometry

The transitional veins studied had one isolated LV fluid inclusion in sample V6.5NWC 342.4 that was large enough to provide a clear signal for data reduction. The Cu/Na, Au/Na and Cu/Au ratios for this inclusion are 2.4E-2,

1.7E-4 and 1.4E2, and are shown in Figure 19, and reported in Table 6 and Table 7.

Quartz in transitional veins has Cu/Si, Au/Si and Cu/Au ratios (±1 $\sigma_{\bar{x}}$) of 1.2E-4 ±6E-5, 1.2E-6 ±4E-7, 1.5E3 ±1E3, respectively, as reported in Tables 7 and 8.

D-Veins

Petrography

D-vein fluid inclusions large enough to petrographically characterize were found in what was likely quartz "float" in sulfide, i.e., a reopened A-vein in which pyrite precipitated at a later time(Table 2). Float is defined as quartz that grew in a vein that was reopened by the D-vein, i.e., quartz that is no longer in place, similar to alluvial material. Quartz float may still be attached to a vein wall, or may be a piece of quartz surrounded by sulfide. The quartz surrounded by sulfide may be the result of a quartz crystal attached to the vein wall in the third dimension, that is above or below the plane that the section was cut from the billet, or as a piece of quartz that broke free from the wall during vein reopening. While this quartz may elucidate some past processes, it does not provide information on the formation of the D-vein that it is now contained in.

D-veins typically are quartz poor. The D-veins in this study lacked quartz of sufficient crystal size to host suitable FIAs. Thus, it was challenging to locate suitable FIAs that were primary with respect to the formation of the D-vein. Since no fluid inclusions were observed in quartz that were contemporaneous with

pyrite or any other sulfide, no inclusion descriptions or analyses were made.

Cathodoluminesence

Since CL is best suited for elucidating compositional variation in quartz, and quartz within D-veins is generally isolated, or restricted to the vein margin where it is likely precipitated in an earlier vein forming event, no instructive observations were made using CL imaging.

Laser Ablation Inductively Coupled Plasma Mass Spectrometry

No LA-ICP-MS analyses were performed on D-veins. Since quartz float would be difficult to place into the context of deposit formation, float was not considered as a viable quartz type for analysis.

Quartz-Alunite Ledges

Petrography

Quartz-alunite ledges are comprised of quartz that formed by intense silicification and replacement of wallrock, and contain fine-grained intergrowths of quartz and alunite. The ledge sample chosen for this study lacked a crystal host to support an inclusion assemblage, or a single inclusion, large enough to be petrographically characterized or observed. Quartz-alunite ledges do contain quartz that appears petrographically distinguishable. The most interesting of these variations are small veins that appear to contain dark bands, as seen in the banded and transitional veins. These are likely preexisting banded veins. The quartz in sample RP028 from Pancho differs in that the quartz remains fine grained, and does not support inclusions with enough size to be observed

petrographically.

Laser Ablation Inductively Coupled Plasma Mass Spectrometry

Bulk quartz analyses of the quartz-alunite ledges are reported data in Tables 7 and 8. These data are prsented grapically in Figure 19. The bulk quartz have Cu/Si, Au/Si and Cu/Au values (±1 $\sigma_{\bar{x}}$) of 1.7E-4 ±6E-5, 6.4E-7 ±3E-7, and 6.6E2 ±3E2, respectively.

CHAPTER 4

DISCUSSION AND CONCLUSIONS

Discussion

Low Cu/Au Ratio

An unanswered question about porphyry and high-sulfidation epithermal deposits is the process that controls the ore metal ratios and concentrations found in a given deposit. The deposits of the Refugio district differ from most porphyry Cu-Au deposits in that they exhibit lower Cu/Au ratios and Au is the only economically exploitable metal. Figure 3 shows the bulk ore Cu/Au ratios of deposits from the Maricunga Belt as well as other porphyry Cu±Au deposits. Figure 22 shows plots of bulk ore and fluid inclusion data from several porphyry deposits, as well as deposits in the Maricunga Belt. The Cu/Au ratios of the bulk ore, brine fluid inclusions and vapor fluid inclusions from Grasberg, Earth's richest porphyry-Au deposit, are 3E4 (Kesler et al., 2002), 8E4 (Klemm, 2007) and 2E4 (Klemm, 2007), respectively. The Cu/Au ratios of the bulk ore, intermediate density fluid inclusions and vapor fluid inclusions from Bingham Canyon, a porphyry-Cu-Mo deposit, are 2.3E4 (Kesler et al. 2002), 1.7E3 (Klemm, 2007) and 3.6E3 (Klemm, 2007), respectively. The Cu/Au ratios of the bulk ore and brine fluid inclusions from Granisle are 3.1E4 (Kesler et al. 2002) and 2.1E4 (Klemm, 2007), respectively. The Cu/Au ratios of the bulk ore and brine fluid inclusions from Bajo de la Alumbrera are 8.4E3 (Kesler et al. 2002) and 5.0E3 (Klemm, 2007), respectively. The Cu/Au ratios of the bulk ore, A-vein

LV fluid inclusions and A-vein LVD fluid inclusions from Pancho are 7E3 (Fig. 22, Muntean 1998), 2E3 and 4E4, respectively (Table6). Absolute Au and Cu abundances were not determined in fluid inclusions from Verde or Pancho because Na concentrations could not be quantified, the ability to use Na, or any other major fluid inclusion cation, as an internal standard was eliminated. In order to plot the Au/Cu ratio of fluid inclusions from Verde and Pancho on Figure 22, the Au/Na and Cu/Na ratios (Table 6) define the slope of Au vs. Cu on Figure 22. The ratio of Au/Na and Cu/Na allows one to plot a line, but not a point. The slope (i.e., the ratio of Au/Na to Cu/Na) for Pancho is shown as a green line and for Verde as a blue line. The slope of the Pancho LVD line is 3.9E-4. The slop of the Verde V line is 2.7E-4. The absolute ratio of Au to Cu (i.e., if the absolute abundances of Au and Cu could be determined) in vapor fluid inclusions at Verde and for LVD inclusions in Pancho should fall on their respective line in Figure 22. The Cu/Au ratios for bulk ore, the transitional vein LV fluid inclusion and banded vein V inclusions at Verde are 3.2E2 (Fig. 22, Muntean 1998), 1.4E2 and 7.3E3, respectively (Table 6). The Cu/Au ratios of the bulk ore and vapor fluid inclusions from Marte are 3.4E2 (Muntean, 1998) and 7.5E2 (Klemm, 2007), respectively. The fluid inclusion data from Pancho and Verde, albeit limited, suggest that the LV fluid was Cu poor, i.e., a low Cu/Au ratio, with respect to other porphyry Cu deposits. However, A-vein LVD inclusions have measured Cu/Au ratios that seem reasonable with respect to other porphyry Cu deposits. The Verde banded vein V inclusions, which represent the fluids that resulted from flashing, have

measured Cu/Au ratios higher than that of the LV inclusions, but lower than those of the A-vein LVD inclusions (Fig. 24).

As discussed earlier, Muntean and Einaudi (2000) proposed that the bulk ore of the deposits of the Refugio District have a low Cu/Au ratio owing to the loss of S to the vapor phase during a flashing event. Loss of S to the vapor results in Fe precipitating as magnetite, and Au precipitating as both native Au and Au hosted in magnetite. Copper is unable to precipitate efficiently without S and, thus, Cu is flushed through the system in the ascending vapor. Were this the nature of these deposits, one would expect that syn-flashing fluid inclusions would contain Cu/Au ratios that are elevated relative to pre-flashing fluid inclusions, because the Au concentration would have fallen with the flashing event. Further, the early A-vein Cu/Au ratio would align much more closely with those of “typical” porphyry copper deposits.

In this document, I have proposed an alternative hypothesis for the observed bulk ore Cu/Au of deposits in the Refugio District: the pre- and syn-ore magmatic-hydrothermal fluids had a low Cu/Au ratio. This would arise as a result of partitioning of Cu into sulfide(s) in the magma chamber prior to degassing, and the D-veins have elevated S as a result of magma chamber recharge with a S-rich mafic magma as described in Hattori and Keith (2001) for the Mt. Pinatubo eruption and the Bingham Canyon Cu-Mo-porphyry ore deposit. As the causative magma chamber degassed, the exsolved fluid scavenged incompatible metals less likely to form sulfide phases in the magma chamber (eg., Au), and

those that were in excess in the magma chamber (eg., Fe).

From the LA-ICP-MS data for Au and Cu plotted in Figure 23 it should be noted that an increase in Cu in V inclusions in banded veins from Verde seems tied to a nearly proportional increase in Au. The proportionality of the increase is approximately 1:1, to maintain a relative constant Cu/Au ratio in the V inclusions. The more constant Cu/Au ratio of the V inclusions compared to the other inclusions shows a linear trend in Figure 23 when contrasted to the other inclusion types. Cu and Au abundances in A-vein fluid inclusions are scattered, owing to more varied Cu/Au ratios. LV fluid inclusions analyzed in banded veins at both Pancho and in transitional veins at Verde have some of the lowest Cu/Au ratios, likely owing to Au enrichment, though it may be the result of Cu depletion. The lack of trends among the inclusion populations renders difficult, if not impossible, speculation about the magnitude and behavior of the Cu/Au ratios. Plotting the Cu/Au ratios directly (Fig. 24) shows immense scatter, however the Cu/Au ratio of Verde V inclusion is the most tightly constrained. Further, it is abundantly clear that the Verde banded vein V inclusions (inclusions that represent the ore stage flashing event) do not have the highest Cu/Au ratios, but a more average value consistent with the A-vein LV inclusion Cu/Au ratios. LVD inclusions contain both the highest and lowest Cu/Au values suggesting that the fluid metal composition may be more complex than indicated by microthermometry, as some fluids may be condensed vapor or ore possibly formed during multiple fluid events.

Verde, in both grade and vein assemblage represents a significant shift from standard porphyry Cu deposits. The deepest and earliest veins collected to date are transitional veins, representing a possible transition from banded veinlets, the dominant vein type at Verde, to deeper unexposed A-veins. Conversely, these may be the earliest veins, indicating that Verde evolved in a way that differed from the neighboring Pancho deposit, which shares many of the vein characteristics of other porphyry Cu-deposits. Verde does exhibit exceptionally well developed examples of banded veins. In both the banded and transitional veins of Verde, a low Cu/Au ratio was measured.

As in some explosive volcanic eruptions where there is excess S (e.g., Keppler 1999), the quantity of S contained in the D-veins exceeds that expected based on the low S-abundance in pre-D-veins. Muntean and Einaudi (2001) suggest that magma recharge is responsible for the excess S. Recharging the magma body, after formation of A-, transitional and banded veins, with a S- and metals-rich mafic magma that over pressurizes the system, causes fracturing of the magma chamber-roof rock interface, delivering a S-rich fluid to the superjacent environment where cooling and decompression of the fluid forms D-veins. After a potential surge of S-rich fluids from the mafic recharge, fluids with a low Cu/Au ratio could have predominated to form D veins and the quartz-alunite ledges that represent the high-sulfidation epithermal environment at this locality.

Plotting the Cu/Au ratio of the whole rock assays from drill core P-8-C

along the length of the drill hole, reveals that the Cu/Au ratio does not change with changes in vein assemblages, or lithology. (Fig. 25). While P-8-C does not intercept large zones of banded veins, which are present at elevations above P-8-C at Pancho, it does cross several intrusions and zones of transitional veins. Thus, the assays from P-8-C reveal very little changes in Cu/Au ratio across the lithologies and vein types it does cross. The banded veins likely have an effect on the Cu/Au ratio at elevations above P-8-C. The assay values do suggest that specific intrusions and transitional veins may be less important in controlling Cu/Au ratios than other processes.

Interpretation of Fluid Evolution

Fluid evolution from pre-, to syn-, to post-ore is evinced from the evolution of vein types within porphyry deposits. This evolution is not well characterized owing to difficulty in finding deposits where aliquots of formative fluids trapped as fluid inclusions over the integrated lifetime and vertical extent of the magmatic-hydrothermal system are observed. Given the geology of the Refugio District, the limitations of this type of analysis are reduced owing to significant exposure of a telescopically condensed deposit. Further, multiple deposits have been constrained to be related both temporally and spatially. However, the characteristics of banded veins, the ore-stage mineralization, and the lack of exposure of A-veins at Verde, as well as limited fluid inclusion data, restrict the possibility of a detailed understanding of the fluid evolution in the Refugio district.

The close proximity in time and space between the Verde and Pancho

deposits strongly suggest their formative magmatic-hydrothermal fluids were exsolved from the same underlying magma chamber. All fluids at Pancho and Verde, regardless of inclusion or vein type, show the similar patterns when plotted as element/Na ratios (cps/cps) (Fig. 19). This plot was done to compare the values of all of the elements analyzed in each fluid inclusion and quartz sample. The values plotted are averages, except for the values for transitional veins and banded veins at Pancho, for which there was only one analysis of each. Fluid inclusion data from other deposits was also plotted in Figure 19C. Other deposits show similar low Au/Na ratios, however, deposits do appear to have different ratios of element of interest/Na. Marte, another Maricunga Belt porphyry Au deposit, compared to Verde and Pancho, exhibits much higher Au. When two inclusion types from the same deposit are examined, similar trends distinguish the deposit from the other deposits. This can be seen best in the intermediate and vapor fluid inclusions at Bingham (Fig. 19C). While the brine and vapor inclusions at Grasberg overlap less closely, similar trends do seem to distinguish it from it from the other deposits, but with less certainty than with Bingham, where the inclusion types are much more similar. While the plots (Fig. 19) are not conclusive, there are similarities between the elemental ratios of Verde and Pancho, and differences with other deposits. This suggests that the formative magmatic-hydrothermal fluids for A-veins and banded veins at Pancho and Verde originated in the same magma chamber.

The earliest veins in the system at both Verde (transitional veins) and

Pancho (A-veins) contain relatively high K/Na, Fe/Na and Au/Na ratios and relatively low Ti/Na and Ag/Na ratios in fluid inclusions. Quartz in these veins also contain relatively high K/Si, Fe/Si and Au/Si ratios and relatively low Ti/Si and Ag/Si ratios. Key differences between the two earliest vein sets are the Pb/Na ratio, which is higher than Au/Na ratios in the A-veins, but relatively low compared to Au/Na ratio in the transitional veins. This difference between the veins is not seen in quartz analyses. Figure 19 shows similar patterns for banded veins; however, Fe/Na is higher by an order of magnitude in the banded veins relative to both the A- and transitional veins. High Fe ratios do not seem to correlate with elevated Au ratios, suggesting that the changing Au grades in the veins may be a result of precipitation during the flashing event, and not of fluid evolution prior to flashing. In the transitional veins, only Zn/Na and Pb/Na show transitional values between A- and banded veins. Transitional veins exhibit a petrographic transition, but the elemental ratios of the fluids do not define a gradual transition from A-veins to banded veins. Rather, they seem to exhibit *punctuated equilibrium* characterized by significant and abrupt shifts in fluid chemistry, followed by a period of relative stasis. The evolution of veins by punctuated equilibrium may suggest conditions in the magma chamber change suddenly. This would build on the idea of punctuated differentiation of Marsh (1996). Punctuated differentiation describes sudden changes in the chemistry of a magma owing to partial crystallization removing a significant portion of the magma with a single or limited mineralogy. While the term punctuated

differentiation is a good description of the processes occurring within the magma, punctuated equilibrium seems a more fitting description of the fluid evolution. These processes are likely intimately linked where punctuated differentiation of the magma, combined with magma chamber recharge, may be the root cause of the punctuated equilibrium of the fluids exsolving from the magma.

Punctuated equilibrium envisages a relatively static fluid chemistry forming a single vein type over a distinct period of time in the formation of the deposit followed by a comparatively quick change in the magmatic-hydrothermal fluid being introduced to the country rock by either magma chamber recharge (Hattori and Keith, 2001), or by cyclicity in magma chamber cupola fracture and sealing (Burnham, 1979). This is evidenced in these deposits by the formation of vein types in specific time steps, where a single vein type forms over a given time period, followed by a potentially large shift in vein type, e.g., banded veins to D-veins. While the magmatic-hydrothermal fluid chemistry may respond quickly to magmatic processes, the P-T conditions are likely slower to respond. The more gradual changes in the P-T conditions cause the formation of veins that have physically transitional appearance, with distinct chemistry. Considering both the gradual evolution of P-T conditions and punctuated equilibria of the magma chamber, and thus magmatic-hydrothermal fluids, explains the chemical relationships of the veins and the vertical zonation of the deposits.

Conclusions

The deposits of the Refugio District have distinct properties that differentiate them from most Cu porphyry deposits. Chief among these is the low Cu/Au ratio in pre- and syn-ore veins, leading to their designation as Au porphyries. Gold ore is mainly contained in zones of abundant banded veins that contain high concentrations of Fe and Au, but low Cu. LA-ICP-MS analyses of fluid inclusions from Pancho and the Verde deposits place some constraint on the fluid chemistries from various depths and pre-, syn- and post-ore deposition. In combination with previously published mapping and $^{40}Ar/^{39}Ar$ geochronologic constraints (Muntean and Einaudi, 2000), the data suggests the following. (1) The Pancho and Verde deposits likely formed from a single magmatic-hydrothermal system. (2) At Verde, where banded veins predominate, the Cu/Au ratio is fairly consistent throughout the deposit. This is not true at Pancho where relatively high Cu/Au ratios do not vary with vein type or lithology at deeper levels in zones of A and transitional veinlets, but relatively low Cu/Au ratios occur at shallow levels of the deposits in zones of abundant banded veins. (3) High Au grade is not necessarily associated with a low Cu/Au ratio in the deep parts of Pancho (i.e., hole P-8-C).

The limited data available for this study do not falsify either the Muntean and Einaudi (2000) flashing hypothesis, where Cu and S are lost to the vapor phase; or the magmatic control hypothesis, where the formative magmatic-hydrothermal fluids had an initially low Cu/Au ratio owing to conditions in in the

magma plumbing system. The data and conclusions of this study suggest that future work could be useful to better elucidate the processes at work in the Refugio district. This future work should include the collection of new samples accompanied with a detailed review of the drill core to better identify the vein assemblages found at different elevations within the deposit. Sulfur should also be analyzed in the fluid inclusions to identify if S was lost to the vapor phase, or if the magmatic-hydrothermal fluids were S poor.

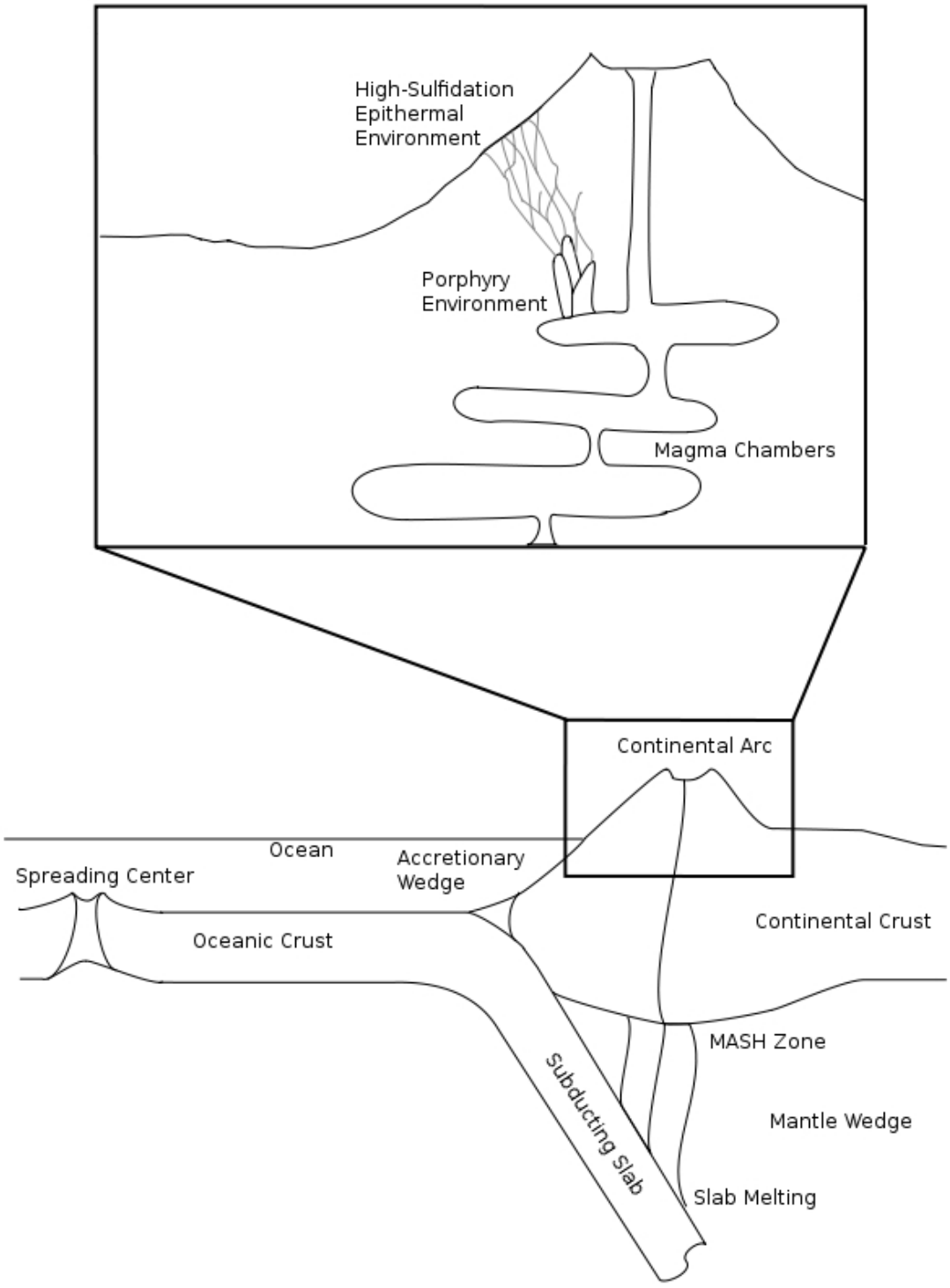

Figure 1: Schematic of a volcanic-hydrothermal system and the plate tectonic setting of the Maricunga Belt. Porphyry deposits form in belts along continental volcanic arcs. When the subducting slab exsolves water, and melts, the less dense fluids rise to the base of the continental crust through the mantle wedge,

partially melting the mantle wedge. Upon contact with the continental crust, the rising melt pools in an area of melting, assimilation, storage and homogenization (MASH), before rising into the continental crust. As the melt moves through the crust, it pools in magma chambers where the composition changes by punctuated differentiation. From the shallow magma chambers, intrusions may penetrate the country rock. Porphyry deposits form centered around these intrusions, where magmatic-hydrothermal fluids rise through the host rock, and any early intrusions. The porphyry environment, for most porphyry Cu-Au deposits, forms between 1 and 6 km depth. The deposits of the Refugio District formed at approximately 1 km depth, and probably higher above the top of the magma chamber (Muntean and Einaudi 2000). Above the porphyry environment high-sulfidation epithermal deposits form from the magmatic-hydrothermal fluids. (after Hendenquist and Lowenstern, 1994)

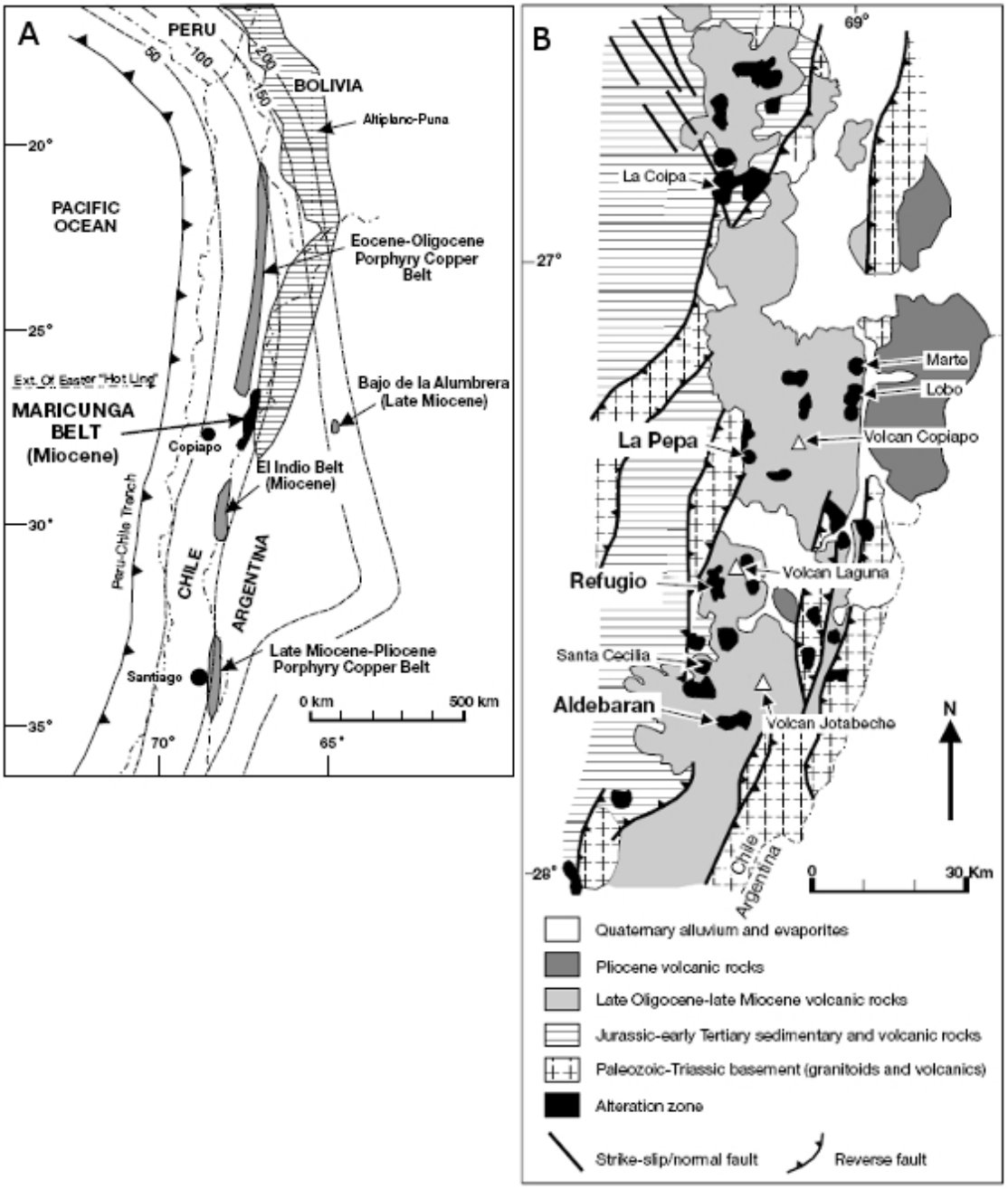

Figure 2: (**A**) Location map of the Maricunga Belt in relation to other copper and gold belts of Northern Chile, the tectonic margin and the depth to the Benioff Zone in kilometers (contour lines) (From Muntean and Einaudi, 2001). (**B**) Location of mining districts of the Maricunga Belt and the simplified geology of the region (From Muntean and Einaudi, 2001).

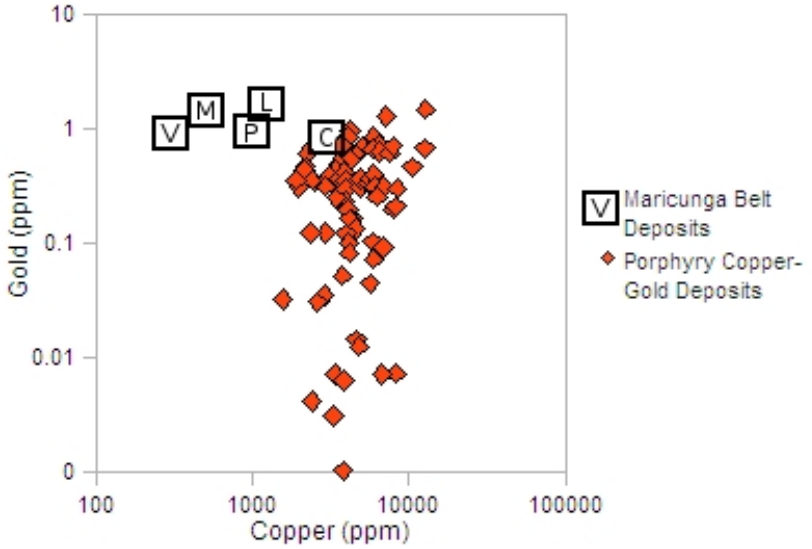

Figure 3: Cu/Au ratios of porphyry copper deposits. Maricunga belt deposit names are indicated by the letter in the symbol, where V is Verde, M is Marte, P is Pancho, L is Lobo and C is Casale Hill. Note, only Casale Hill of the deposits of the Refugio district falls within the zone of "average" porphyry copper deposits. Pancho and Verde fall much below the standard porphyries. The exceptionally low value of Verde seems to be related to the very well developed banded veins. (Based on compilation by Muntean, 1998)

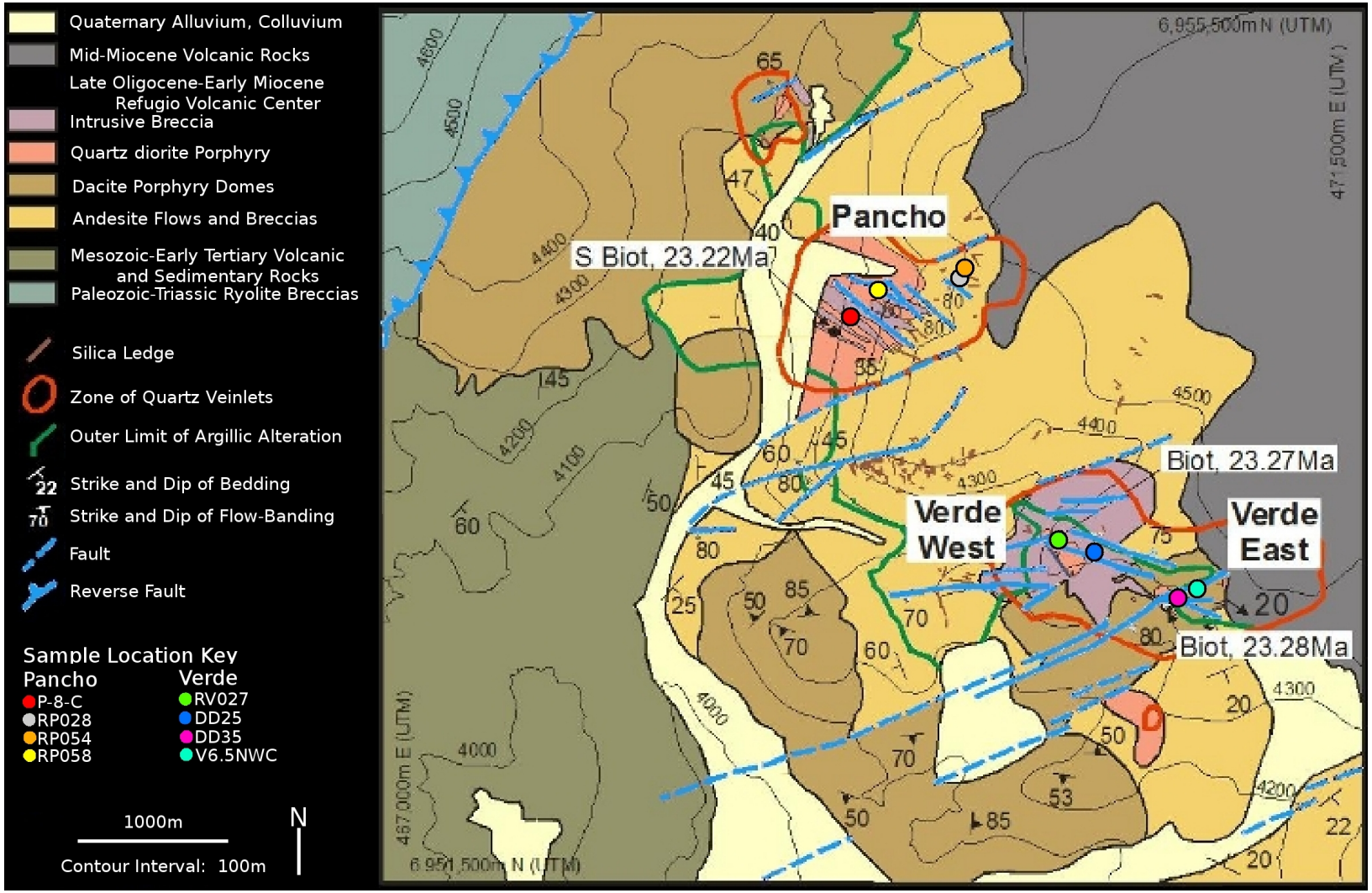
Quaternary Alluvium, Colluvium
Mid-Miocene Volcanic Rocks
Late Oligocene-Early Miocene
Refugio Volcanic Center
Intrusive Breccia
Quartz diorite Porphyry
Dacite Porphyry Domes
Andesite Flows and Breccias
Mesozoic-Early Tertiary Volcanic
and Sedimentary Rocks
Paleozoic-Triassic Ryolite Breccias
Silica Ledge
Zone of Quartz Veinlets
Outer Limit of Argillic Alteration
Strike and Dip of Bedding
Strike and Dip of Flow-Banding
Fault
Reverse Fault
Sample Location Key
Pancho
P-8-C
RP028
RP054
RP058
Verde
RV027
DD25
DD35
V6.5NWC
1000m
Contour Interval: 100m
N
6,955,500m N (UTM)
471,500m E (UTM)
487,000m E (UTM)
6,951,500m N (UTM)
Pancho
S Biot, 23.22Ma
Biot, 23.27Ma
Verde West
Verde East
Biot, 23.28Ma

Figure 4: Refugio district geologic map showing locations of the major deposits of the Refugio district. Also shown are the locations of the samples that were age dated, and the samples used in this study. Core samples for this study indicate the collar location of the drill hole. Thus, the drill hole name is given without the depth, e.g., P-8-C rather than P-8-C 486m. (Modified from Muntean and Einaudi 2000)

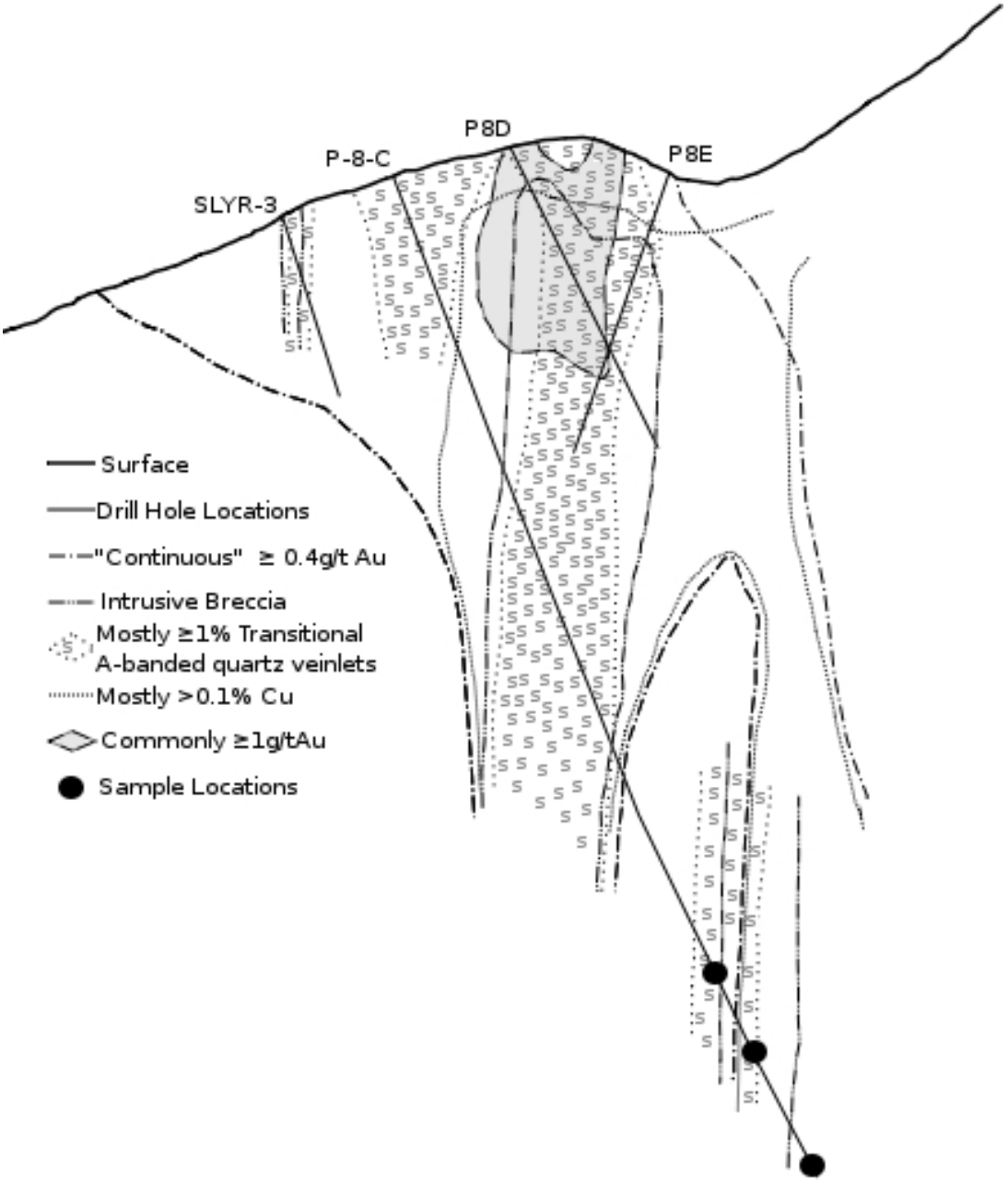
P8D
P-8-C
P8E
SLYR-3
Surface
Drill Hole Locations
"Continuous" ≥ 0.4g/t Au
Intrusive Breccia
Mostly ≥1% Transitional
A-banded quartz veinlets
Mostly >0.1% Cu
Commonly ≥1g/tAu
Sample Locations

Figure 5: Cross section of Pancho showing the sample locations from drill hole P-8-C. Samples were taken from 486m, 539m and 600m depth. Three thin sections were cut from the sample taken from 539m. With increasing depth, the five samples taken from this hole were P-8-C 486m, P-8-C 539_1, P-8-C 539_2, P-8-C 539_3, and P-8-C 600m. (Modified from Muntean, 2006)

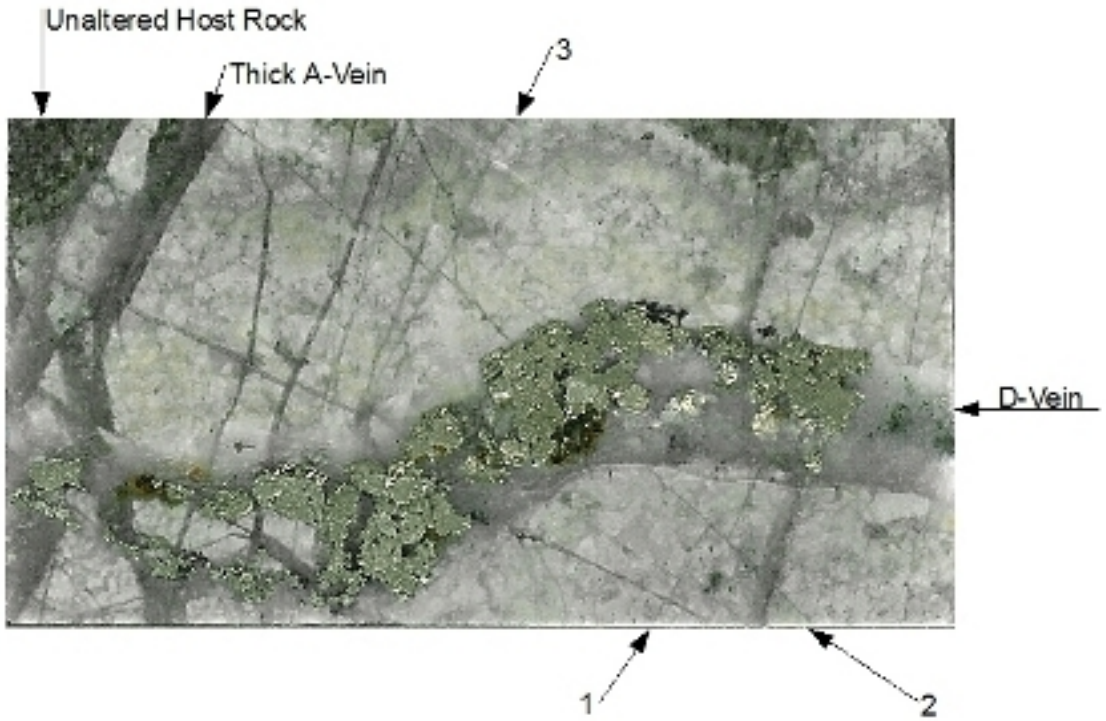

Figure 6: A-veinlets and a thicker D-vein can be seen in this sample from deep drill core taken at Pancho (Pancho sample P-8-C 600). Thin, irregular early A-veinlets appear as background in the light colored rock around the more visible later, straighter A-veins. In the upper left, the dark grey of the unaltered host rock can be contrasted to the light alteration halo around the veins comprising the rest of the sample. A thick A-vein runs vertically on the left side of the thin section. A-veins of similar thickness and form can be observed as having formed at different times by cross-cutting relationships, noted as 1, 2 and 3. Where vein 1 is cut and offset by vein 2. Vein 2 is cut by the D-vein, and cut and offset by vein 3. The thick D-vein cutting across the center of the section likely reopened early veins, inheriting much of the quartz from those veins. D-veins commonly contain anhydrite, but were not seen to contain abundant quartz that was texturally clearly related to the formation of the D-veins. Dimensions of sample are approximately 2x3.6 cm.

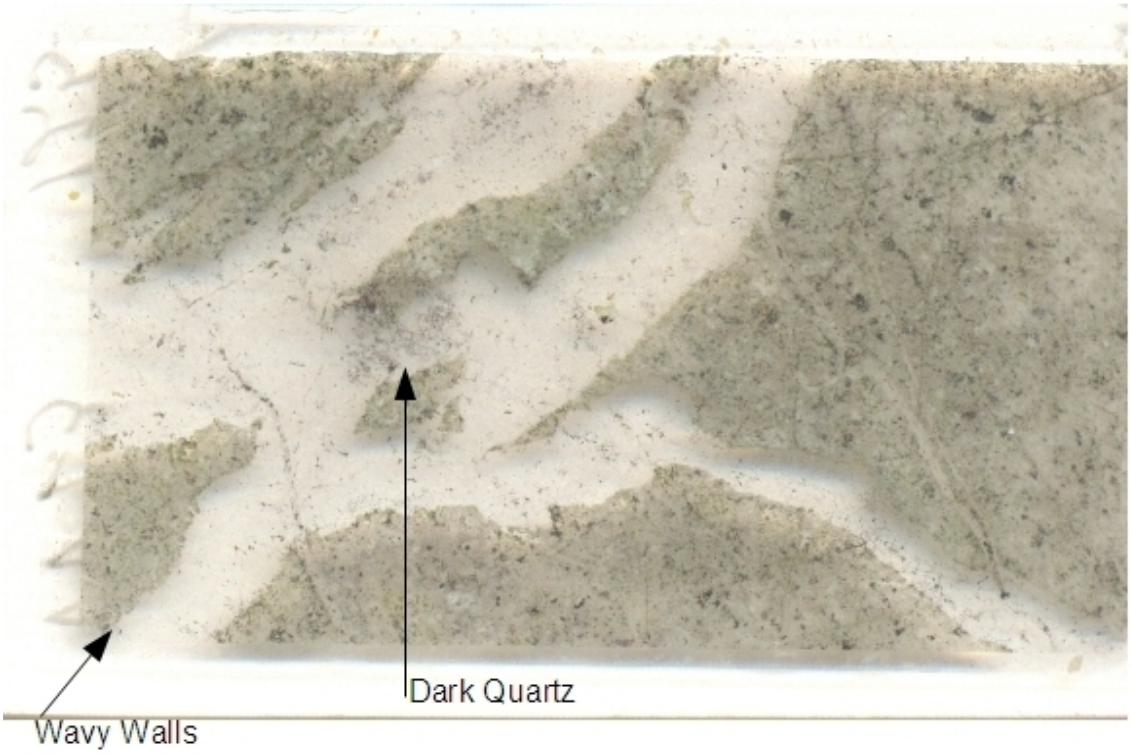

Figure 7: Transitional veins from sample V6 SNWC 324.4. Note the wavy vein walls, and dark quartz, especially just left of center at the vein intersection. Field of view is approximately 2x3.6cm.

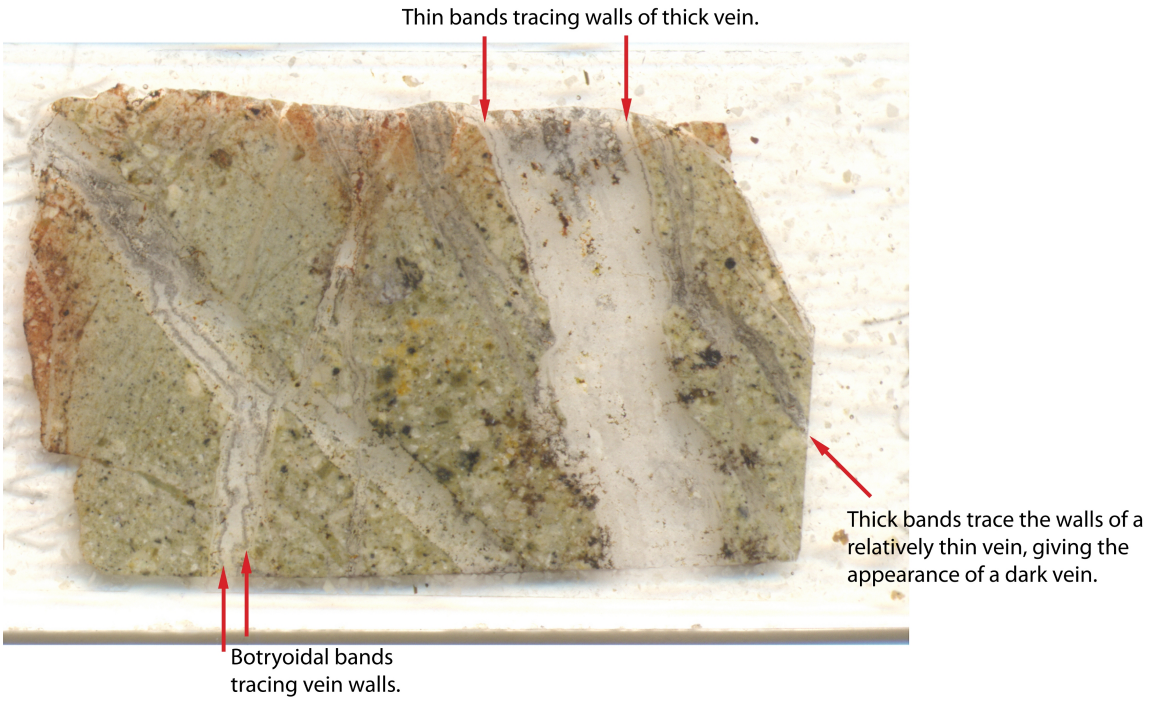

Figure 8: Scanned thin section cut from sample RV027 from Verde showing banded veins. This sample has many banded veins that show somewhat varied appearances. On the left side, annotated on bottom, two botryoidal dark bands can be seen running sub-parallel to the vein walls. Annotated on the top-right, a thick vein can be seen with thin bands along either wall. On the right side, a thin vein containing two rather thick dark bands appears as simply a dark vein. Dimensions of sample are approximately 2x3.6 cm.

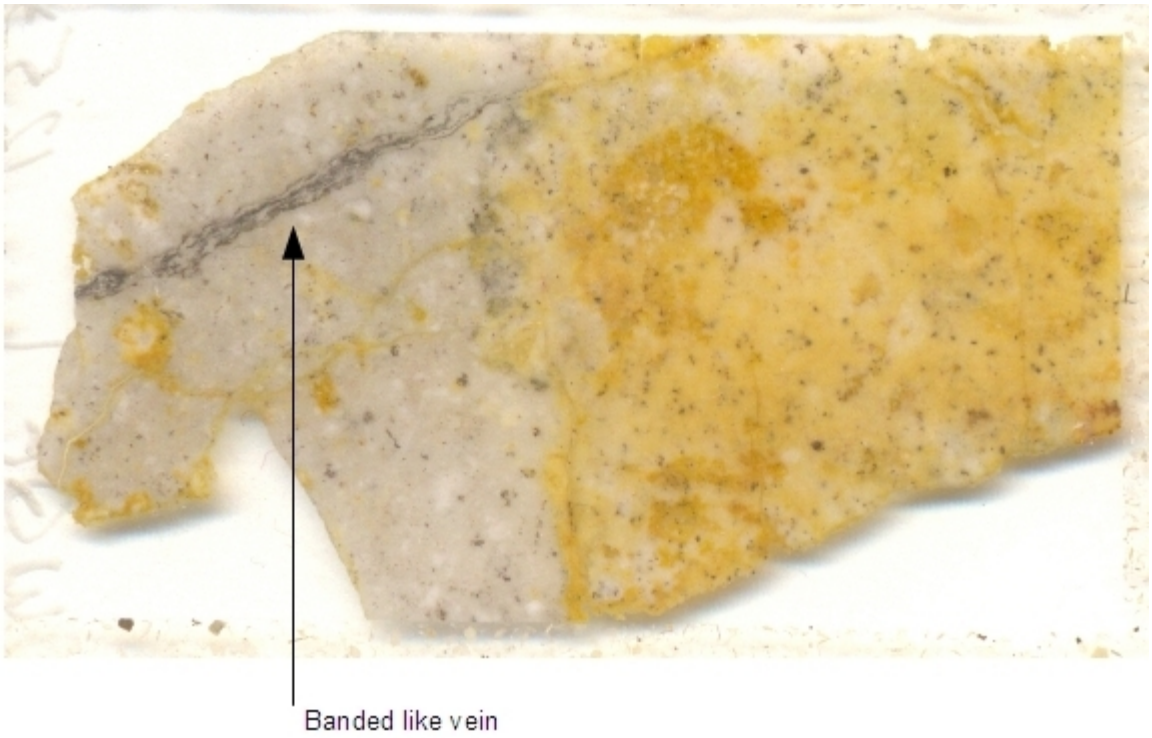

Figure 9: Quartz-alunite ledge showing a banded vein. The quartz found in this ledge is microcrystalline and is of replacement origin, and lacked drusy quartz filling vugs as seen in some ledges elsewhere in the Maricunga belt. Quartz analyses using LA-ICP-MS were performed on quartz from the host rock, across the dark quartz vein, into the host rock on the opposite side at approximately the arrow. Field of view is approximately 2x3.6cm.

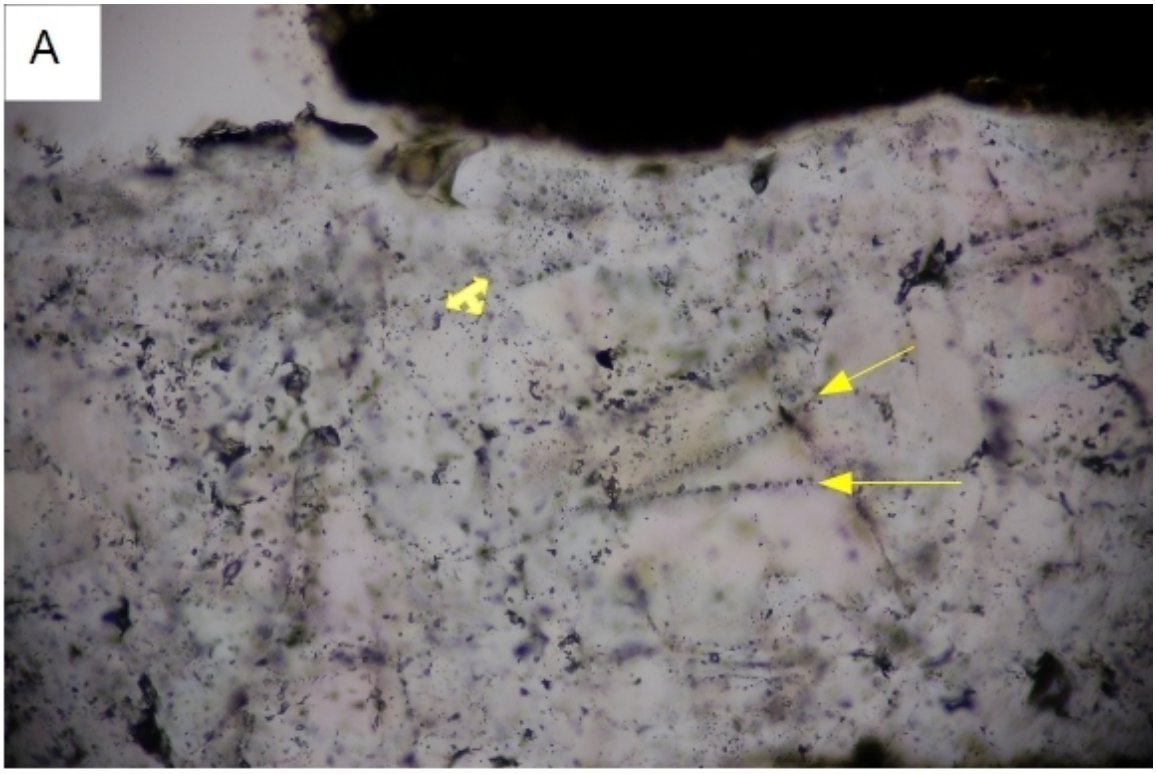
A

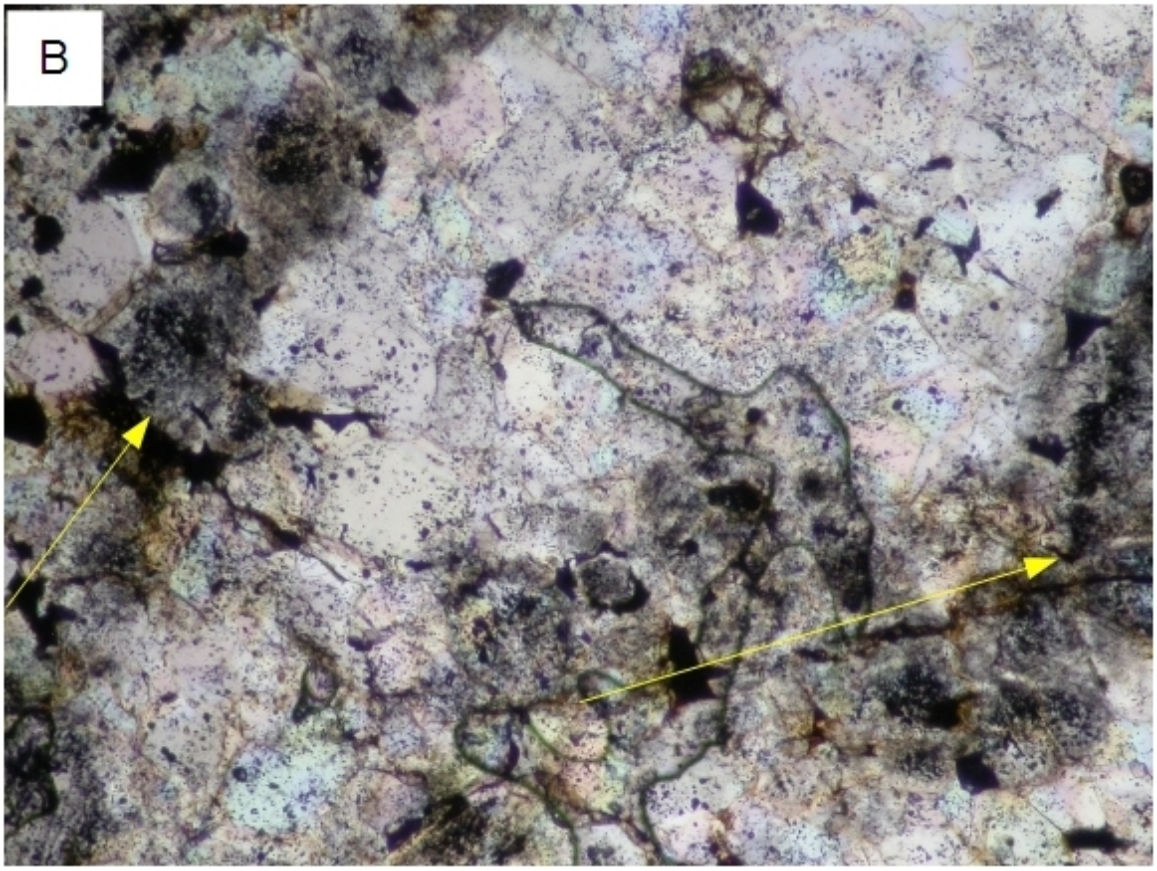
B

Figure 10: Complex fluid inclusion geometries making fluid inclusion origin determination difficult. (A) While secondary inclusion trails (arrows), or planes (three point arrow), may be easy to spot, determining origin and assemblages becomes difficult where multiple secondary FIA meet, sample DD25. (B) In this photomicrograph of sample RV027 showing dark quartz bands (arrows), the relatively clear quartz between the two dark bands contains inclusions whose origins are difficult to determine.

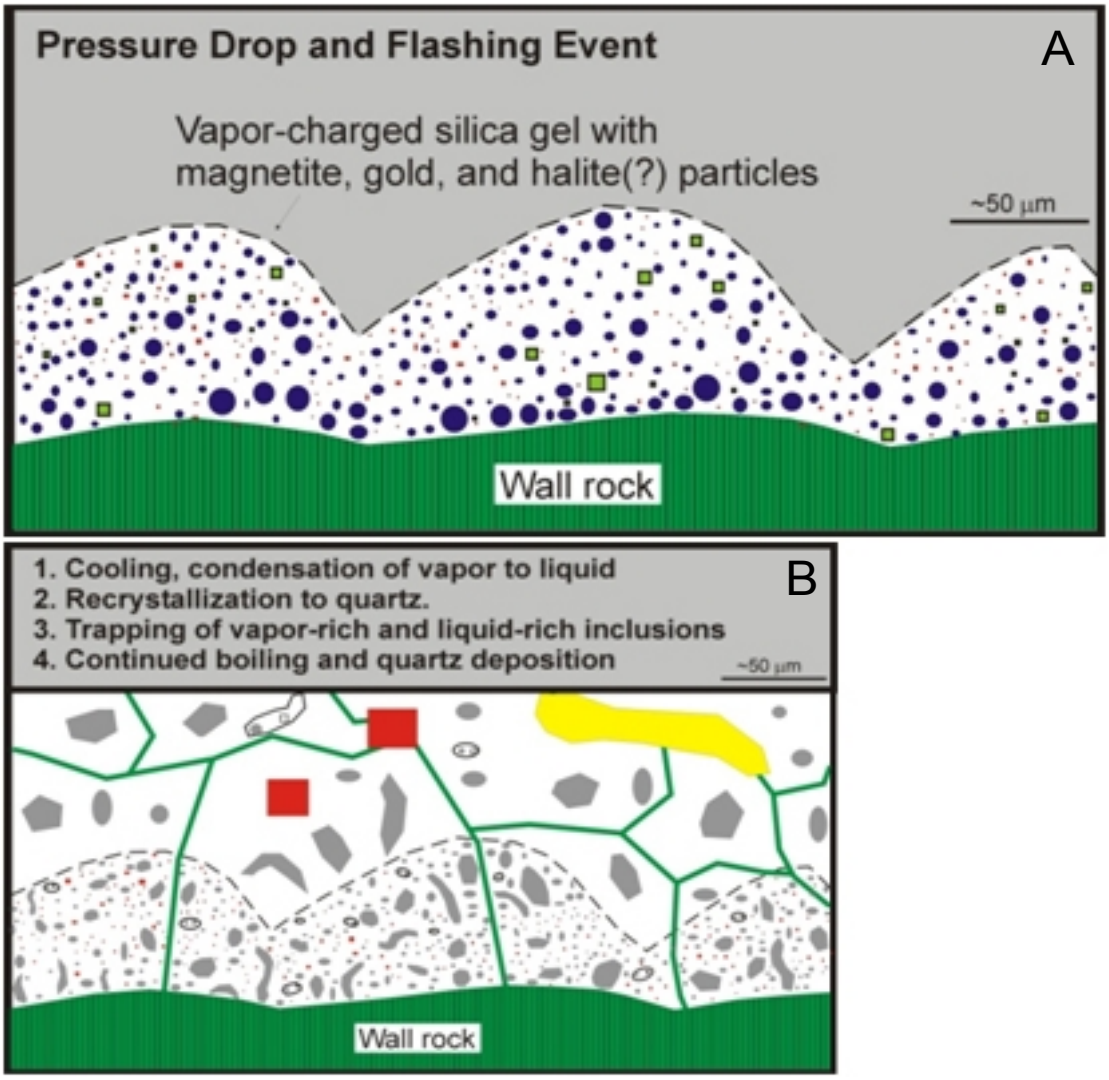

Figure 11: Schematic diagram of banded vein formation showing precipitation of a vapor-charged silica gel with magnetite and gold as a result of a flashing event (A). Later, continued cooling causes the silica gel to recrystallize to quartz, with continued quartz deposition, to form optically continuous quartz across the botryoidal bands (B). In B, the yellow represents pyrite, the red squares represent magnetite, the solid grey bodies represent vapor-rich fluid inclusions, grey outlines represent liquid-rich fluid inclusions and the green outlines delineate quartz crystal boundaries. (Slightly modified from Muntean and Einaudi 2000)

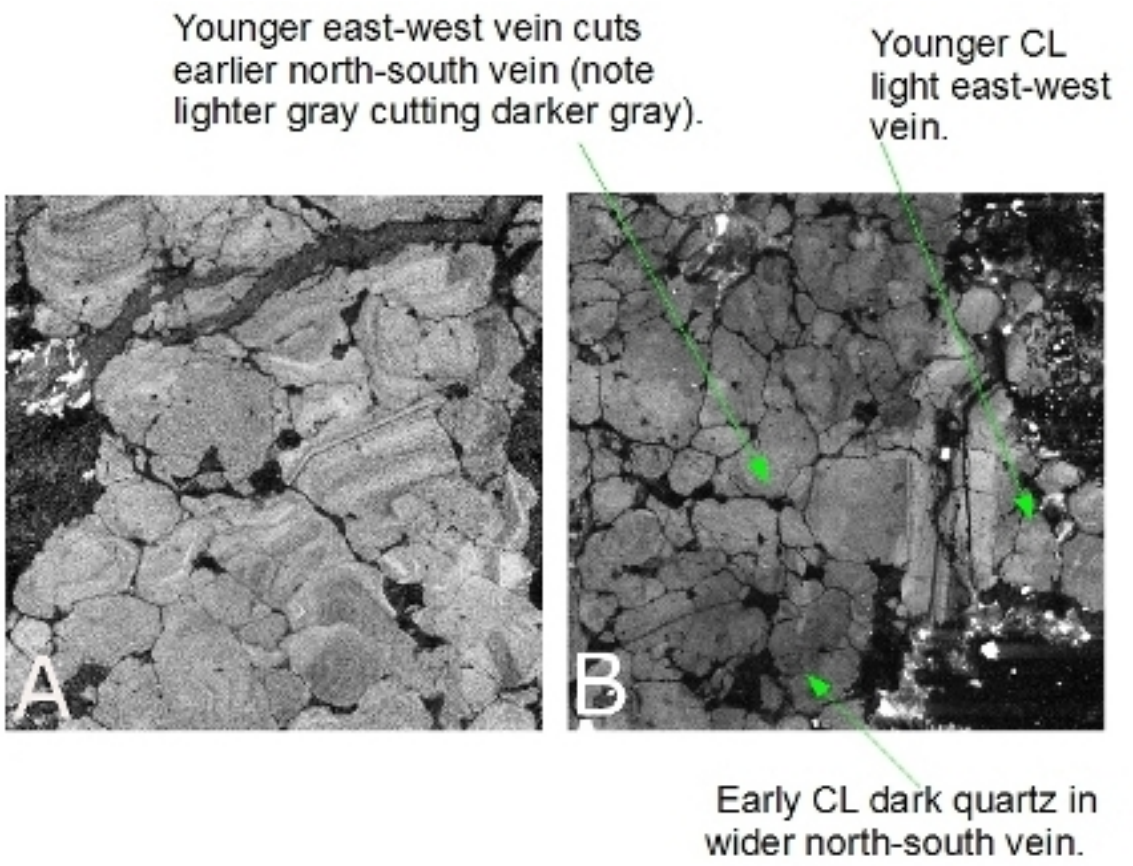

Figure 12: Cathodoluminescence of A-veinlets from deep drill core at Pancho. (**A**) Growth zones in quartz grains (sample P-8-C 539-1, image s3_13AX). (**B**) Two quartz generations related to different A-veins. The earlier, thicker top-bottom trending vein is darker than the younger left-right trending vein. It appears that some of the quartz in the early vein is actually related to the younger vein. (sample P-8-C 600, image s7_1_beamx10AX)

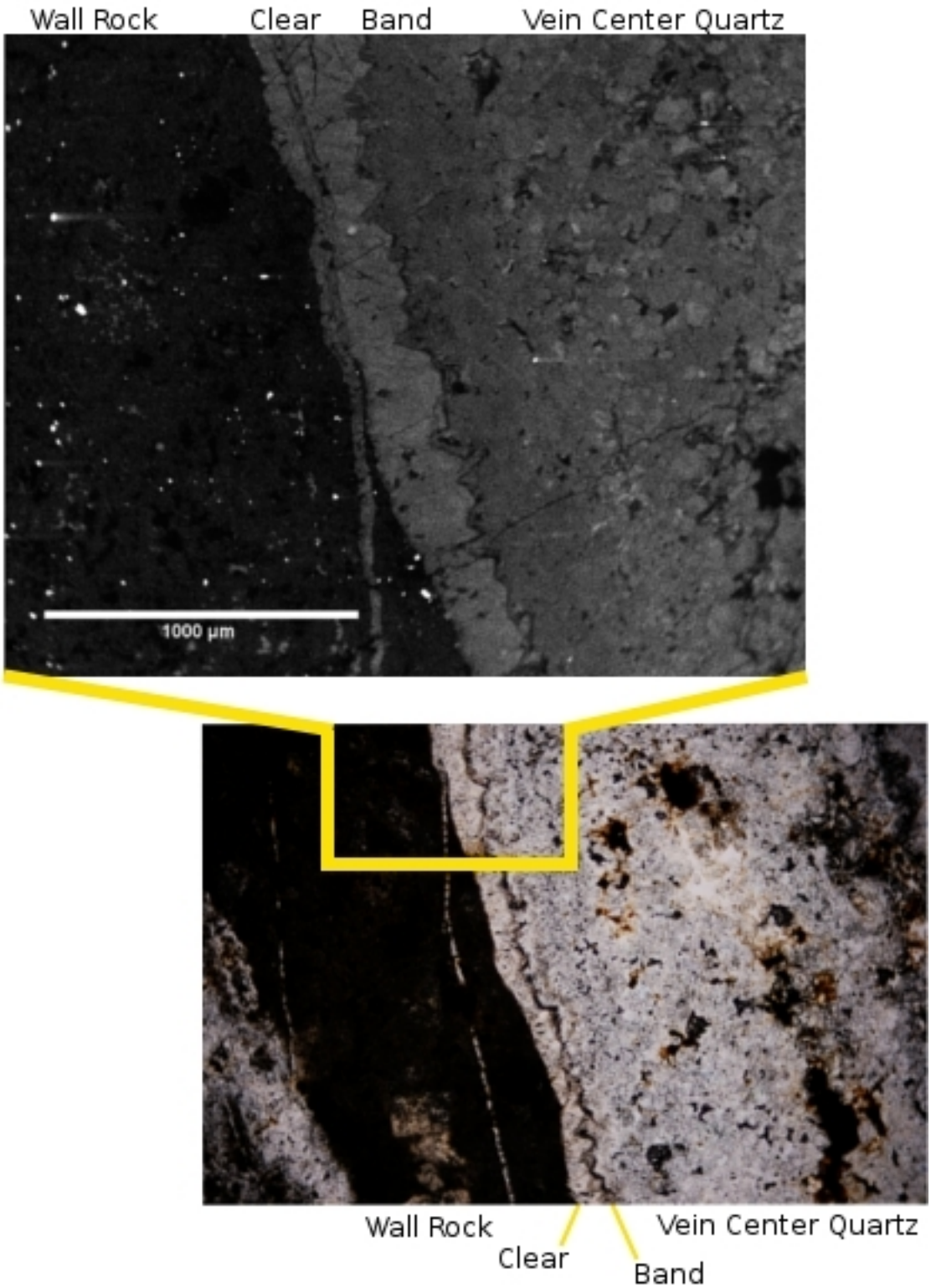

Figure 13: Photomicrograph and CL image showing the generations of quartz in a banded vein. The wall rock is the dark material on the right side of both

images. The bright spots in the wall rock in the CL image are likely polishing compound. The quartz is labeled clear, band and vein center quartz for the clear quartz found at the vein wall, the dark band, and the later quartz at vein center, respectively. In the CL, the clear quartz is the lightest grey. The dark band appears dark grey to nearly black, and the later quartz appears nearly stippled.

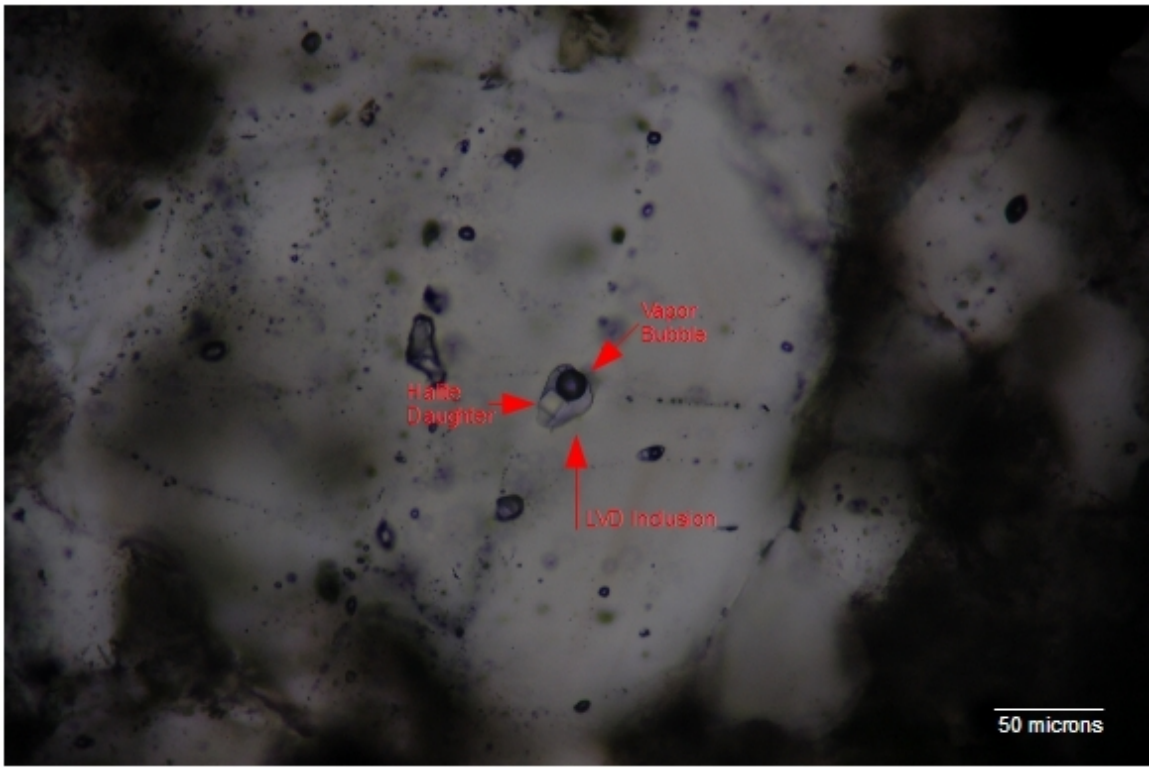

Figure 14: An A-vein LVD inclusion from P-8-C 539_3 highlighted at center with red arrows. Both the halite daughter, and the vapor bubble are visible within the inclusion. The halite daughter appears as a light colored square. The vapor bubble is a dark circle at upper right.

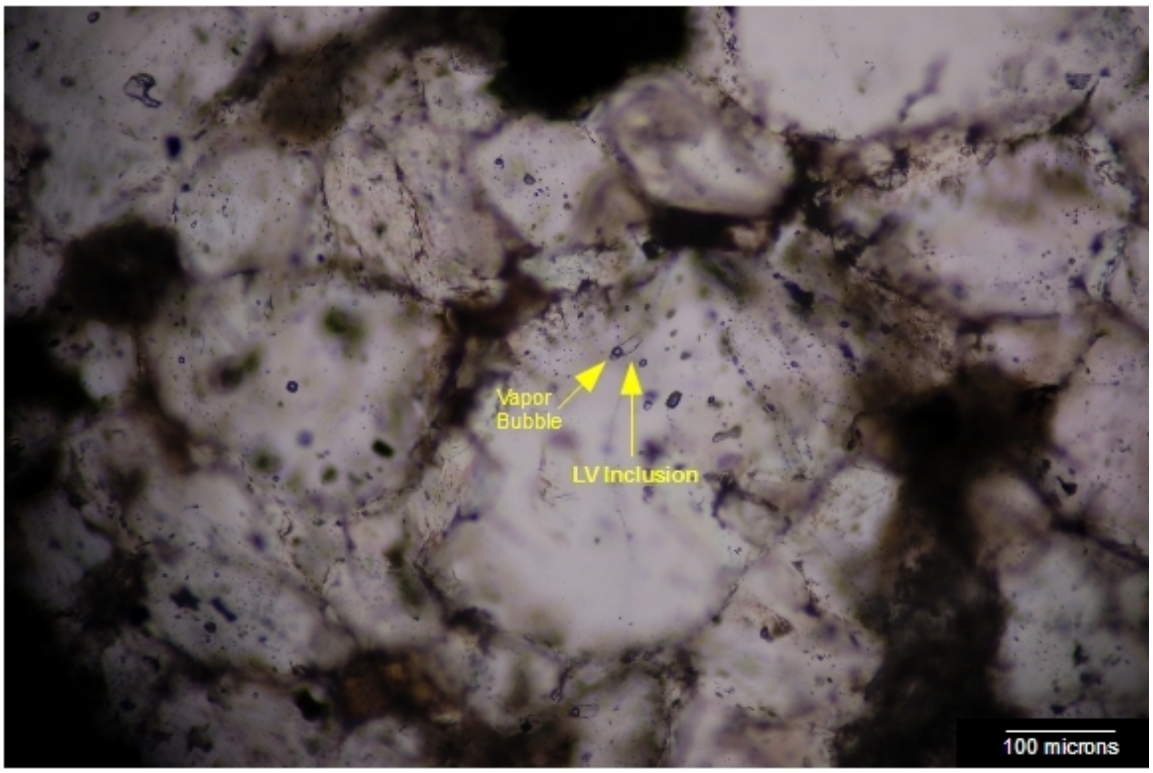

F**igure 15:** Several A-vein LV inclusions from sample P-8-C 539_2 are visible in this photomicrograph. A large LV inclusion is highlighted by the yellow arrows. The vapor bubble is at lower left in the inclusion.

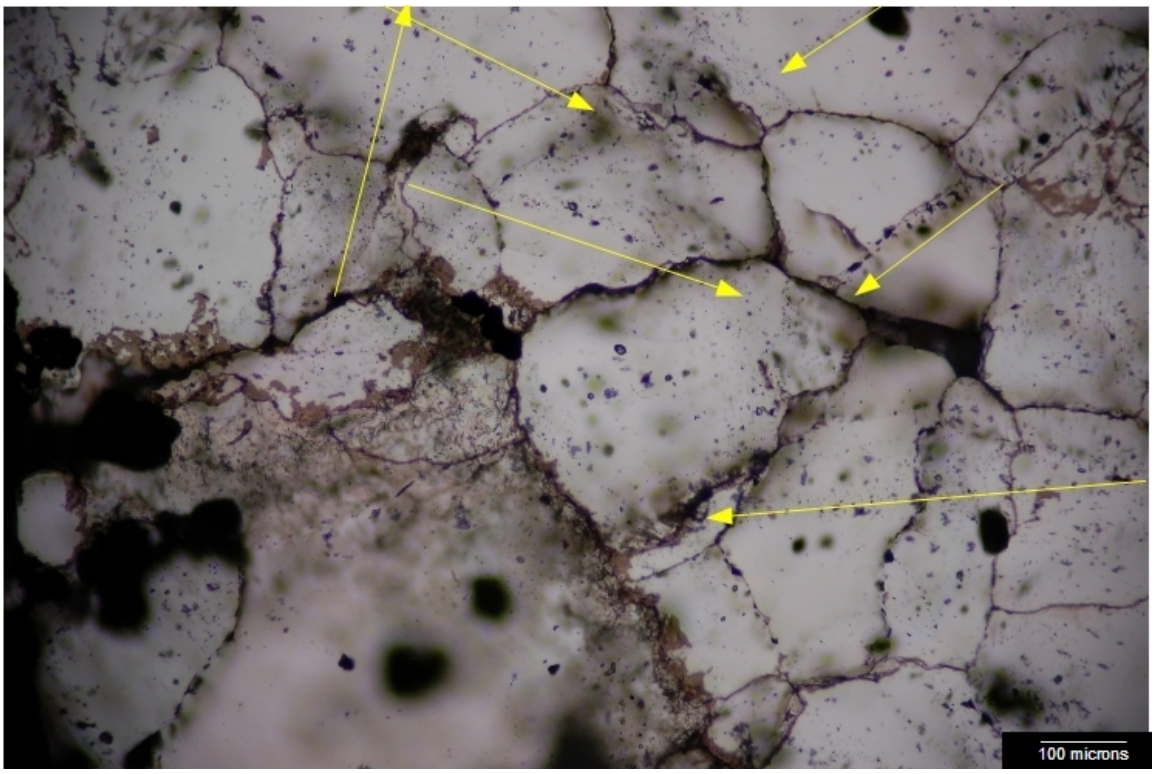

Figure 16: Secondary trails of V inclusion cut across quartz crystals in this photomicrograph from and A-vein in sample P-8-C 539_1. The V inclusions are the small dark spots surrounded by light grey quartz.

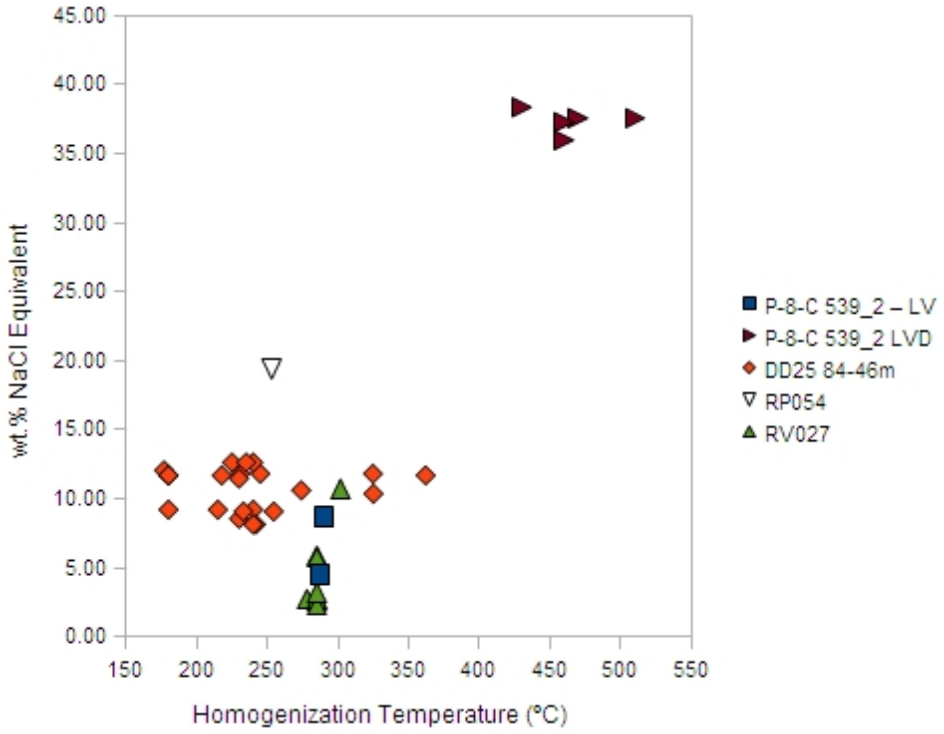

Figure 17: Th versus wt.% NaCl eq. The banded veins are samples DD25, RP054 and RV027. A-vein inclusions are from P-8-C 539_2. Samples from Verde are DD25 and RV027. Samples from Pancho are P-8-C and RP054.

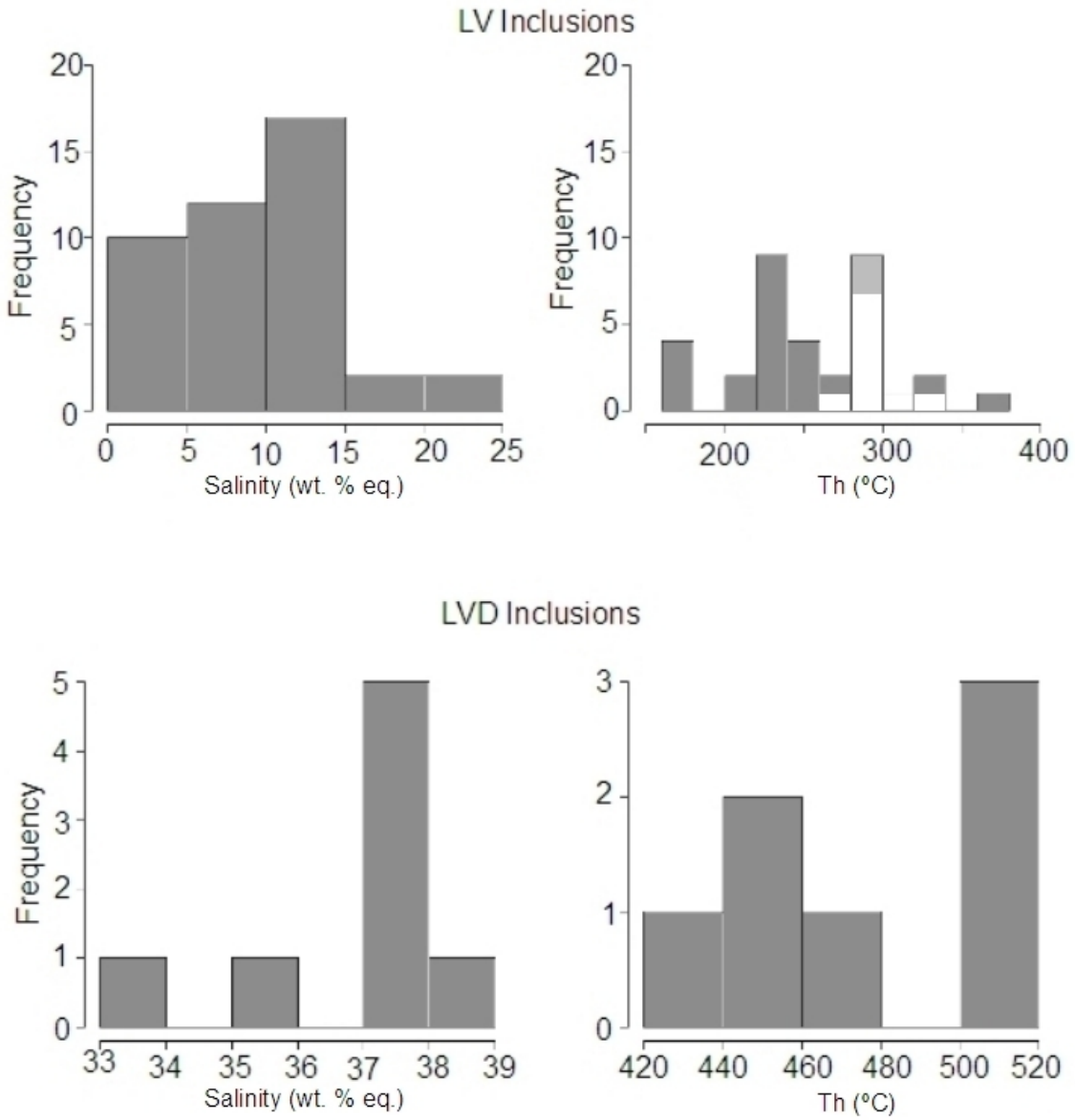

Figure 16: Salinity and Th histograms for LV and LVD inclusions. The Th histogram for LV inclusions contains three populations of inclusions. Inclusions from deep A-veins (light grey), syn-ore banded vein inclusions (dark grey) and post-ore inclusions from RV027 (white). Eliminating the A-vein and post-ore inclusions leaves a fairly uni-modal distribution of Th in banded vein LV inclusions.

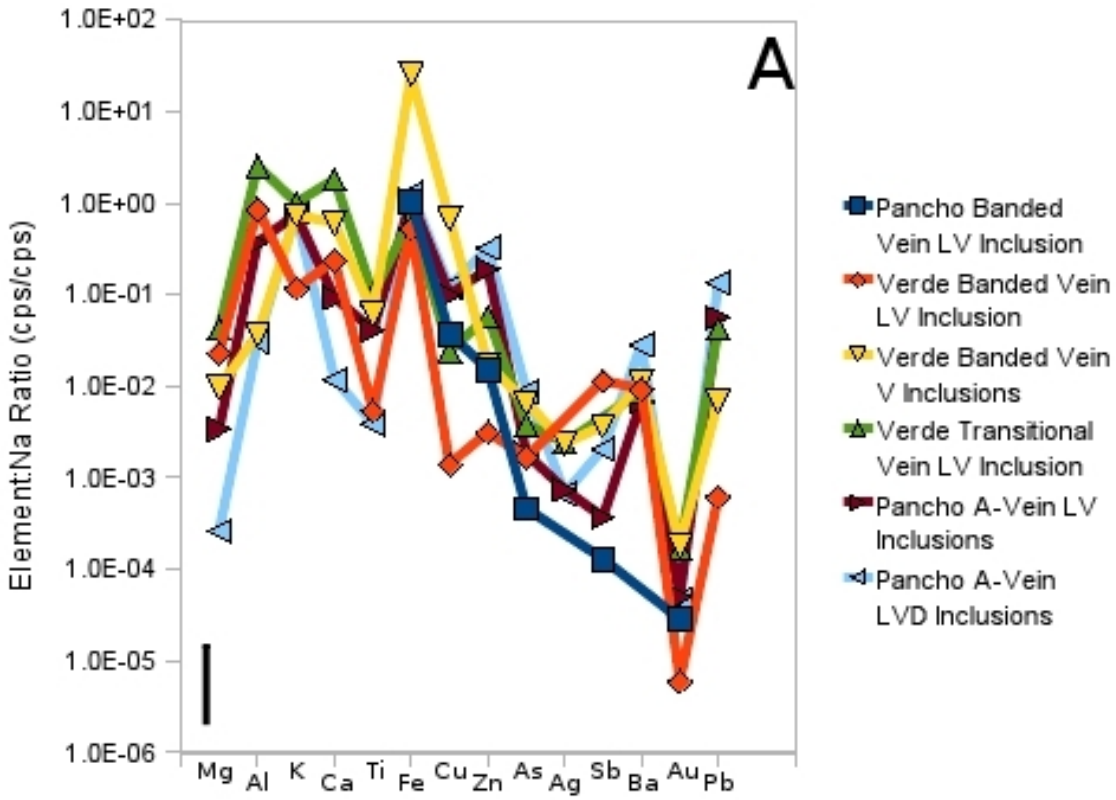
A
Element:Na Ratio (cps/cps)
1.0E+02
1.0E+01
1.0E+00
1.0E-01
1.0E-02
1.0E-03
1.0E-04
1.0E-05
1.0E-06
Mg Al K Ca Ti Fe Cu Zn As Ag Sb Ba Au Pb
Pancho Banded Vein LV Inclusion
Verde Banded Vein LV Inclusion
Verde Banded Vein V Inclusions
Verde Transitional Vein LV Inclusion
Pancho A-Vein LV Inclusions
Pancho A-Vein LVD Inclusions

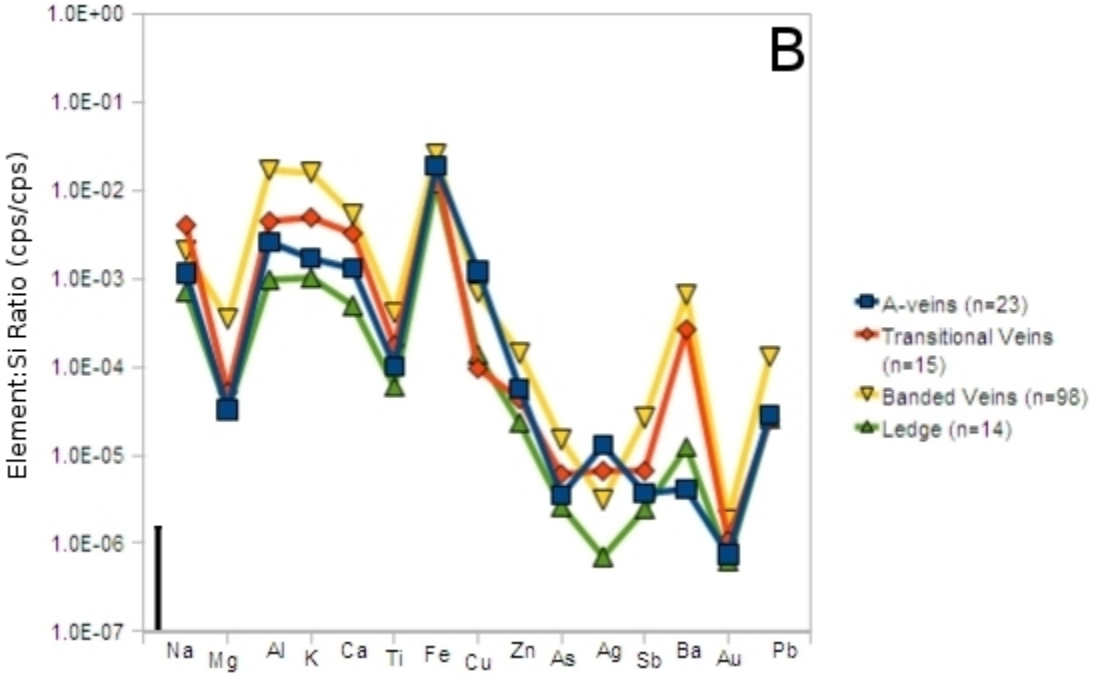
B
Element:Si Ratio (cps/cps)
1.0E+00
1.0E-01
1.0E-02
1.0E-03
1.0E-04
1.0E-05
1.0E-06
1.0E-07
Na Mg Al K Ca Ti Fe Cu Zn As Ag Sb Ba Au Pb
A-veins (n=23)
Transitional Veins (n=15)
Banded Veins (n=98)
Ledge (n=14)

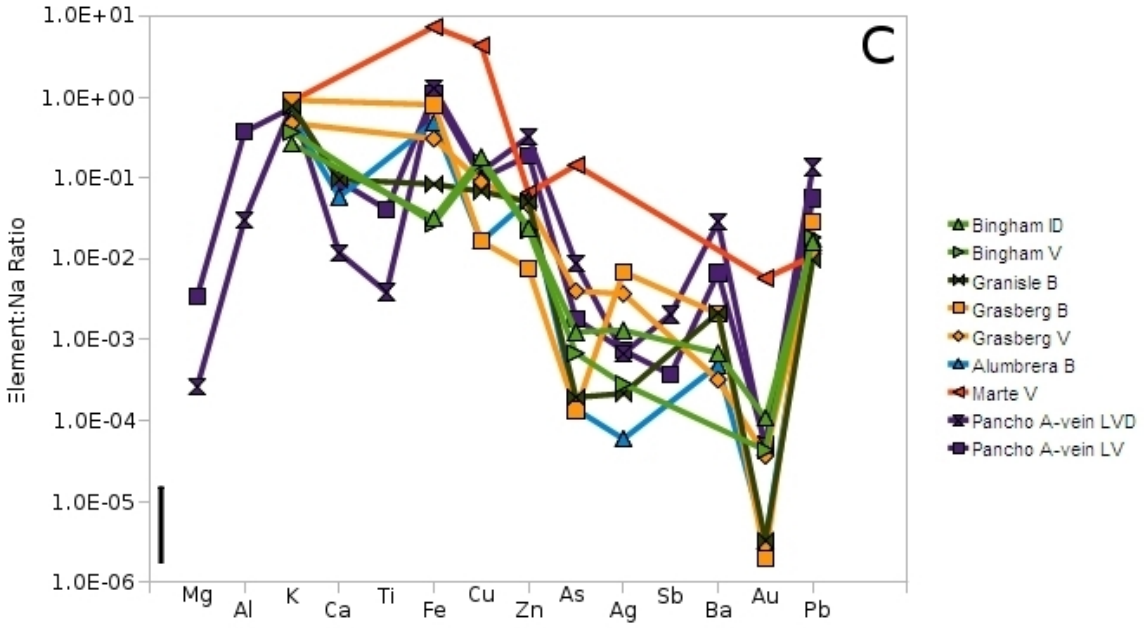

Figure 19: LA-ICP-MS analyses of fluid inclusion and quartz from the Refugio district, and fluid inclusions from other deposits. Standard deviation of the mean is generally approximately the size of the symbol, however the maximum error is shown in the lower left corner of each figure. (A) Fluid inclusions grouped by vein type and inclusion characteristics. (B) Quartz analyses by vein type. (C) Fluid inclusion data from several other porphyry deposits obtained from Klemm (2005), where ID is intermediate density, V is vapor and B is brine. Standard deviation presented in Klemm (2005) is larger than the standard deviation of the mean given in this study, up to approximately ±100%.

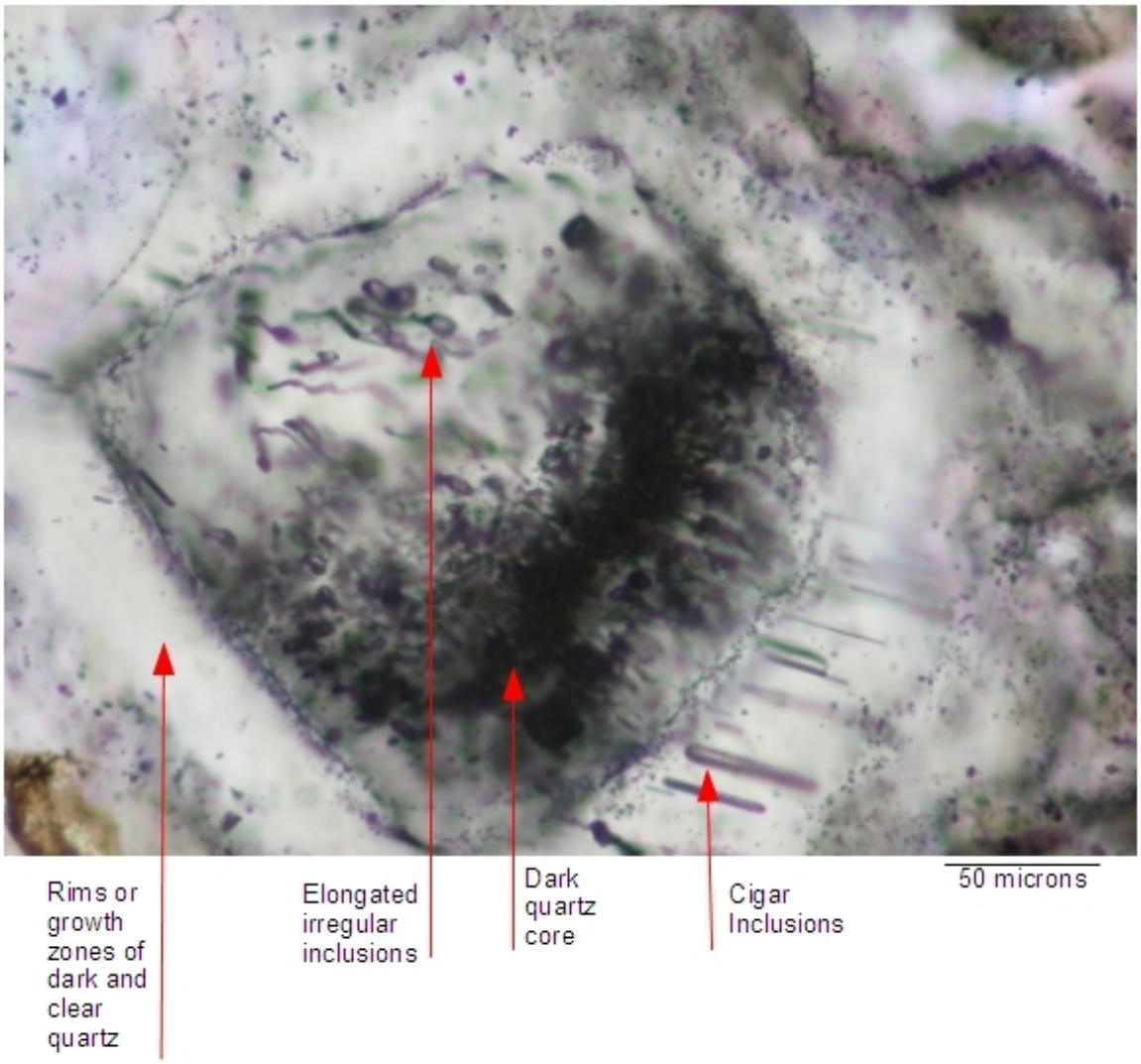

Figure 20: Dark and clear quartz zoning in a quartz crystal within a dark band in RV027. Note the growth zones marked by “rings” of dark and clear quartz. At the center of the crystal, a dark quartz core contains a significant number of V inclusions. Note that the V inclusions at the center are elongated, wavy and generally have a large head at one end, this is typical of irregular V inclusions. Cigar inclusions are elongated out from the crystal core in the clear quartz that borders the dark core. Note the generally dark quartz at the right of the image near the crystal boundary (above the scale).

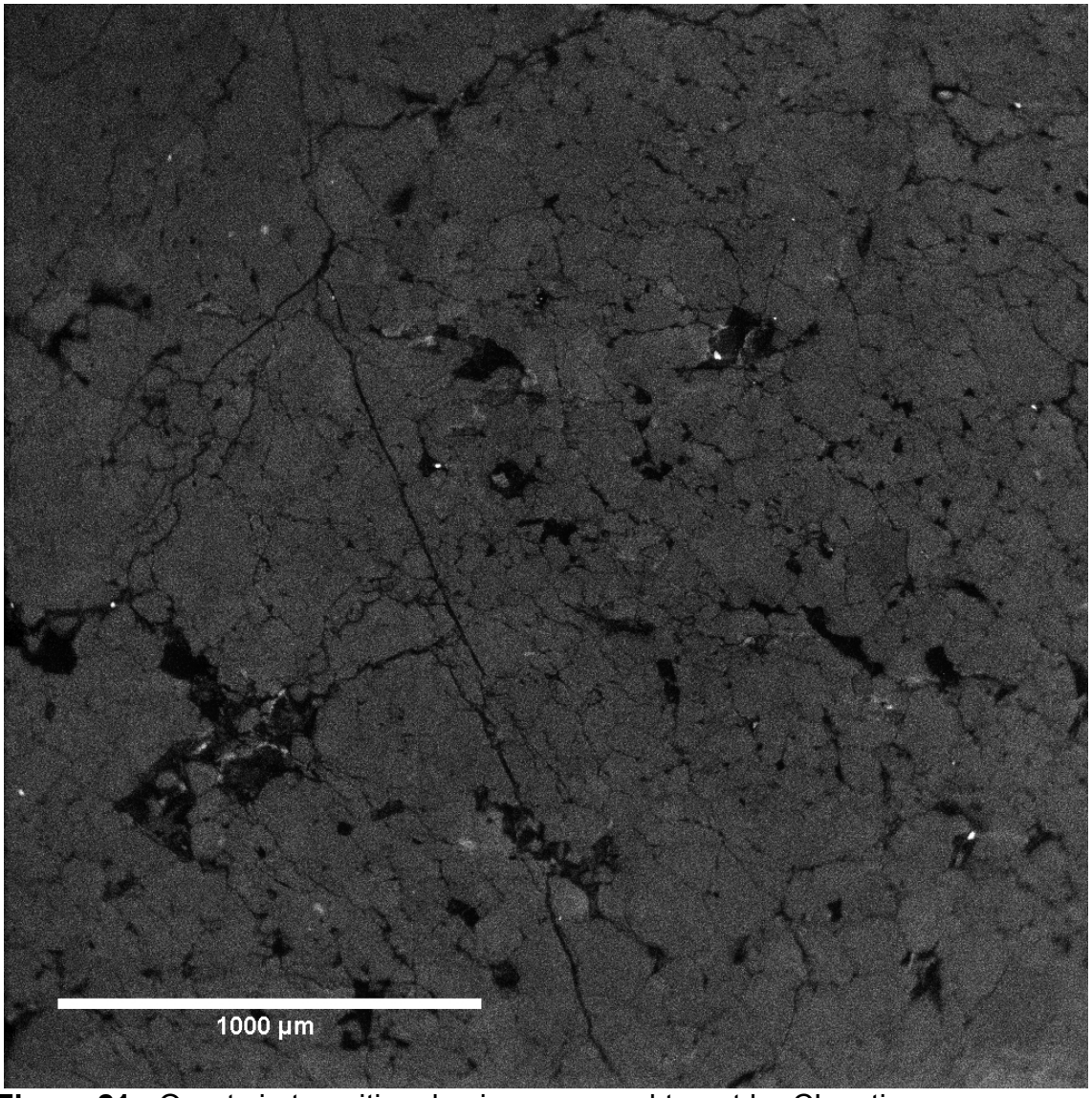

Figure 21: Quartz in transitional veins appeared to not be CL active.

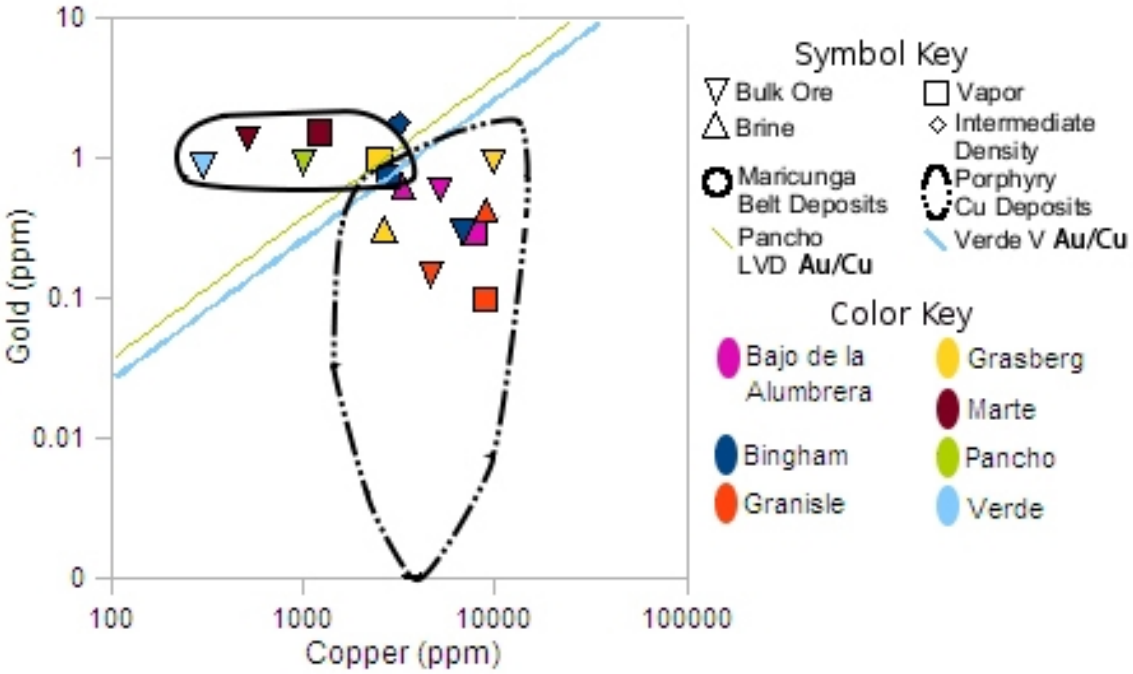

Figure 22: Plot of bulk ore and fluid inclusions from six deposits. The outlined regions show the bulk ore values for Maricunga Belt deposits (solid line), and for most porphyry Cu deposits (dash-dot-dot line). The fluid inclusions from Pancho and Verde are plotted as lines representing a constant Cu/Au ratio, as explained in Chapter 4. Standard deviations are not given for bulk ore in Kesler (2002); brine, vapor and intermediate density inclusions have error up to 100%; and Pancho and Verde inclusions have errors as detailed in Figure 19. (Bulk ore values for Bajo de la Alumbrera, Bingham, Granisle and Grasberg are from Kesler (2002). Bulk ore for Marte, Pancho, Verde and the Maricunga Belt and porphyry Cu fields are from Muntean (1998). Fluid inclusion data for Bajo de la Alumbrera, Bingham, Granisle, Grasberg and Marte are from Klemm (2005).)

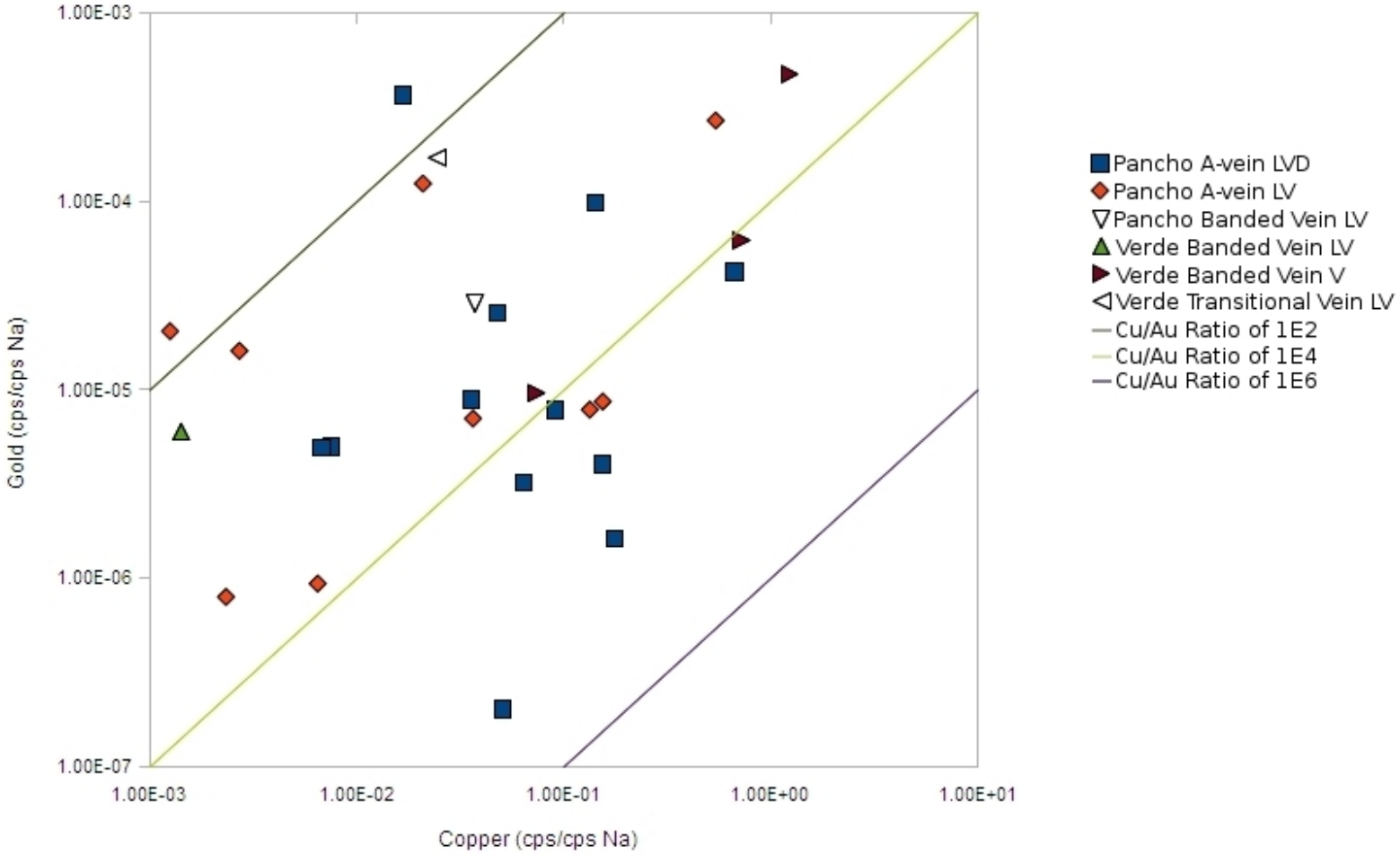

Figure 23: Fluid inclusion ratios of Cu (cps/cps Na) plotted against Au ratios (cps/cps Na).

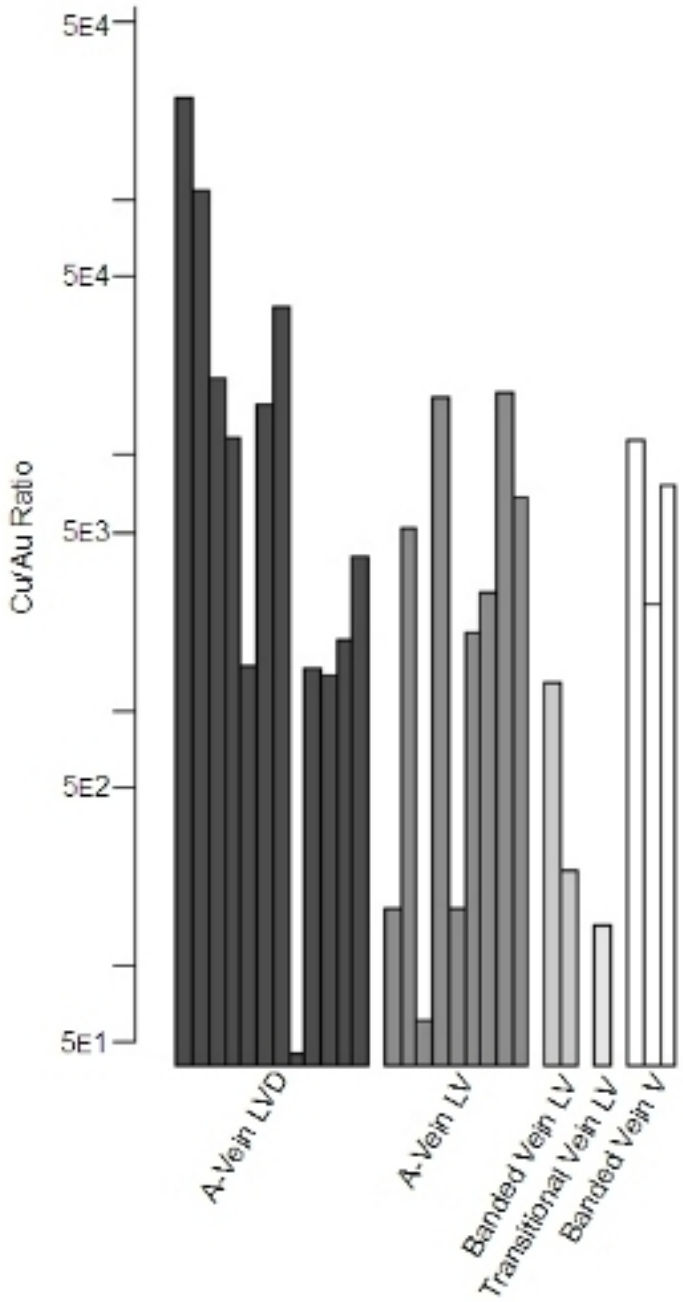

Figure 24: Cu/Au ratios plotted on a log scale. A-vein LVD inclusions show an enormous range of Cu/Au ratios (>3 orders of magnitude), ratios of LVD inclusions in the A-veins are higher than Cu/Au ratios found in the banded veins. If Cu was being lost to the vapor phase, and Au was precipitating during flashing, one would expect the Au concentrations to decrease in the fluids. A drop in Au concentration would mark an increase in the Cu/Au ratio, not seen in this chart.

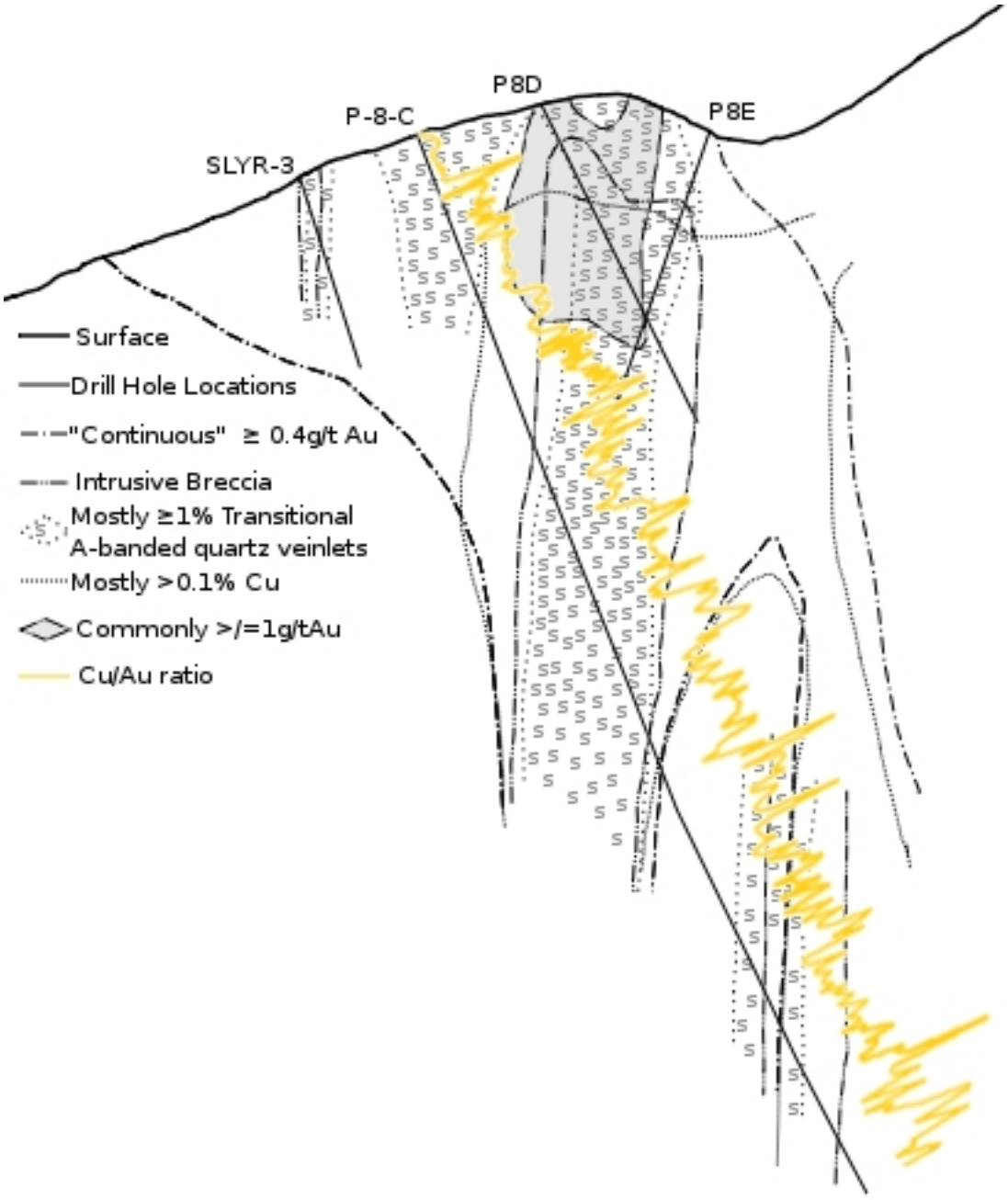

Figure 25: Pancho cross section with Cu/Au ratio from drill core assays. Note that while the Cu/Au ration increases (higher Cu/lower Au) and decreases (lower Cu/higher Au), the overall value remains fairly constant after the near surface transitional veins, and does not seem to systematically change based on vein type or lithology shown on this cross section. The legend refers to as "transitional A-banded quartz veinlets," the core logs that this cross section is based on were the original descriptions for transitional veins, and the nomenclature was kept true to the original cross section and core logs.

Transitional A-banded quartz veinlets at Pancho are similar to the transitional veins described at Verde in this study. (Cross section modified from, and assay values from Muntean (2006))

Table 1: $^{40}Ar/^{39}Ar$ dates published by Muntean and Einaudi (2001) with errors reported to 2σ.

Deposit	Date (Ma)	Mineral Dated
Pancho	23.22±0.06	Hydrothermal Biotite
Verde East	23.28±0.06	Igneous Biotite
Verde West	23.27±0.06	Igneous Biotite

Table 2: Summary table of the vein types found in the Maricunga Belt. Descriptions are from Muntean and Einaudi (2000) (columns labeled “M&E,” except transitional vein descriptions which are from John Muntean, personal communication) and Gustafson and Hunt (1975) (columns labeled “G&H”). Gustafson and Hunt (1975) do not have different generations of A-veins, however, their descriptions of A-veins are given inline with Muntean and Einaudi (2000) four A-vein subtypes for easier comparison. This study uses the descriptions of Muntean and Einaudi (2000) and John Muntean (personal communication) in all but three descriptions. (1) A-veins in this study refers only to A-3 and A-4 late A-veins. (2) Transitional veins at Verde do not show significant pyrite. (3) D-veins observed to have at most only minor quartz, except where the D-veins reopened A-veins, with abundant anhydrite and considerable abundances of other sulfides, aligning much more closely with the Gustafson and Hunt (1975) description.

Vein Type	Relative Age	M&E Mineralogy	G&H Silicate Mineralogy
A-1 (early)	Earliest	Major Biotite & quartz w/ magnetite & chalcopyrite, and minor pyrite & sphalerite	Quartz-K-spar-anhydrite-sulfide with rare traces biotite; quartz ranges from 50% to 95%. The K-spar is usually perthitic. The fine equigranular texture of quartz is shared by the other minerals which are evenly disseminated through the vein. No vein symmetry is typical, but banding of K-spar at the edges or center is not uncommon. More or less sutured contacts between quartz and K-spar are common.
A-2 (early)	Cut A 1	Major quartz w/ magnetite & chalcopyrite, and minor chlorite & apatite	
A-3 (late)	Cut A 1-2	Major quartz w/ Magnetite & chalcopyrite, and minor chlorite, bitotite, barite, bornite & specular hematite	
A-4 (late)	Cut A 1-3	Major quartz w/ chalcopyrite, and minor pyrite	
B-veins	n/a	n/a	Quartz-anhydrite-sulfide, with K-spar characterisitcally abasent. The quartz is relatively coarse grained and tends to be elongated perpendicular to the walls, occasionally approaching “cockscomb” texteur. Granular quartz, expecially in sheared bands is common. Vein symmetry, of sulfides, anhydrite or granularity along center-lines, margins or irregular parallel bands, is typicaly but unevenly developed.
Transitional	Cut A-veins, emplaced during emplacement of intrusions at Pancho	Major quartz w/ pyrite (up to 10%) & magnetite, and uncommonly chalcopyrite	
Banded	Cut and offset A-veinlets and transitional veins, but may be observed in clasts within intrusions	Outside dark bands; major quartz, K-spar, calcite & chlorite w/ pyrite & magnetite, and minor illite, epidote, garnet, gypsum, chalcopyrite, sphalerite, galena, molybdenite & cassiterite. Inside dark bands; Major quartz w/ magnetite, and minor chalcopyrite, bornite &	
D-veins	Cut and offset A- and Banded veins, and intrusions	Major quartz w/ pyrite, and minor chalcopyrite & molybdenite	Sulfide-anhydrite with minor quartz (except where superimposed on B-veins) and occasional carbonate. The quartz is typically free of inclusions, and tends to show crystal form. Anhydrite locally forms coarse cyrstalline masses and is commonly banded with the sulfides.
Quartz-Alunite Ledges	Cross-cut A- and Banded veins	Major quartz & alunite w/ pyrite, and minor rutile, dickite, diaspore & barite	

Table 2: *Continued*

Vein Type	G&H Sulfide Assemblage	M&E Alteration Halo	G&H Alteration Halo	M&E Thickness
A-1 (early)	Disseminated chalcopyrite-bornite, with proportions usually similar to the background sulfide; traces of molybdenite locally.	Biotite, or K-spar, oligoclase	Halos of K-spar, usually perthitic, are more or less developed about most veins. These may be very thin and inconspicuous, especially in stong K-silicate altered rock. They are strongest and most obvious about late veins in relatively fresh rock	<0.2cm
A-2 (early)		K-spar and quartz		<0.2cm
A-3 (late)		none		<1-2cm
A-4 (late)		none		<1-2cm
B-veins	Molybdenite-chalcopyrite is characteristic. Traces of bornite occur in some, but more commonly minor pyrite occurs in contract to bornite-chalcopyrite in the walls. Sulfides tend to be coarse grained and occupy banding parallel to the walls or cracks perpendicular to them.		Lack of alteration halos is characteristic. Occasionally faint and irregular bleached halos are present, but most are probably due to superimposed veining.	
Transitional		none		up to 3 cm
Banded		none		mms-2cm
D-veins	Pyrite is usually predominant, with chalcopyite, bornite, enargite, tenantite, sphalerite and galena common. Minor molybdenite and may other sulfides occure locally. “Reaction” texterures are typical.	Quartz, sericite, pyrite	Feldspar-destructive halos are characteristic, but patterns vary and have not been well documented. Sericite or sericite-chlorite halos may or may not have outer kaolinite-calcite halos.	<1mm-3cm
Quartz-Alunite Ledges		Quartz, kaolinite, pyrite		0.5-40m

Table 2: Continued

Vein Type	M&E Structure	G&H Age and Structural Style
A-1 (early)	Discontinuous, irregular walls	A quartz veins are the earliest of all veins, invariably cut by B quartz veins... The earliest veins are most randomly oriented and discontinuous, commonly segmented and "whispy." Widths usually range from 1 to 25 mm, and strike continuity from centimeters to a few meters.
A-2 (early)	Discontinuous, irregular walls	
A-3 (late)	Continuous, straight walls	
A-4 (late)	Continuous, straight walls	
B		Younger than "A" veins and older than "D" veins. They are characteristically regular and continuous, and tend to have flat attitudes. Widths usually range from 5 to 50 mm, and strike continuity from meters to tens of meters.
Transitional	Slightly wavy parallel walls. Locally vuggy vein centers. Discontinuous patches of dark quartz with quartz finer grained, more granular and locally toothy appearance than the A-veins.	
Banded	Continuous , wavy walls	
D-veins	Continuous	"D" veins cut all "A" and "B" quartz veins… They are continuous, though locally irregular and "lacing," and occupy sytematic structure patterns. Widths usually rant from 1 to 75 mm, and strike continuity from meters to tens of meters.
Quartz-Alunite Ledges	Continuous, replacement, breccia common	

Table 3: Microthermometry data from Muntean (1998). The microthermometry data was collected for geobarometry work, inclusions are grouped by inclusion group. NR is not reported, * indicates conversion from Nash (1976) nomenclature to nomenclature used in this study.

Sample	Vein Type	Group	Origin	Inclusion	Inclusion Type	Th	Halite Dissolution	Tm	Salinity
						°C	°C	°C	Wt.%NaCl eq.
RV027	banded	1	primary	2	LVD*	225	205	N/A	32.1
				3	LVD*	225	200	N/A	31.9
				4	LVD	230	275	N/A	36.3
				5	LVD*	>400	230	N/A	33.5
				6	LVD*	>400	290	N/A	37.4
				7	LVD	215	220	N/A	32.9
				8	LVD	245	275	N/A	36.3
RV027	banded	2	primary	13	LV*	240	NR	NR	NR
				14	LV*	270	NR	NR	NR
				15	LV*	330	NR	NR	NR
				16	LV*	245	NR	NR	NR
				17	LV*	260	N/A	-13.5	17.5
RV027	banded	3	primary	18	LV*	280	NR	NR	NR
				19	LV*	285	NR	NR	NR
				20	LV*	260	NR	NR	NR
				21	LV*	255	NR	NR	NR
RV027	banded	4	primary	1	LVD*	215	215	N/A	32.6
				2	LVD*	215	215	N/A	32.6
				3	LVD*	270	NR	NR	NR
				4	LVD*	225	225	N/A	33.2
RV027	banded	5	uncertain	1	LVD*	255	230	N/A	33.5
				2	LVD*	255	230	N/A	33.5
				3	LVD*	245	230	N/A	32.9†

Table 3: *Continued*

Sample	Vein Type	Group	Origin	Inclusion	Inclusion Type	Th	Halite Dissolution	Tm	Salinity
						°C	°C	°C	Wt.%NaCl eq.
RV041	banded	1	secondary	1	LV*	355	NR	NR	NR
				2	LV*	365	NR	NR	NR
				3	LV*	330	N/A	-13	16.9
				4	LV*	335	NR	NR	NR
				5	LV*	380	NR	NR	NR
				6	LV*	355	NR	NR	NR
				7	LV*	385	NR	NR	NR
RV041	banded	2	secondary	4	LV*	305	NR	NR	NR
				5	LV*	305	N/A	-2	3.4
				6	LV*	310	N/A	-2	3.4
RV041	banded	3	secondary	1	LV*	325	NR	NR	NR
				2	LV*	320	NR	NR	NR
				3	LV*	310	N/A	-41.5	NR
				4	LVD*	310	115	N/A	28.4
				5	LVD*	315	140	N/A	29.3
DD-25 84-86m	“banded”	1	secondary	3	LV*	350	N/A	-6.8	10.2
				5	LV*	350	NR	NR	NR
				7	LV*	350	NR	NR	NR
				8	LV*	350	N/A	-6.8	10.2
LYR-2 33.9m	A	1	secondary	2	LVD*	230	200	N/A	31.9
				3	LVD	255	NR	NR	NR
				4	LVD	270	NR	NR	NR
				6	LVD*	245	200	N/A	31.9
				8	LVD	250	230	N/A	33.5
LYR-2 45.7m	A	1	uncertain	1	LVD	>700	630	N/A	78.3
				3	LVD	>700	675	N/A	84.5

Table 3: *Continued*

Sample	Vein Type	Group	Origin	Inclusion	Inclusion Type	Th	Halite Dissolution	Tm	Salinity
						°C	°C	°C	Wt.% NaCl eq.
ALC-1 292.8m	A	1	uncertain	1	LVD*	>700	580	N/A	71.1
				2	LVD*	500	545	N/A	66
				3	LVD*	445	575	N/A	70.3
				4	LVD*	505	560	N/A	71.1†
				5	LVD*	475	510	N/A	61.1
				6	LVD*	525	575	N/A	70.3
				7	LVD*	400	560	N/A	68.2
				8	LVD*	505	585	N/A	71.8
				9	LVD*	560	585	N/A	71.8
				10	LVD*	415	570	N/A	69.6
				11	LVD	>700	535	N/A	64.6
				13	LVD*	610	535	N/A	64.6
				14	LVD*	250	570	N/A	69.6
				1a	LVD*	530	575	N/A	70.3
				2a	LVD*	560	565	N/A	68.9
				3a	LVD*	495	585	N/A	71.8
				4a	LVD*	535	585	N/A	71.8
				5a	LVD*	565	585	N/A	71.8
				6a	LVD*	585	585	N/A	71.8
				7a	LVD*	>700	565	N/A	68.9
				9a	LVD*	645	575	N/A	70.3
				10a	LVD*	500	565	N/A	68.9
				11a	LVD*	610	580	N/A	71.1

Table 3: *Continued*

Sample	Vein Type	Group	Origin	Inclusion	Inclusion Type	Th	Halite Dissolution	Tm	Salinity
						°C	°C	°C	Wt.% NaCl eq.
ACS024	banded	1	secondary	1	LVD*	485	305	N/A	38.6
				2	LVD*	385	300	N/A	38.2
				3	LVD*	280	255	N/A	35
				6	LVD*	305	240	N/A	34.1
				7	LVD*	380	295	N/A	37.8
				8	LVD*	>700	390	N/A	46.4
				9	LVD*	385	280	N/A	36.7
				10	LVD*	375	240	N/A	34.1
				11	LVD*	650	360	N/A	43.3
ALC-1 19.9m	polymetallic	1	primary	1	LVD*	185	NR	NR	NR
				2	LVD*	185	NR	NR	NR
				3	LVD*	155	NR	NR	NR
				4	LVD*	180	NR	NR	NR
				5	LVD*	195	NR	NR	NR
				5a	LVD*	190	NR	NR	NR
				6	LVD*	200	NR	NR	NR
				7	LVD*	175	NR	NR	NR
				7a	LVD*	155	NR	NR	NR
ALC-1 19.9m	polymetallic	2	primary	9	LVD*	165	NR	NR	NR
				10	LVD*	120	NR	NR	NR
				12	LVD*	170	NR	NR	NR
				13	LVD*	170	NR	NR	NR
				15	LVD*	180	NR	NR	NR

Table 3: *Continued*

Sample	Vein Type	Group	Origin	Inclusion	Inclusion Type	Th	Halite Dissolution	Tm	Salinity
						°C	°C	°C	Wt.% NaCl eq.
CAV-1 110.1m	A	1	uncertain	1	LVD*	385	395	N/A	46.9
				2	LVD*	440	380	N/A	45.3
				3	LVD*	>700	395	N/A	46.9
				4	LVD*	315	425	N/A	50.3
				5	LVD*	305	425	N/A	50.3
				6	LVD*	>700	420	N/A	49.7
				7	LVD*	500	420	N/A	49.7
				8	LVD*	>700	425	N/A	50.3
				9	LVD*	405	425	N/A	50.3
				10	LVD*	660	405	N/A	48
				11	LVD*	410	420	N/A	49.7
				12	LVD*	395	420	N/A	49.7
				13	LVD*	590	405	N/A	48
CAV-1 110.1m	A	2	uncertain	1	LVD*	340	NR	NR	NR
				2	LVD*	315	260	N/A	35.3
				3	LVD*	430	285	N/A	37
				4	LVD*	385	280	N/A	36.7
				5	LVD*	280	NR	NR	NR
				6	LVD*	615	290	N/A	37.4
				7	LVD*	360	290	N/A	37.4
				8	LVD*	375	330	N/A	40.6
				9	LVD*	330	295	N/A	37.8
				10	LVD*	335	260	N/A	35.3

Table 4: Summary of fluid inclusion petrographic observations for both deposits. Percentages are given as visually estimated volume percent. Visual estimation of volumes do not account for the third dimension, combined with optical distortion, lend to estimates with generally low confidence (Roedder and Bodnar, 1980). For microthermometry and LA-ICP-MS, n is the number of analyses.

Vein Type	A-Vein	A- & Banded Vein
Inclusion Type	LVD	LV
Vapor Bubble (% volume)	10-40%	15-30%
Halite Daughter (% volume)	5-25%	n/a
Opaque Daughter (% volume)	≤5%	n/a
n, Microthermometry	8	43
n, LA-ICP-MS	12	12

Table 5: Microthermometry data. All inclusions homogenize to liquid.

Sample	Deposit	Assemblage	Origin	Inclusion Type	Final Ice Melting	Halite Dissolution	Salinity	Homogenization Temperature
					(ºC)	(ºC)	(wt.%NaCl eq.)	(ºC)
DD25 84-46m	Verde	11	Primary(?)	LV	-6		9	215
		11	Primary(?)	LV	-5.5		9	230
		18	Primary(?)	LV	-8.1		12	245
		18	Primary(?)	LV	-8.1		12	231
		18	Primary(?)	LV	-8		12	362
		18	Primary(?)	LV	-7.8		11	230
		18	Primary(?)	LV	-8.3		12	177
		18	Primary(?)	LV	-8		12	217.7
		18	Primary(?)	LV	-8		12	180
		18	Primary(?)	LV	-6		9	180
		18	Primary(?)	LV	-8		12	180
		18	Primary(?)	LV	-8.1		12	324.7
		18	Primary(?)	LV	-5.9		9	254.5
		21	Primary	LV	-6		9	240
		21	Primary	LV	-5.9		9	233
		8	Primary(?)	LV	-8.8		13	225
		8	Primary(?)	LV	-8.8		13	240
		8	Primary(?)	LV	-5.2		8	242
		8	Primary(?)	LV	-5.2		8	240
		8	Primary(?)	LV	-8.8		13	235
		8	Primary(?)	LV	-6.9		10	325
		8	Primary(?)	LV	-7.1		11	274

Table 5: Continued

Sample	Deposit	Assemblage	Origin	Inclusion Type	Final Ice Melting	Halite Dissolution	Salinity	Homogenization Temperature
					(ºC)	(ºC)	(wt.%NaCl eq.)	(ºC)
P-8-C 539_2	Pancho	3	Primary(?)	LVD		290	38	510
		3	Primary(?)	LVD		290	38	510
		3	Primary(?)	LVD		290	38	510
		3	Primary(?)	LVD		300	38	430
		3.75	Primary(?)	LV	-5.6		9	290
		3.75	Primary(?)	LV	-2.7		4	287
		3.75	Primary(?)	LV				287
		4	Primary(?)	LVD		290	38	510
		4	Primary(?)	LVD		290	38	470
		4.5	Primary(?)	LVD		286	37	460
		4.5	Primary(?)	LVD		286	36	460
RP054	Pancho	I	Primary(?)	LV	-15.9		19	253
RV027	Verde	19	Primary	LV	-1.6		3	278
		19	Primary	LV	-1.6		3	285
		19	Primary	LV	-1.5		3	285
		19	Primary	LV	-1.6		3	285
		19	Primary	LV	-3.6		6	285
		19	Primary	LV	-1.3		2	285
		19	Primary	LV	-3.5		6	285
		19	Primary	LV	-1.9		3	285
		19	Primary	LV	-7.2		11	301.7

Table 6: Average values from LA-ICP-MS analyses of fluid inclusions. n is the number of inclusions analyzed, n/a is not analyzed, and σ_x is the standard deviation of the mean. All values are element of interest/Na, except for the Cu/Au values.

Deposit	Pancho	Verde	Verde		Verde	Pancho		Pancho	
Vein Type	Banded	Banded	Banded		Transitional	A-vein		A-vein	
Inclusion Type	LV	LV	V		LV	LV		LVD	
Sample	RP058	RV027	RV027		V6.5NWC	All		All	
n	1	1	3		1	9		12	
Function	Value	Value	Mean	σ_x	Value	Mean	σ_x	Mean	σ_x
Mg/Na	n/a	2.3E-02	9.7E-03	1.6E-03	4.3E-02	3.4E-03	6.1E-04	2.6E-04	1.1E-05
Al/Na	n/a	8.6E-01	3.7E-02	2.8E-02	2.5E+00	3.7E-01	1.4E-01	3.1E-02	1.8E-03
Si/Na	6.3E+01	2.8E+02	1.6E+03	1.1E+03	1.0E+03	3.6E+02	1.7E+02	3.5E+02	2.4E+02
K/Na	n/a	1.2E-01	7.4E-01	6.5E-02	1.0E+00	7.4E-01	7.8E-02	7.9E-01	1.1E-01
Ca/Na	n/a	2.3E-01	6.1E-01	3.5E-01	1.8E+00	9.3E-02	3.0E-02	1.2E-02	2.9E-03
Ti/Na	n/a	5.4E-03	6.1E-02	4.3E-02	1.0E-01	4.1E-02	2.0E-02	3.9E-03	4.6E-04
Fe/Na	1.0E+00	5.2E-01	2.5E+01	1.5E+01	6.9E-01	1.1E+00	3.9E-01	1.3E+00	5.4E-01
Cu/Na	3.7E-02	1.4E-03	6.7E-01	3.3E-01	2.4E-02	1.0E-01	5.8E-02	1.2E-01	5.2E-02
Zn/Na	1.5E-02	3.1E-03	1.7E-02	3.6E-03	5.7E-02	1.9E-01	9.9E-02	3.2E-01	1.6E-01
As/Na	4.6E-04	1.7E-03	6.7E-03	4.6E-03	3.8E-03	1.8E-03	7.5E-04	8.9E-03	7.6E-03
Ag/Na	n/a	n	2.4E-03	1.1E-03	2.4E-03	7.4E-04	2.3E-04	6.8E-04	8.2E-05
Sb/Na	1.3E-04	1.1E-02	3.7E-03	2.0E-03	n	3.7E-04	1.5E-04	2.1E-03	1.1E-03
Ba/Na	n/a	9.4E-03	1.1E-02	3.1E-03	8.8E-03	6.8E-03	1.7E-03	2.8E-02	1.3E-02
Au/Na	2.9E-05	6.0E-06	1.8E-04	1.5E-04	1.7E-04	5.1E-05	3.0E-05	4.7E-05	3.0E-05
Pb/Na	n/a	6.2E-04	6.8E-03	7.2E-04	4.2E-02	5.6E-02	6.5E-03	1.4E-01	3.1E-02
Cu/Au	1.3E+03	2.3E+02	7.3E+03	2.6E+03	1.4E+02	5.8E+03	2.3E+03	3.8E+04	2.1E+04

Table 7: Raw LA-ICP-MS from successful fluid inclusion analyses. Successful fluid inclusion analyses were those that contained a noticeable Na peak for deconvolution using the SILLS program. Blank fields indicate that the isotope was not analyzed for that sample. Negative fields indicate the value was less than the 3σ limit of detection, which is the value in the negative fields. Inclusions from the same location belong in the same group, inclusions that have the same location and FIA belong to the same assemblage.

Analysis	RP058_5j1_4	539_1_5j1_2	539_1_5j1_3	539_1_5j1_4	539_1_5j1_5	539_1_5j1_6	539_1_5j1_7
Deposit	Pancho	Pancho	Pancho	Pancho	Pancho	Pancho	Pancho
Sample	RP058	P-8-C 539_1	P-8-C 539_1	P-8-C 539_1	P-8-C 539_1	P-8-C 539_1	P-8-C 539_1
Location	5j1	5j1	5j1	5j1	5j1	5j1	5j1
FIA							
^{23}Na	1.36E+05	3.76E+05	4.25E+05	1.74E+05	1.27E+05	1.43E+05	3.01E+05
^{25}Mg							
^{27}Al							
^{28}Si	8.59E+06	7.92E+06	4.61E+06	7.85E+06	7.76E+06	1.01E+07	7.94E+06
^{39}K							
^{40}Ca							
^{49}Ti							
^{56}Fe	1.39E+05	2.72E+05	2.49E+05	5.84E+04	1.74E+05	3.06E+05	2.00E+05
^{63}Cu	5.06E+03	6.45E+03	4.08E+04	8.82E+03	2.23E+04	3.59E+04	1.93E+04
^{66}Zn	2.07E+03	2.37E+04	3.04E+04	2.04E+04	6.30E+03	1.33E+04	4.37E+04
^{75}As	6.30E+01	7.60E+01	2.01E+00	4.41E+02	1.69E+01	2.06E+00	-6.77E+00
^{107}Ag							
^{121}Sb	1.78E+01	7.28E+01	-7.12E+01	8.20E+01	-2.79E+01	5.21E+01	3.82E+01
^{138}Ba							
^{197}Au	3.91E+00	-4.57E-01	-3.00E-01	3.51E-02	2.05E-01	9.50E-01	9.70E-01
^{208}Pb							

Table 7: *Continued*

Analysis	539_1_5j1_8	539_1_5j1_9	539_1_5j2_1	539_1_5j3_1	539_1_5j3_2	539_1_5j3_3	539_1_5j3_4
Deposit	Pancho	Pancho	Pancho	Pancho	Pancho	Pancho	Pancho
Sample	P-8-C 539_1	P-8-C 539_1	P-8-C 539_1	P-8-C 539_1	P-8-C 539_1	P-8-C 539_1	P-8-C 539_1
Location	5j1	5j1	5j2	5j3	5j3	5j3	5j3
FIA							
^{23}Na	1.54E+05	1.52E+05	1.48E+05	4.18E+04	1.88E+04	1.44E+05	8.92E+04
^{25}Mg							
^{27}Al							
^{28}Si	3.27E+06	3.68E+06	9.00E+06	5.97E+06	1.20E+06	2.28E+07	3.17E+06
^{39}K							
^{40}Ca							
^{49}Ti							
^{56}Fe	1.31E+05	1.27E+05	8.56E+04	1.04E+04	7.41E+04	2.36E+05	1.34E+05
^{63}Cu	1.40E+04	1.28E+04	1.11E+03	2.83E+02	5.07E+01	5.22E+03	1.81E+04
^{66}Zn	1.95E+04	1.87E+04	1.74E+04	1.50E+03	1.81E+04	3.52E+04	6.44E+03
^{75}As	1.04E+01	-4.05E+00	1.55E+00	7.36E+01	2.41E+01	1.86E+02	8.41E+00
^{107}Ag							
^{121}Sb	-2.10E+01	-1.86E+01	-4.41E+01	6.04E+01	-4.47E+01	3.26E+01	1.02E+01
^{138}Ba							
^{197}Au	1.20E+00	3.22E-02	7.37E-01	-2.94E-01	3.03E-01	1.01E+00	-8.10E-01
^{208}Pb							

Table 7: *Continued*

Analysis	539_1_5j3_5	539_1_5j4_1	539_1_5j4_2	539_1_5j5_1	539_1_5j5_2	539_1_5j6_1	539_2_4j1_3
Deposit	Pancho	Pancho	Pancho	Pancho	Pancho	Pancho	Pancho
Sample	P-8-C 539_1	P-8-C 539_1	P-8-C 539_1	P-8-C 539_1	P-8-C 539_1	P-8-C 539_1	P-8-C 539_2
Location	5j3	5j4	5j4	5j5	5j5	Pancho	4j1
FIA							
^{23}Na	3.63E+04	7.33E+04	7.74E+04	3.20E+05	1.59E+05	4.37E+05	1.87E+05
^{25}Mg							
^{27}Al							
^{28}Si	2.61E+06	1.88E+07	8.00E+06	1.02E+07	7.36E+06	3.47E+07	8.10E+06
^{39}K							
^{40}Ca							
^{49}Ti							
^{56}Fe	2.76E+04	8.37E+03	5.26E+05	1.34E+05	1.09E+05	4.59E+05	1.50E+04
^{63}Cu	5.31E+03	9.16E+01	5.15E+04	1.03E+05	2.12E+04	6.70E+04	1.18E+03
^{66}Zn	4.38E+03	2.23E+03	8.82E+04	2.61E+04	1.16E+04	3.57E+04	7.89E+03
^{75}As	-3.00E+01	1.99E+02	5.24E+01	2.42E+01	3.84E+01	2.32E+01	2.64E+02
^{107}Ag							
^{121}Sb	-5.36E+01	1.09E+01	-7.33E+00	-2.80E+00	-1.14E+01	3.75E+00	3.63E+01
^{138}Ba							
^{197}Au	-7.99E-01	1.50E+00	3.28E+00	-3.56E-01	1.25E+00	1.76E+00	1.16E+00
^{208}Pb							

Table 7: *Continued*

Analysis	539_2_4j2_1	539_2_4j3_1	539_2_4j4_1	539_3_5_3	539_3_5_4	539_3_6area_1	539_3_6area_2
Deposit	Pancho	Pancho	Pancho	Pancho	Pancho	Pancho	Pancho
Sample	P-8-C 539_2	P-8-C 539_2	P-8-C 539_2	P-8-C 539_3	P-8-C 539_3	P-8-C 539_3	P-8-C 539_3
Location	4j2	4j3	4j4	5	5	6area	6area
FIA				5	5	6area	6area
^{23}Na	2.36E+05	3.61E+03	1.59E+04	6.48E+03	1.61E+05	1.39E+05	1.39E+05
^{25}Mg				3.94E+01	7.93E+01	5.88E+02	3.24E+01
^{27}Al				4.63E+03	4.98E+03	5.79E+04	5.23E+03
^{28}Si	8.72E+06	1.05E+07	1.18E+07	7.58E+06	8.07E+06	3.06E+07	7.41E+06
^{39}K				5.98E+03	2.89E+05	8.75E+04	1.68E+05
^{40}Ca				8.66E+02	2.19E+03	4.57E+05	3.19E+03
^{49}Ti				3.13E+02	1.77E+02	4.37E+03	7.29E+02
^{56}Fe	1.13E+05	9.57E+03	7.99E+03	5.48E+03	4.74E+04	2.94E+04	6.74E+04
^{63}Cu	1.12E+04	6.00E+01	2.27E+03	3.50E+03	9.59E+03	8.61E+02	6.66E+03
^{66}Zn	1.48E+04	6.28E+03	1.70E+03	5.97E+02	2.42E+04	2.85E+03	1.36E+04
^{75}As	3.60E+02	3.18E+02	3.47E+01	4.35E+01	4.95E+01	1.09E+02	3.05E+00
^{107}Ag				7.38E+00	1.62E+02	3.94E+01	1.38E+02
^{121}Sb	1.05E+02	3.85E+01	3.76E+01	7.59E+00	5.79E+00	-2.39E+01	1.35E+01
^{138}Ba				7.07E+01	2.02E+03	2.28E+03	1.10E+04
^{197}Au	-1.43E+00	1.32E+00	1.57E+00	1.75E+00	-2.97E-01	-2.04E+00	3.55E+00
^{208}Pb				3.41E+02	2.01E+04	3.68E+03	3.57E+04

Table 7: *Continued*

Analysis	539_3_4area_2	539_3_4area_3	539_3_4area_4	539_3_4area_5	539_3_5_1	RV027_ee_1	RV027_ee_2
Deposit	Pancho	Pancho	Pancho	Pancho	Pancho	Verde	Verde
Sample	P-8-C 539_3	P-8-C 539_3	P-8-C 539_3	P-8-C 539_3	P-8-C 539_3	RV027	RV027
Location	4area	4area	4area	4area	5	ee	ee
FIA	4area	4area	4area	4area	5	ee	ee
^{23}Na	2.29E+05	1.73E+04	1.29E+02	1.50E+04	5.96E+05	2.90E+04	6.60E+03
^{25}Mg	7.04E+01	3.27E+01	3.68E-01	5.23E+01	2.57E+03	1.92E+02	7.01E+01
^{27}Al	6.34E+03	5.49E+03	1.20E+02	5.44E+03	1.58E+04	2.72E+03	4.36E+01
^{28}Si	8.47E+06	8.22E+06	1.74E+05	8.34E+06	1.91E+07	2.61E+07	2.46E+07
^{39}K	9.66E+04	3.82E+04	6.08E+01	1.46E+04	7.69E+05	1.97E+04	4.40E+03
^{40}Ca	2.11E+03	7.34E+02	5.98E+00	3.10E+02	1.62E+04	6.20E+03	2.02E+03
^{49}Ti	9.86E+02	8.21E+02	1.87E+01	7.88E+02	5.63E+02	9.29E+02	9.61E+02
^{56}Fe	2.38E+04	1.91E+04	2.72E+01	7.91E+03	4.61E+05	6.16E+05	3.48E+05
^{63}Cu	1.54E+03	1.88E+03	2.68E+00	1.74E+03	5.44E+03	2.09E+04	8.09E+03
^{66}Zn	1.79E+04	7.09E+03	1.63E+01	1.95E+03	8.65E+04	2.92E+02	1.34E+02
^{75}As	5.65E+02	2.41E+02	4.86E-01	-3.54E+01	3.93E+03	1.01E+02	1.04E+02
^{107}Ag	1.34E+02	2.70E+01	2.24E-01	1.96E+00	2.41E+02	8.37E+01	2.62E+01
^{121}Sb	1.58E+02	2.82E+01	-2.57E-01	-1.36E+01	5.61E+02	6.76E+01	5.08E+01
^{138}Ba	6.12E+02	1.74E+02	2.05E-01	2.78E+02	1.96E+03	3.08E+02	1.10E+02
^{197}Au	1.13E+00	9.97E-01	1.60E-02	1.23E+00	-4.13E-01	1.81E+00	3.13E+00
^{208}Pb	1.17E+04	4.59E+03	1.17E+01	8.88E+02	7.12E+04	1.86E+02	3.80E+01

Table 7: *Continued*

Analysis	RV027_ff_1	V6_16_1	539_1_5area_2	539_2_4_1	539_2_4_2	539_2_4b_1	539_2_4b_3
Deposit	Verde	Verde	Pancho	Pancho	Pancho	Pancho	Pancho
Sample	RV027	V6.5NWC 342.4	P-8-C 539_1	P-8-C 539_2	P-8-C 539_2	P-8-C 539_2	P-8-C 539_2
Location	ff	16	5area	4	4	4b	4b
FIA				4	4	4b	4b
^{23}Na	6.01E+04	7.73E+03	2.34E+05	4.44E+04	1.11E+05	2.47E+04	5.10E+04
^{25}Mg	7.15E+02	3.33E+02	9.56E+03	9.38E+00	5.09E+01	5.18E+02	1.67E+02
^{27}Al	6.05E+02	1.95E+04	4.90E+04	2.53E+03	4.48E+03	1.92E+04	3.26E+04
^{28}Si	9.83E+06	7.87E+06	5.52E+06	4.70E+06	7.85E+06	1.56E+07	2.24E+07
^{39}K	5.21E+04	7.74E+03	1.29E+05	8.28E+03	2.64E+04	4.86E+04	1.03E+05
^{40}Ca	7.85E+04	1.40E+04	4.54E+03	7.02E+02	8.75E+02	1.28E+04	1.32E+04
^{49}Ti	3.50E+02	7.88E+02	8.33E+02	4.62E+02	8.80E+02	2.85E+03	3.40E+03
^{56}Fe	1.34E+05	5.31E+03	1.13E+05	1.79E+03	6.72E+03	1.55E+04	2.32E+04
^{63}Cu	4.41E+03	1.88E+02	1.86E+03	2.47E+02	2.38E+02	8.45E+03	5.31E+02
^{66}Zn	1.28E+03	4.44E+02	9.53E+03	1.63E+03	4.05E+03	2.08E+03	1.31E+04
^{75}As	4.72E+01	2.94E+01	3.60E+02	7.14E+01	1.79E+02	-6.00E+00	3.74E+02
^{107}Ag	1.59E+01	1.87E+01	8.34E+01	4.88E+01	8.25E+01	1.39E+02	1.97E+01
^{121}Sb	6.40E+01	-9.35E+01	2.36E+02	5.77E+01	1.01E+02	4.15E+01	7.57E+01
^{138}Ba	3.54E+02	6.79E+01	7.83E+02	4.37E+01	2.06E+02	6.67E+02	4.12E+03
^{197}Au	5.80E-01	1.32E+00	-1.39E+00	-1.37E+00	-2.20E+00	1.62E+00	1.02E+00
^{208}Pb	4.91E+02	3.27E+02	1.02E+04	1.98E+03	3.62E+03	3.35E+03	4.48E+03

Table 7: *Continued*

Analysis	600_9area_2	600_9area_3	600_11area_1	600_I_1_cps	600_I_2_cps	600_wall_1_cps	RV027_5area_4
Deposit	Pancho	Pancho	Pancho	Pancho	Pancho	Pancho	Verde
Sample	P-8-C 600	P-8-C 600	P-8-C 600	P-8-C 600	P-8-C 600	P-8-C 600	RV027
Location	9area	9area	11area	I	I	wall	5area
FIA	9area	9area					5area
^{23}Na	2.14E+05	6.20E+05	2.57E+05	1.95E+05	2.90E+05	2.06E+04	1.13E+02
^{25}Mg	2.64E+02	2.65E+03	7.08E+02	1.49E+02	7.13E+01	3.83E+01	-1.11E-01
^{27}Al	2.28E+04	2.76E+04	1.79E+04	1.93E+04	7.63E+03	6.63E+03	5.96E-01
^{28}Si	2.08E+07	1.72E+07	8.09E+06	1.41E+07	6.83E+06	8.26E+06	1.58E+04
^{39}K	1.56E+05	6.40E+05	1.44E+05	1.34E+05	2.13E+05	1.61E+04	4.60E+00
^{40}Ca	4.90E+04	6.39E+03	1.12E+04	1.02E+03	1.03E+03	2.35E+03	1.79E+00
^{49}Ti	1.19E+03	1.08E+03	1.09E+03	1.07E+03	6.24E+02	7.44E+02	2.28E-01
^{56}Fe	1.65E+05	5.72E+05	1.48E+05	3.57E+03	5.54E+04	1.60E+04	2.88E+01
^{63}Cu	3.29E+04	4.00E+03	5.98E+02	8.82E+01	1.04E+04	3.57E+03	2.26E+01
^{66}Zn	1.23E+04	4.71E+04	1.10E+04	6.66E+03	2.46E+04	1.39E+03	-4.61E-02
^{75}As	3.72E+01	3.00E+01	5.16E+01	3.68E+01	3.06E+02	2.14E+01	1.48E-01
^{107}Ag	1.16E+02	5.26E+01	5.49E+01	7.85E+01	1.29E+02	9.05E+00	8.07E-02
^{121}Sb	1.64E+01	-4.77E+00	6.23E+01	-5.99E+01	-1.04E-01	2.15E+01	-2.30E-01
^{138}Ba	2.11E+03	4.82E+02	2.73E+03	2.11E+02	9.95E+02	2.91E+02	6.93E-01
^{197}Au	1.86E+00	5.83E-01	2.05E-01	-1.74E+00	2.57E+00	2.71E+00	2.54E-02
^{208}Pb	9.30E+03	2.86E+04	1.26E+04	2.62E+04	2.91E+04	1.25E+03	3.21E-02

Table 7: *Continued*

Analysis	RV027_5area_9	RV027_19_1	RV027_19_3	RV027_19_5	RP058_I_1	RP058_I_2	RP058_I_3
Deposit	Verde	Verde	Verde	Verde	Pancho	Pancho	Pancho
Sample	RV027	RV027	RV027	RV027	RP058	RP058	RP058
Location	5area	19	19	19	I	I	I
FIA	5area	19	19	19	I	I	I
^{23}Na	3.27E+01	2.77E+02	1.41E+02	4.85E+02	2.16E+01	6.23E+00	4.56E+00
^{25}Mg	2.19E-01	-8.88E-02	1.96E+00	1.12E+01	1.14E-01	6.85E-01	3.06E-01
^{27}Al	2.89E+00	1.23E+03	3.55E+01	4.18E+02	1.05E+00	-6.44E-01	4.97E-01
^{28}Si	9.91E+04	1.28E+05	6.32E+04	1.35E+05	8.59E+04	8.75E+04	9.80E+04
^{39}K	6.45E+00	1.60E+01	9.52E+00	5.68E+01	1.31E+01	-3.39E+00	-3.71E+00
^{40}Ca	1.33E+00	2.09E+01	9.80E+00	1.14E+02	2.65E+00	2.21E+01	5.33E-01
^{49}Ti	2.89E+00	1.69E-01	1.22E-03	2.62E+00	8.89E+00	8.54E+00	7.89E+00
^{56}Fe	5.99E+02	3.80E-02	4.30E+01	2.53E+02	1.81E+03	2.25E+03	1.45E+03
^{63}Cu	2.12E+01	5.56E-01	4.06E-03	6.85E-01	2.09E+01	8.75E+00	9.76E+00
^{66}Zn	1.70E-01	7.61E-01	-3.74E-02	1.53E+00	6.87E-01	7.84E-01	5.68E-01
^{75}As	1.94E-02	1.13E+00	2.38E-01	8.09E-01	1.10E+00	5.75E-01	9.10E-01
^{107}Ag	5.18E-02	-1.75E-02	2.94E-01	-7.08E-02	-1.99E-01	9.60E-02	8.38E-02
^{121}Sb	-2.21E-02	1.45E+00	-2.63E-01	5.56E+00	-1.29E-01	4.79E-01	1.87E-01
^{138}Ba	1.59E-01	7.99E-01	1.59E-01	4.54E+00	3.04E-01	1.12E-01	5.42E-02
^{197}Au	-1.37E-02	-1.63E-02	-6.49E-03	2.92E-03	-6.19E-02	-2.40E-02	-5.09E-02
^{208}Pb	1.77E-01	-8.57E-03	-1.35E-01	3.01E-01	4.14E-02	2.25E-01	6.77E-02

Table 7: *Continued*

Analysis	RP058_I_4
Deposit	Pancho
Sample	RP058
Location	I
FIA	I
^{23}Na	2.15E+01
^{25}Mg	1.57E+00
^{27}Al	9.71E+00
^{28}Si	2.24E+05
^{39}K	1.06E+01
^{40}Ca	2.97E+01
^{49}Ti	1.67E+01
^{56}Fe	2.69E+03
^{63}Cu	3.50E+00
^{66}Zn	9.90E-01
^{75}As	1.85E+00
^{107}Ag	-7.37E-03
^{121}Sb	1.04E+00
^{138}Ba	6.43E-01
^{197}Au	-2.50E-02
^{208}Pb	4.30E-01

Table 8: LA-ICP-MS analyzed for trace elements in quartz, either unsuccessful fluid inclusion analysis or intentional quartz analyses. Blank fields indicate that the isotope was not analyzed for that sample, negative values are the detection limits and indicate that the analysis was less than the limit of detection.

Analysis	RP058_5j1_1	RP058_5j1_2	RP058_5j1_3	RP058_5j2_1	539_2_4j1_2	539_2_4j1_quartz2	539_2_4j1_quartz
Deposit	Pancho	Pancho	Pancho	Pancho	Pancho	Pancho	Pancho
Sample	RP058	RP058	RP058	RP058	P-8-C 539_2	P-8-C 539_2	P-8-C 539_2
Location	5j1	5j1	5j1	5j2	4j1	4j1	4j1
^{23}Na	1.03E+03	2.93E+03	1.31E+04	1.73E+04	2.29E+04	2.65E+02	1.31E+03
^{25}Mg							
^{27}Al							
^{28}Si	8.26E+06	1.73E+07	7.35E+06	8.06E+06	1.53E+07	7.91E+06	1.02E+07
^{39}K							
^{40}Ca							
^{49}Ti							
^{56}Fe	6.80E+04	2.30E+05	1.31E+05	3.58E+05	7.07E+03	4.55E+02	1.67E+03
^{63}Cu	2.36E+02	1.23E+04	8.25E+03	1.08E+05	3.78E+03	5.20E+01	1.36E+01
^{66}Zn	3.12E+02	3.56E+02	1.59E+03	1.23E+03	6.72E+02	4.08E+01	4.61E+01
^{75}As	2.82E+00	1.28E+02	6.96E+01	6.19E+01	2.41E+01	5.73E+00	2.73E+01
^{107}Ag							
^{121}Sb	-1.68E+01	6.61E+01	4.82E+01	4.52E+01	-8.22E+01	2.53E+01	7.55E+00
^{138}Ba							
^{197}Au	6.86E-01	8.82E-01	1.68E+00	1.24E+01	6.44E-01	1.26E-02	-1.78E+00
^{208}Pb							

Table 8: *Continued*

Analysis	539_2_4j2_quartz	RV027_4j2_1	RV027_4j2_2	RV027_4j2_3	RV027_4j2_4	RV027_4j2_5	RV027_4j2_6
Deposit	Pancho	Verde	Verde	Verde	Verde	Verde	Verde
Sample	P-8-C 539_2	RV027	RV027	RV027	RV027	RV027	RV027
Location	4j2	4j2	4j2	4j2	4j2	4j2	4j2
^{23}Na	-1.33E+02	2.37E+03	6.99E+02	1.41E+03	1.47E+03	1.19E+03	2.91E+04
^{25}Mg							
^{27}Al							
^{28}Si	7.49E+06	1.56E+07	7.21E+06	6.82E+06	7.91E+06	8.02E+06	9.77E+07
^{39}K							
^{40}Ca							
^{49}Ti							
^{56}Fe	9.87E+01	1.41E+05	4.69E+04	4.39E+04	2.54E+04	6.99E+04	2.12E+06
^{63}Cu	-1.04E+02	1.01E+03	2.57E+02	1.31E+03	6.22E+02	9.23E+02	1.42E+05
^{66}Zn	-2.53E+01	1.19E+02	4.57E+01	6.96E+01	3.07E+01	3.73E+01	1.34E+03
^{75}As	1.94E+01	5.06E+01	1.84E+01	2.73E+01	-2.32E+00	2.33E+00	3.01E+02
^{107}Ag							
^{121}Sb	2.47E+01	3.94E+00	5.37E+01	-3.16E+01	-4.24E+00	-2.06E+01	2.15E+02
^{138}Ba							
^{197}Au	6.41E-02	2.19E+00	4.99E-01	2.25E-01	3.86E-02	-1.32E+00	7.98E+02
^{208}Pb							

Table 8: *Continued*

Analysis	RV027_4j3_1	RV027_4j3_2	RV027_4j3_3	RV027_4j3_4	RV027_4j3_5	RV027_4j3_6	539_3_6area_3
Deposit	Verde	Verde	Verde	Verde	Verde	Verde	Pancho
Sample	RV027	RV027	RV027	RV027	RV027	RV027	P-8-C 539_3
Location	4j3	4j3	4j3	4j3	4j3	4j3	6area
^{23}Na	1.92E+05	8.70E+04	1.81E+04	4.45E+03	2.06E+03	2.19E+03	2.19E+02
^{25}Mg							4.14E+00
^{27}Al							1.46E+03
^{28}Si	8.64E+07	9.33E+06	8.72E+06	1.12E+07	8.13E+06	1.01E+07	2.53E+06
^{39}K							-1.18E+02
^{40}Ca							1.91E+02
^{49}Ti							2.21E+02
^{56}Fe	5.57E+06	1.03E+05	1.36E+06	1.92E+05	1.40E+05	2.16E+05	3.36E+02
^{63}Cu	9.53E+04	1.13E+03	2.21E+04	3.57E+03	2.10E+03	5.38E+02	5.17E+01
^{66}Zn	3.48E+03	4.35E+03	5.77E+02	1.49E+02	6.86E+01	7.74E+01	6.26E+01
^{75}As	2.81E+02	4.18E+01	2.51E+01	3.01E+01	2.51E+01	-1.14E+01	1.38E+01
^{107}Ag							9.56E+00
^{121}Sb	1.11E+02	-1.84E+01	4.53E+01	-1.60E+00	-4.10E+01	-7.35E+00	-2.14E+01
^{138}Ba							1.74E+00
^{197}Au	2.06E+02	6.30E-01	2.58E+00	5.14E-01	6.37E+00	-1.01E+00	5.16E-01
^{208}Pb							1.99E+01

Table 8: *Continued*

Analysis	DD35_3_1	DD35_3area_1	DD35_3area_2	DD35_3area_3	DD35_3area_4	RP028_2	RP028_3
Deposit	Verde	Verde	Verde	Verde	Verde	Pancho	Pancho
Sample	DD35	DD35	DD35	DD35	DD35	RP058	RP058
Location	3	3	3area	3area	3area	2	3
^{23}Na	1.95E+04	6.63E+02	2.97E+04	3.22E+03	4.22E+03	4.25E+02	3.38E+03
^{25}Mg	7.08E+02	1.79E+02	6.64E+02	2.98E+02	5.40E+02	2.00E+02	1.97E+02
^{27}Al	7.53E+03	2.51E+04	4.02E+04	7.16E+04	4.94E+04	2.99E+04	4.03E+04
^{28}Si	1.37E+04	9.68E+06	8.69E+06	9.90E+06	1.02E+07	8.71E+06	1.01E+07
^{39}K	5.51E+04	2.10E+03	2.73E+04	4.78E+04	8.79E+03	3.04E+03	5.08E+03
^{40}Ca	1.88E+08	1.91E+02	3.31E+04	2.76E+03	1.19E+04	9.86E+02	2.31E+03
^{49}Ti	2.26E+03	1.09E+03	8.82E+02	2.30E+03	1.26E+03	6.88E+02	7.28E+02
^{56}Fe	1.65E+04	4.07E+03	4.41E+04	8.37E+03	1.04E+05	5.33E+03	3.40E+04
^{63}Cu	3.36E+01	1.68E+01	4.11E+04	1.80E+02	7.56E+02	-4.80E+00	1.47E+02
^{66}Zn	8.84E+01	1.01E+02	7.31E+02	1.48E+02	4.66E+02	1.55E+02	1.28E+02
^{75}As	-1.38E+01	-3.03E+00	2.23E+01	3.24E+00	6.99E+01	7.42E+01	7.96E+01
^{107}Ag	2.61E+00	-1.96E+01	1.91E+02	4.10E+00	2.37E+01	-3.51E+00	1.65E+01
^{121}Sb	-1.39E+01	5.31E+01	2.90E+01	-2.24E+01	1.08E+02	6.98E+01	1.03E+02
^{138}Ba	1.19E+01	4.07E-01	1.01E+02	1.63E+01	1.06E+02	1.68E+02	1.87E+02
^{197}Au	-1.52E+00	-1.16E-01	1.06E+00	-3.38E+00	9.21E+00	3.40E+00	6.41E+00
^{208}Pb	1.87E+01	2.00E-02	6.83E+02	2.83E+01	2.95E+02	5.39E+00	2.81E+01

Table 8: *Continued*

Analysis	RP028_4	RP028_5	RP028_6	RP028_7	RP028_8	RP028_9	RP028_10
Deposit	Pancho	Pancho	Pancho	Pancho	Pancho	Pancho	Pancho
Sample	RP058	RP058	RP058	RP058	RP058	RP058	RP058
Location	4	5	6	7	8	9	10
^{23}Na	6.71E+02	3.62E+03	2.95E+02	8.00E+02	1.01E+03	2.02E+03	1.67E+02
^{25}Mg	1.88E+02	7.10E+01	3.86E+02	1.04E+02	2.02E+02	1.43E+02	4.30E+02
^{27}Al	4.17E+04	1.78E+04	3.53E+04	3.02E+04	5.68E+04	5.23E+04	3.69E+04
^{28}Si	8.19E+06	9.14E+06	9.30E+06	9.14E+06	1.06E+07	9.02E+06	1.03E+07
^{39}K	2.46E+04	8.77E+03	5.26E+03	3.44E+03	6.77E+03	3.69E+03	3.66E+03
^{40}Ca	2.28E+03	1.47E+03	6.33E+02	4.22E+03	4.44E+03	2.63E+03	4.14E+02
^{49}Ti	1.65E+03	2.70E+02	1.69E+03	4.91E+02	1.04E+03	2.06E+02	1.42E+03
^{56}Fe	6.95E+03	4.84E+05	1.12E+04	7.35E+04	8.34E+03	1.47E+05	1.00E+04
^{63}Cu	3.59E+01	2.46E+02	2.71E+01	2.60E+01	2.92E+01	1.77E+02	3.04E+00
^{66}Zn	1.31E+02	4.37E+02	2.00E+02	1.56E+02	1.15E+02	1.45E+02	2.95E+02
^{75}As	1.84E+01	2.01E+02	7.42E+01	5.90E+01	3.41E+01	1.02E+02	2.95E+01
^{107}Ag	-1.10E-01	8.31E+00	-1.73E+01	5.11E+00	8.27E+00	4.16E+00	1.82E+00
^{121}Sb	-3.30E+00	1.65E+02	1.49E+01	1.14E+02	1.19E+01	4.29E+01	1.78E+01
^{138}Ba	8.63E+01	1.69E+02	6.23E+00	1.16E+03	3.59E+02	3.31E+02	1.10E+01
^{197}Au	2.71E+00	1.75E+00	2.21E-01	1.37E+01	1.33E+00	2.27E+00	-1.32E+00
^{208}Pb	4.73E+01	4.20E+02	9.15E+00	2.46E+01	2.89E+01	7.66E+01	8.13E+00

Table 8: *Continued*

Analysis	RP028_11	RP028_12	RP028_13	RP028_14	RP028_15	RV027_aa_1	RV027_aa_2
Deposit	Pancho	Pancho	Pancho	Pancho	Pancho	Verde	Verde
Sample	RP058	RP058	RP058	RP058	RP058	RV027	RV027
Location	11	12	13	14	15	aa	aa
^{23}Na	8.73E+01	3.07E+02	1.09E+02	4.06E+03	1.12E+03	1.35E+03	7.69E+02
^{25}Mg	3.91E+02	6.43E+01	5.92E+02	1.78E+02	1.59E+02	6.98E+01	1.27E+01
^{27}Al	3.98E+04	1.06E+04	6.07E+04	4.27E+04	2.34E+04	9.35E+03	1.20E+02
^{28}Si	1.11E+07	1.05E+07	1.12E+07	1.06E+07	7.45E+06	9.68E+06	2.35E+06
^{39}K	1.20E+04	2.59E+02	8.40E+03	8.32E+03	3.29E+03	2.20E+03	-6.97E+02
^{40}Ca	1.64E+03	1.08E+03	1.83E+03	3.02E+03	1.08E+03	5.24E+02	8.62E+02
^{49}Ti	1.69E+03	4.68E+02	2.51E+03	1.05E+03	6.67E+02	1.33E+03	5.73E+01
^{56}Fe	8.92E+03	1.59E+05	1.53E+04	1.57E+05	4.84E+03	8.77E+02	2.21E+04
^{63}Cu	1.31E+01	-1.49E+01	-8.18E+00	1.26E+02	7.22E+02	5.34E+01	3.81E+01
^{66}Zn	2.69E+02	2.05E+02	4.37E+02	2.98E+02	1.63E+02	1.31E+02	4.30E+01
^{75}As	4.66E+01	1.89E+02	4.48E+01	2.68E+02	9.80E+01	-1.58E+00	3.12E+01
^{107}Ag	-3.54E+00	-1.69E+00	-1.22E+00	9.88E+00	-7.77E+00	5.70E+00	-5.07E+00
^{121}Sb	1.77E+01	8.29E+01	5.95E+01	1.04E+02	8.59E+01	-2.00E+01	-4.88E+01
^{138}Ba	5.74E+01	4.95E+01	1.02E+02	2.38E+02	2.32E+02	6.05E+00	2.50E+00
^{197}Au	1.24E-01	-6.32E-01	-1.15E+00	8.99E+01	1.33E+02	2.19E+00	-1.76E+00
^{208}Pb	4.96E+01	1.11E+01	2.29E+01	7.32E+01	2.84E+01	9.71E+00	9.94E+00

Table 8: *Continued*

Analysis	RV027_aa_3	RV027_aa_4	RV027_bb_1	RV027_bb_2	RV027_cc_1	RV027_cc_2	RV027_dd_1
Deposit	Verde	Verde	Verde	Verde	Verde	Verde	Verde
Sample	RV027	RV027	RV027	RV027	RV027	RV027	RV027
Location	aa	aa	bb	bb	cc	cc	dd
^{23}Na	1.70E+03	2.26E+03	3.11E+03	3.65E+03	8.74E+02	3.37E+02	8.00E+02
^{25}Mg	2.84E+01	3.73E+01	3.91E+01	1.33E+02	9.92E+01	1.08E+02	4.82E+01
^{27}Al	8.53E+01	7.19E+01	6.88E+02	2.61E+03	1.55E+03	3.01E+03	1.75E+03
^{28}Si	1.09E+07	9.62E+06	1.60E+07	2.09E+07	1.99E+07	2.02E+07	1.01E+07
^{39}K	3.62E+03	1.51E+03	5.53E+03	2.89E+03	1.20E+03	-2.49E+02	1.34E+03
^{40}Ca	5.49E+02	4.74E+02	1.22E+03	6.85E+03	3.91E+02	2.94E+02	6.93E+02
^{49}Ti	3.50E+02	2.91E+02	4.36E+02	7.78E+02	7.24E+02	1.15E+03	4.37E+02
^{56}Fe	1.86E+05	1.43E+05	1.26E+05	3.67E+05	2.70E+05	3.00E+05	1.32E+05
^{63}Cu	1.58E+03	2.02E+03	1.39E+03	3.57E+03	6.48E+02	3.62E+02	4.10E+02
^{66}Zn	1.51E+02	6.24E+01	6.76E+01	2.11E+02	1.12E+02	9.70E+01	1.26E+02
^{75}As	-4.05E+00	1.45E+01	2.97E+01	2.63E+01	4.27E+01	7.87E+01	2.27E+01
^{107}Ag	-1.07E+00	-9.39E+00	-6.23E-01	9.57E+00	-1.36E-01	8.75E+00	5.53E+00
^{121}Sb	3.54E+01	-2.31E+01	5.22E-01	-3.62E+01	3.65E+01	7.13E+01	4.26E+00
^{138}Ba	1.77E+01	2.47E+01	9.94E+00	1.78E+02	1.91E+01	7.48E+00	2.66E+01
^{197}Au	-7.37E-01	-7.40E-01	2.68E+00	4.91E+01	2.21E+00	3.19E+00	2.26E+00
^{208}Pb	3.22E+01	1.79E+01	1.87E+01	3.52E+01	1.30E+01	-2.24E+00	1.10E+01

Table 8: *Continued*

Analysis	RV027_dd_2	RV027_ff_2	V6_23_1	V6_23_a	V6_23area_1	V6_23area_2	V6_23area_3
Deposit	Verde	Verde	Verde	Verde	Verde	Verde	Verde
Sample	RV027	RV027	V6 SNWC 342.4	V6 SNWC 342.4	V6 SNWC 342.4	V6 SNWC 342.4	V6 SNWC 342.4
Location	dd	ff	23	23	23area	23area	23area
^{23}Na	2.18E+04	1.21E+05	1.99E+04	1.36E+03	1.74E+03	6.27E+03	6.20E+02
^{25}Mg	3.53E+03	9.29E+02	2.97E+03	8.62E+01	2.01E+02	4.07E+02	6.19E+01
^{27}Al	7.14E+04	5.05E+03	2.75E+04	1.07E+04	1.74E+04	2.98E+04	7.67E+03
^{28}Si	3.35E+07	2.13E+07	1.77E+07	6.93E+06	7.29E+06	7.25E+06	7.87E+06
^{39}K	4.04E+04	1.36E+05	7.93E+03	3.84E+03	2.91E+03	1.50E+04	-8.61E+02
^{40}Ca	2.64E+04	1.70E+04	6.27E+04	-1.95E+02	7.42E+02	3.63E+03	1.08E+03
^{49}Ti	1.95E+03	6.42E+02	1.24E+03	8.93E+02	8.94E+02	7.30E+02	4.28E+02
^{56}Fe	1.33E+06	3.66E+05	4.59E+04	2.84E+03	1.86E+04	2.63E+04	3.25E+03
^{63}Cu	1.62E+04	2.71E+03	1.70E+03	1.19E+01	1.68E+01	2.70E+01	3.84E+03
^{66}Zn	7.49E+02	6.45E+02	2.30E+03	2.99E+01	2.81E+02	2.00E+02	1.08E+02
^{75}As	1.28E+01	6.72E+01	8.58E+01	-2.91E+01	2.43E+01	7.65E+00	4.81E+01
^{107}Ag	2.07E+01	5.89E+00	2.25E+01	3.68E+00	5.23E-01	3.15E+00	1.95E+01
^{121}Sb	2.60E+01	2.08E+01	4.83E+01	-1.14E+01	-1.01E+01	-3.54E+00	6.56E+01
^{138}Ba	3.61E+02	1.29E+02	9.41E+02	1.01E+02	4.90E+01	4.40E+02	1.24E+01
^{197}Au	1.08E+01	1.06E+00	3.03E+01	-3.10E-01	-3.63E-01	-4.90E-03	5.55E+00
^{208}Pb	1.32E+02	1.70E+02	4.81E+03	9.17E+00	1.24E+01	2.59E+02	7.47E+01

Table 8: *Continued*

Analysis	V6_23area_4	V6_23area_5	V6_band_1	V6_band_2	V6_band_3	V6_band_4	V6_band_7
Deposit	Verde	Verde	Verde	Verde	Verde	Verde	Verde
Sample	V6 SNWC 342.4	V6 SNWC 342.4	V6 SNWC 342.4	V6 SNWC 342.4	V6 SNWC 342.4	V6 SNWC 342.4	V6 SNWC 342.4
Location	23area	23area	band	band	band	band	band
^{23}Na	3.07E+02	3.00E+02	8.92E+02	1.92E+04	6.68E+03	1.99E+05	2.15E+04
^{25}Mg	1.02E+02	1.88E+02	1.98E+02	2.29E+03	4.99E+02	2.86E+05	1.83E+02
^{27}Al	1.05E+04	1.84E+04	2.24E+04	4.29E+04	1.78E+04	6.07E+06	6.11E+03
^{28}Si	7.71E+06	7.70E+06	6.76E+06	6.94E+06	7.70E+06	1.08E+07	8.84E+06
^{39}K	-7.99E+02	6.84E+02	9.70E+03	2.45E+04	5.32E+03	3.23E+06	2.42E+04
^{40}Ca	2.38E+02	5.76E+01	-1.58E+03	1.08E+04	4.63E+03	4.10E+06	2.64E+03
^{49}Ti	8.18E+02	8.75E+02	8.54E+02	1.11E+03	1.32E+03	3.05E+05	2.59E+02
^{56}Fe	2.61E+03	4.62E+03	2.58E+04	1.60E+06	4.53E+05	8.82E+06	6.68E+05
^{63}Cu	-1.60E+01	1.13E+02	5.64E+02	2.76E+05	1.18E+04	9.40E+02	2.12E+04
^{66}Zn	8.41E+01	1.42E+02	2.81E+02	1.86E+03	8.21E+02	1.23E+04	2.39E+03
^{75}As	1.27E+01	3.90E+01	1.94E+01	6.66E+01	-2.15E+01	7.50E+03	-7.76E+00
^{107}Ag	2.49E+00	-1.02E+01	-3.94E+00	1.30E+02	5.89E+01	4.49E+01	9.30E+01
^{121}Sb	-3.96E+01	-6.57E+01	2.13E+01	1.16E+02	6.43E+01	4.08E+03	3.20E+01
^{138}Ba	1.06E+00	1.85E+01	5.21E+02	8.54E+01	6.70E+01	1.46E+04	6.18E+01
^{197}Au	-1.31E+00	-9.34E-01	3.54E-01	3.08E+02	3.24E+01	5.21E+01	1.26E+02
^{208}Pb	5.85E+00	2.72E+01	3.83E+01	2.79E+03	5.14E+02	4.17E+03	1.32E+03

Table 8: *Continued*

Analysis	V6_band_8	V6_band_9	V6_band_10	486_2area_1	486_2area_2	486_2area_3	486_2area_4
Deposit	Verde	Verde	Verde	Pancho	Pancho	Pancho	Pancho
Sample	V6.5NWC 342.4	V6.5NWC 342.4	V6 SNWC 342.4	P-8-C 486	P-8-C 486	P-8-C 486	P-8-C 486
Location	band	band	band	2area	2area	2area	2area
^{23}Na	1.01E+04	1.95E+04	3.67E+03	1.18E+03	3.72E+03	4.89E+03	1.91E+03
^{25}Mg	4.58E+02	5.23E+03	8.61E+02	1.82E+00	-7.48E+00	1.80E+01	1.28E+01
^{27}Al	4.65E+04	2.06E+05	2.55E+04	2.77E+04	1.21E+05	9.92E+04	1.07E+05
^{28}Si	9.17E+06	1.73E+07	7.03E+06	7.50E+06	8.75E+06	9.01E+06	1.19E+07
^{39}K	2.26E+04	1.34E+05	4.02E+03	7.56E+02	-7.11E+02	1.03E+03	-9.39E+02
^{40}Ca	9.44E+03	1.53E+04	5.14E+03	-1.18E+03	2.94E+03	1.53E+03	9.20E+01
^{49}Ti	1.71E+03	4.90E+03	1.02E+03	1.43E+01	7.06E+01	6.29E+01	6.33E+01
^{56}Fe	1.39E+04	1.36E+05	3.67E+05	4.10E+01	3.62E+02	8.58E+02	4.12E+01
^{63}Cu	1.11E+02	8.98E+01	2.32E+04	4.11E-01	9.62E+00	2.15E+01	4.87E+00
^{66}Zn	3.13E+02	1.04E+03	1.04E+03	3.33E+01	4.27E+01	1.52E-01	6.19E+01
^{75}As	3.23E+00	7.91E+01	2.99E+01	8.79E+01	3.91E+02	1.29E+02	1.56E+02
^{107}Ag	2.79E+00	-1.30E+00	3.41E+01	-9.72E+00	1.30E+01	-5.61E+00	6.49E-01
^{121}Sb	1.96E+01	2.68E+01	-1.36E+01	1.34E+02	4.80E+03	5.34E+02	5.35E+02
^{138}Ba	3.09E+02	3.87E+02	1.50E+01	2.05E+01	1.48E+02	5.17E+02	1.78E+01
^{197}Au	2.87E-01	-5.02E-01	2.89E+01	-1.24E+00	3.45E-01	1.67E+00	7.17E-01
^{208}Pb	1.34E+02	4.82E+02	7.39E+02	1.82E+00	7.47E+00	1.20E+01	1.54E+01

Table 8: *Continued*

Analysis	486_2area_5	486_I_1	486_I_2	539_1_5area_1	539_1_5area_3	539_2_3	539_2_3b
Deposit	Pancho	Pancho	Pancho	Pancho	Pancho	Pancho	Pancho
Sample	P-8-C 486	P-8-C 486	P-8-C 486	P-8-C 539_1	P-8-C 539_1	P-8-C 539_2	P-8-C 539_2
Location	2area	I	I	5area	5area	2	2
^{23}Na	3.47E+02	1.08E+04	1.10E+04	5.09E+02	1.15E+02	9.49E+03	1.32E+04
^{25}Mg	-2.21E+00	4.71E+02	6.37E+02	2.25E+01	2.40E+01	3.22E+02	4.82E+02
^{27}Al	2.00E+04	-1.35E+02	2.79E+01	4.87E+03	5.16E+03	5.62E+03	8.73E+02
^{28}Si	5.78E+06	4.29E+03	3.29E+03	7.76E+06	7.89E+06	2.34E+06	1.77E+06
^{39}K	8.05E+01	9.56E+02	-5.69E+01	6.12E+01	4.82E+01	1.78E+04	1.06E+04
^{40}Ca	-1.82E+02	6.27E+07	5.84E+07	5.02E+02	3.27E+02	2.06E+03	5.09E+04
^{49}Ti	1.52E+01	3.35E+01	3.13E+01	9.21E+02	9.66E+02	1.70E+02	1.44E+02
^{56}Fe	1.41E+02	6.39E+05	8.02E+05	4.24E+02	3.92E+02	1.28E+04	9.93E+03
^{63}Cu	4.09E+01	1.11E+02	-8.69E+00	3.20E+01	3.76E+01	1.43E+02	1.35E+04
^{66}Zn	4.44E+01	4.68E+01	1.16E+01	5.58E+01	5.12E+00	1.68E+03	9.69E+02
^{75}As	3.08E+01	5.54E+01	4.64E+00	-1.42E+01	-2.26E+01	8.55E+01	5.26E+01
^{107}Ag	-3.35E+00	-4.33E+00	-2.49E+00	4.70E+00	2.51E+00	1.60E+01	4.69E+01
^{121}Sb	1.69E+02	-1.24E+01	-3.58E+01	3.14E+00	2.88E+01	5.91E+00	8.58E+01
^{138}Ba	1.82E+01	2.26E+02	1.31E+02	4.91E+00	4.73E+00	1.93E+02	1.27E+02
^{197}Au	5.65E-01	7.05E-01	-6.00E-01	1.23E+00	-7.85E-01	-4.91E+00	-2.60E-02
^{208}Pb	2.50E+00	1.36E+02	9.50E+01	1.41E+01	3.52E+00	1.50E+03	9.65E+02

Table 8: *Continued*

Analysis	600_9area_1	600_11area_2	600_band2_1	600_band_1	600_band_2	600_center_1	600_quartz_1
Deposit	Pancho	Pancho	Pancho	Pancho	Pancho	Pancho	Pancho
Sample	P-8-C 600	P-8-C 600	P-8-C 600	P-8-C 600	P-8-C 600	P-8-C 600	P-8-C 600
Location	9area	11area	band2	band	band	center	quartz
^{23}Na	1.16E+05	5.71E+04	5.69E+04	3.58E+04	3.37E+04	3.29E+02	5.51E+03
^{25}Mg	7.12E+01	2.63E+02	8.10E+03	1.14E+03	1.03E+03	3.23E+01	4.49E+01
^{27}Al	1.10E+03	5.13E+04	1.01E+06	6.45E+04	1.80E+05	8.25E+03	7.50E+03
^{28}Si	1.17E+06	1.64E+07	6.41E+06	1.64E+07	1.70E+07	8.78E+06	8.29E+06
^{39}K	1.42E+05	9.74E+04	1.01E+06	5.03E+04	1.63E+05	4.99E+02	5.99E+03
^{40}Ca	4.96E+02	2.08E+03	8.06E+04	1.32E+04	3.24E+05	3.13E+02	1.90E+03
^{49}Ti	2.91E+01	1.68E+03	1.02E+03	1.73E+03	2.32E+03	5.88E+02	6.55E+02
^{56}Fe	8.51E+04	6.75E+04	2.25E+05	8.29E+04	1.00E+05	3.52E+02	7.42E+03
^{63}Cu	-2.14E+01	7.42E+02	8.03E+02	2.89E+03	8.67E+03	-9.38E+00	1.18E+03
^{66}Zn	8.57E+03	6.75E+03	4.78E+02	5.77E+03	1.30E+04	5.67E+01	3.77E+02
^{75}As	2.15E+01	-4.66E+00	9.29E-02	3.67E+01	4.24E+01	3.14E+00	3.93E+01
^{107}Ag	5.75E+01	1.38E+01	2.14E+01	1.48E+01	4.56E+01	-7.00E+00	9.29E+00
^{121}Sb	-5.33E+01	-5.63E+01	2.44E+01	1.18E+02	1.18E+01	2.74E+01	-1.60E+01
^{138}Ba	5.46E+01	4.22E+02	1.06E+04	5.44E+02	1.51E+03	3.03E+00	6.94E+01
^{197}Au	2.48E+00	4.89E-01	2.52E+00	4.28E-01	2.93E+00	-1.43E+00	-6.30E-01
^{208}Pb	5.13E+03	8.74E+03	3.65E+02	2.94E+03	2.66E+03	3.25E+00	4.56E+02

Table 8: *Continued*

Analysis	600_wall_2	RV027_5area_3	RV027_5area_5	RV027_5area_6	RV027_5area_7	RV027_5area_8	RV027_5area_10
Deposit	Pancho	Verde	Verde	Verde	Verde	Verde	Verde
Sample	P-8-C 600	RV027	RV027	RV027	RV027	RV027	RV027
Location	wall	5area	5area	5area	5area	5area	5area
^{23}Na	8.70E+02	5.89E+00	1.12E+01	1.91E+01	1.93E+01	6.15E+00	2.89E+01
^{25}Mg	6.44E+01	1.61E-01	1.89E-01	2.38E-01	2.19E-01	1.97E-01	3.31E-01
^{27}Al	1.89E+04	2.96E-01	8.93E-01	3.57E-01	1.07E+00	-1.97E-01	-3.30E-01
^{28}Si	7.98E+06	9.62E+04	8.51E+04	9.44E+04	1.06E+05	9.41E+04	2.37E+04
^{39}K	1.10E+04	5.93E+00	6.78E+00	1.36E+01	2.01E+01	1.05E+01	3.39E+01
^{40}Ca	8.97E+02	2.63E+00	3.78E+00	5.68E+00	2.59E+00	3.59E+00	2.83E+01
^{49}Ti	1.10E+03	1.67E+00	1.14E+00	1.65E+00	3.25E+00	1.43E+00	5.78E-01
^{56}Fe	2.03E+03	5.33E+02	3.36E+02	4.38E+02	1.53E+03	2.71E+02	6.38E+01
^{63}Cu	1.27E+01	1.72E+00	8.92E+00	1.75E+01	2.31E+01	2.38E+00	6.21E-01
^{66}Zn	5.87E+01	5.69E-01	2.20E-01	7.10E-01	4.40E-01	2.29E-01	3.77E-01
^{75}As	1.17E+01	6.72E-02	1.70E-02	8.84E-02	2.88E-01	3.65E-01	3.58E-01
^{107}Ag	3.92E-01	3.88E-02	4.19E-02	3.16E-02	6.82E-02	-5.28E-02	-1.05E-01
^{121}Sb	2.05E+01	9.12E-01	1.89E-02	-6.63E-02	-5.76E-01	-5.73E-01	6.92E-01
^{138}Ba	4.57E+01	4.59E-02	1.13E-01	1.26E-01	3.25E-01	1.17E-02	1.70E-01
^{197}Au	-2.72E+00	-1.02E-02	3.15E-02	-9.50E-03	8.26E-03	-1.29E-02	1.09E-02
^{208}Pb	3.37E+01	-3.71E-02	-5.25E-02	2.21E-01	2.30E-01	-3.42E-02	2.41E-01

Table 8: *Continued*

Analysis	RV027_7area_1	RV027_7area_3	RV027_7area_4	RV027_14area_1	RV027_14area_2	RV027_14area_3	RV027_14area_4
Deposit	Verde	Verde	Verde	Verde	Verde	Verde	Verde
Sample	RV027	RV027	RV027	RV027	RV027	RV027	RV027
Location	7area	7area	7area	14area	14area	14area	14area
^{23}Na	1.05E+00	4.40E+01	2.72E+01	1.97E+00	1.11E+00	5.22E+00	-3.19E-01
^{25}Mg	-5.08E-02	6.87E+00	3.38E+00	2.70E-01	1.62E-01	3.67E-01	1.07E-01
^{27}Al	-1.93E-01	1.89E+02	1.02E+02	-1.74E-01	-5.58E-01	3.85E-01	1.90E+00
^{28}Si	8.38E+04	8.48E+04	6.91E+04	7.95E+04	9.20E+04	9.48E+04	1.04E+05
^{39}K	-5.77E+00	1.29E+02	2.52E+02	-5.64E-01	-3.45E-01	-1.31E+01	2.25E+00
^{40}Ca	1.69E+00	1.36E+02	3.89E+01	1.74E+00	1.69E+00	-1.13E+00	2.18E+00
^{49}Ti	2.15E+00	3.12E+00	9.34E+00	2.77E+00	3.76E+00	4.52E+00	2.83E+00
^{56}Fe	3.66E+02	4.00E+03	3.29E+03	1.41E+03	1.47E+03	2.58E+03	3.80E+02
^{63}Cu	9.23E-01	3.51E+01	1.70E+01	2.34E+01	6.86E+00	1.61E+02	1.23E+00
^{66}Zn	4.15E-01	2.36E+00	3.61E+00	3.57E-01	3.60E-01	7.66E-01	3.45E-01
^{75}As	3.06E-01	3.26E-02	2.68E-01	2.54E-01	1.84E-01	2.13E-01	1.68E-01
^{107}Ag	-5.00E-02	1.35E-01	-7.26E-02	1.67E-02	-1.47E-01	2.52E-01	-5.63E-02
^{121}Sb	-4.88E-01	-2.42E-01	-2.00E-01	3.89E-01	-2.43E-01	-7.09E-02	2.74E-01
^{138}Ba	5.33E-02	9.38E-01	3.24E-01	7.52E-03	3.11E-02	8.14E-02	3.70E-01
^{197}Au	-3.83E-02	-7.07E-03	1.29E-01	-4.51E-03	-7.31E-03	1.04E+00	-6.73E-03
^{208}Pb	2.75E-02	6.43E-01	4.14E-01	1.31E-02	5.69E-03	1.91E-01	3.22E-01

Table 8: *Continued*

Analysis	RV027_14area_5	RV027_19_8	RV027_19_a	RV027_19_band2	RV027_19_band	RV027_19_quartz2	RV027_19_quartz
Deposit	Verde	Verde	Verde	Verde	Verde	Verde	Verde
Sample	RV027	RV027	RV027	RV027	RV027	RV027	RV027
Location	14area	19	19	19	19	19	19
^{23}Na	3.31E+01	4.55E+01	6.80E+01	3.09E+00	1.74E+01	3.04E+01	3.76E+01
^{25}Mg	2.76E+00	1.85E-02	1.58E-02	3.40E+00	2.48E+00	2.50E+00	3.33E+00
^{27}Al	5.87E+01	3.56E+02	1.33E+02	9.83E+01	3.19E+01	3.75E+02	4.20E+02
^{28}Si	1.17E+05	7.14E+04	7.05E+04	8.26E+04	7.53E+04	1.92E+05	1.47E+05
^{39}K	1.99E+01	2.05E+01	1.30E+01	1.69E+01	2.99E+01	1.43E+02	1.63E+02
^{40}Ca	3.52E+01	1.06E+01	2.15E+01	3.97E+00	6.20E+00	2.00E+01	1.47E+01
^{49}Ti	4.76E+00	9.99E-02	-2.42E-02	1.97E+01	4.90E+00	4.07E+01	3.75E+01
^{56}Fe	3.15E+03	4.27E-01	1.79E-01	4.76E+03	8.46E+03	6.20E+01	7.75E+01
^{63}Cu	3.02E+01	2.59E-01	4.20E-01	2.94E+00	9.42E+00	4.56E-01	6.77E-01
^{66}Zn	1.41E+00	3.16E-01	8.56E-02	4.10E+00	3.50E+00	7.11E-01	1.04E+00
^{75}As	1.85E-01	2.72E-01	4.20E-01	-7.12E-02	4.18E-01	-4.59E-02	2.31E-01
^{107}Ag	5.65E-02	9.03E-02	-5.87E-02	1.02E-01	1.30E-01	-1.46E-01	1.01E-01
^{121}Sb	-1.96E-01	1.37E-01	1.29E-01	-1.10E-01	8.32E-02	-1.16E+00	-2.13E-02
^{138}Ba	9.04E-01	1.70E+00	7.69E-01	2.94E-01	2.67E-01	1.33E-01	1.83E-01
^{197}Au	-7.49E-03	-6.70E-03	-2.65E-02	1.23E-01	1.70E-01	-2.99E-02	1.00E-01
^{208}Pb	8.50E-01	-3.45E-02	-2.15E-02	1.93E-02	3.11E-01	2.78E-03	4.61E-02

Table 8: *Continued*

Analysis	RV0277area_2	RV027_5area_1	RV027_5area_2	RP058_I_5	RP054_5area_1	RP054_5area_2	RP054_5area_3
Deposit	Verde	Verde	Verde	Pancho	Pancho	Pancho	Pancho
Sample	RV027	RV027	RV027	RP058	RP054	RP054	RP054
Location	7area	5area	5area	I	5area	5area	5area
^{23}Na	1.23E+01	2.85E+00	3.28E+00	8.43E+01	4.83E+02	3.20E+00	2.04E+01
^{25}Mg	5.43E+00	3.43E-01	2.26E-01	6.73E-01	5.89E-01	1.37E-01	6.72E-01
^{27}Al	1.13E+02	9.28E-01	-4.50E-01	6.07E+01	5.37E+00	2.31E+00	3.24E+00
^{28}Si	9.22E+04	9.41E+04	9.24E+04	9.66E+04	7.82E+04	9.62E+04	8.54E+04
^{39}K	2.71E+01	-3.38E+00	-1.31E+00	6.39E+01	1.27E+02	-5.47E+00	-5.52E-01
^{40}Ca	9.03E+01	7.34E-01	6.03E+00	2.95E+01	3.48E+01	1.60E+00	1.11E+01
^{49}Ti	2.06E+00	3.50E+00	3.69E+00	1.26E+01	9.51E+00	1.26E+01	1.51E+01
^{56}Fe	2.17E+03	1.67E+03	1.87E+03	2.13E+03	5.86E+02	7.35E+02	1.58E+03
^{63}Cu	1.86E+01	5.66E+00	2.55E+00	1.47E+01	7.53E-01	1.04E+00	2.43E+00
^{66}Zn	7.87E-01	5.94E-01	4.93E-01	1.37E+00	3.79E-01	1.05E-01	2.01E-01
^{75}As	1.35E-01	6.05E-02	3.80E-02	1.14E-02	6.54E-01	4.93E-01	3.17E-01
^{107}Ag	-2.41E-03	4.09E-02	-5.63E-02	9.21E-02	1.13E-01	2.20E-02	-1.04E-01
^{121}Sb	-1.98E-01	6.56E-01	-2.34E-01	-4.98E-02	1.21E-01	4.46E-01	-1.03E-01
^{138}Ba	3.40E-01	1.70E-01	1.05E-01	1.13E+00	1.49E+00	-2.91E-03	4.58E-01
^{197}Au	-6.70E-03	5.82E-02	-1.90E-02	1.55E-02	4.42E-02	-2.08E-02	-3.91E-02
^{208}Pb	2.29E-01	7.40E-02	6.95E-02	4.99E-01	3.73E-01	8.65E-02	4.26E-01

Table 8: *Continued*

Analysis	RP054_5area_4	RP054_5area_5	RP054_5area_6	RP054_5area_7	RP054_5area_8	RP054_band_1	RP054_band_2
Deposit	Pancho	Pancho	Pancho	Pancho	Pancho	Pancho	Pancho
Sample	RP054	RP054	RP054	RP054	RP054	RP054	RP054
Location	5area	5area	5area	5area	5area	band	band
^{23}Na	6.12E+00	3.53E+00	9.12E+00	2.23E+00	2.28E-01	2.30E+02	9.91E+02
^{25}Mg	-4.22E-02	-5.92E-02	2.98E-02	1.25E-01	9.46E-03	3.34E+01	5.15E+01
^{27}Al	1.63E+00	3.49E-01	1.01E+00	2.24E-01	-2.16E-01	6.48E+03	2.69E+04
^{28}Si	6.82E+04	1.70E+04	9.63E+04	7.23E+04	9.61E+04	7.47E+04	7.23E+04
^{39}K	-4.58E+00	-5.46E+00	4.11E+00	-5.65E+00	-1.19E+01	4.50E+03	2.70E+04
^{40}Ca	-2.86E-01	1.24E+00	3.18E+01	2.67E+01	-3.59E+00	6.44E+01	7.90E+01
^{49}Ti	6.80E+00	1.68E+00	1.11E+01	7.99E+00	1.33E+01	2.78E+00	5.07E+00
^{56}Fe	1.60E+02	2.61E+01	1.52E+02	1.05E+02	1.80E+02	4.72E+03	7.46E+03
^{63}Cu	1.71E+00	1.92E-01	7.45E+00	3.41E+00	7.60E-02	2.33E+01	1.30E+02
^{66}Zn	9.13E-02	-7.47E-02	3.44E-01	-2.70E-02	2.43E-01	5.78E+00	1.27E+01
^{75}As	2.97E-01	2.94E-01	5.52E-01	4.56E-01	6.04E-01	1.92E+00	1.55E+00
^{107}Ag	-2.18E-01	2.28E-02	2.80E-02	3.42E-02	1.45E-02	5.02E-02	6.29E-01
^{121}Sb	1.71E-01	3.48E-01	1.30E-01	5.84E-02	1.30E-01	9.39E+00	1.19E+01
^{138}Ba	1.33E-01	-5.07E-03	2.46E-01	-6.03E-03	6.80E-02	5.56E+02	3.60E+03
^{197}Au	2.30E-03	6.36E-02	-2.44E-04	2.88E-02	1.79E-02	4.36E-02	1.29E-01
^{208}Pb	1.42E-01	-3.88E-02	2.13E-01	9.79E-02	7.86E-02	7.11E+01	1.77E+02

Table 8: *Continued*

Analysis	RP054_I_1	RP054_I_2	RP054_I_a	RP054_I_b	RP054_I_c	RP054_I_d	RP054_I_e
Deposit	Pancho	Pancho	Pancho	Pancho	Pancho	Pancho	Pancho
Sample	RP054	RP054	RP054	RP054	RP054	RP054	RP054
Location	I	I	I	I	I	I	I
^{23}Na	8.46E-01	-2.21E-01	2.69E+01	4.82E+00	5.91E+00	4.33E+01	3.84E+01
^{25}Mg	8.32E-02	1.13E-01	6.46E-03	-3.20E-02	2.09E-01	7.07E-01	1.52E+00
^{27}Al	4.61E+00	-3.93E-01	-2.24E-03	-1.39E-01	1.25E-01	-2.40E+00	3.34E+01
^{28}Si	6.67E+04	2.20E+04	8.93E+04	1.00E+05	9.81E+04	8.74E+04	8.46E+04
^{39}K	-2.83E+00	-6.61E+00	8.19E+00	-5.12E-01	-1.48E+00	2.90E+01	2.81E+01
^{40}Ca	8.49E+00	5.06E-01	8.18E+00	4.07E-01	2.28E+00	4.60E+00	1.11E+01
^{49}Ti	9.60E+00	2.58E+00	9.83E+00	1.35E+01	1.36E+01	1.39E+01	1.77E+01
^{56}Fe	1.46E+02	5.44E+02	1.15E+03	9.49E+02	1.28E+03	1.94E+03	2.64E+03
^{63}Cu	1.69E-01	-1.70E-02	3.13E-01	1.97E-01	4.96E-01	2.19E+01	6.75E+00
^{66}Zn	1.92E-01	1.73E-01	2.60E-01	-6.59E-02	2.99E-01	6.54E-01	8.65E-01
^{75}As	2.56E-01	2.40E-01	7.97E-01	6.86E-01	1.10E+00	7.64E-01	1.22E-01
^{107}Ag	9.24E-02	2.64E-02	1.09E-01	-8.46E-02	6.70E-02	1.61E-02	1.99E-01
^{121}Sb	1.80E-01	-5.00E-02	2.77E-01	3.45E-01	-2.41E-01	3.84E-01	2.57E-01
^{138}Ba	1.32E-01	7.91E-02	2.57E-01	4.58E-02	8.91E-02	4.53E-01	1.57E+00
^{197}Au	-1.34E-02	7.75E-03	-3.72E-02	-2.71E-02	4.12E-02	9.13E-03	-4.89E-02
^{208}Pb	1.01E-01	1.08E-01	1.14E-01	1.03E-01	1.16E-01	2.28E-01	7.45E-01

Table 8: *Continued*

Analysis	RP054_I_f	RP054_Quartz	RP058_3_1	RP058_3_2	RP058_3_3	RP058_3_4	RP058_3_5
Deposit	Pancho	Pancho	Pancho	Pancho	Pancho	Pancho	Pancho
Sample	RP054	RP054	RP058	RP058	RP058	RP058	RP058
Location	I	Quartz	3	3	3	3	3
^{23}Na	8.51E+01	1.13E+01	3.37E+00	-2.61E-01	1.01E+01	4.67E+01	1.58E+00
^{25}Mg	1.18E+00	2.68E-01	2.90E-01	1.84E-02	5.23E-01	8.87E-01	5.17E-02
^{27}Al	7.65E-01	1.43E+01	-7.74E-01	1.35E+00	-8.50E-01	2.02E+03	7.30E-01
^{28}Si	8.22E+04	8.48E+04	7.69E+04	9.05E+04	9.00E+04	8.92E+04	7.83E+04
^{39}K	5.15E+01	1.43E+01	-1.21E+01	-7.19E+00	9.60E-01	5.98E+01	-1.68E+01
^{40}Ca	4.12E+01	7.52E+00	1.82E+00	-1.76E+00	8.02E-01	5.85E+01	1.60E+00
^{49}Ti	1.39E+01	1.05E+01	3.01E+01	3.14E+01	1.56E+01	1.37E+01	1.51E+01
^{56}Fe	6.97E+02	7.87E+01	8.83E+02	4.46E+02	1.69E+03	2.09E+03	5.86E+02
^{63}Cu	1.21E+00	2.21E-01	2.53E-01	1.71E-01	2.57E+00	1.88E+01	1.30E-01
^{66}Zn	1.88E+00	3.32E-01	2.81E-01	3.79E-01	9.95E-01	6.40E+00	2.68E-01
^{75}As	5.31E-01	9.49E-01	5.02E-01	7.86E-01	6.60E-01	5.25E-01	3.62E-01
^{107}Ag	7.56E-02	-5.37E-02	-4.39E-02	3.03E-01	-1.20E-01	2.35E-01	1.16E-01
^{121}Sb	-3.96E-01	5.09E-01	1.93E-01	8.14E-02	-4.32E-01	-1.22E-01	2.46E-02
^{138}Ba	4.01E-01	1.57E-01	3.60E-02	2.80E-01	1.68E+00	6.83E-01	2.29E-02
^{197}Au	1.37E-02	-4.71E-03	5.69E-03	4.92E-03	-1.49E-03	9.18E-02	-4.84E-02
^{208}Pb	3.36E-01	1.53E-01	-1.28E-03	-1.72E-02	4.12E-01	3.22E-01	-6.37E-02

Table 8: *Continued*

Analysis	RP058_3_6	RP058_3_7	RP058_3_8	RP058_9area_1	RP058_9area_2	RP058_9area_3	RP058_24area_1
Deposit	Pancho	Pancho	Pancho	Pancho	Pancho	Pancho	Pancho
Sample	RP058	RP058	RP058	RP058	RP058	RP058	RP058
Location	3	3	3	9area	9area	9area	24area
^{23}Na	2.71E+01	6.37E+00	8.10E+01	4.34E-01	8.84E+00	1.37E+02	2.90E+00
^{25}Mg	3.36E-01	5.56E-01	4.71E-01	6.85E-02	1.21E+00	1.05E+00	1.34E-01
^{27}Al	1.01E+01	1.18E+00	6.77E-01	5.66E+00	2.40E+01	-9.81E-01	-8.94E-02
^{28}Si	8.48E+04	9.91E+04	7.41E+04	9.23E+04	2.03E+05	8.76E+04	6.29E+04
^{39}K	1.22E+01	-1.35E+01	4.34E+01	-5.08E+00	-5.15E+00	1.03E+02	-2.81E+00
^{40}Ca	4.06E+00	2.96E+00	7.40E+00	1.08E+01	2.16E+01	1.52E+01	-2.17E-01
^{49}Ti	2.92E+01	2.15E+01	1.08E+01	5.74E+00	1.64E+01	1.20E+01	1.13E+01
^{56}Fe	9.70E+02	1.34E+03	1.61E+03	7.71E+02	2.91E+03	2.74E+03	4.58E+02
^{63}Cu	4.63E+00	6.39E-01	2.79E+01	6.88E-02	5.91E+00	3.11E+01	8.32E-02
^{66}Zn	4.26E-01	7.93E-01	6.78E-01	2.06E+00	4.81E-01	7.95E-01	3.61E-01
^{75}As	5.16E-01	7.70E-01	3.21E-01	9.43E-01	1.80E+00	3.23E-01	5.74E-01
^{107}Ag	4.34E-02	6.25E-01	3.36E-02	-9.23E-02	-3.67E-02	1.08E-01	-4.82E-02
^{121}Sb	4.77E-01	1.87E-01	-1.64E-01	-1.26E-01	6.46E-01	2.73E-01	4.69E-01
^{138}Ba	1.04E-01	2.22E-02	3.33E-01	8.20E-02	7.88E-02	6.17E-01	1.58E-02
^{197}Au	3.16E-02	1.19E-02	6.77E-02	4.72E-02	1.36E-01	1.51E-02	-1.41E-02
^{208}Pb	2.75E-01	2.79E-02	4.01E-01	1.19E-01	7.80E-02	7.97E-01	-2.66E-02

Table 8: *Continued*

Analysis	RP058_24area_2	RP058_24area_3	RP058_24area_4	DD25_8_1	DD25_8_11	DD25_13_1	DD25_13_2
Deposit	Pancho	Pancho	Pancho	Verde	Verde	Verde	Verde
Sample	RP058	RP058	RP058	DD25 84-86m	DD25 84-86m	DD25 84-86m	DD25 84-86m
Location	24area	24area	24area	8	8	13	13
^{23}Na	1.02E+01	7.68E+01	7.85E+01	7.25E+01	1.23E+01	4.43E+01	5.28E+02
^{25}Mg	1.94E-01	8.90E-01	8.68E-01	7.07E-01	1.30E+00	2.95E-01	2.85E+01
^{27}Al	1.09E+01	5.34E+00	3.59E+00	1.37E+02	2.06E+02	4.59E+01	1.79E+03
^{28}Si	7.18E+04	8.33E+04	1.01E+05	5.86E+04	6.17E+04	1.50E+04	5.37E+04
^{39}K	8.47E+00	4.69E+01	4.18E+01	1.62E+01	1.30E+01	1.92E+01	2.27E+03
^{40}Ca	2.57E+00	1.62E+01	1.73E+01	1.07E+02	3.09E+01	4.69E+01	3.89E+02
^{49}Ti	9.06E+00	3.09E+01	1.98E+01	9.49E+00	1.17E+01	3.29E+00	1.02E+01
^{56}Fe	5.47E+02	1.41E+03	1.87E+03	2.16E+01	3.90E+01	5.74E+00	2.20E+03
^{63}Cu	3.11E+00	3.56E+01	3.79E+01	3.93E-01	1.95E-01	4.51E-01	6.02E+00
^{66}Zn	4.73E+00	2.78E+00	2.43E+00	7.02E-01	7.90E-01	4.28E-01	8.65E+00
^{75}As	5.85E-01	6.79E-01	6.72E-01	2.03E-01	2.23E-01	-2.35E-01	1.34E-01
^{107}Ag	2.68E-02	4.93E-02	1.07E-02	1.52E-01	2.74E-02	1.06E-01	5.34E-01
^{121}Sb	2.53E-01	1.75E-02	5.44E-01	1.59E+00	2.28E-01	-2.87E-01	-1.60E-01
^{138}Ba	8.74E-02	1.16E+00	1.18E+00	8.42E-01	-1.82E-03	6.00E-02	1.89E+02
^{197}Au	-2.12E-02	1.64E-02	3.51E-03	3.30E-02	1.41E-02	-3.25E-02	-1.98E-02
^{208}Pb	7.45E-01	2.37E+00	1.53E+00	9.17E-01	7.27E-02	-2.24E-02	1.08E+01

Table 8: *Continued*

Analysis	DD25_17_B	DD25_21_2	DD25_21_3	DD25_band_1	DD25_band_2	DD25_band_3	DD25_17_a
Deposit	Verde	Verde	Verde	Verde	Verde	Verde	Verde
Sample	DD25 84-86m	DD25 84-86m	DD25 84-86m	DD25 84-86m	DD25 84-86m	DD25 84-86m	DD25 84-86m
Location	17	21	21	band	band	band	17
^{23}Na	4.22E+02	8.68E+02	1.08E+03	5.05E+01	8.89E+01	9.27E+01	9.90E+01
^{25}Mg	8.12E-01	1.11E+00	1.04E+00	1.10E+00	1.87E+00	5.03E-01	-9.43E-02
^{27}Al	3.65E+02	2.68E+02	3.04E+02	3.14E+01	1.18E+02	4.11E+01	4.18E+01
^{28}Si	8.35E+04	7.39E+04	6.30E+04	7.55E+04	9.40E+04	7.02E+04	1.42E+04
^{39}K	4.26E+02	2.12E+02	3.85E+02	2.95E+01	1.40E+02	4.19E+01	1.37E+02
^{40}Ca	1.24E+02	1.02E+03	6.37E+02	1.88E+01	3.47E+01	1.13E+01	1.28E+02
^{49}Ti	1.66E+01	1.81E+01	1.29E+01	1.30E+00	7.69E+00	4.45E+00	1.25E+00
^{56}Fe	1.22E+02	3.40E+01	3.54E+01	2.74E+03	1.16E+04	1.49E+03	6.98E+00
^{63}Cu	2.55E-02	-1.01E-01	-2.35E-01	7.09E+00	1.11E+01	4.32E+00	3.92E-02
^{66}Zn	9.76E-01	1.05E+00	6.18E-01	2.41E+00	8.18E+00	2.11E+00	2.51E+00
^{75}As	-1.82E-01	5.99E-02	-3.07E-01	3.59E-01	1.15E+00	9.43E-02	2.50E-01
^{107}Ag	2.27E-01	-1.04E-02	1.02E-02	1.95E-01	3.33E-01	1.09E-01	7.73E-01
^{121}Sb	-2.16E-01	-6.02E-01	-3.23E-01	6.25E-01	1.82E-01	-7.92E-02	-1.31E+00
^{138}Ba	8.98E-01	2.19E-01	6.67E-01	3.22E-01	4.49E-01	2.73E-01	1.61E+00
^{197}Au	-6.32E-04	3.35E-02	2.79E-02	8.00E-02	6.90E-02	2.60E-01	1.59E-02
^{208}Pb	3.69E-01	4.46E-02	5.40E-02	1.07E+00	1.43E+00	1.63E+00	3.87E-01

Table 8: *Continued*

Analysis	DD25_8_quartz	DD25_21_a
Deposit	Verde	Verde
Sample	DD25 84-86m	DD25 84-86m
Location	8	21
^{23}Na	3.43E+01	2.90E+00
^{25}Mg	1.33E+00	4.20E-01
^{27}Al	3.48E+02	3.79E+01
^{28}Si	8.41E+04	1.77E+04
^{39}K	1.39E+02	1.29E+01
^{40}Ca	4.79E+00	4.74E+00
^{49}Ti	1.70E+01	3.58E+00
^{56}Fe	4.26E+01	4.32E+00
^{63}Cu	2.52E-01	2.23E-01
^{66}Zn	6.66E-01	1.09E-01
^{75}As	-6.24E-03	-3.73E-02
^{107}Ag	7.25E-02	-1.57E-01
^{121}Sb	6.65E-03	-6.46E-02
^{138}Ba	1.26E-01	1.19E-02
^{197}Au	-2.81E-03	5.93E-02
^{208}Pb	1.58E-01	8.07E-02

Table 9: Cu/Au, Au/Si and Cu/Si, all in cps/cps, for each of the veins; n is the number of analyses.

Vein Type	Function	Cu/Au	Au/Si	Cu/Si
A-Veins	Average	6.6E+03	7.9E-07	1.5E-03
	Standard Deviation of the Mean	2.2E+03	4.6E-07	7.6E-04
	Maximum	3.9E+04	8.2E-06	1.3E-02
	Minimum	1.0E+02	1.6E-09	6.6E-06
	Range	3.9E+04	8.2E-06	1.3E-02
	n			18
Transitional Veins	Average	1.5E+03	1.2E-06	1.2E-04
	Standard Deviation of the Mean	1.2E+03	4.5E-07	5.5E-05
	Maximum	1.1E+04	3.7E-06	4.3E-04
	Minimum	2.5E+00	3.5E-08	2.8E-06
	Range	1.1E+04	3.7E-06	4.2E-04
	n			9
Banded Veins	Average	5.0E+02	5.2E-06	1.4E-03
	Standard Deviation of the Mean	1.5E+02	3.0E-06	8.2E-04
	Maximum	6.8E+03	1.6E-04	4.0E-02
	Minimum	1.4E+00	1.1E-08	4.1E-07
	Range	6.8E+03	1.6E-04	4.0E-02
	n			56
Ledge	Average	6.6E+02	6.4E-07	1.7E-04
	Standard Deviation of the Mean	2.8E+02	2.7E-07	6.2E-05
	Maximum	2.6E+03	2.4E-06	4.9E-04
	Minimum	5.6E+01	5.0E-08	1.8E-05
	Range	2.5E+03	2.3E-06	4.7E-04
	n			9

APPENDIX

ADDITIONAL IMAGES

Photomicrographs

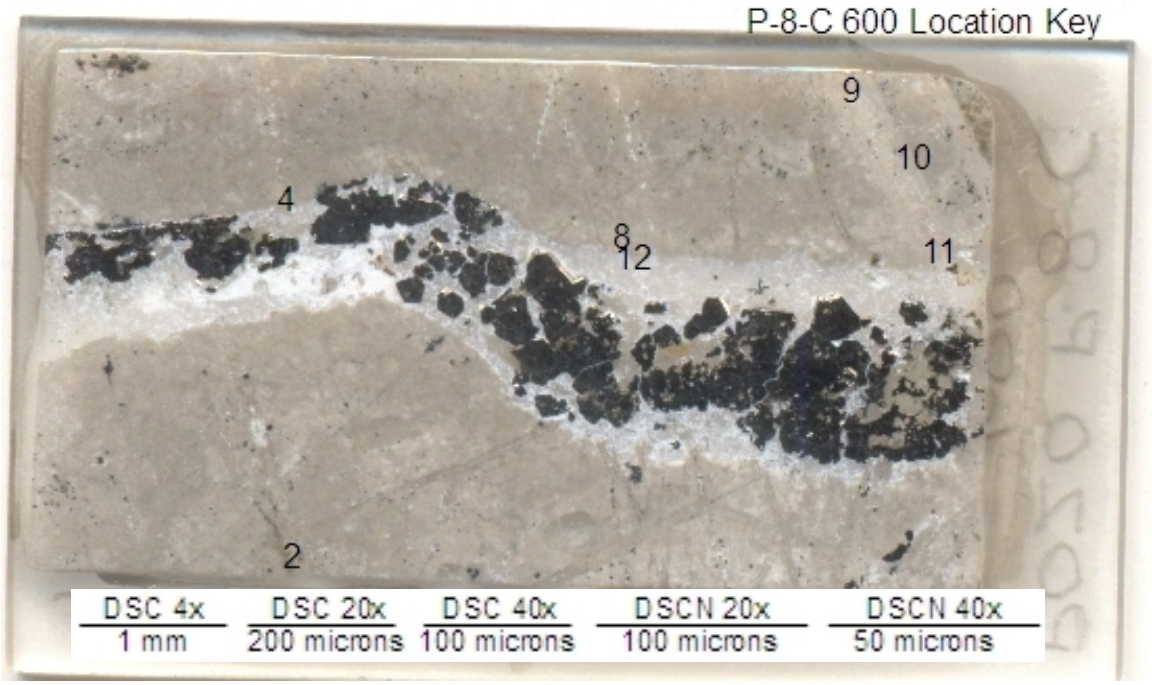

P-8-C 600 Photomicrographs: Photomicrographs were taken at the location shown on the P-8-C 600 Location Key, above. The photomicrographs are centered at approximately the center of the integer that corresponds to the location of each image. The fluid inclusion plate was approximately 2x3.6 cm (field of view above), and were 125 microns thick. Due to the thick nature of these sections, many photomicrographs may be taken in the same location of at a different focal depth, bringing fluid inclusions from different depths into focus. The scale bars correspond to images by image prefix and the objective used. The focal length of images prefixed as “DSC” was fixed. “DCSN” images did not have a fixed focal length, but were all taken with the camera fully zoomed, making the scale fixed based on objective. (4095, 4096) Growth zone evident as lines of smaller inclusions, location 2 (20x). (4098-4100) Plane of secondary inclusions, location 4 (40x). (4107, 4108) More banded textures in an A-vein at the D-vein intersection, location 8 (20x). (4109-4111) Inclusions, some with hematite daughters, location 9 (20x). (4112) Large (20 micron) LVD inclusion, location 10 (20x). (4114-4118) Many secondary inclusion trails, some primary(?) LVD inclusions are visible in crystal right of center, location 11 (20x). (4119) D-vein intersection, location 12 (10x).

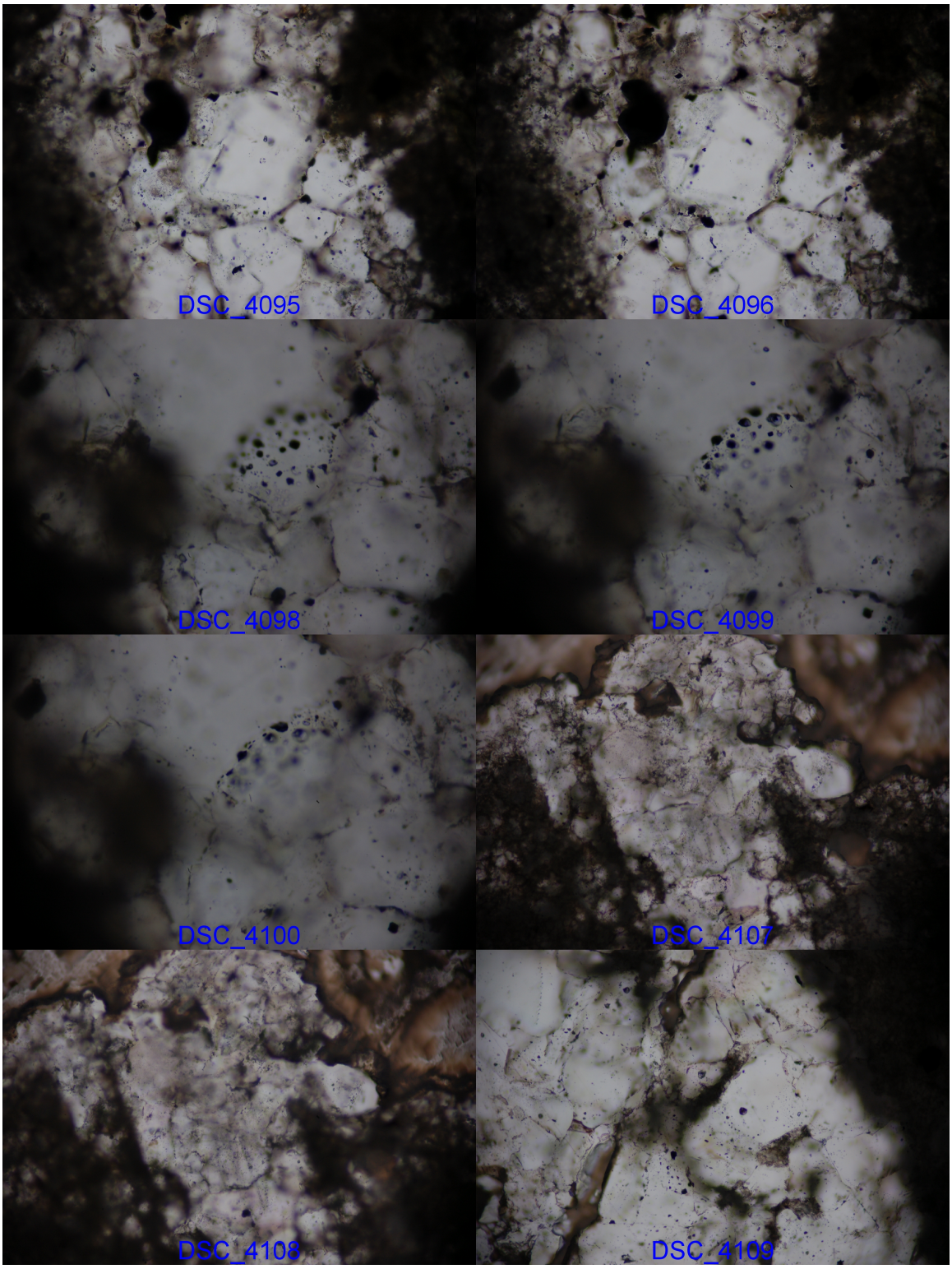
DSC_4095
DSC_4096
DSC_4098
DSC_4099
DSC_4100
DSC_4107
DSC_4108
DSC_4109

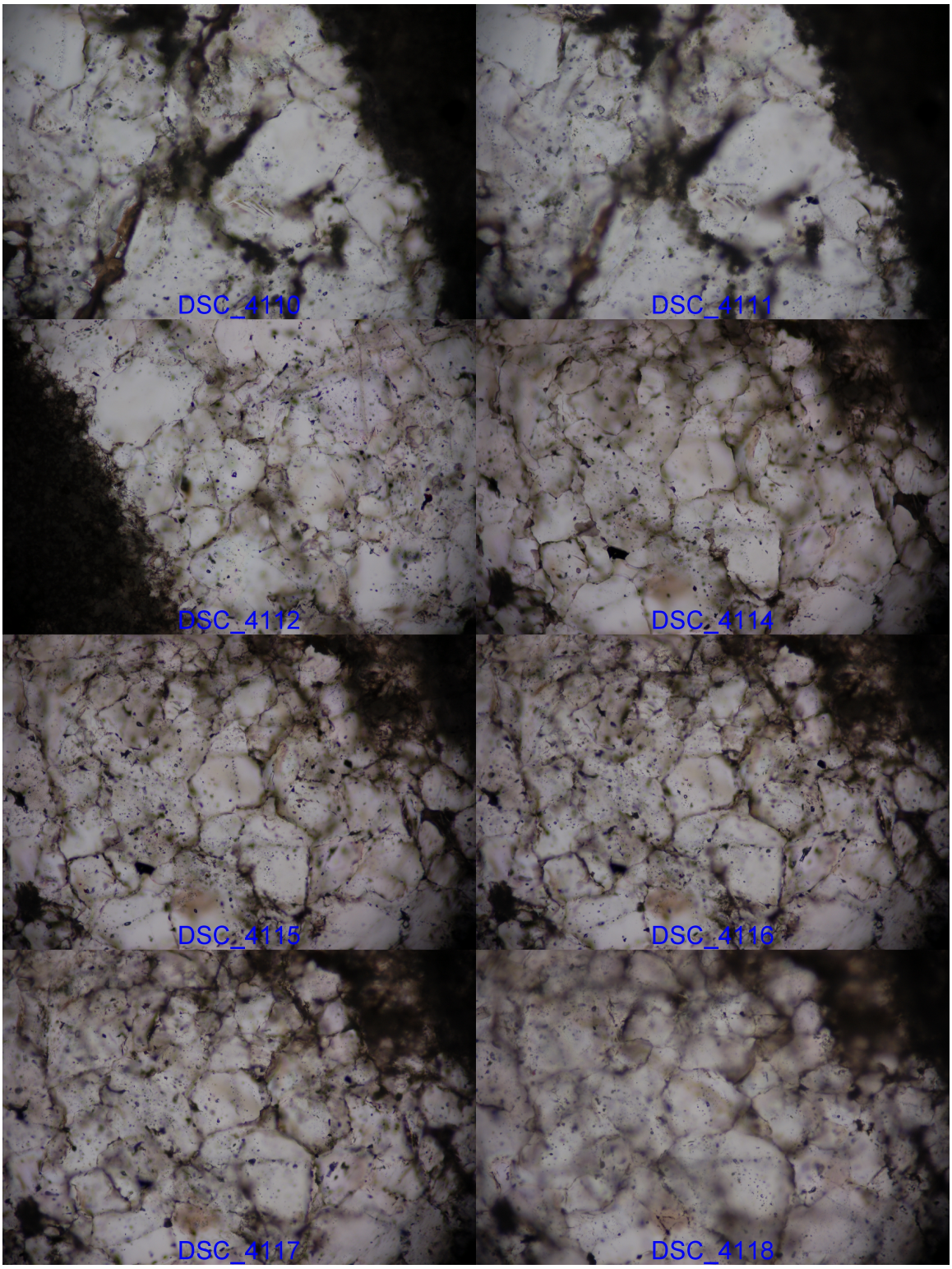
DSC_4110
DSC_4111
DSC_4112
DSC_4114
DSC_4115
DSC_4116
DSC_4117
DSC_4118

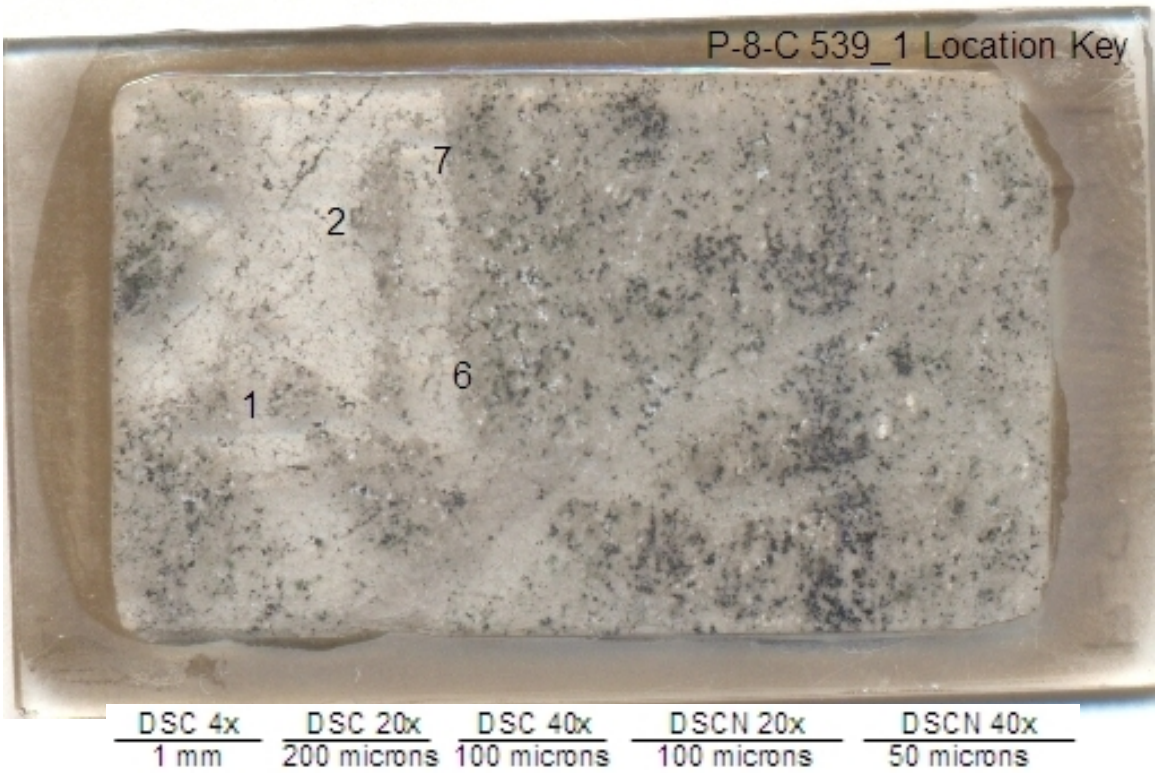

P-8-C 539_1 Photomicrographs: Photomicrographs were taken at the location shown on the P-8-C 539_1 Location Key, above. The photomicrographs are centered at approximately the center of the integer that corresponds to the location of each image. The fluid inclusion plate was approximately 2x3.6 cm (field of view above), and were 125 microns thick. Due to the thick nature of these sections, many photomicrographs may be taken in the same location of at a different focal depth, bringing fluid inclusions from different depths into focus. The scale bars correspond to images by image prefix and the objective used. (3983-3985) Inclusions in quartz, location 1 (20x). (3986) LVD inclusion at center of image, location 2 (20x). (3987) Same inclusion as previous image (40x). (3998-4001) LV and LVD primary(?) inclusions with long traces of secondary inclusions, location 6 (20x). (4002-4004) Secondary LV inclusions, location 7 (20x).

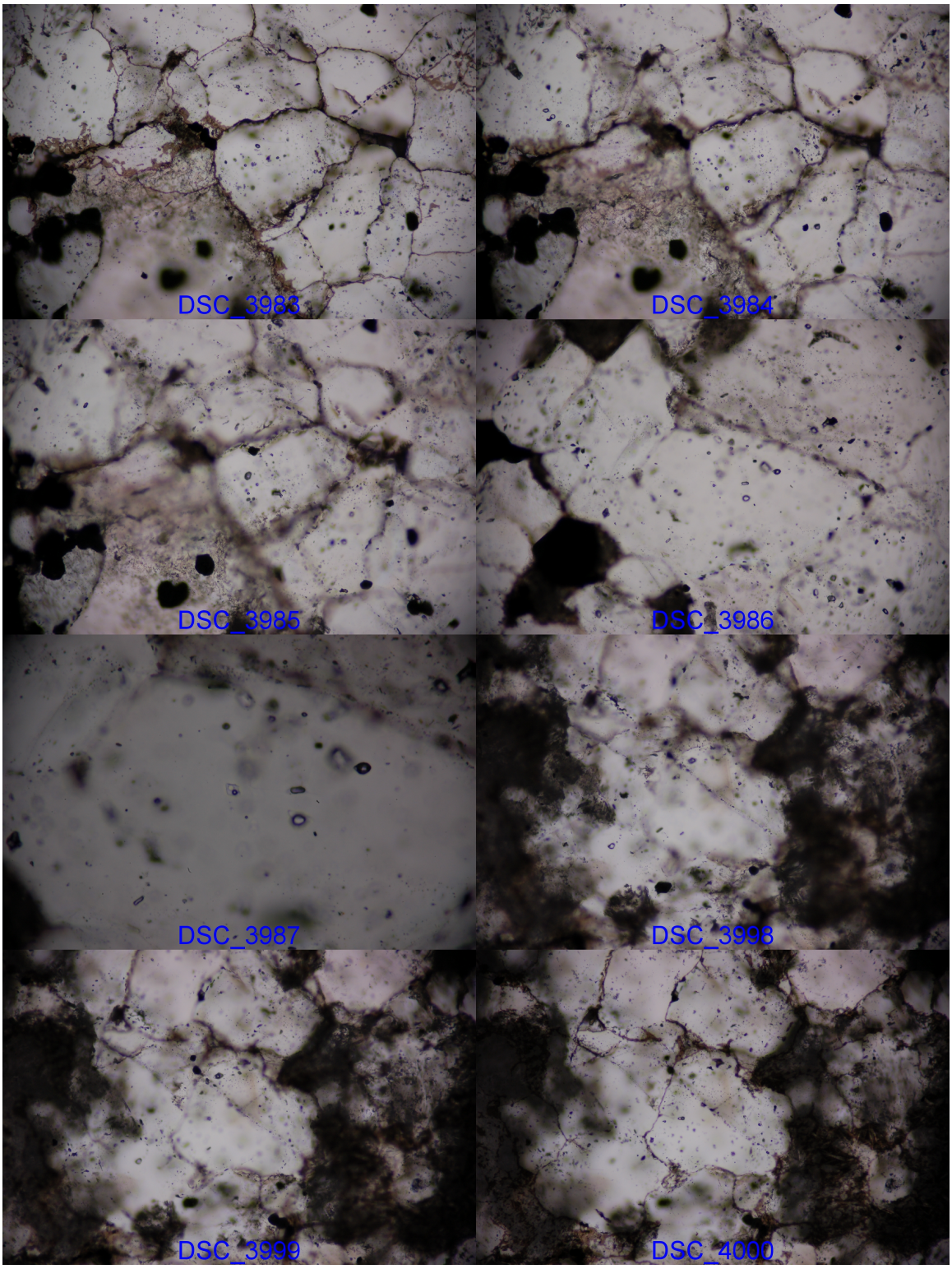
DSC_3983
DSC_3984
DSC_3985
DSC_3986
DSC_3987
DSC_3998
DSC_3999
DSC_4000

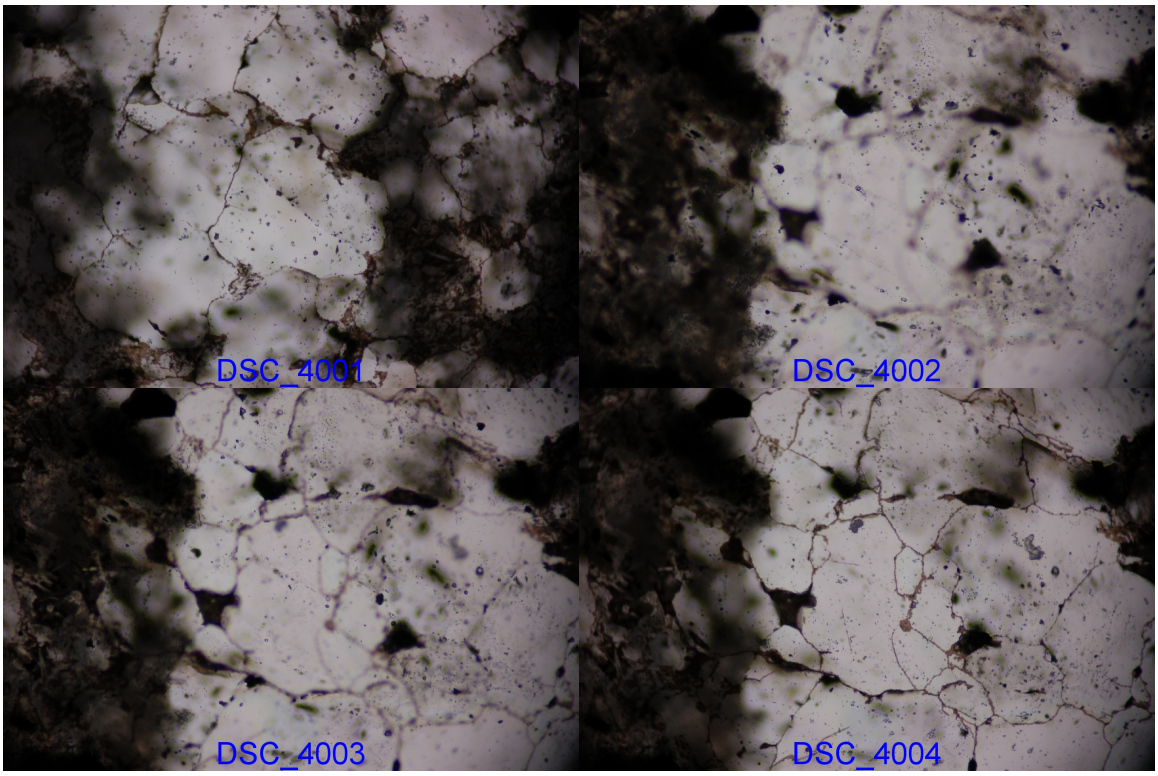
DSC_4001
DSC_4002
DSC_4003
DSC_4004

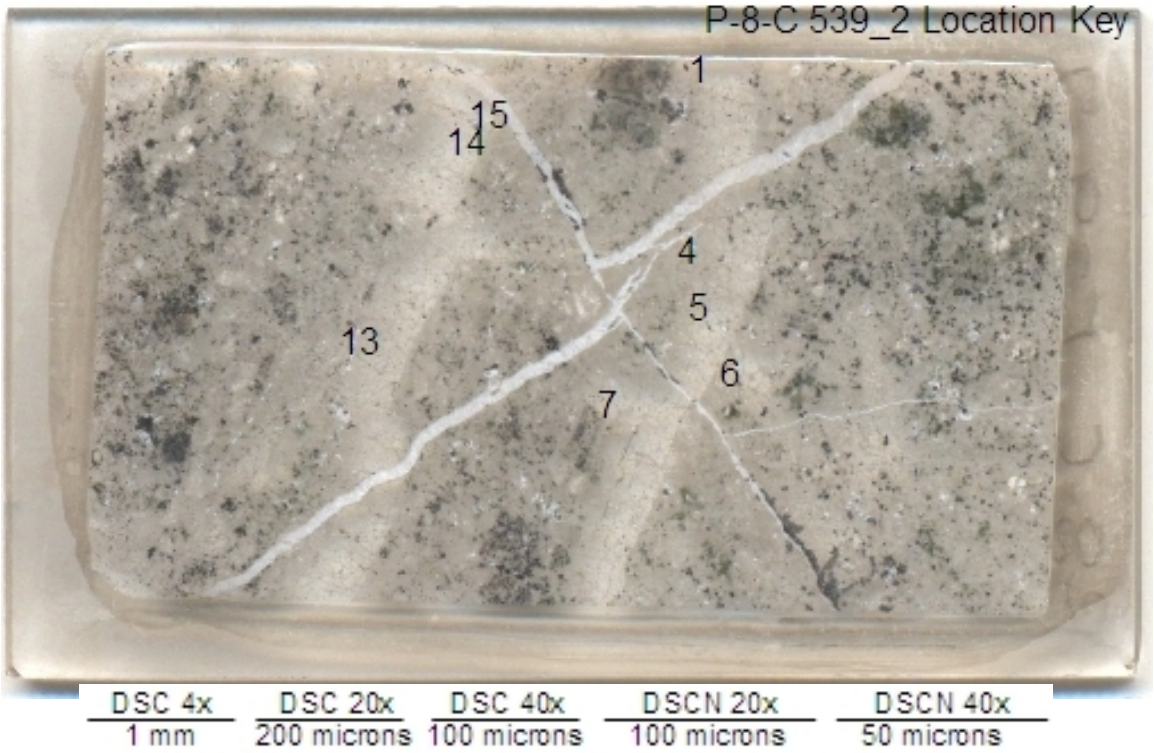

P-8-C 539_2 Photomicrographs: Photomicrographs were taken at the location shown on the P-8-C 539_2 Location Key, above. The photomicrographs are centered at approximately the center of the integer that corresponds to the location of each image. The fluid inclusion plate was approximately 2x3.6 cm (field of view above), and were 125 microns thick. Due to the thick nature of these sections, many photomicrographs may be taken in the same location of at a different focal depth, bringing fluid inclusions from different depths into focus. The scale bars correspond to images by image prefix and the objective used. The focal length of images prefixed as “DSC” was fixed. “DCSN” images did not have a fixed focal length, but were all taken with the camera fully zoomed, making the scale fixed based on objective. (4015-4019) Secondary and primary(?) inclusions, location 1 (20x). (4030-4032) Secondary inclusions trails with several larger inclusions, location 4 (20x). (4033-4035) LVD inclusions in crystal at top center, just below large dark region, location 5 (20x). (40396-4039) LVD inclusions, at center of 4036 is prominent LVD inclusion with prominent daughter minerals including a hematite daughter, location 6 (40x). Inclusion rich quartz, location 7 (20x). LVD inclusion, location 13 (20x). (4068-4071) Irregular LVD inclusion with necked-like tail, location 14 (20x). (4073) LV inclusion, location 15 (20x).

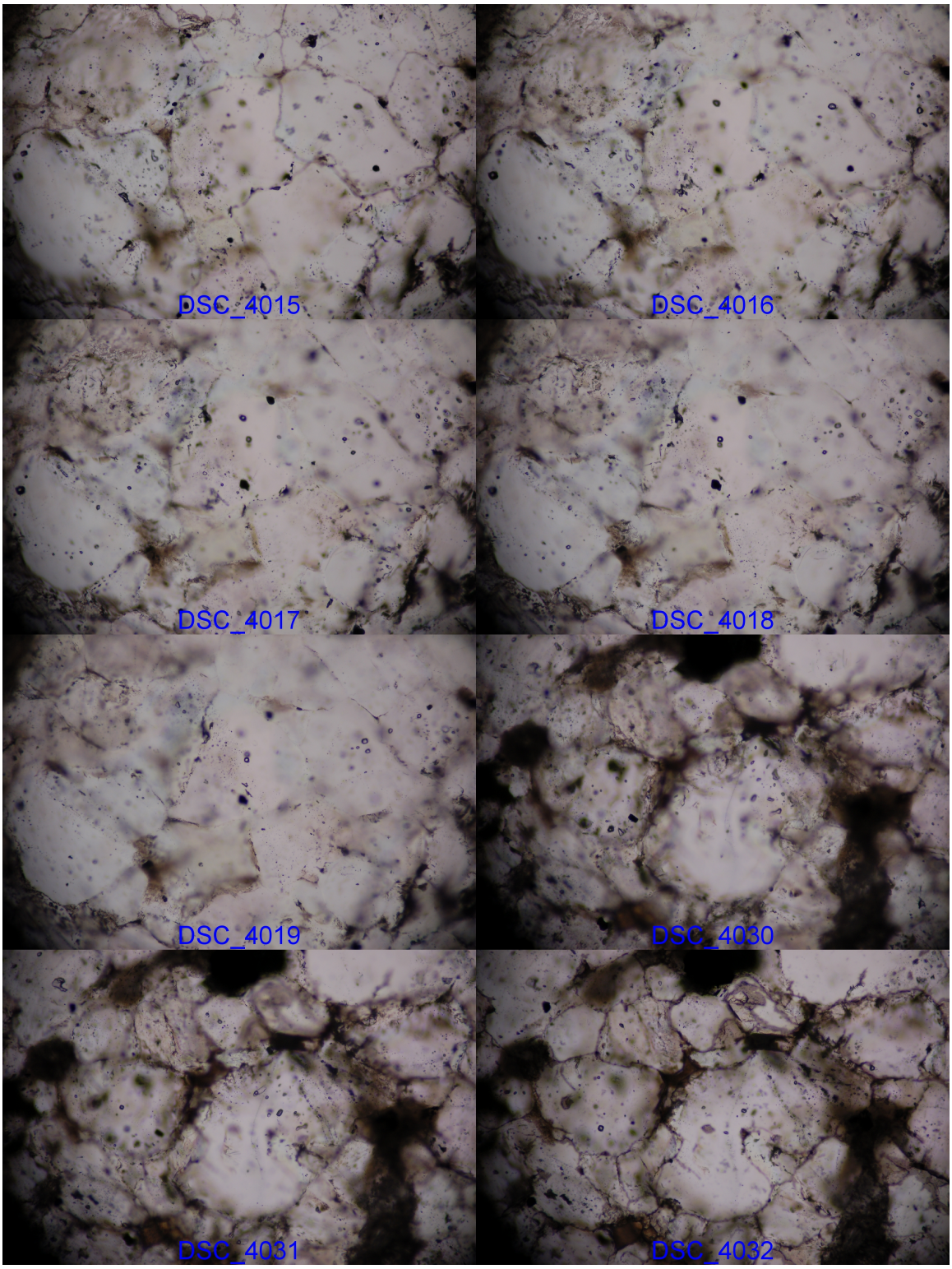
DSC_4015
DSC_4016
DSC_4017
DSC_4018
DSC_4019
DSC_4030
DSC_4031
DSC_4032

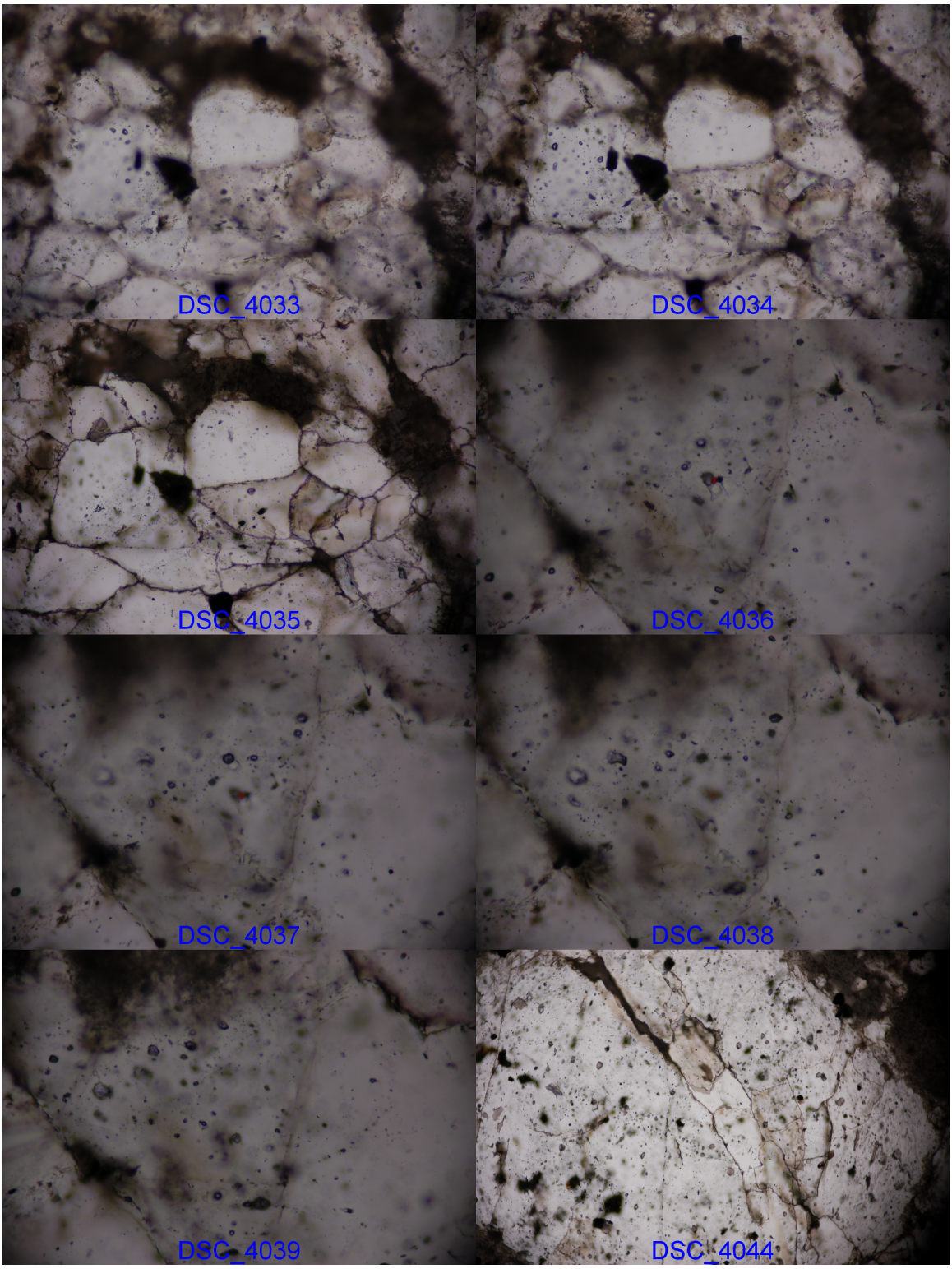
DSC_4033
DSC_4034
DSC_4035
DSC_4036
DSC_4037
DSC_4038
DSC_4039
DSC_4044

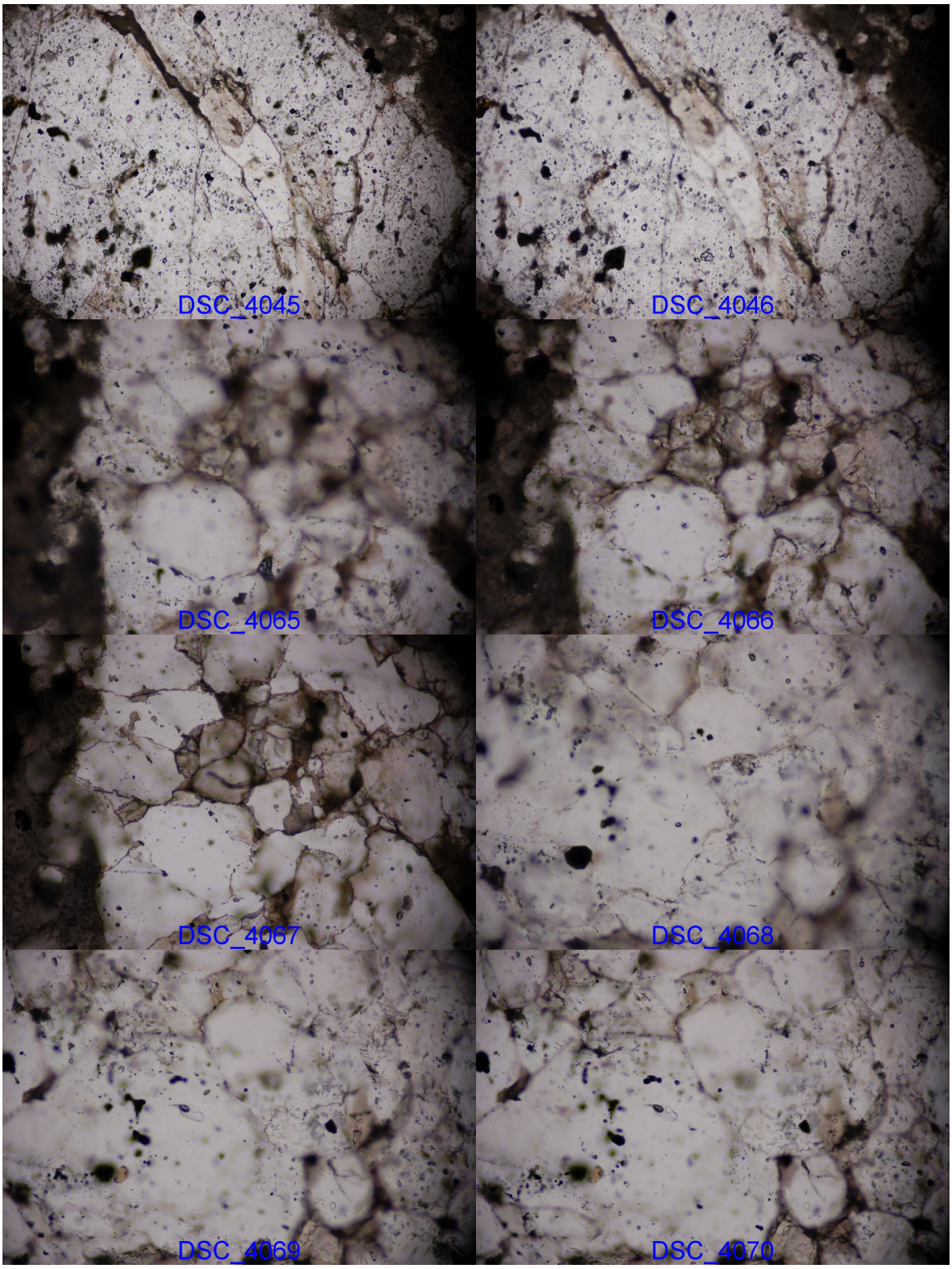
DSC_4045
DSC_4046
DSC_4065
DSC_4066
DSC_4067
DSC_4068
DSC_4069
DSC_4070

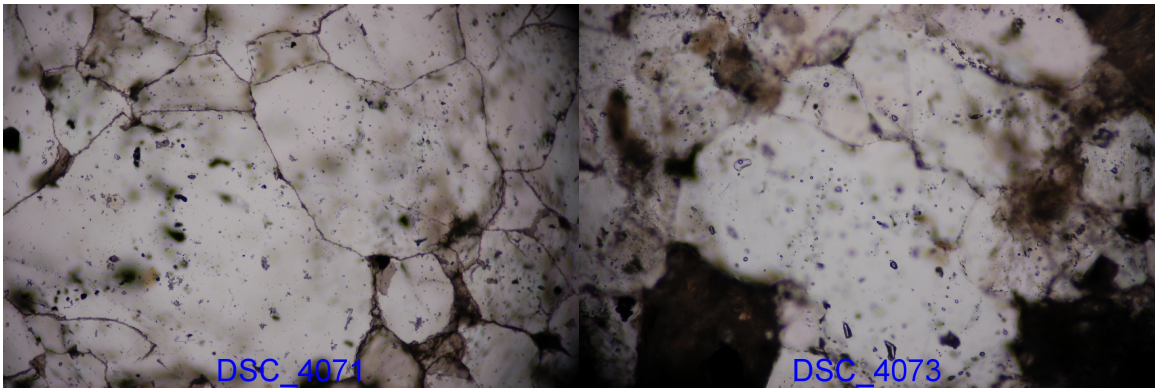
DSC_4071
DSC_4073

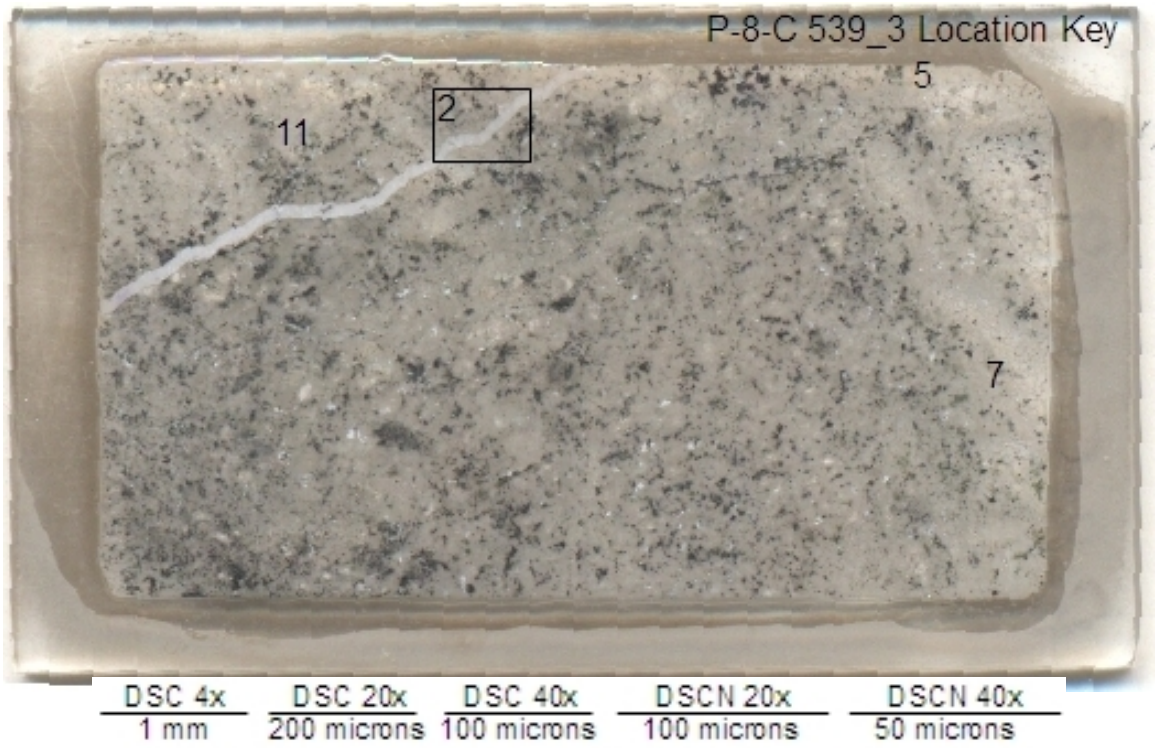

P-8-C 539_3 Photomicrographs: Photomicrographs were taken at the location shown on the P-8-C 539_3 Location Key, above. The photomicrographs are centered at approximately the center of the integer that corresponds to the location of each image, except image location 2, which is denoted by the rectangle. The fluid inclusion plate was approximately 2x3.6 cm (field of view above), and were 125 microns thick. Due to the thick nature of these sections, many photomicrographs may be taken in the same location of at a different focal depth, bringing fluid inclusions from different depths into focus. The scale bars correspond to images by image prefix (i.e. DSC) and the objective used. (3935-3936) An anhydrite vein cuts a quartz vein, location 2 (4x). (3946-3950) Inclusions in quartz against the vein wall, location 5 (20x). (3958, 3959) LVD inclusion between secondary trails, location 7 (20x). (3971) LVD secondary(?) inclusion, location 11 (20x). Location 11 is a loose approximation of the location of the photomicrograph, inferred as the location between locations 10 and 12. (3972) Same as previous image (40x).

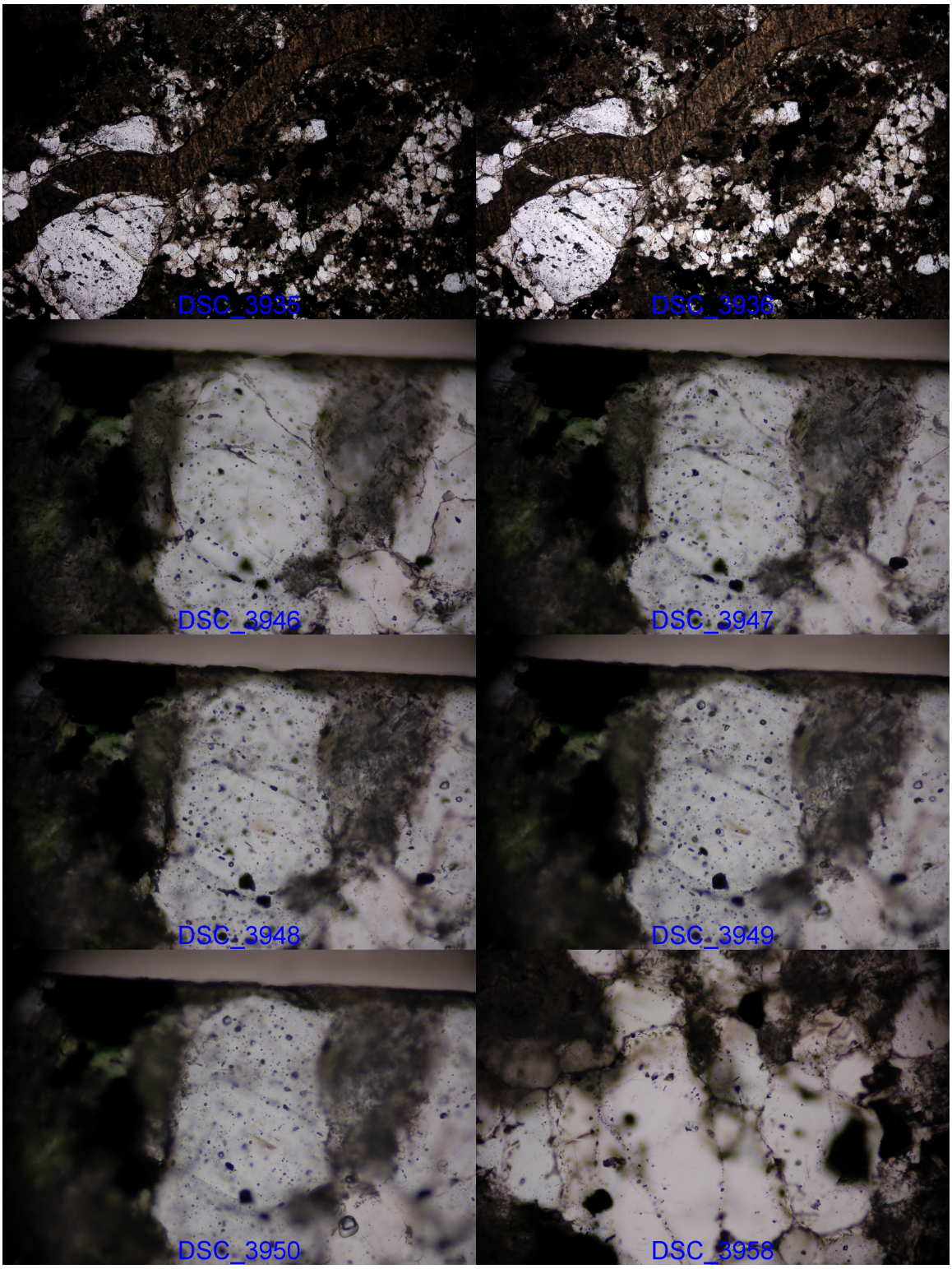
DSC_3935
DSC_3936
DSC_3946
DSC_3947
DSC_3948
DSC_3949
DSC_3950
DSC_3958

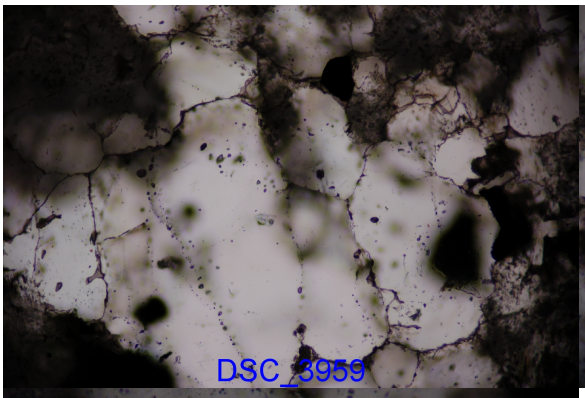
DSC_3959

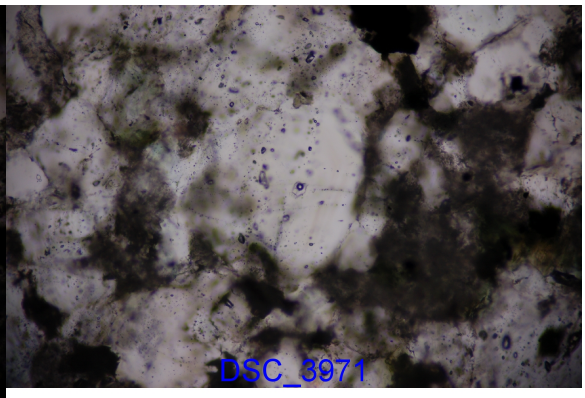
DSC_3971

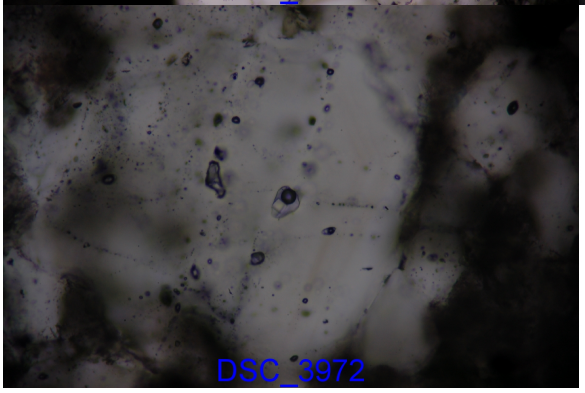
DSC_3972

DSC 4x 1 mm | DSC 20x 200 microns | DSC 40x 100 microns | DSCN 20x 100 microns | DSCN 40x 50 microns

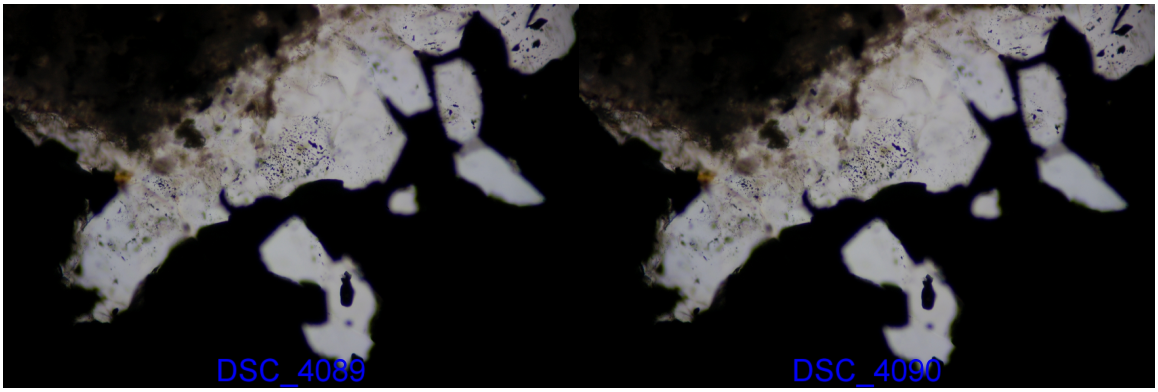

P-8-C 486 Photomicrographs: Photomicrographs were taken at the location shown on the P-8-C 486 Location Key, above. The photomicrographs are centered at approximately the center of the integer that corresponds to the location of each image. The fluid inclusion plate was approximately 2x3.6 cm (field of view above), and were 125 microns thick. Due to the thick nature of these sections, many photomicrographs may be taken in the same location of at a different focal depth, bringing fluid inclusions from different depths into focus. The scale bars correspond to images by image prefix and the objective used. (4089, 4090) Quartz growing from wall into D-vein, location 2 (20x).

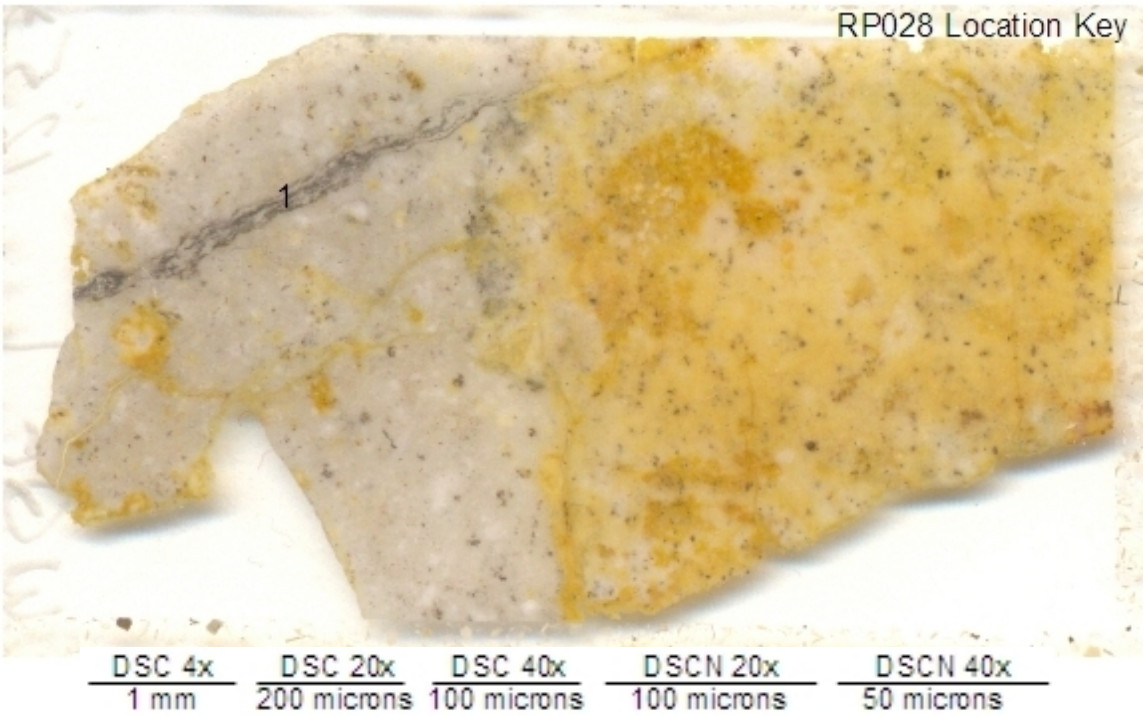

RP028 Photomicrographs: Photomicrographs were taken at the location shown on the RP028 Location Key, above. The photomicrographs are centered at approximately the center of the integer that corresponds to the location of each image. The fluid inclusion plate was approximately 2x3.6 cm (field of view above), and were 125 microns thick. Due to the thick nature of these sections, many photomicrographs may be taken in the same location of at a different focal depth, bringing fluid inclusions from different depths into focus. The scale bars correspond to images by image prefix and the objective used. The focal length of images prefixed as “DSC” was fixed. “DCSN” images did not have a fixed focal length, but were all taken with the camera fully zoomed, making the scale fixed based on objective. (4137, 4138) Ledge texture with banded like vein running through ledge, location 1 (4x). (4139, 4140) Same location as previous images (10x). (4141-4143) Banded texture of vein in previous image location (20x).

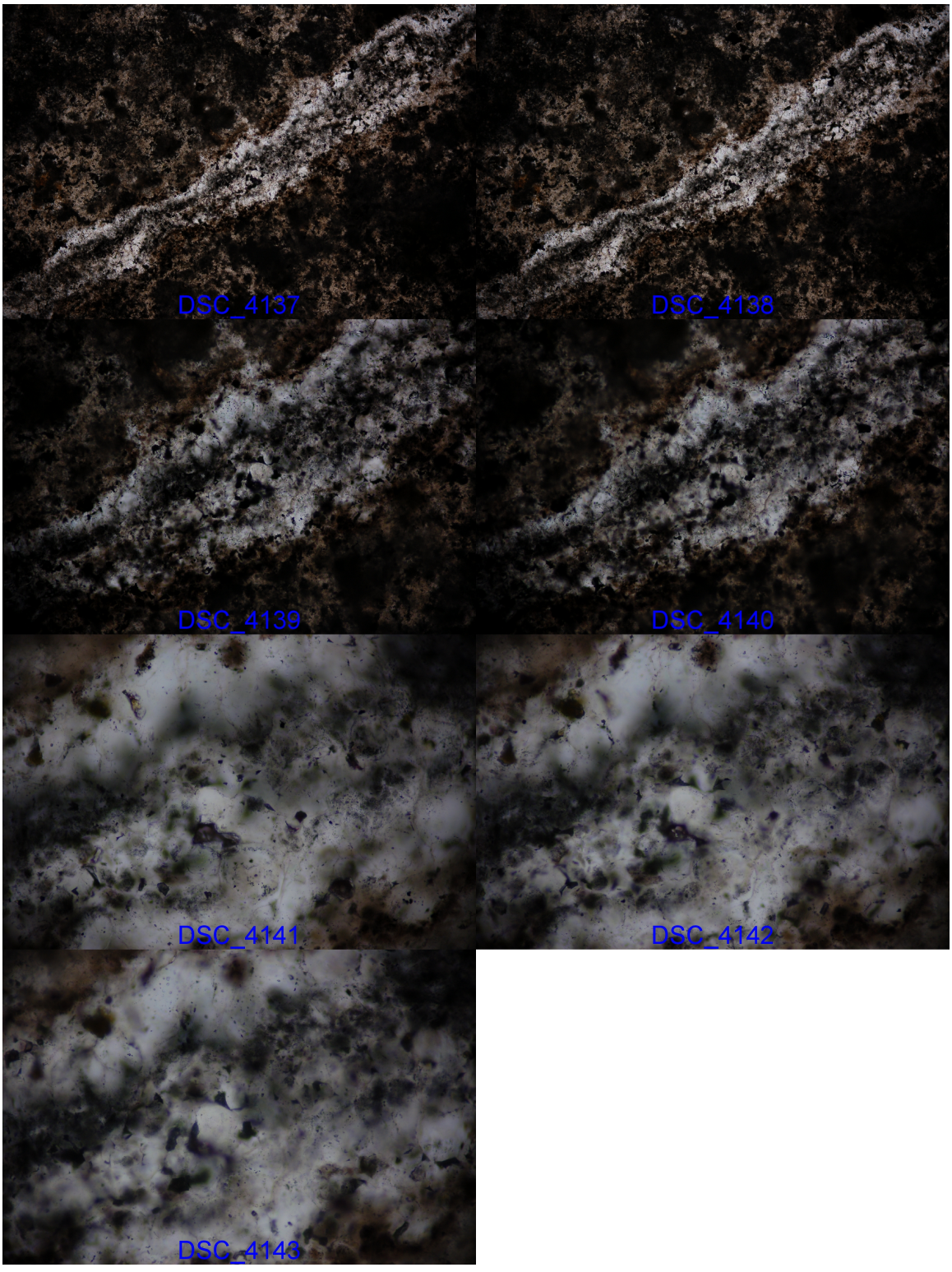
DSC_4137
DSC_4138
DSC_4139
DSC_4140
DSC_4141
DSC_4142
DSC_4143

RP054 Photomicrographs: Photomicrographs were taken at the location shown on the RP054 Location Key, above. The photomicrographs are centered at approximately the center of the integer that corresponds to the location of each image. The fluid inclusion plate was approximately 2x3.6 cm (field of view above), and were 125 microns thick. Due to the thick nature of these sections, many photomicrographs may be taken in the same location of at a different focal depth, bringing fluid inclusions from different depths into focus. The scale bars correspond to images by image prefix and the objective used. The focal length of images prefixed as "DSC" was fixed. "DCSN" images did not have a fixed focal length, but were all taken with the camera fully zoomed, making the scale fixed based on objective. (3644-3646) Bands in across quartz crystals, location 2 (10x). (3663, 3664) Dark bands, location 5 (20x). (3665-3667) Dark quartz, location 6 (20x). (3427-3429) Cigar inclusions, location 7 (20x). (3430) Same cigar inclusions as previous images (40x). (3436) Inclusion trails parallel to a dark band visible as the dark corner in the lower right, location 9 (20x). (3440) Euhedral quartz, location 11 (20x). (3446, 3447) Small inclusions tracing growth zones, location 14 (20x). (3451) A spray of secondary inclusions, location 16 (20x).

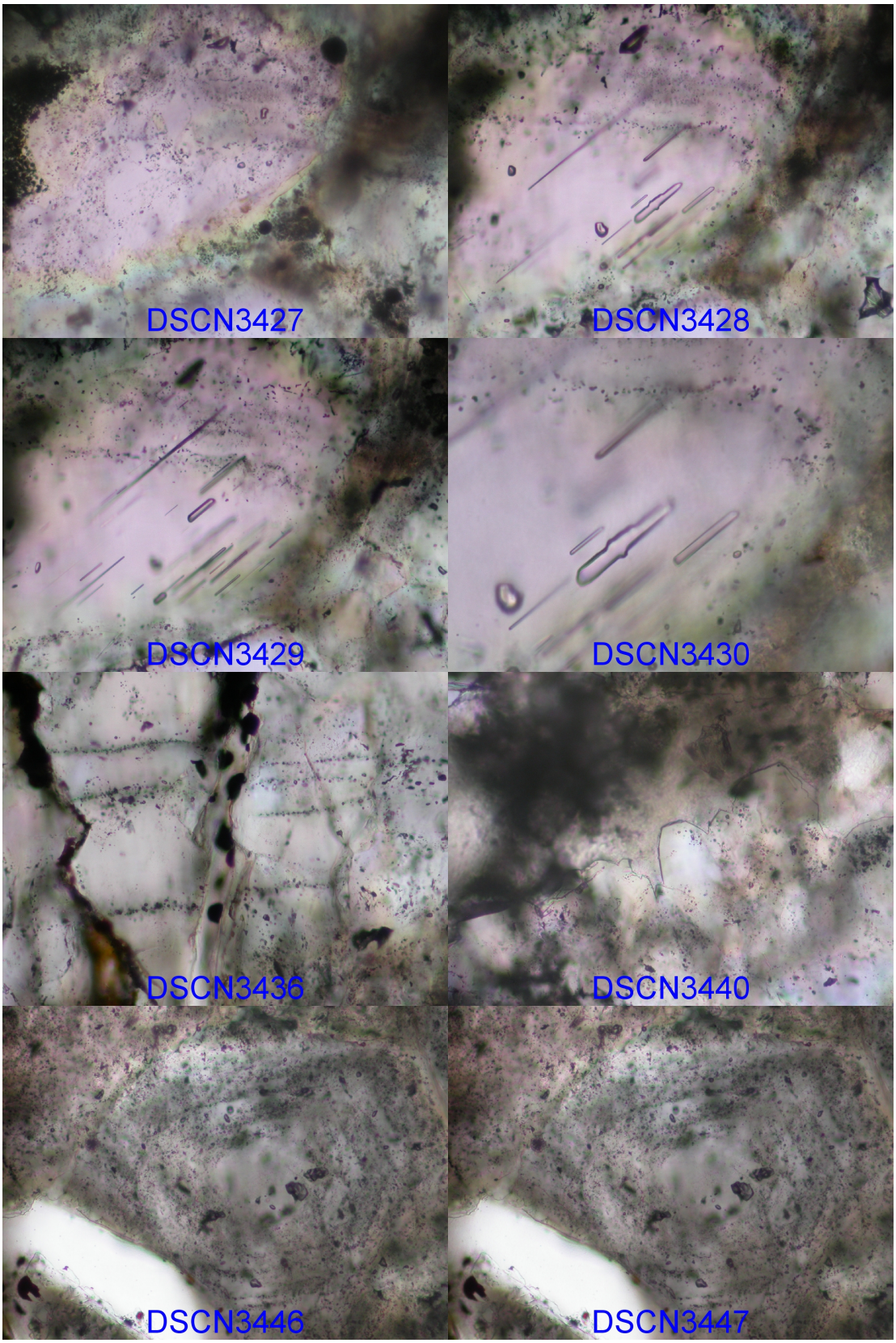
DSCN3427
DSCN3428
DSCN3429
DSCN3430
DSCN3436
DSCN3440
DSCN3446
DSCN3447

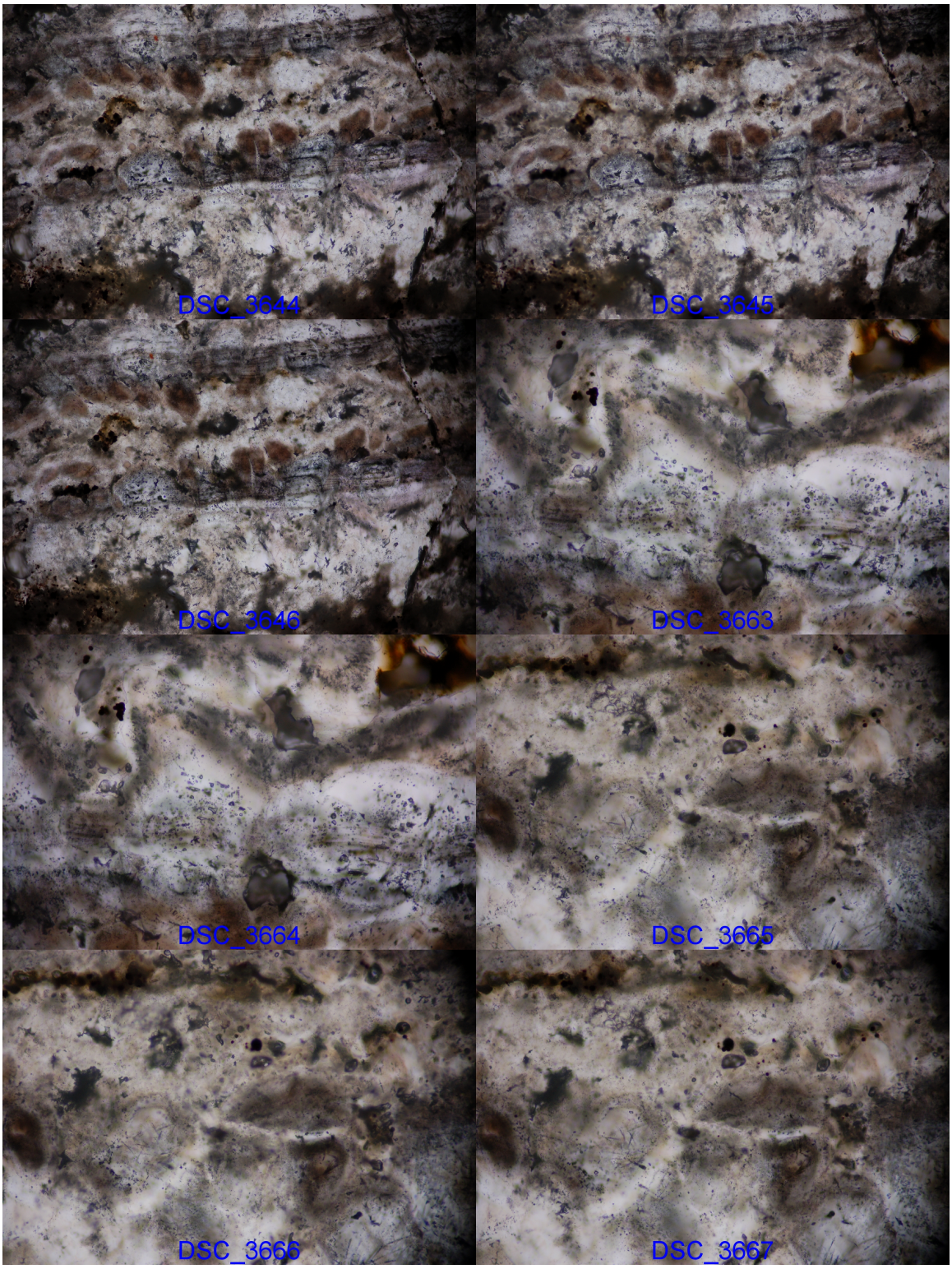
DSC_3644
DSC_3645
DSC_3646
DSC_3663
DSC_3664
DSC_3665
DSC_3666
DSC_3667

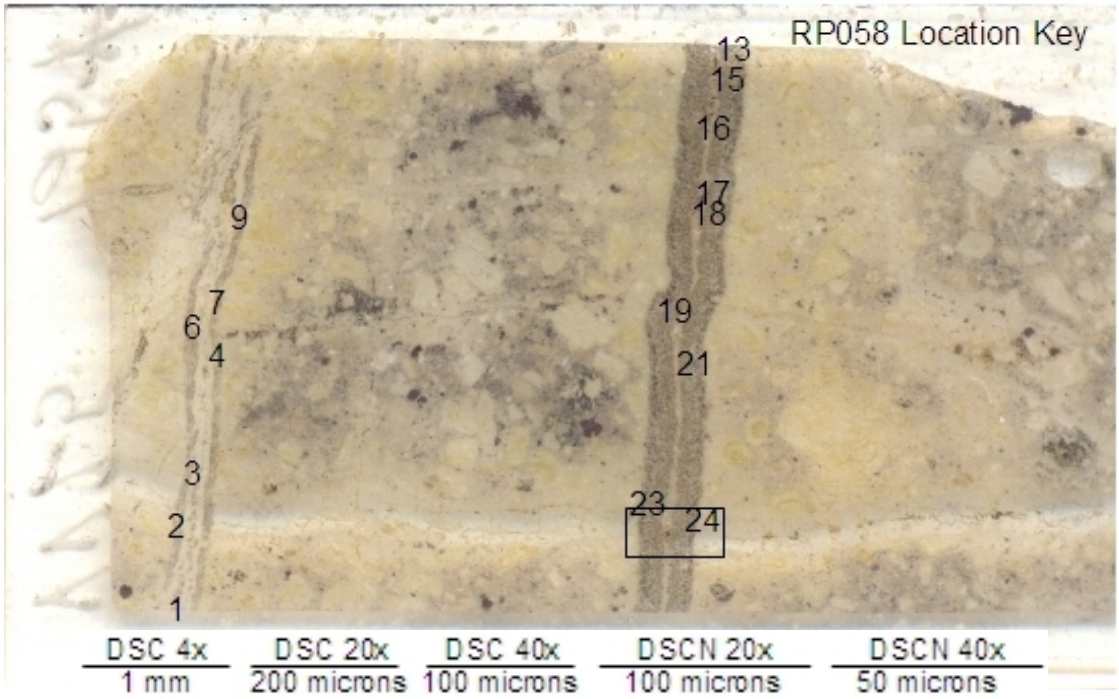

RP058 Photomicrographs: Photomicrographs were taken at the location shown on the RP058 Location Key above. The photomicrographs are centered at approximately the center of the integer that corresponds to the location of each image, except location 24, which is approximately the rectangle bounding the vein intersection. The fluid inclusion plate was approximately 2x3.6 cm (field of view above), and were 125 microns thick. Due to the thick nature of these sections, many photomicrographs may be taken in the same location of at a different focal depth, bringing fluid inclusions from different depths into focus. The scale bars correspond to images by image prefix and the objective used. (3411-3413) Hematite daughters can be seen in fluid inclusion to right of dark quartz band, location 1 (20x). (3644-3646) Bands in across quartz crystals, location 2 (10x). (3418, 3419) Well zoned quartz crystals, location 3 (20x). (3426-3428) Elongated V inclusions, location 4 (20x). (3435) Dark quart rim around a clear quartz core with several large V inclusions, location 6 (20x). (3436-3438) Clear quartz core with several large V inclusions, rimmed by darker quartz, location 7 (20x). (3497-3499) Dark quartz in growth zone, location 9 (40x). (3552, 3553) Dark quartz, location 13 (20x). (3556, 3557) Dark quartz, location 15 (20x). (3558, 3559) Dark quartz, location 16 (20x). (3560, 3561) Dark quartz, location 17 (20x). (3562-3564) Dark quartz cores with clear quartz rims, location 18 (20x). (3565-3567) Dark quartz, location 19 (20x). (3569-3571) Dark quartz with clear quartz cores and rims visible, large V inclusions are visible in cores, location 21 (20x). (3573-3576) Cigar-like inclusions in core of crystal surrounded by dark quartz, location 23 (20x). (3577-3580) Intersection of two veins, the darker vein clearly cuts and offsets the lighter vein, location 24 (4x).

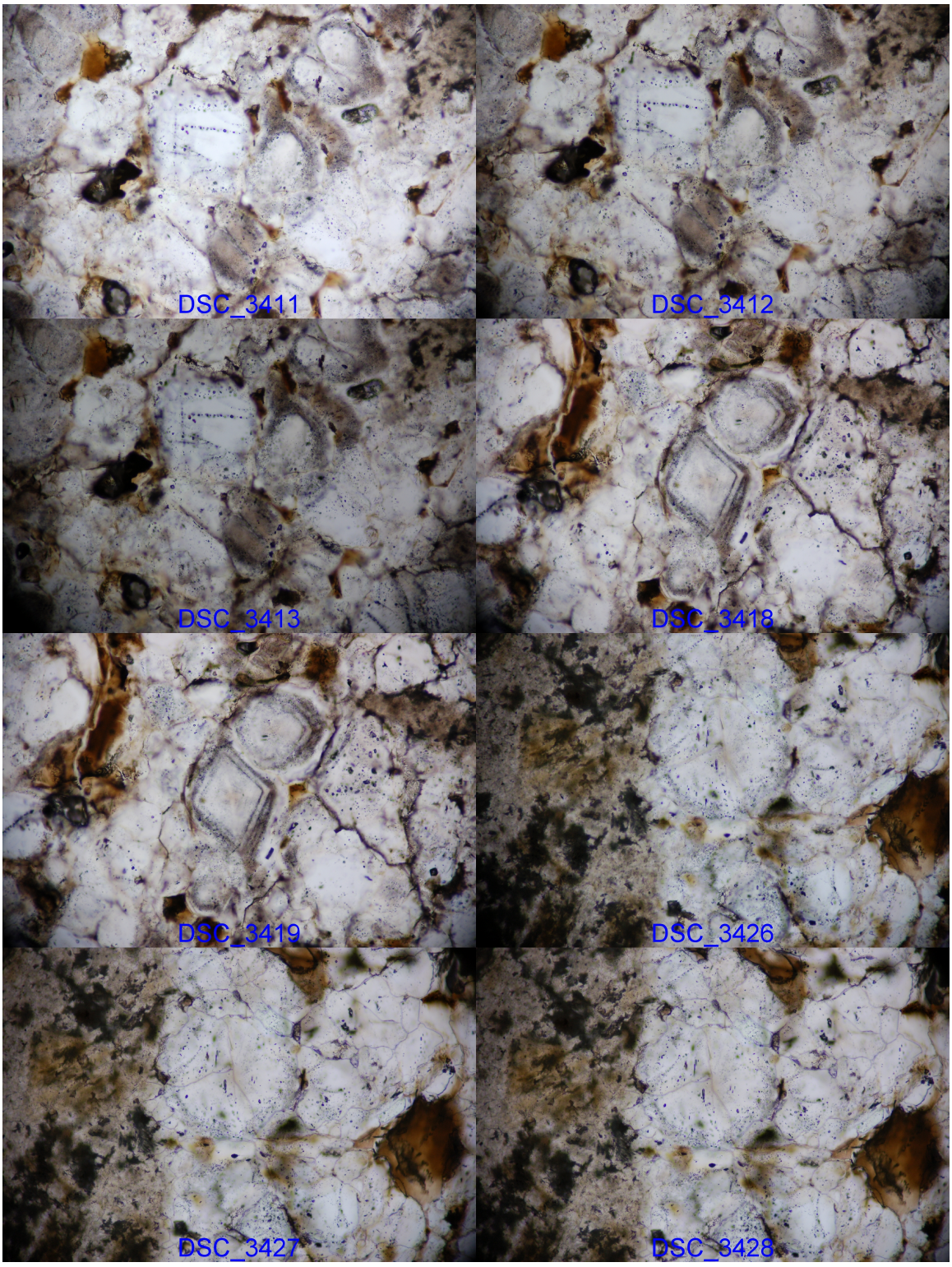
DSC_3411
DSC_3412
DSC_3413
DSC_3418
DSC_3419
DSC_3426
DSC_3427
DSC_3428

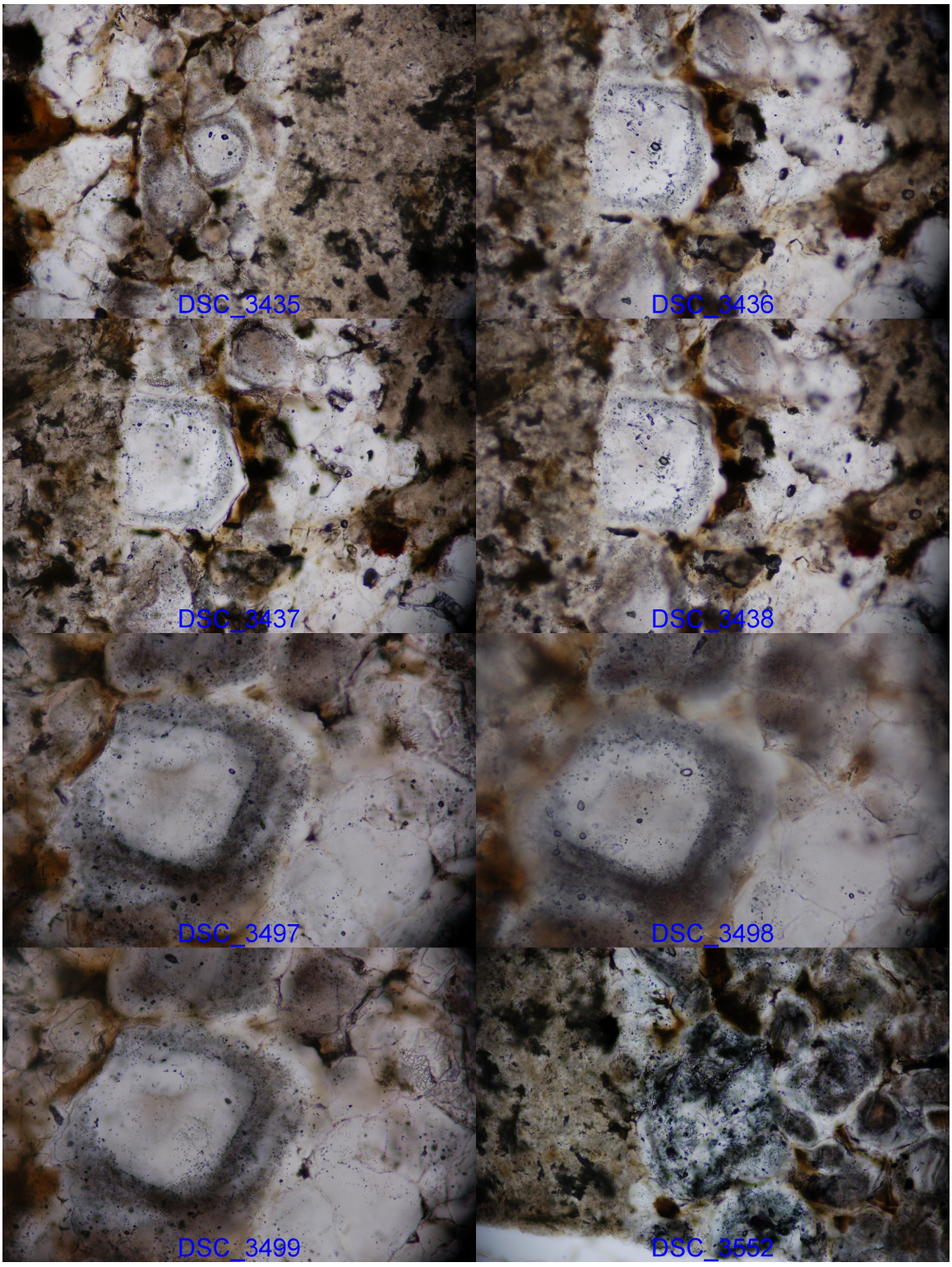
DSC_3435
DSC_3436
DSC_3437
DSC_3438
DSC_3497
DSC_3498
DSC_3499
DSC_3552

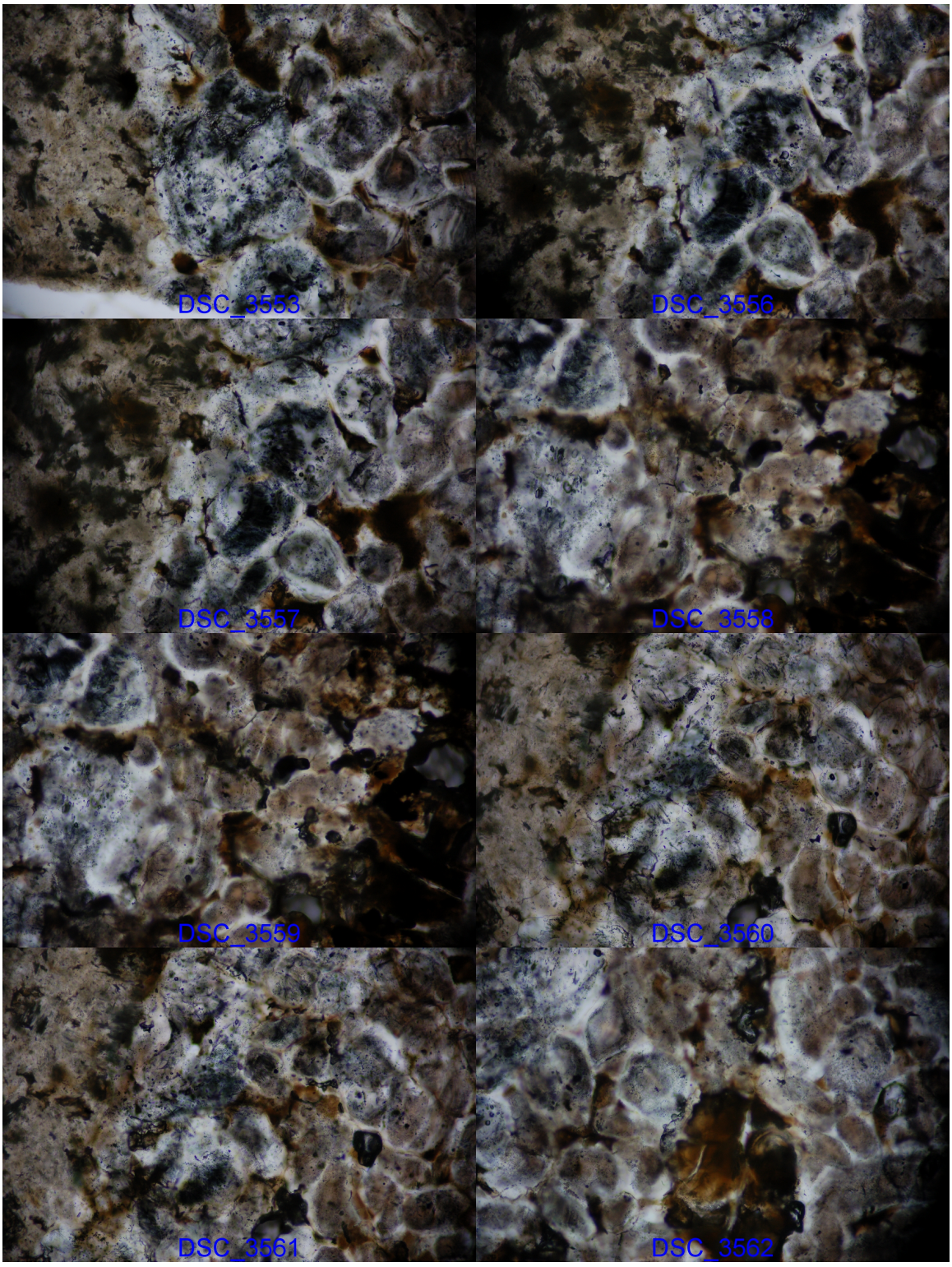
DSC_3553
DSC_3556
DSC_3557
DSC_3558
DSC_3559
DSC_3560
DSC_3561
DSC_3562

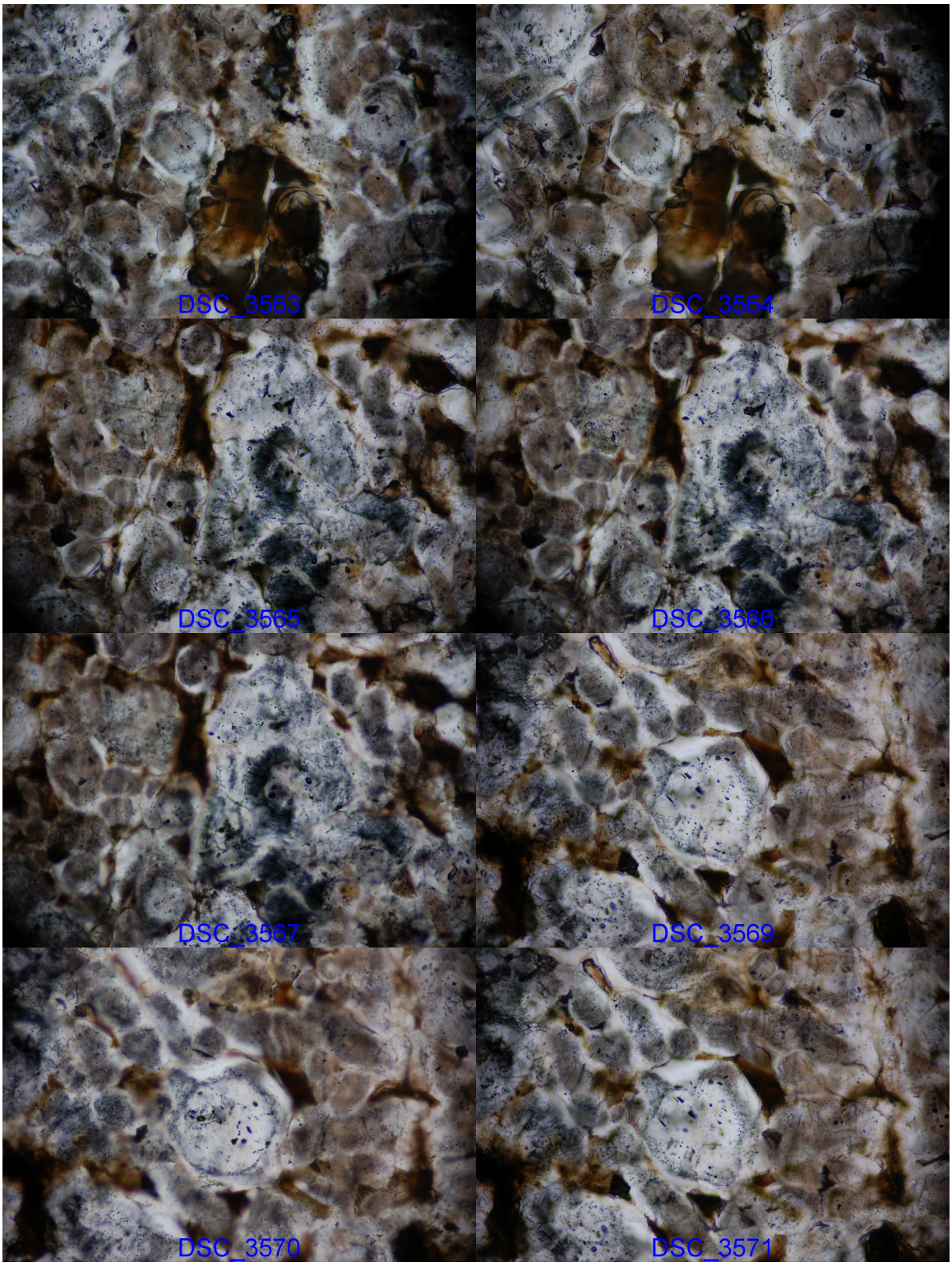
DSC_3563
DSC_3564
DSC_3565
DSC_3566
DSC_3567
DSC_3569
DSC_3570
DSC_3571

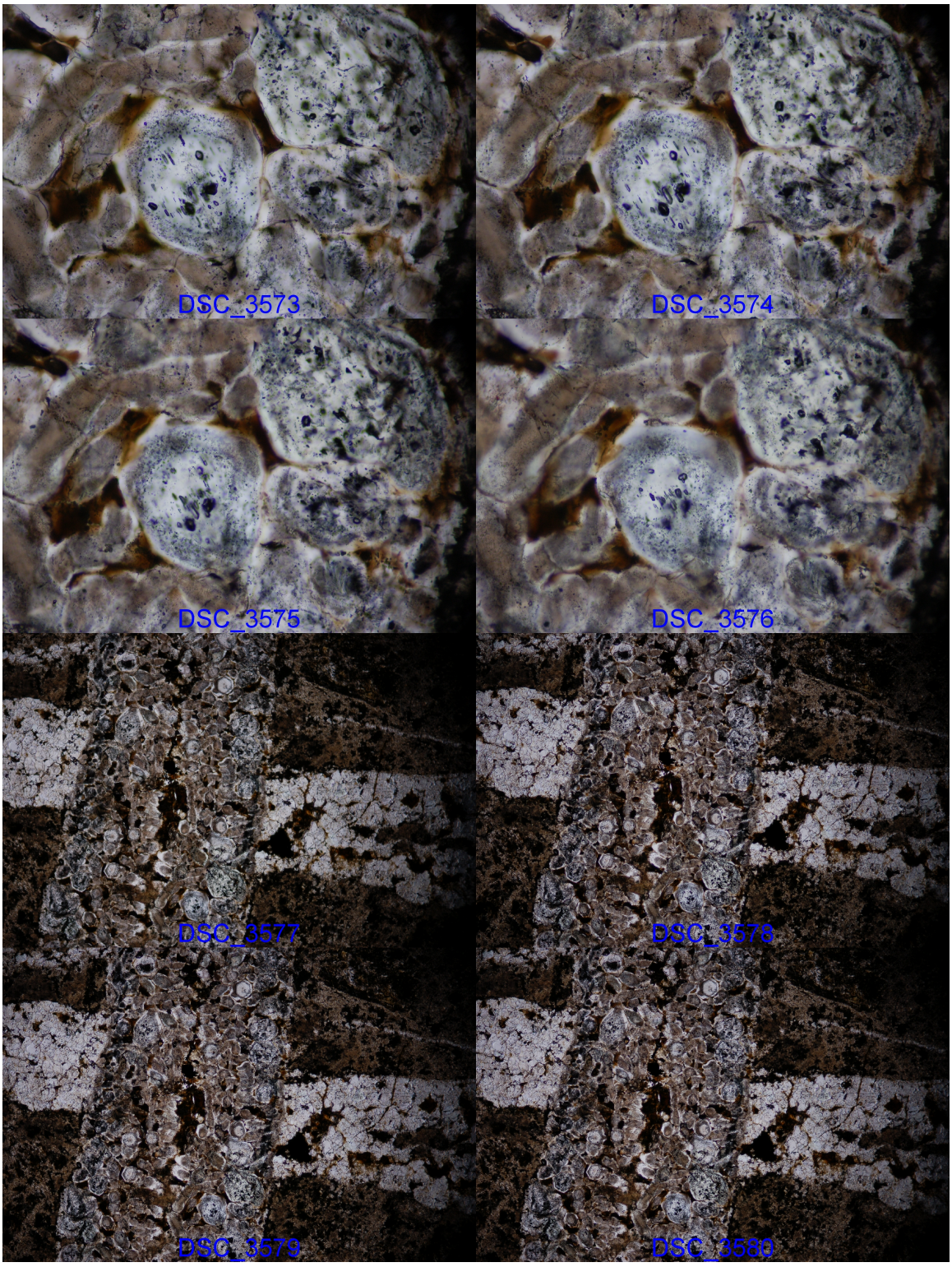
DSC_3573
DSC_3574
DSC_3575
DSC_3576
DSC_3577
DSC_3578
DSC_3579
DSC_3580

V6.5NWC 342.4 Photomicrographs: Photomicrographs were taken at the location shown on the V6 SNWC 342.4 Location Key, above. The photomicrographs are centered at approximately the center of the integer that corresponds to the location of each image, except image location 2, which is denoted by the rectangle. The fluid inclusion plate was approximately 2x3.6 cm (field of view above), and were 125 microns thick. Due to the thick nature of these sections, many photomicrographs may be taken in the same location of at a different focal depth, bringing fluid inclusions from different depths into focus. The scale bars correspond to images by image prefix (i.e. DSCN) and the objective used. (3305-3307) Dark quartz in crystal core, location 2 (20x). (3313, 3314) Fluid inclusions in quartz, location 3 (20x). (3320, 3319) Fluid inclusions and opaque minerals in quartz, location 4 (20x). (3353-3355) Vug filling clear quartz with dark cores, or dark quartz rinds, location 13 (20x). (3414-3419) Irregular LVD inclusions, location 23 (40x).

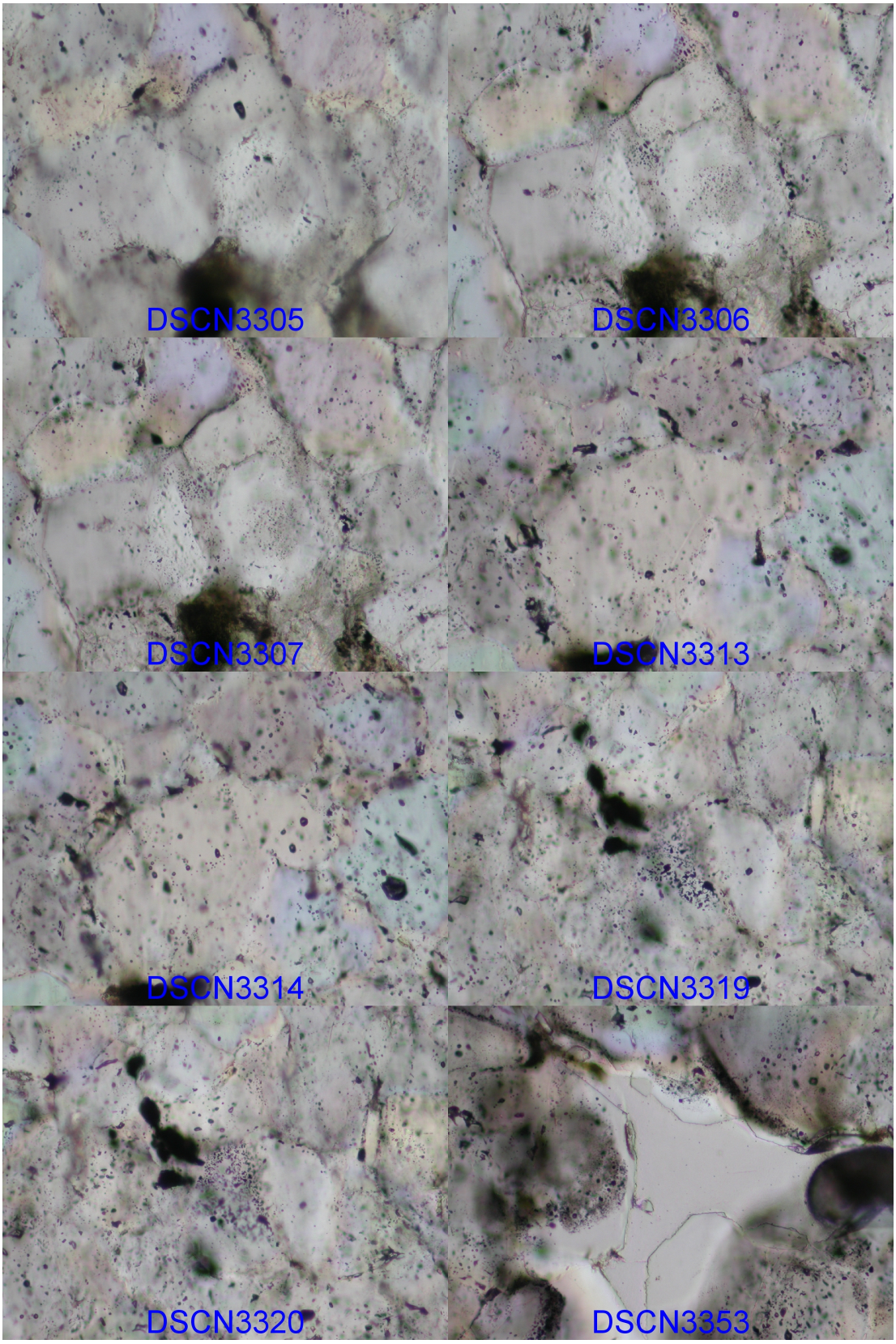
DSCN3305
DSCN3306
DSCN3307
DSCN3313
DSCN3314
DSCN3319
DSCN3320
DSCN3353

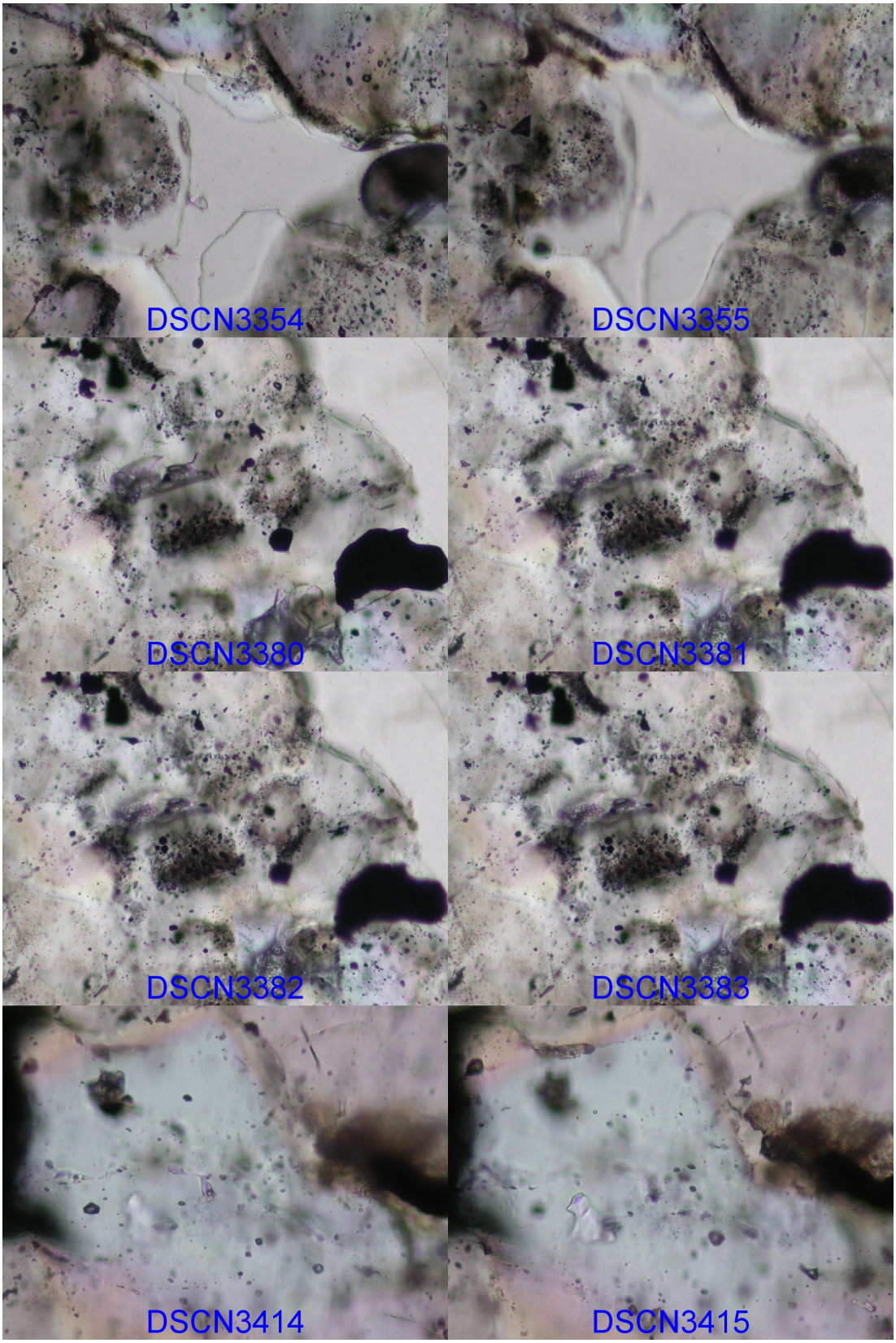
DSCN3354
DSCN3355
DSCN3380
DSCN3381
DSCN3382
DSCN3383
DSCN3414
DSCN3415

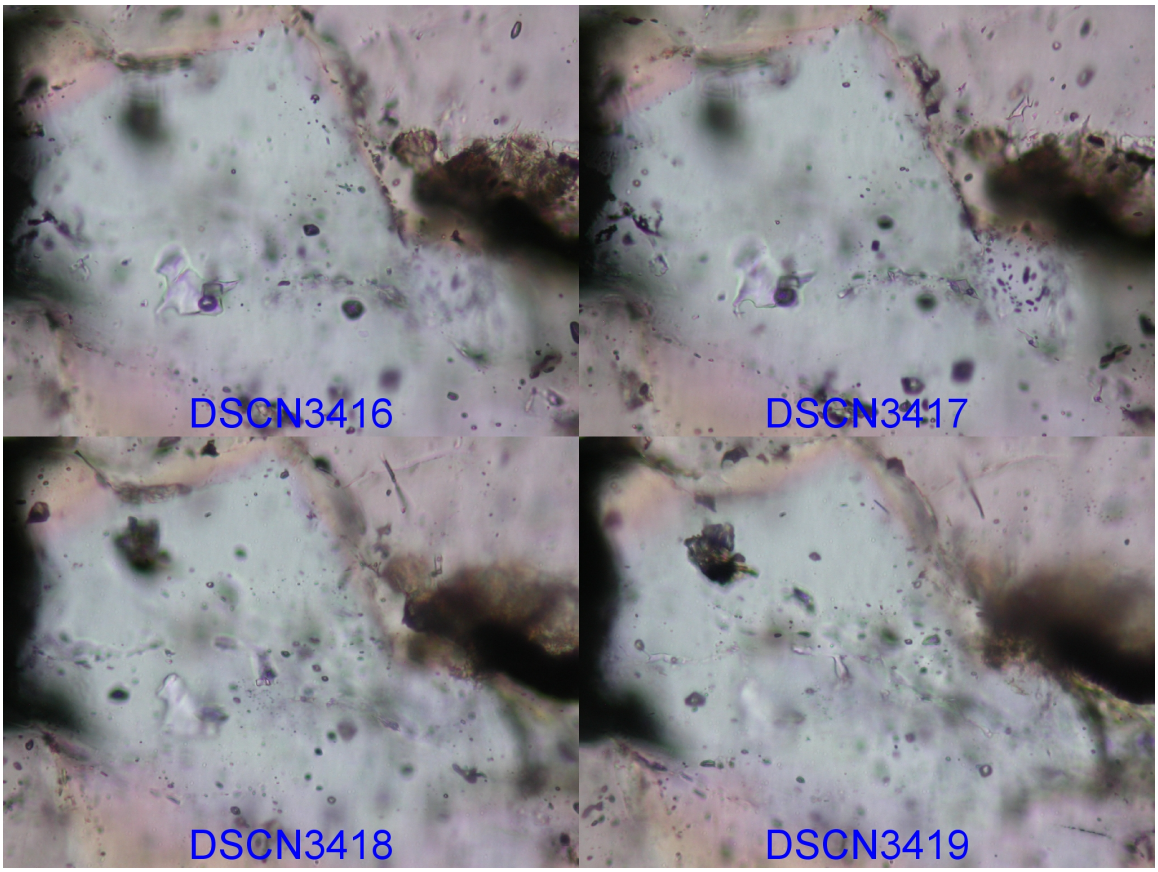
DSCN3416
DSCN3417
DSCN3418
DSCN3419

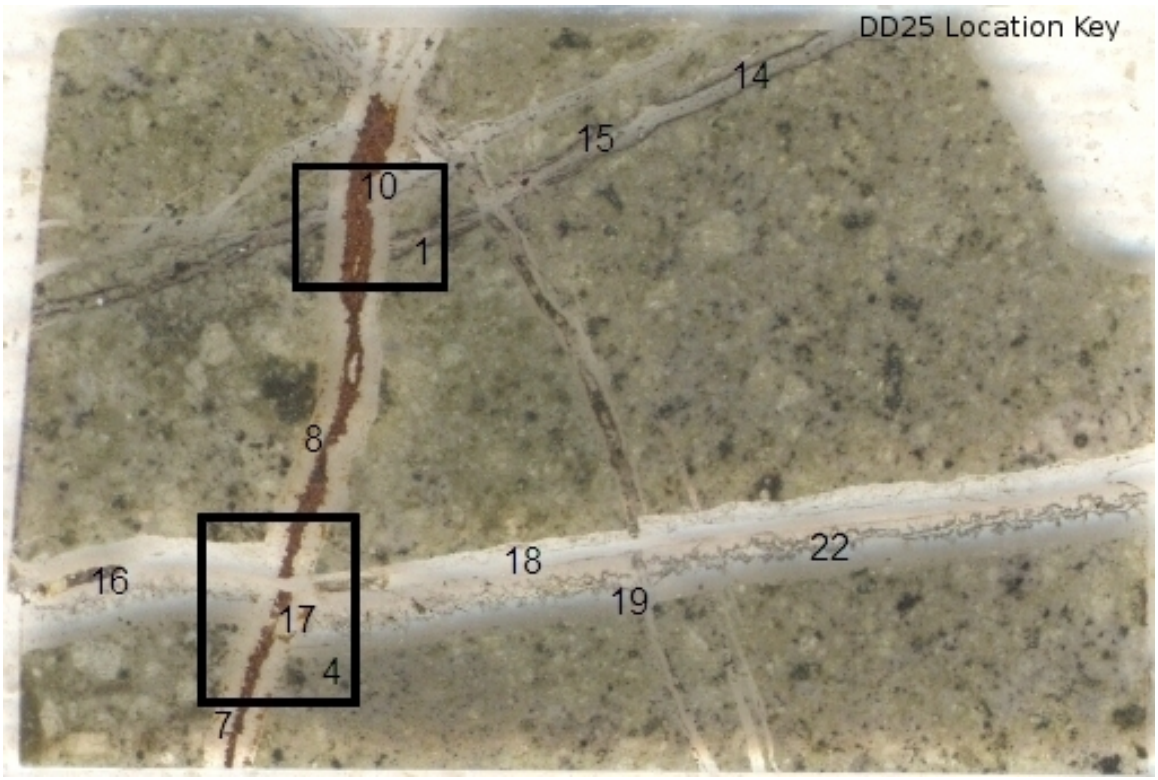

DSC 4x 1 mm | DSC 20x 200 microns | DSC 40x 100 microns | DSCN 20x 100 microns | DSCN 40x 50 microns

DD25 Photomicrographs: Photomicrographs were taken at the location shown on the DD25 Location Key, above. The photomicrographs are centered at approximately the center of the integer that corresponds to the location of each image. The fluid inclusion plate was approximately 2x3.6 cm (field of view above), and were 125 microns thick. Due to the thick nature of these sections, many photomicrographs may be taken in the same location of at a different focal depth, bringing fluid inclusions from different depths into focus. The scale bars correspond to images by image prefix and the objective used. Location 1 and 4 are denoted by the black rectangle to show the approximate field of view in the less magnified images. Photomicrographs at greater magnifications are shown as only a number. (3803) Transmitted light image of location 1 (4x). (3808) Reflected light image of area 1. Note the texturally interesting opaque vein center (4x). (3813) Transmitted light photomicrograph of a vein intersection, taken at area 4 (4x). (3833) Crossed Polarized image of location 4. Notice the change in quartz texture between the veins (4x). (3834) One of the few large fluid inclusions found in these samples. Inclusions of this shape were prone to decrepitation during microthermometry. Taken at area 7 (20x). (3835, 3836,3842) Large fluid inclusions in the same location as 3834. Note that the large primary(?) inclusions are split by a trail of much smaller secondary inclusions. Primary inclusions associated with small secondary inclusions often resulted in extremely convoluted LA-ICP-MS data, as ablation of small inclusions

around the larger primary inclusion was often not possible (40x). (3846, 3849, 3850, 3851, 3853) Fluid inclusions found at location 8. The large inclusions near vein center appear to have occurred post-flashing, as slight dark bands may be observed along the vein walls as brown “smudges.” The black to brown shapes along the right side of the vein are late opaque minerals, frequently oxidized in shallower samples such as this one (20x). (3860, 3861, 3862, 3863) Photomicrographs from area 10 showing dark band along vein wall (20x). (3872, 3873) Dark bands at location 14. Note the heavy dark bands at vein walls, with lesser dark quartz banded to sub-banded towards the vein center (20x). (3875) Repeating dark and light quartz taken at location 15 (20x). (3877, 3878, 3879) Convoluted fluid inclusion assemblages at location 16. Many secondary trails are clearly visible cutting across the crystals (20x). (3893, 3894, 3896, 3897) A secondary fluid inclusion assemblage at 17 shows liquid, vapor and daughter inclusions can be seen tracing an inclined fracture. Each frame is focused deeper through the sample (40x). (3900, 3901, 3902) A primary fluid inclusion assemblage at 18 contains liquid plus vapor inclusions (20x). (3903, 3904) Nebular dark quartz at 19 (20x). (3911, 3912) Primary (?) inclusions containing liquid and vapor phases (20x). (3914) Two dark bands run left-right across the photomicrograph at location 22 (20x). When compared to the reflected light image of the same location and field of view (3917), the dark bands remain visible as a darker shade of brown, and contain most of the highly reflective mineral phases (20x).

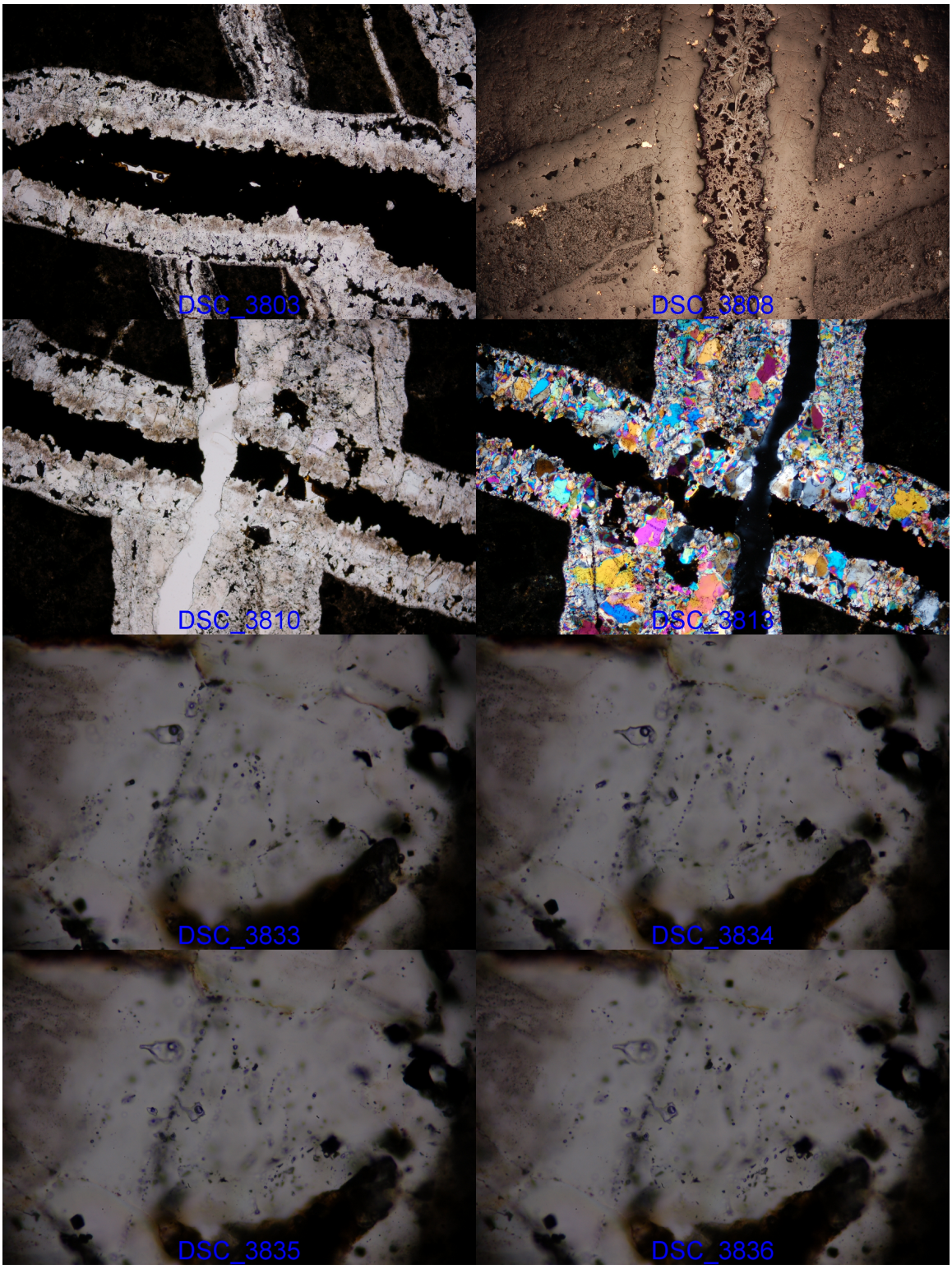
DSC_3803
DSC_3808
DSC_3810
DSC_3813
DSC_3833
DSC_3834
DSC_3835
DSC_3836

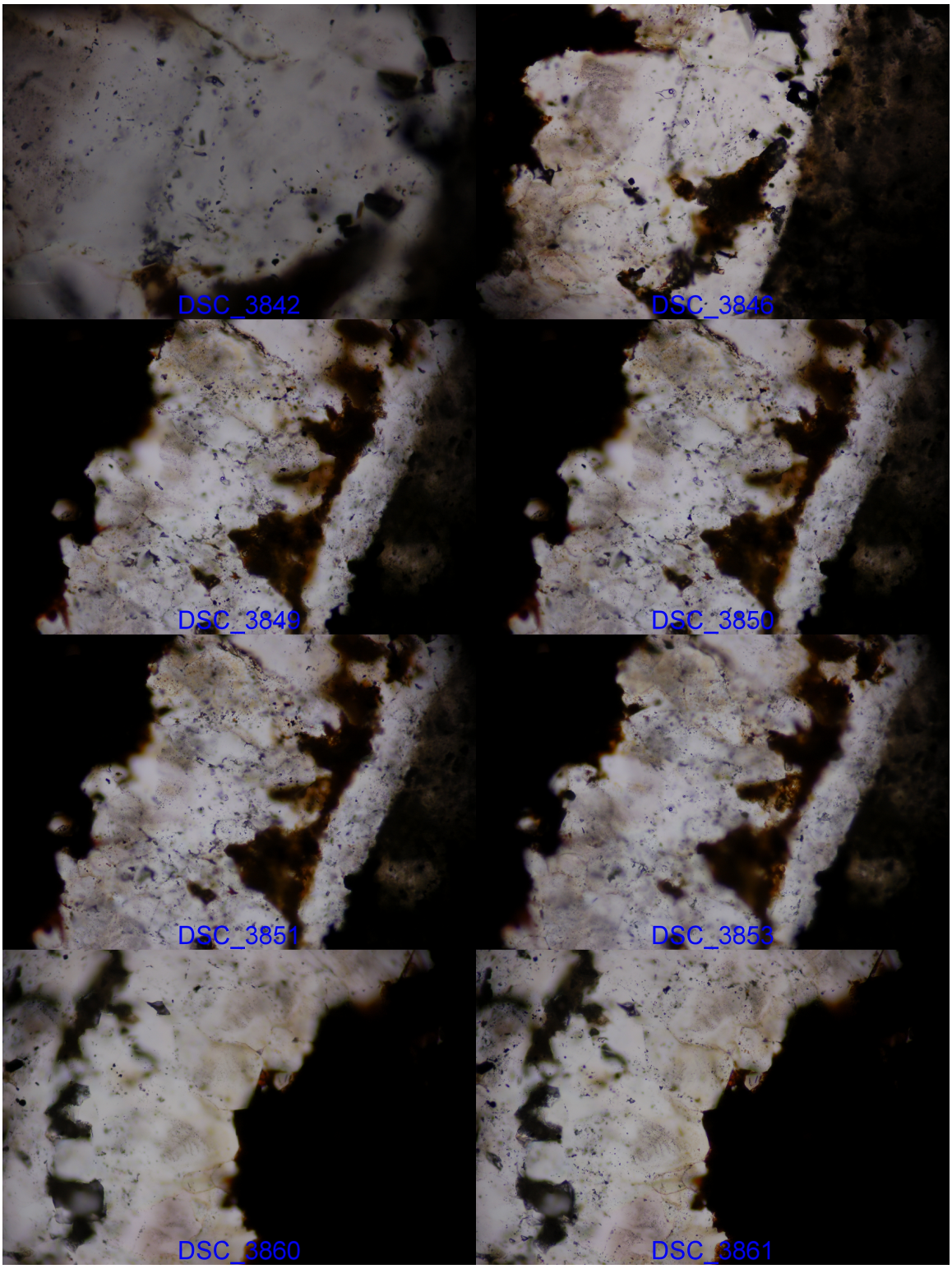
DSC_3842
DSC_3846
DSC_3849
DSC_3850
DSC_3851
DSC_3853
DSC_3860
DSC_3861

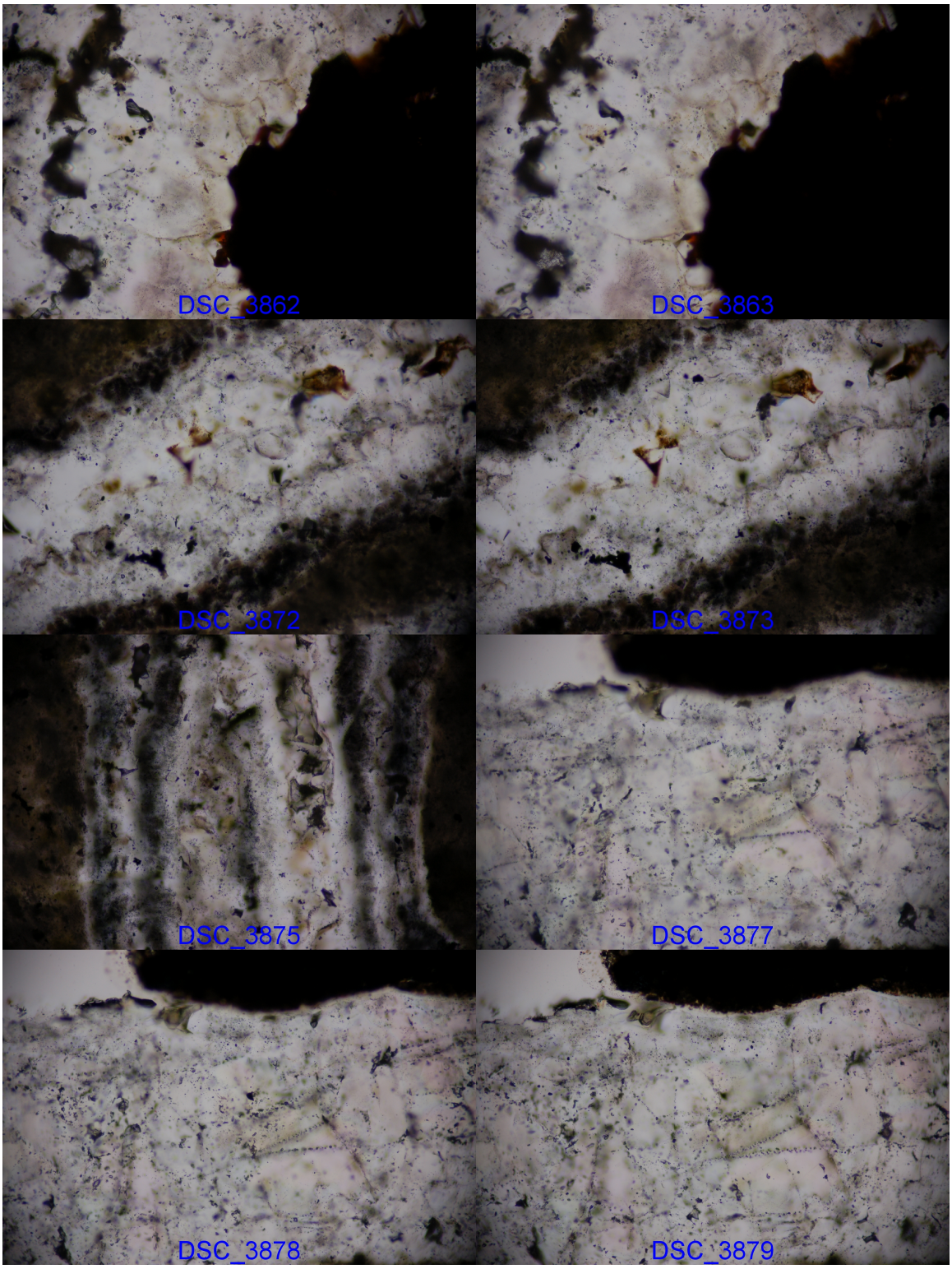
DSC_3862
DSC_3863
DSC_3872
DSC_3873
DSC_3875
DSC_3877
DSC_3878
DSC_3879

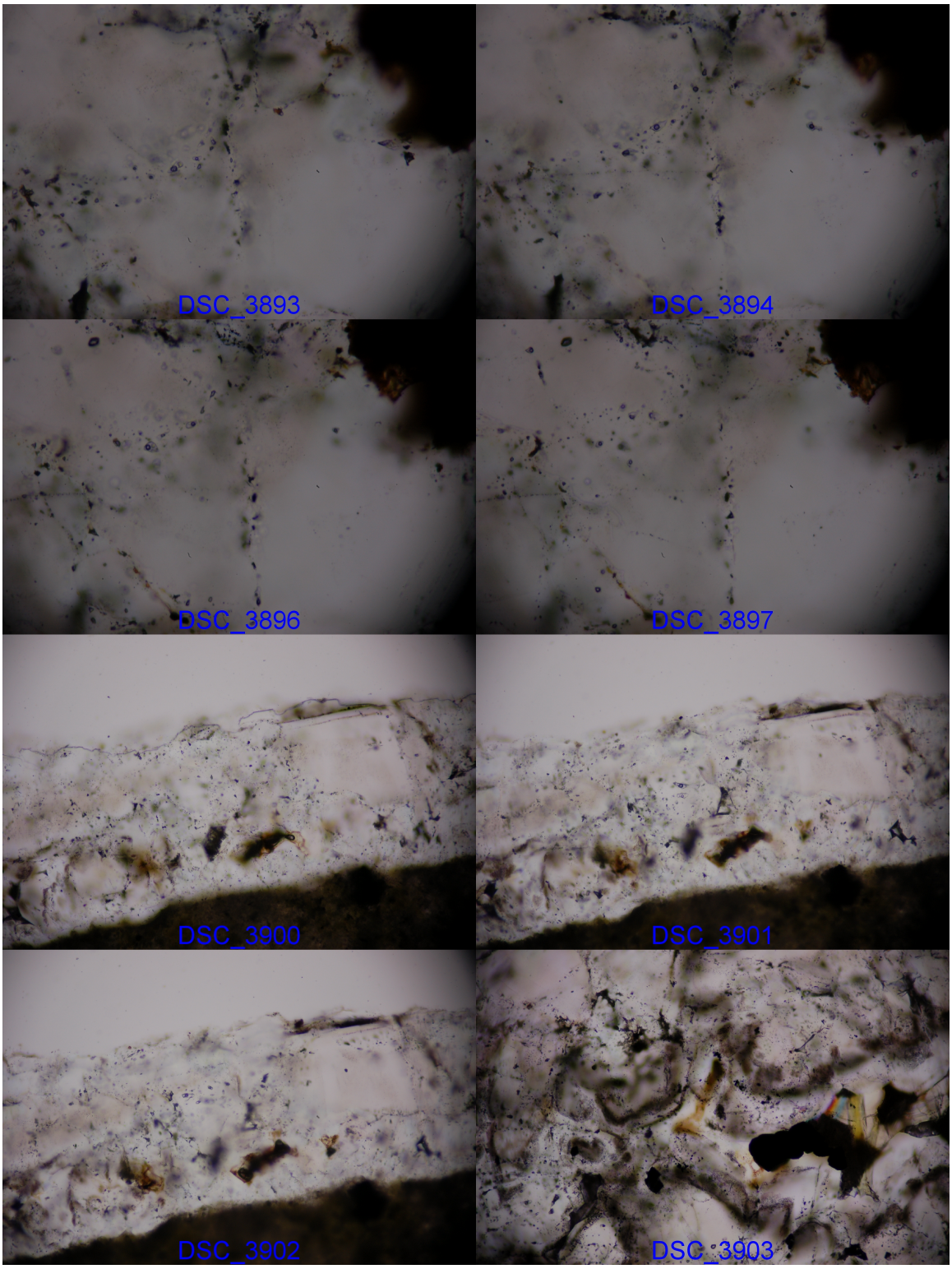
DSC_3893
DSC_3894
DSC_3896
DSC_3897
DSC_3900
DSC_3901
DSC_3902
DSC_3903

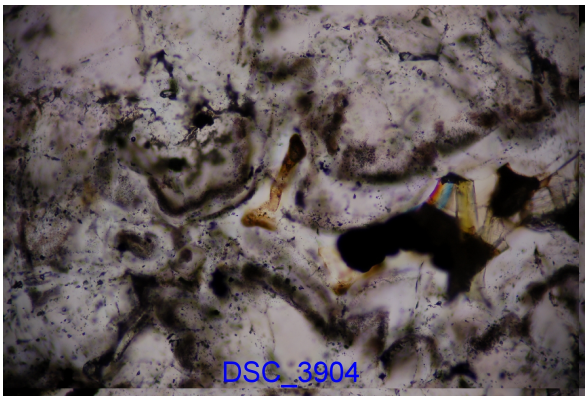
DSC_3904

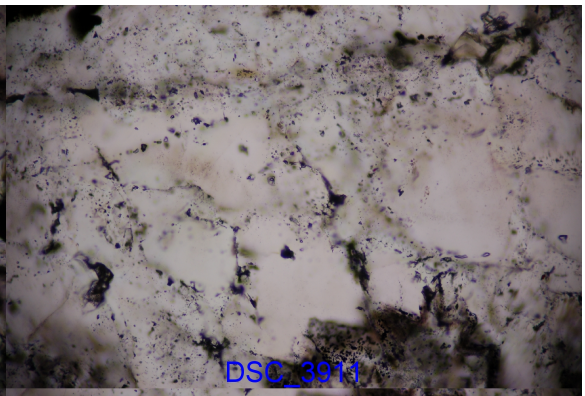
DSC_3911

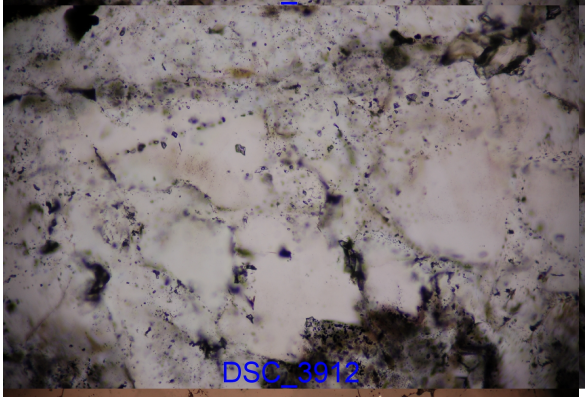
DSC_3912

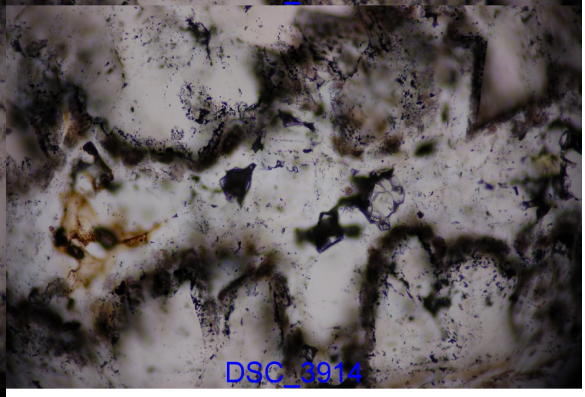
DSC_3914

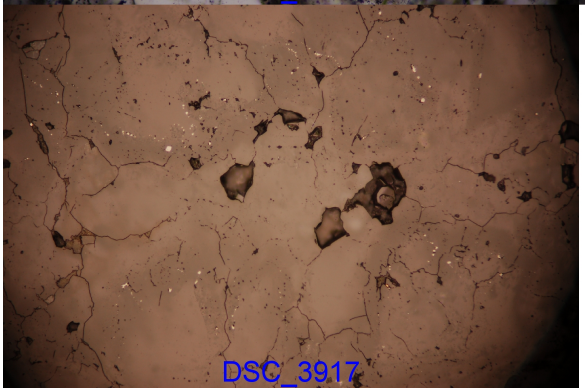
DSC_3917

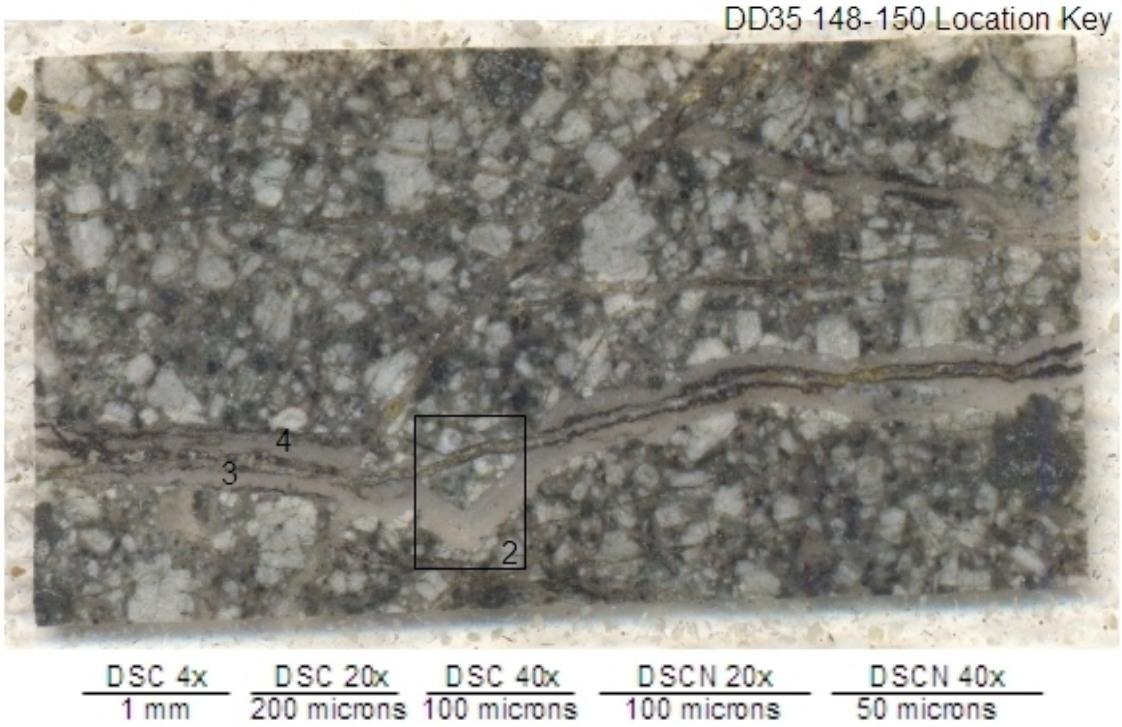

DD35 photomicrographs: Photomicrographs were taken at the location shown on the DD35 Location Key, above. The photomicrographs are centered at approximately the center of the integer that corresponds to the location of each image, except image location 2, which is denoted by the rectangle. The fluid inclusion plate was approximately 2x3.6 cm (field of view above), and were 125 microns thick. Due to the thick nature of these sections, many photomicrographs may be taken in the same location of at a different focal depth, bringing fluid inclusions from different depths into focus. The scale bars correspond to images by image prefix (i.e. DSC) and the objective used. (4173) Banded texture, location 2 (10x). (4175, 4176) Low salinity LV inclusions hosted in calcite, location 3 (20x). (4178-4182) Small inclusions in dark quartz, location 4 (20x).

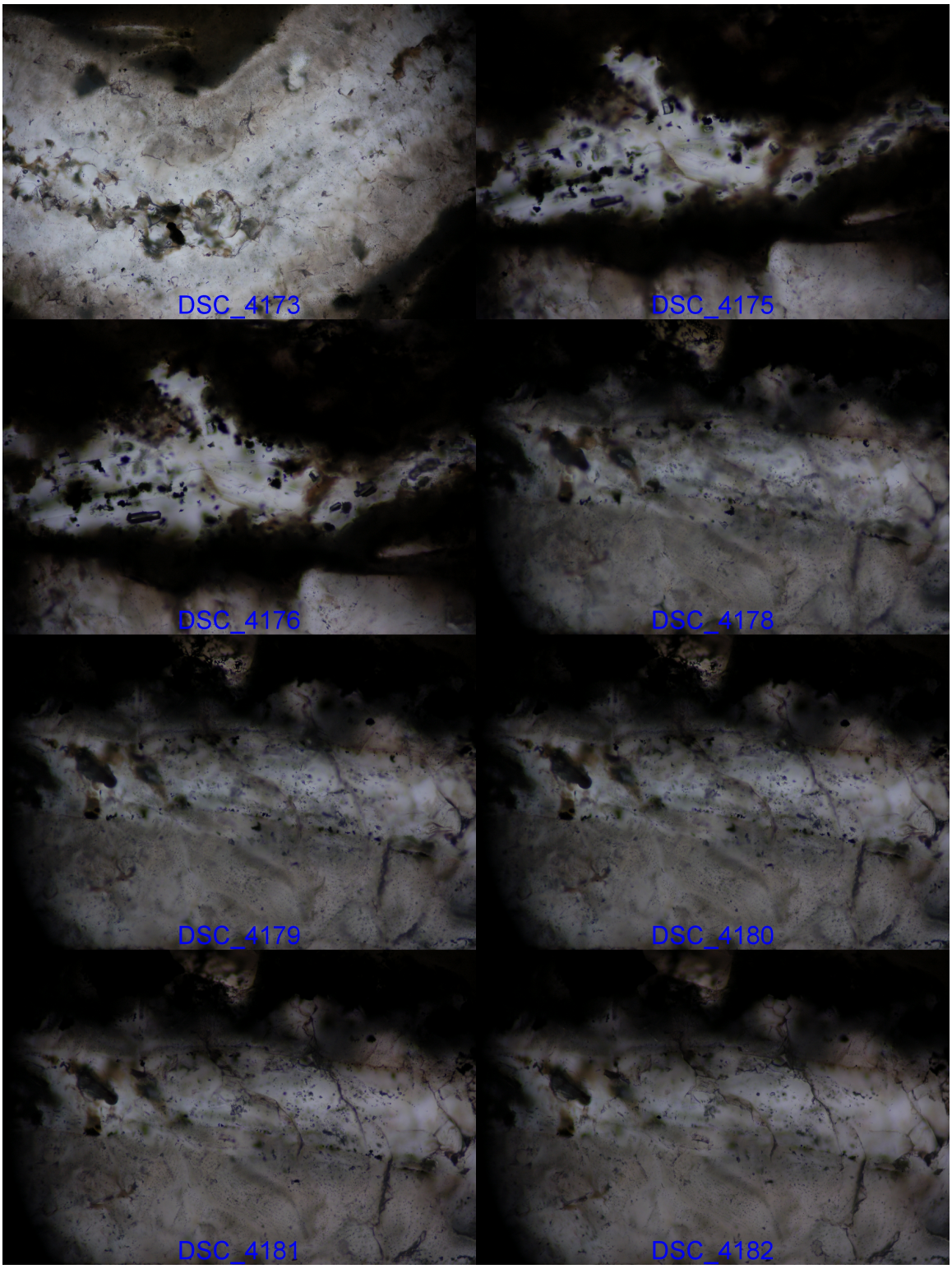
DSC_4173
DSC_4175
DSC_4176
DSC_4178
DSC_4179
DSC_4180
DSC_4181
DSC_4182

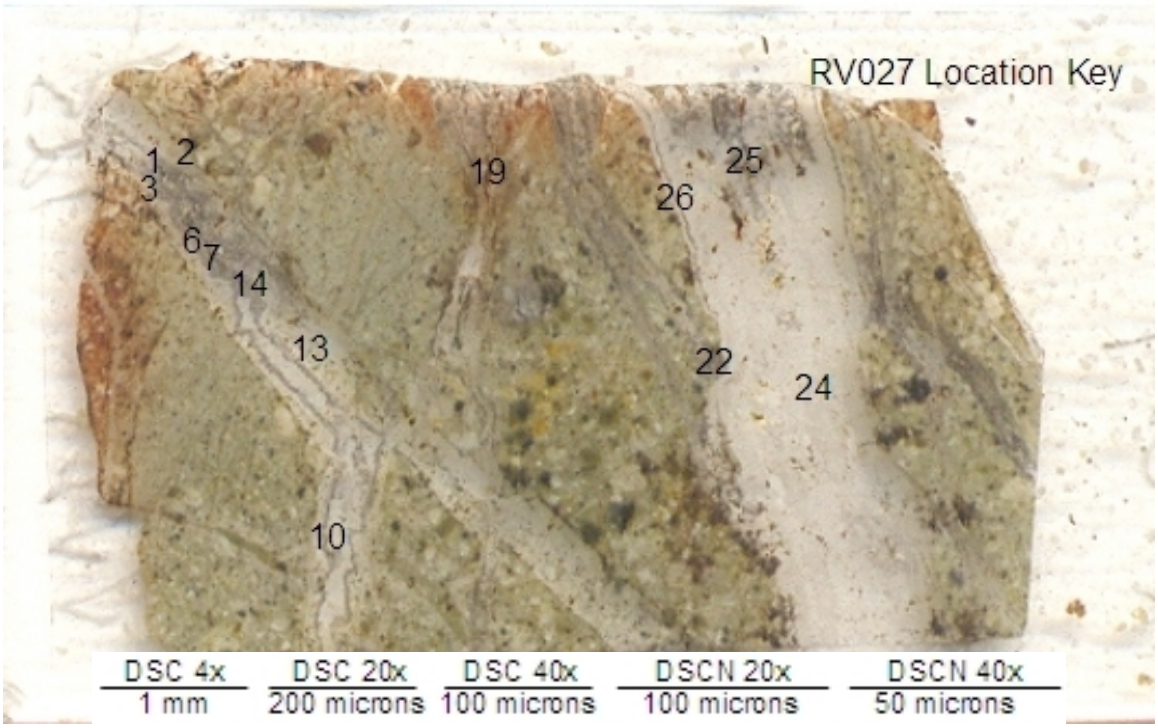

RV027 photomicrographs were taken at the location shown on the RV027 Location Key, above. The photomicrographs are centered at approximately the center of the integer that corresponds to the location of each image. The fluid inclusion plate was approximately 2x3.6 cm (field of view above), and were 125 microns thick. Due to the thick nature of these sections, many photomicrographs may be taken in the same location of at a different focal depth, bringing fluid inclusions from different depths into focus. The scale bars correspond to images by image prefix and the objective used. The focal length of images prefixed as "DSC" was fixed. "DCSN" images did not have a fixed focal length, but were all taken with the camera fully zoomed, making the scale fixed based on objective. (3463, 3464) Dark crystal core with large V inclusions, rimmed by a haze of small inclusions, location 1 (20x). (3468-3470) Dark V inclusions with interspersed LV unknown inclusions, location 2 (20x) SCALE(3469). (3473, 3474, 3476) Primary V inclusions showing growth zones, location 3 (20x). (3482) LVD inclusion in banded vein, location 6 (20x). (3486-3489) V inclusions, showing dark core, growth zones and cigar inclusions, location 7 (20x). (3736) V inclusions capped by growth zones, location 10 (20x). (3746-3748) Growth zones in single crystal within dark band, location 13 (20x). (3749-3751) Dark quartz core, location 14 (20x). (3766-3768) Vug filling post-banding quartz with LV inclusions, location 19 (20x). (3779-3780) Complex dark quartz, location 22 (10x). (3788, 3789) Elongated inclusions, location 24 (20x). (3790-3792) Dark quartz, location 25 (20x). (3793, 3794) Dark quartz, location 25 (10x). (3795) Dark quartz, location 25 (4x). (3796, 3797) A dark band parallels the vein wall in overall dark quartz, location26 (4x).

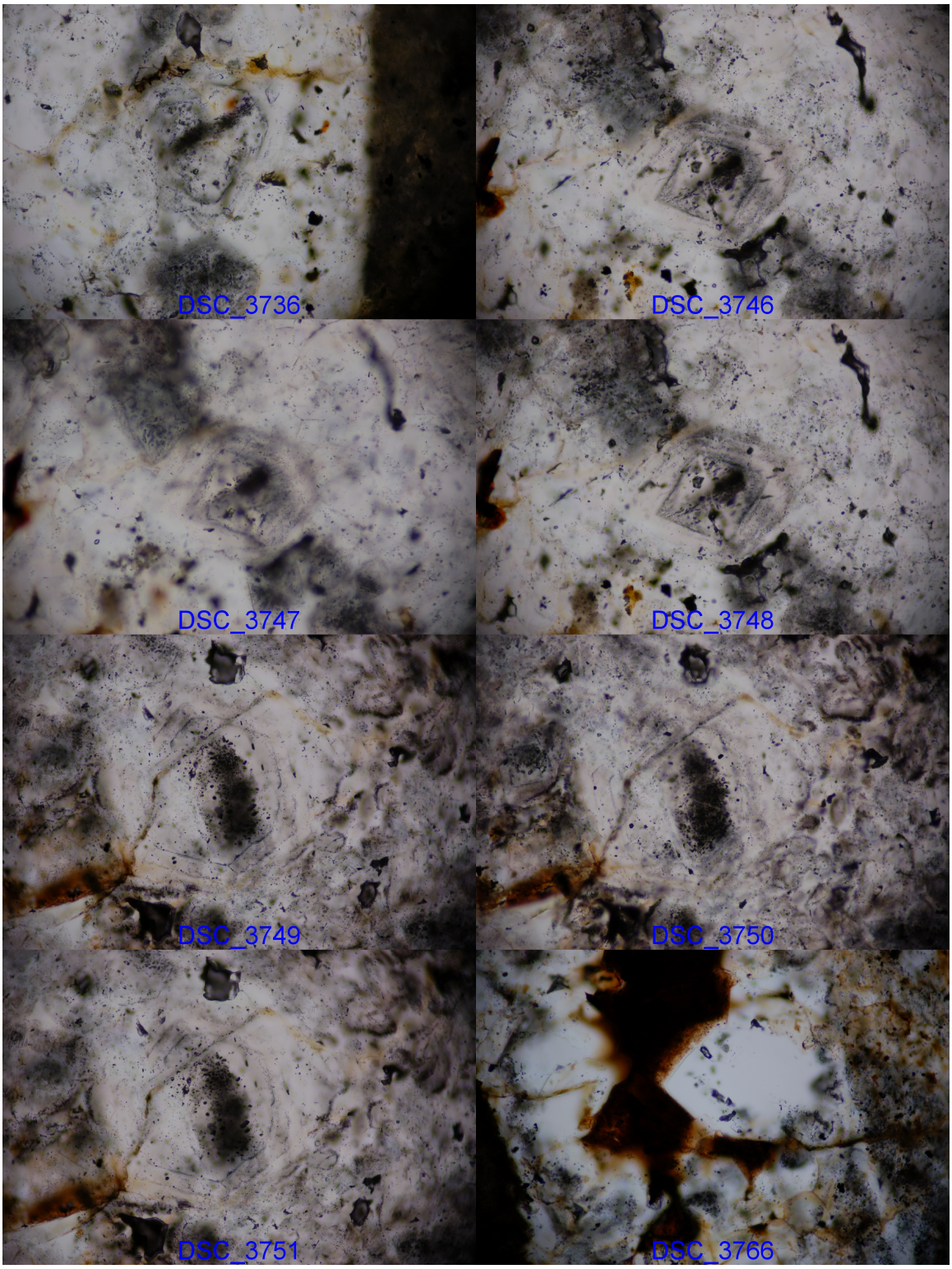
DSC_3736
DSC_3746
DSC_3747
DSC_3748
DSC_3749
DSC_3750
DSC_3751
DSC_3766

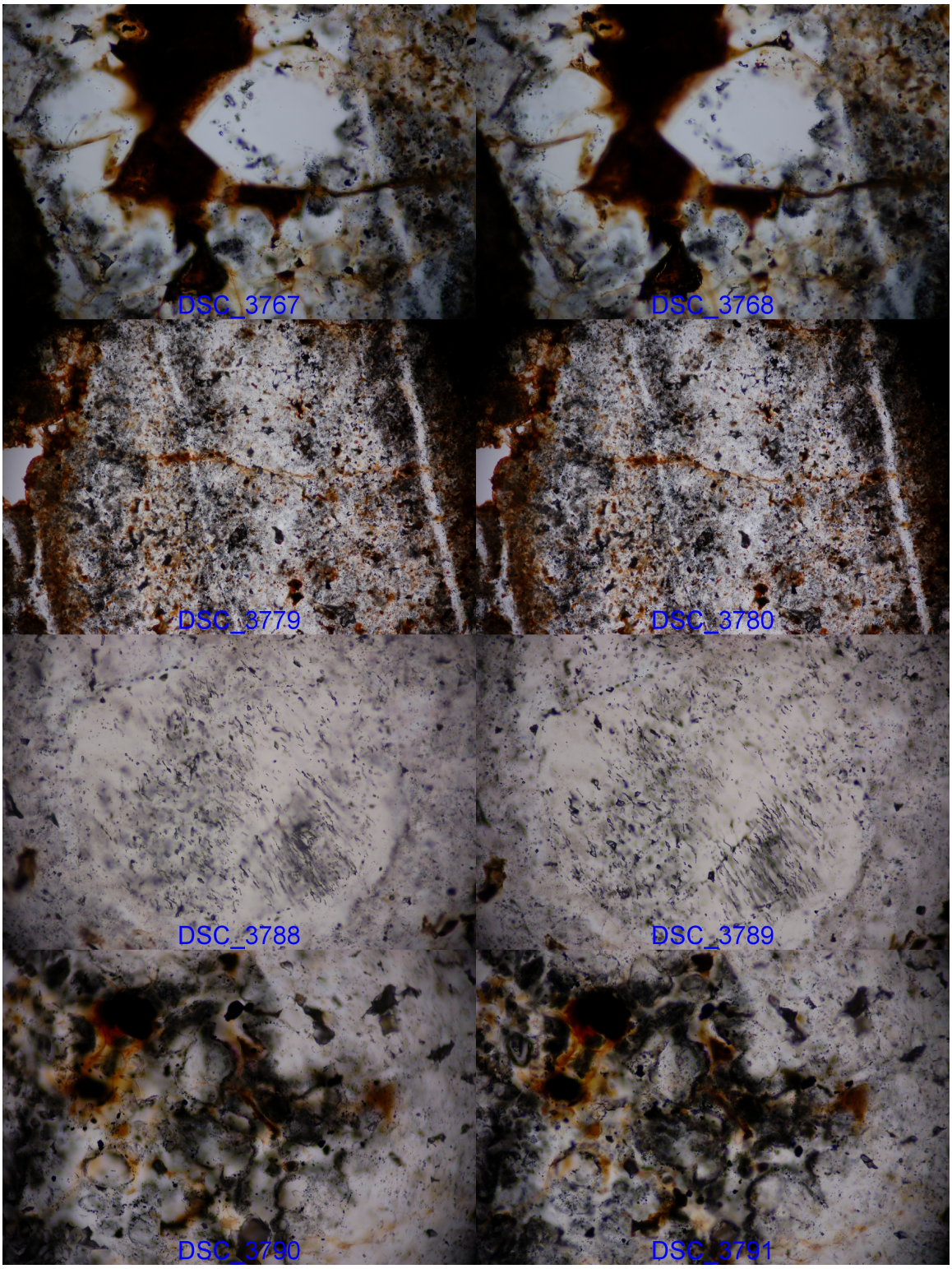
DSC_3767
DSC_3768
DSC_3779
DSC_3780
DSC_3788
DSC_3789
DSC_3790
DSC_3791

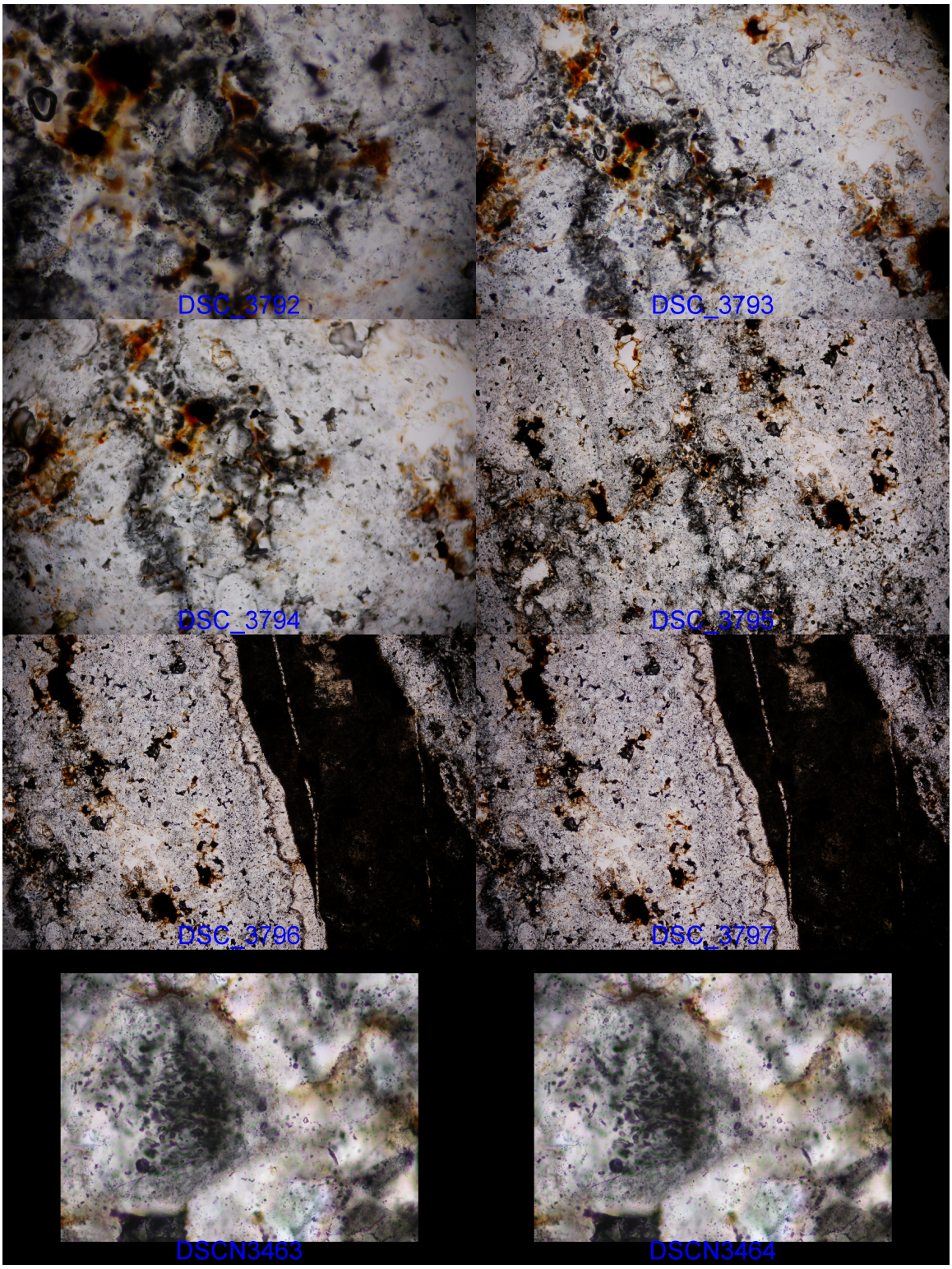
DSC_3792
DSC_3793
DSC_3794
DSC_3795
DSC_3796
DSC_3797
DSCN3463
DSCN3464

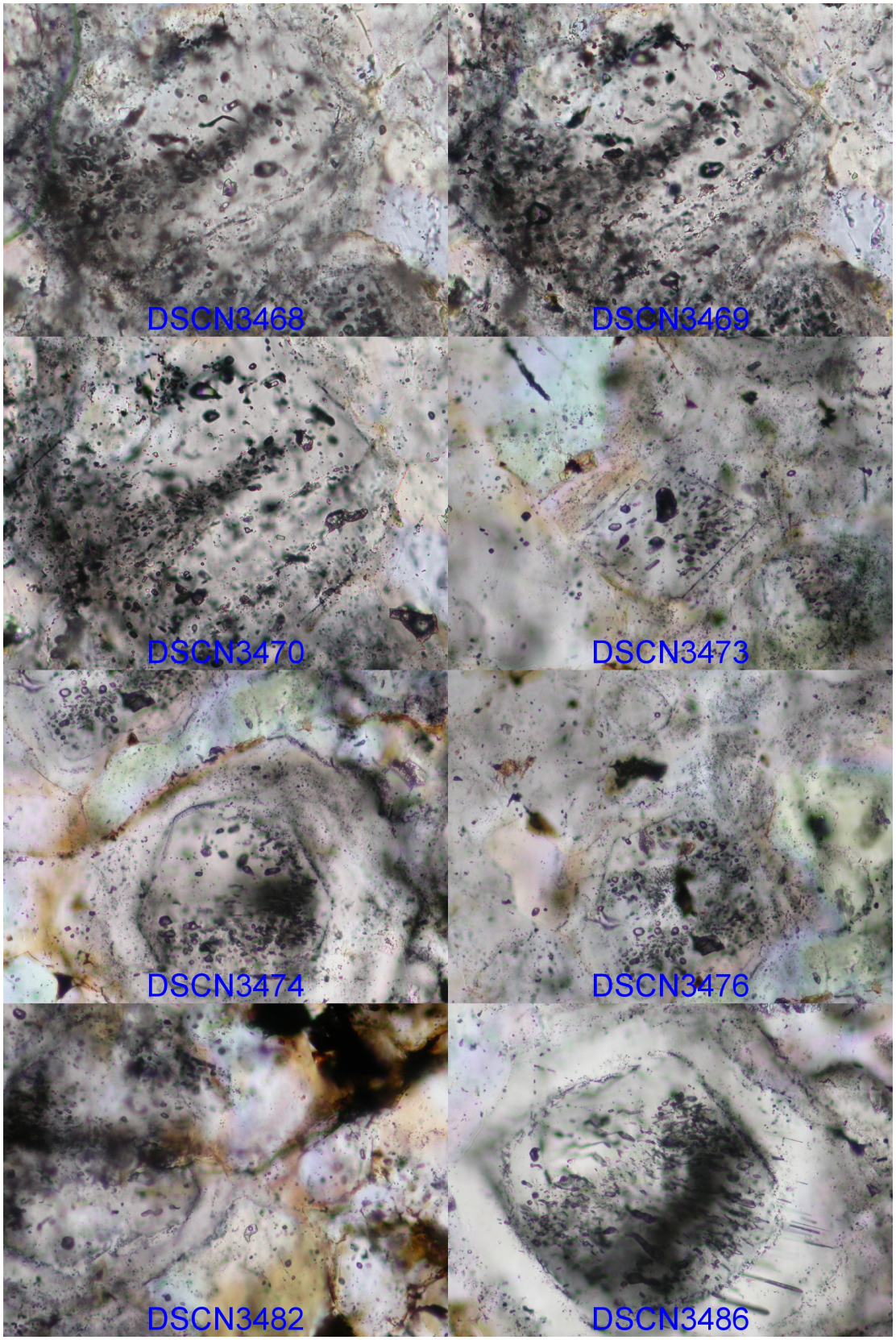
DSCN3468
DSCN3469
DSCN3470
DSCN3473
DSCN3474
DSCN3476
DSCN3482
DSCN3486

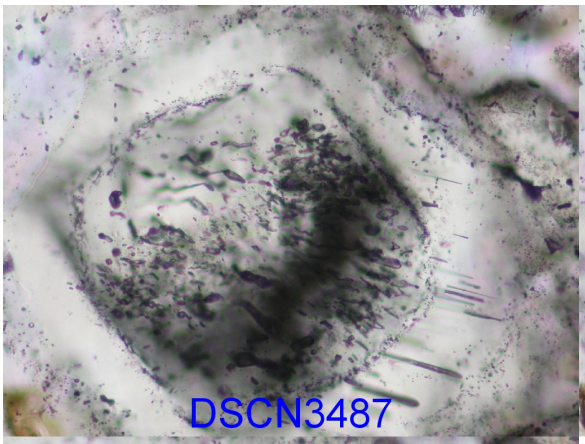
DSCN3487

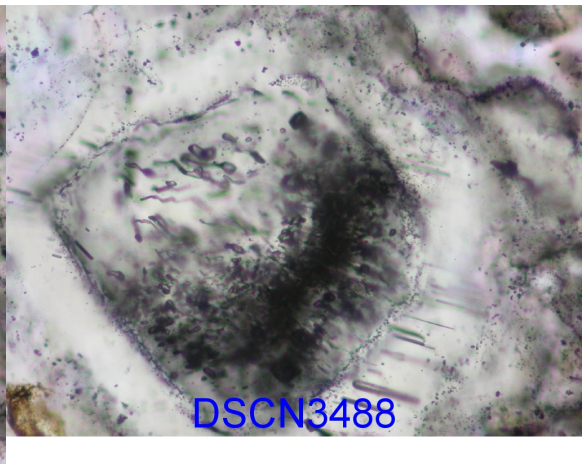
DSCN3488

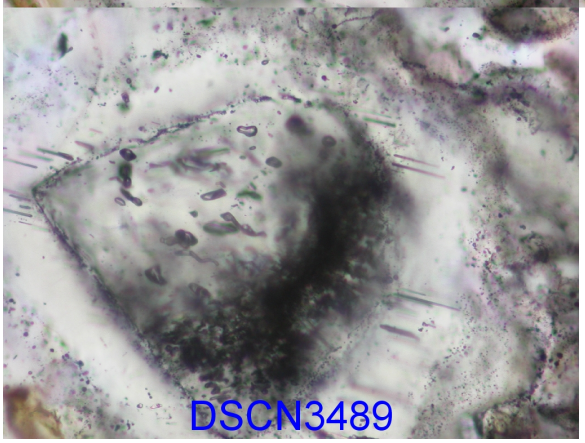
DSCN3489

Cathodoluminescence

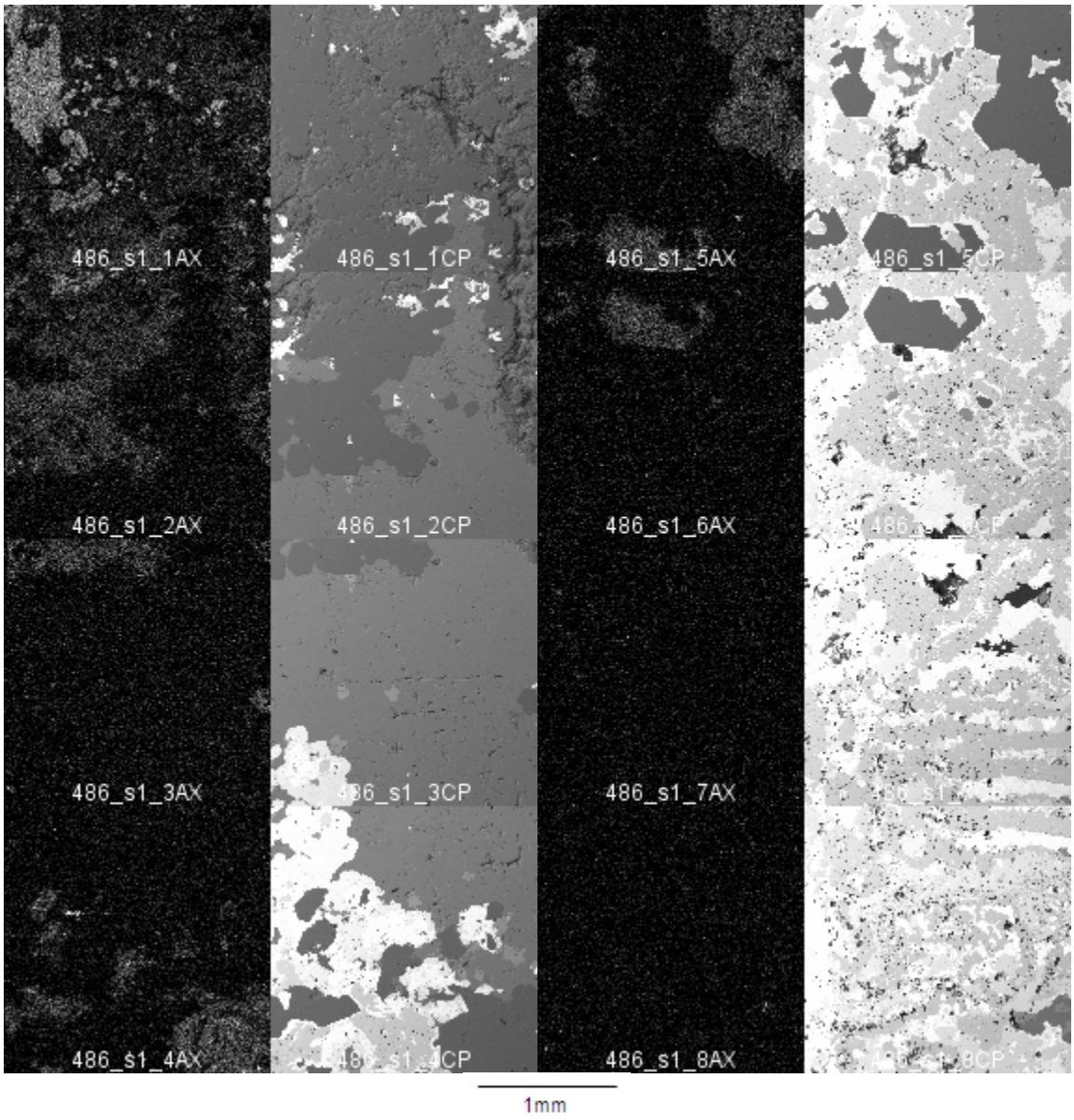

486 s1: EPMA images from sample 486, series 1. The suffix on the image name denotes the image in the series, and the image type, where AX are CL images and CP are back scattered electron images (BEI). CL images change grey intensity possibly owing to changes in the concentration of Al, Ti, K, or other elements causing shifts in the quartz lattice. CL activity in quartz may also be related to the conditions of formation, including temperature and pressure. Non-quartz phases appear either as black regions (sulfides) or as grey to bright white (CL active, non-quartz minerals). In BEI, more dense minerals appear brighter white, where quartz appears as a mid-grey and more dense minerals, e.g. sulfide minerals, appear as light grey or white.

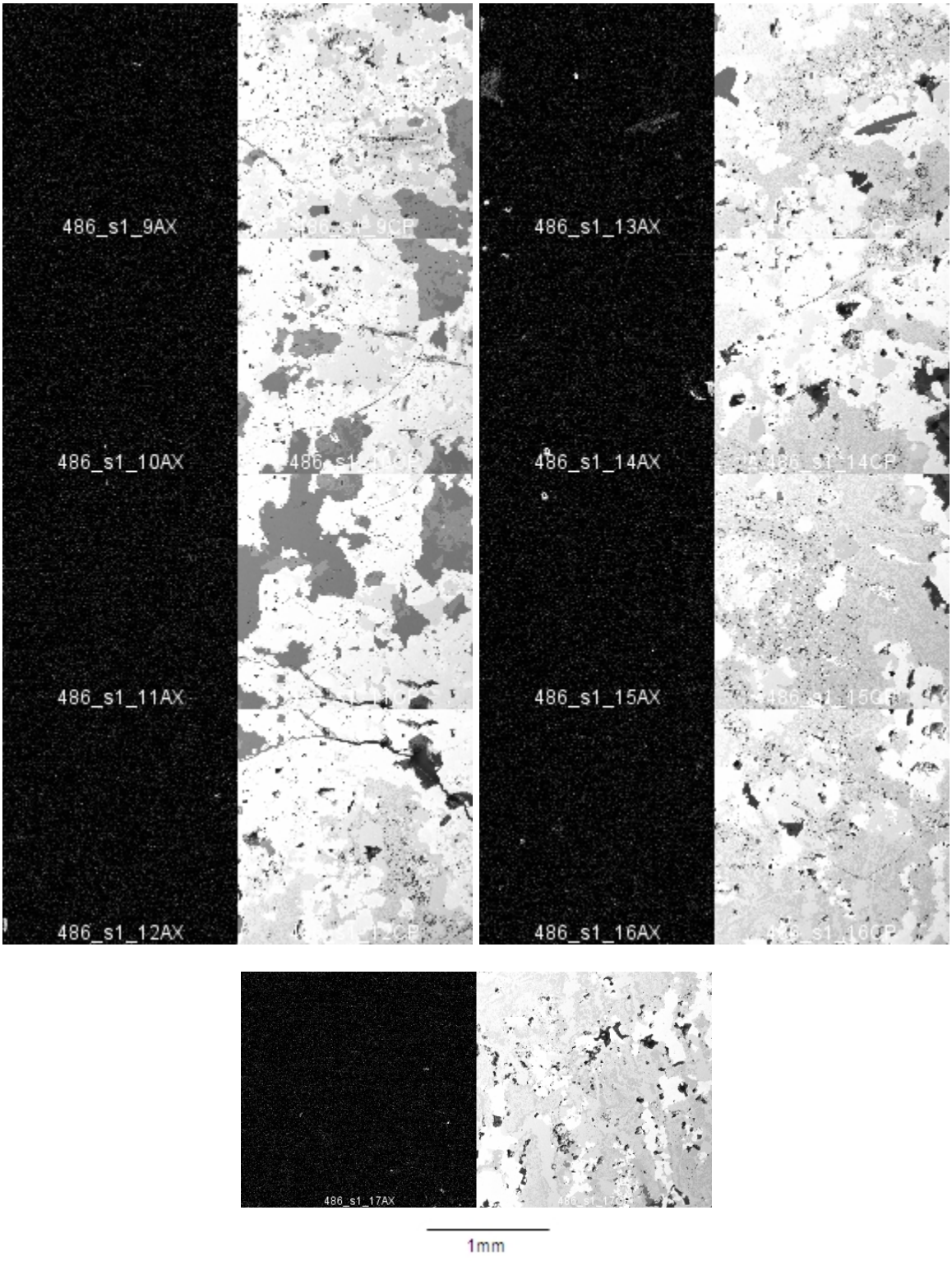
486_s1_9AX
486_s1_13AX
486_s1_10AX
486_s1_14AX
486_s1_11AX
486_s1_15AX
486_s1_12AX
486_s1_16AX
486_s1_17AX
1mm

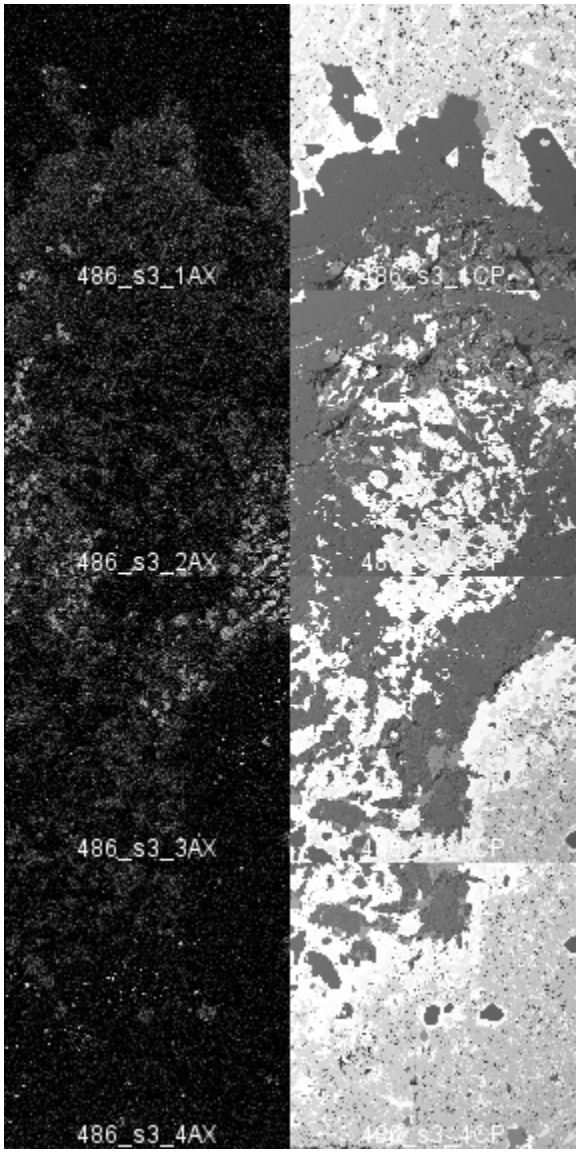

486 s3: EPMA images from sample 486, series 3. The suffix on the image name denotes the image in the series, and the image type, where AX are CL images and CP are back scattered electron images (BEI). CL images change grey intensity possibly owing to changes in the concentration of Al, Ti, K, or other elements causing shifts in the quartz lattice. CL activity in quartz may also be related to the conditions of formation, including temperature and pressure. Non-quartz phases appear either as black regions (sulfides) or as grey to bright white (CL active, non-quartz minerals). In BEI, more dense minerals appear brighter white, where quartz appears as a mid-grey and more dense minerals, e.g. sulfide minerals, appear as light grey or white.

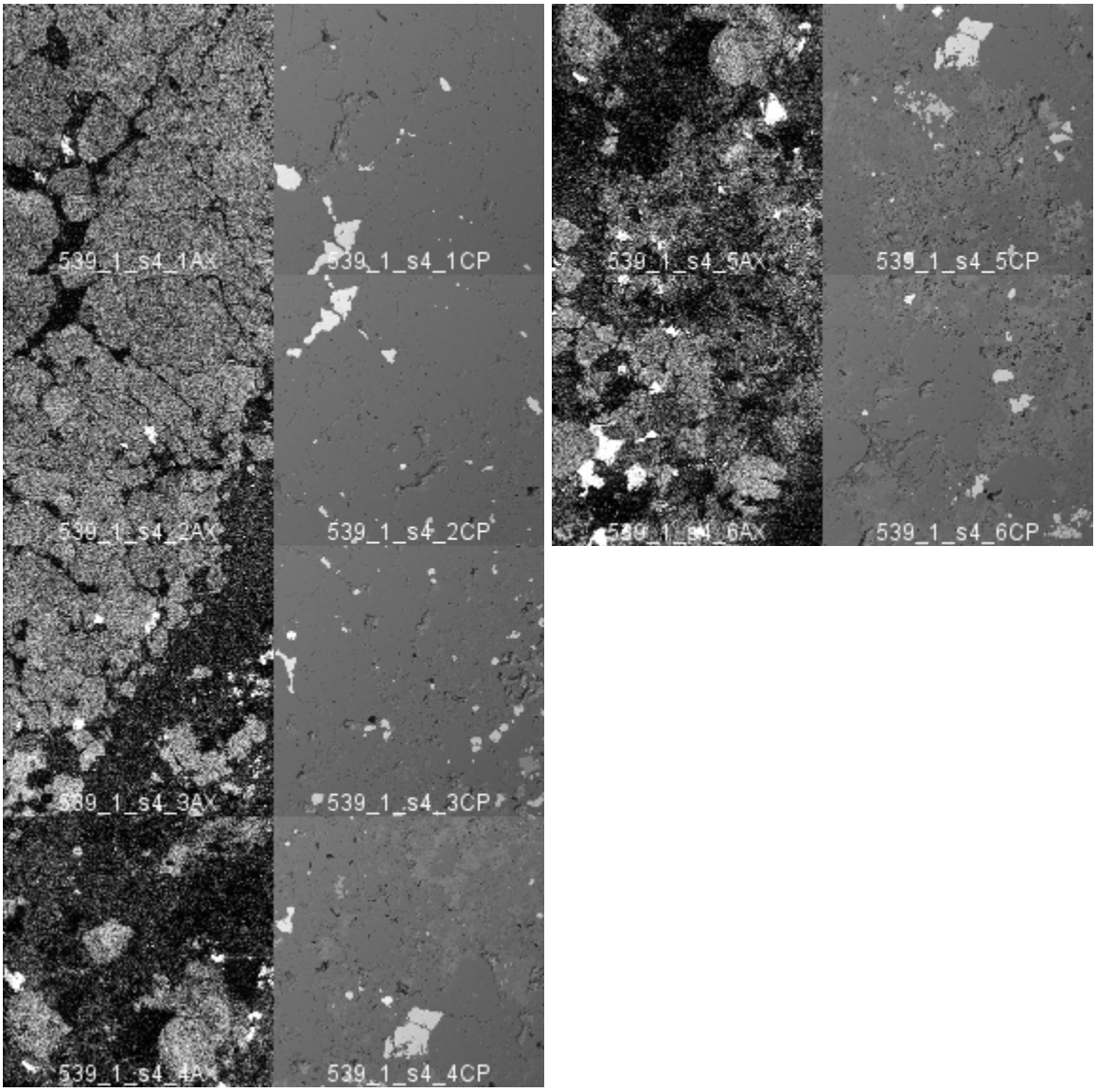

539_1 s4: EPMA images from sample 539_1, series 4. The suffix on the image name denotes the image in the series, and the image type, where AX are CL images and CP are back scattered electron images (BEI). CL images change grey intensity possibly owing to changes in the concentration of Al, Ti, K, or other elements causing shifts in the quartz lattice. CL activity in quartz may also be related to the conditions of formation, including temperature and pressure. Non-quartz phases appear either as black regions (sulfides) or as grey to bright white (CL active, non-quartz minerals). In BEI, more dense minerals appear brighter white, where quartz appears as a mid-grey and more dense minerals, e.g. sulfide minerals, appear as light grey or white.

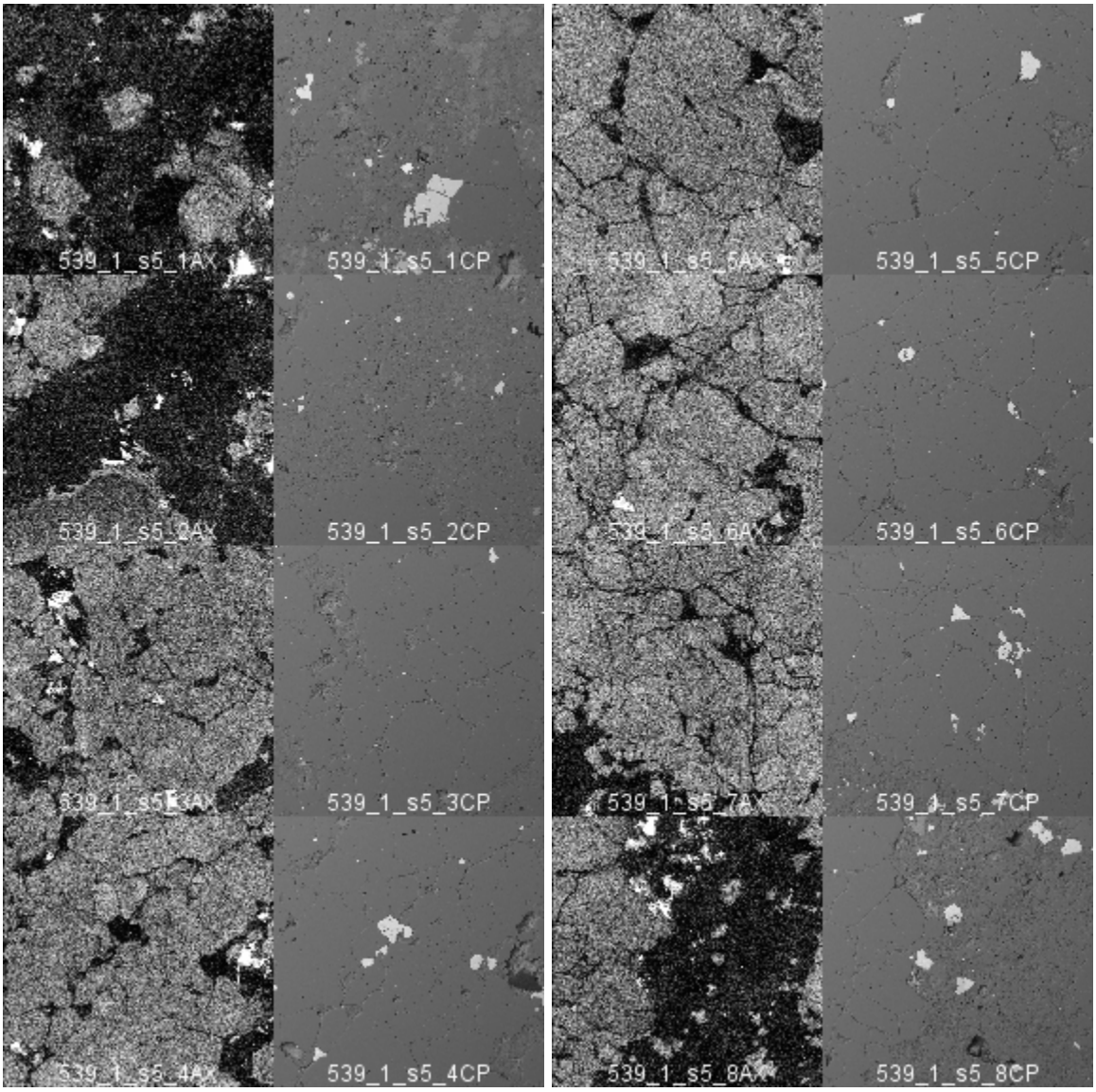

539_1 s5: EPMA images from sample 539_1, series 5. The suffix on the image name denotes the image in the series, and the image type, where AX are CL images and CP are back scattered electron images (BEI). CL images change grey intensity possibly owing to changes in the concentration of Al, Ti, K, or other elements causing shifts in the quartz lattice. CL activity in quartz may also be related to the conditions of formation, including temperature and pressure. Non-quartz phases appear either as black regions (sulfides) or as grey to bright white (CL active, non-quartz minerals). In BEI, more dense minerals appear brighter white, where quartz appears as a mid-grey and more dense minerals, e.g. sulfide minerals, appear as light grey or white.

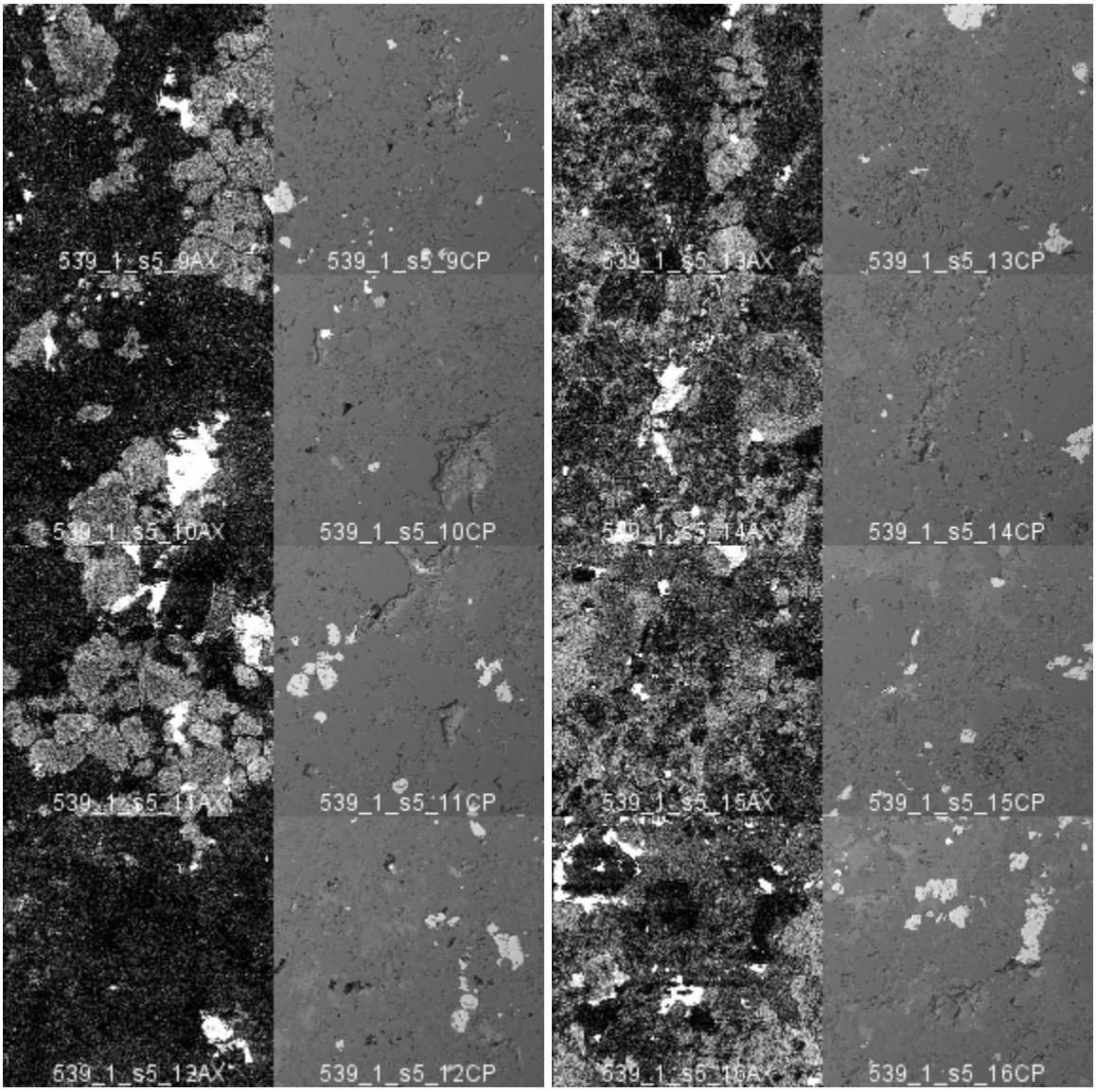
539_1_s5_9AX
539_1_s5_9CP
539_1_s5_13AX
539_1_s5_13CP
539_1_s5_10AX
539_1_s5_10CP
539_1_s5_14AX
539_1_s5_14CP
539_1_s5_11AX
539_1_s5_11CP
539_1_s5_15AX
539_1_s5_15CP
539_1_s5_12AX
539_1_s5_12CP
539_1_s5_16AX
539_1_s5_16CP
1mm

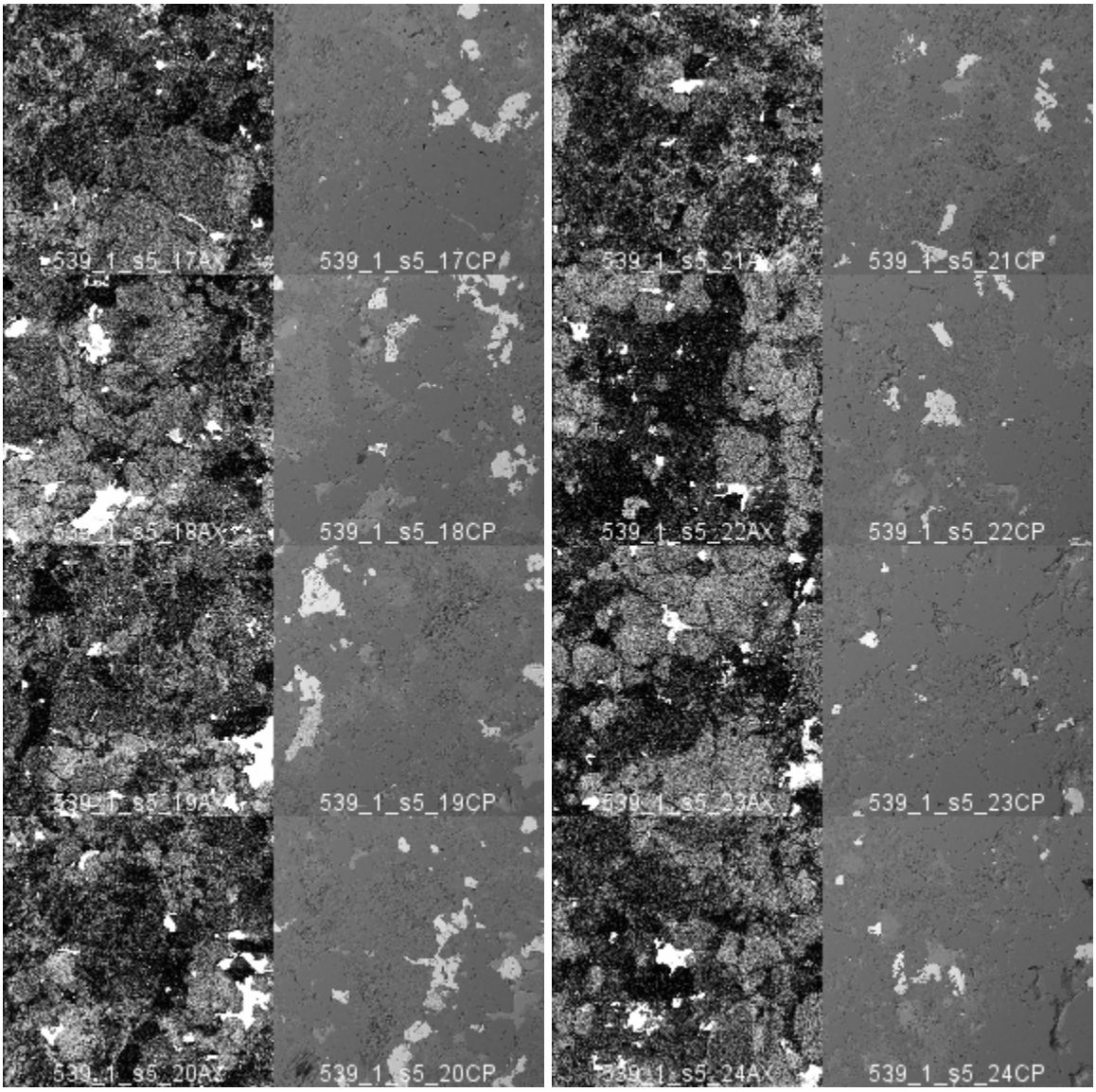
539_1_s5_17AX
539_1_s5_17CP
539_1_s5_18AX
539_1_s5_18CP
539_1_s5_19AX
539_1_s5_19CP
539_1_s5_20AX
539_1_s5_20CP
539_1_s5_21AX
539_1_s5_21CP
539_1_s5_22AX
539_1_s5_22CP
539_1_s5_23AX
539_1_s5_23CP
539_1_s5_24AX
539_1_s5_24CP
1mm

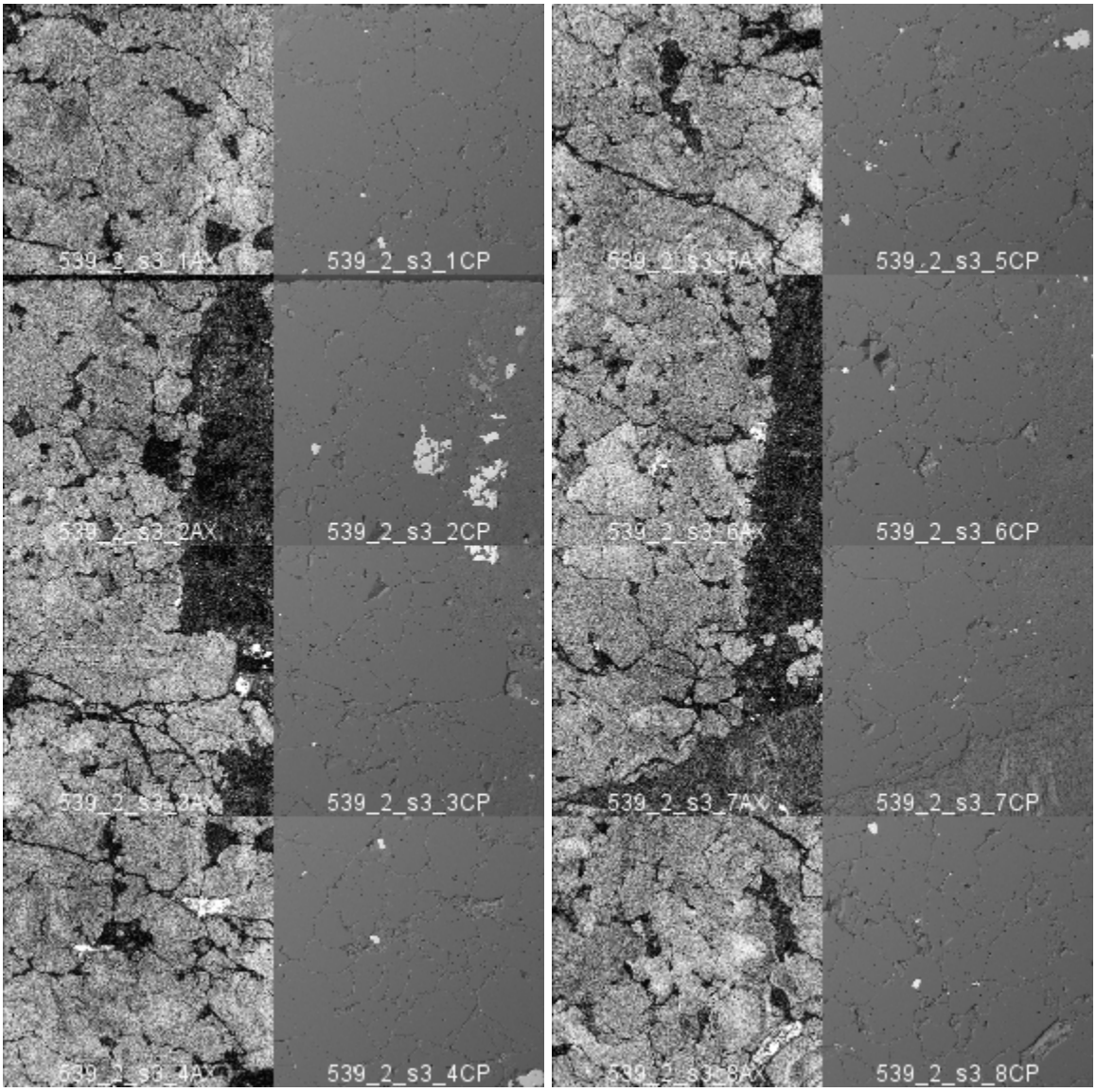

539_2 s3: EPMA images from sample 539_2, series 3. The suffix on the image name denotes the image in the series, and the image type, where AX are CL images and CP are back scattered electron images (BEI). CL images change grey intensity possibly owing to changes in the concentration of Al, Ti, K, or other elements causing shifts in the quartz lattice. CL activity in quartz may also be related to the conditions of formation, including temperature and pressure. Non-quartz phases appear either as black regions (sulfides) or as grey to bright white (CL active, non-quartz minerals). In BEI, more dense minerals appear brighter white, where quartz appears as a mid-grey and more dense minerals. Note the anhydrite vein marked by the shredded texture in both CL and BEI.

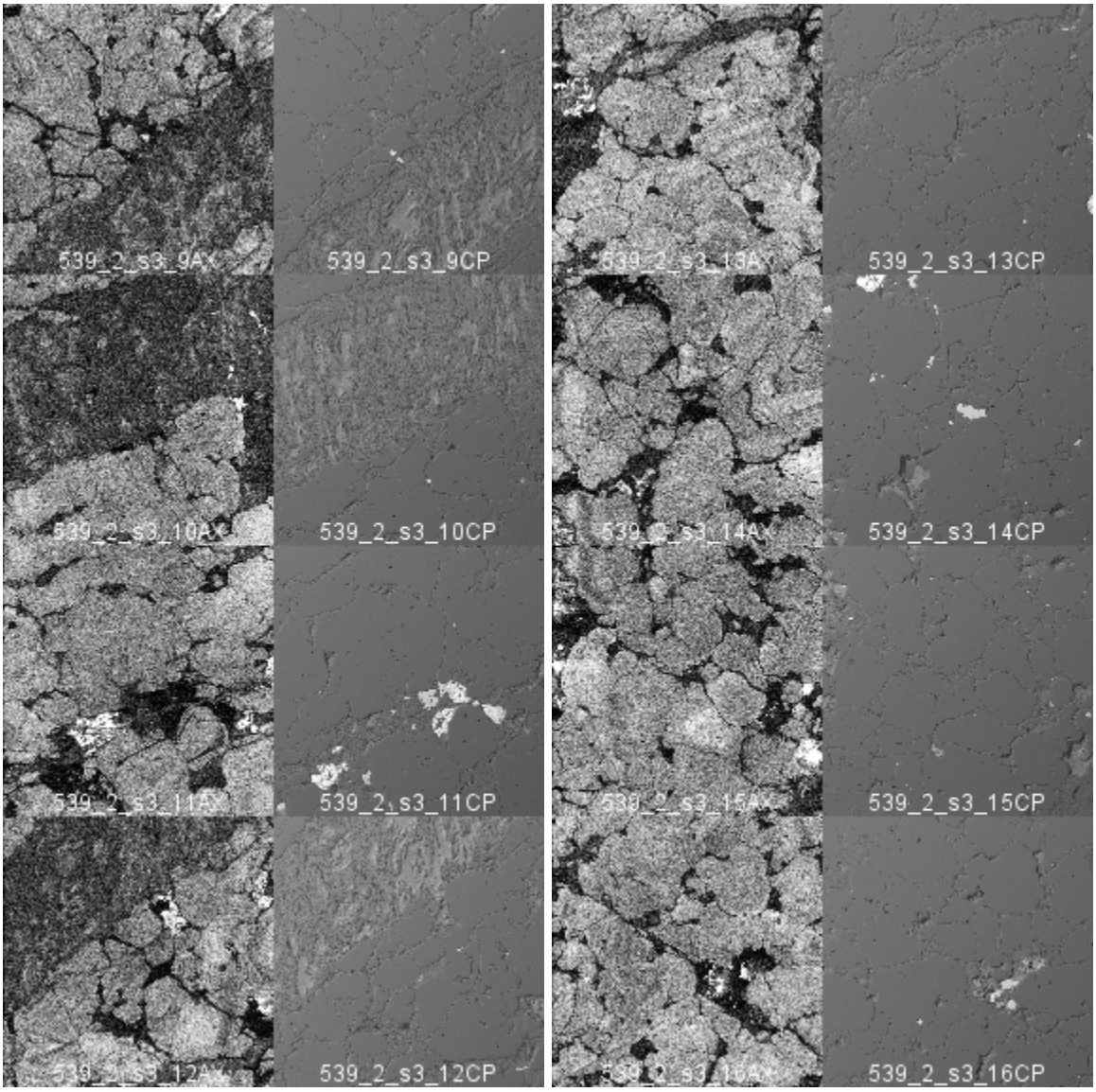
539_2_s3_9AX
539_2_s3_9CP
539_2_s3_13AX
539_2_s3_13CP
539_2_s3_10AX
539_2_s3_10CP
539_2_s3_14AX
539_2_s3_14CP
539_2_s3_11AX
539_2_s3_11CP
539_2_s3_15AX
539_2_s3_15CP
539_2_s3_12AX
539_2_s3_12CP
539_2_s3_16AX
539_2_s3_16CP
1mm

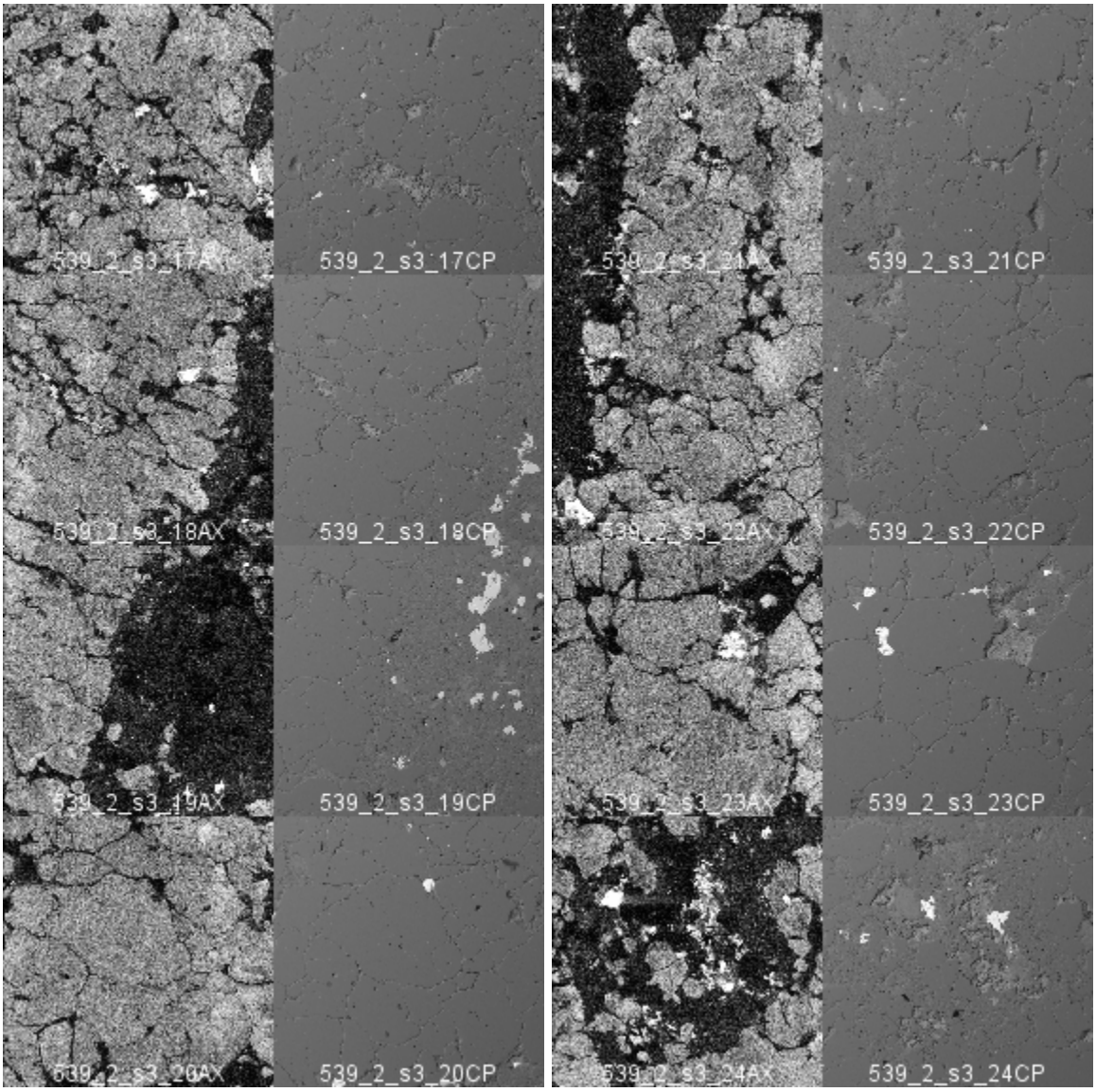
539_2_s3_17CP
539_2_s3_18AX
539_2_s3_18CP
539_2_s3_19AX
539_2_s3_19CP
539_2_s3_20AX
539_2_s3_20CP
539_2_s3_21CP
539_2_s3_22AX
539_2_s3_22CP
539_2_s3_23AX
539_2_s3_23CP
539_2_s3_24AX
539_2_s3_24CP
1mm

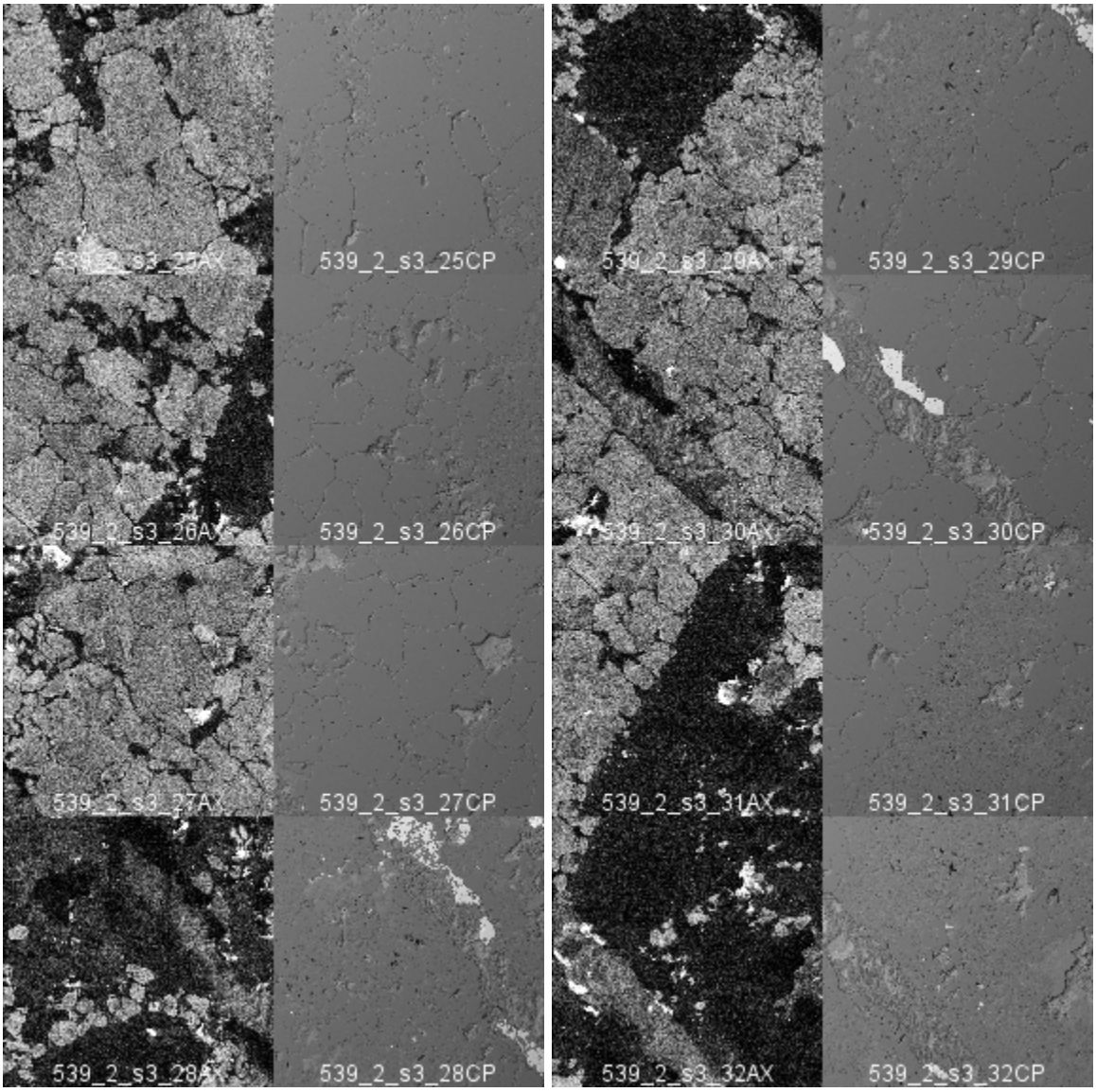
539_2_s3_25CP
539_2_s3_29CP
539_2_s3_26AX
539_2_s3_26CP
539_2_s3_30AX
539_2_s3_30CP
539_2_s3_27CP
539_2_s3_31AX
539_2_s3_31CP
539_2_s3_28CP
539_2_s3_32AX
539_2_s3_32CP
1mm

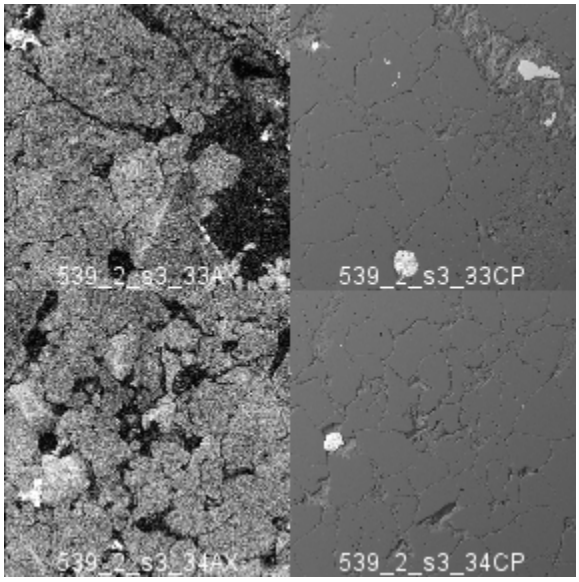
539_2_s3_33AX
539_2_s3_33CP
539_2_s3_34AX
539_2_s3_34CP
1mm

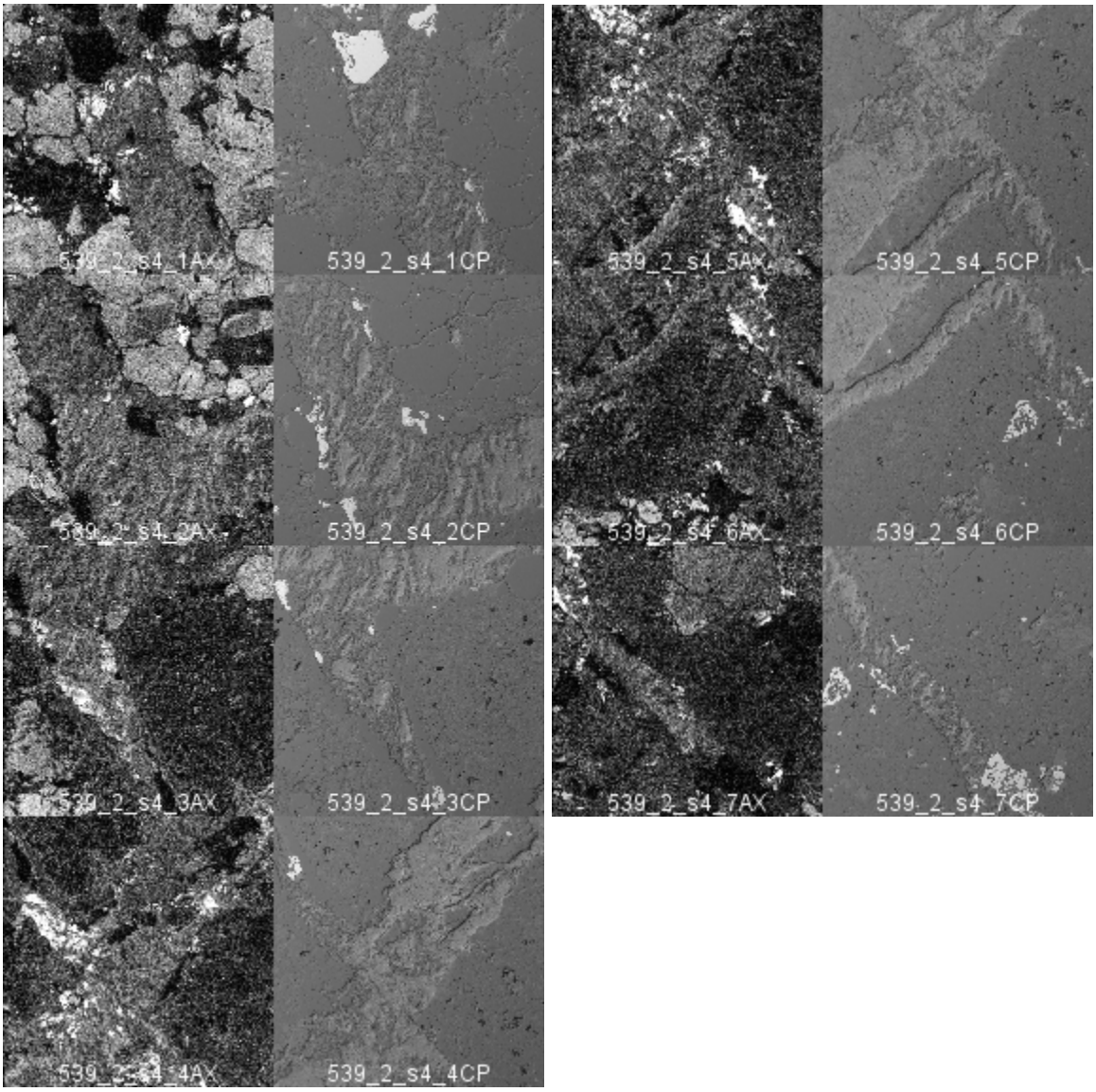

539_2 s4: EPMA images from sample 539_2, series 4. The suffix on the image name denotes the image in the series, and the image type, where AX are CL images and CP are back scattered electron images (BEI). CL images change grey intensity possibly owing to changes in the concentration of Al, Ti, K, or other elements causing shifts in the quartz lattice. CL activity in quartz may also be related to the conditions of formation, including temperature and pressure. Non-quartz phases appear either as black regions (sulfides) or as grey to bright white (CL active, non-quartz minerals). In BEI, more dense minerals appear brighter white, where quartz appears as a mid-grey and more dense minerals. Note the anhydrite vein marked by the shredded texture in both CL and BEI.

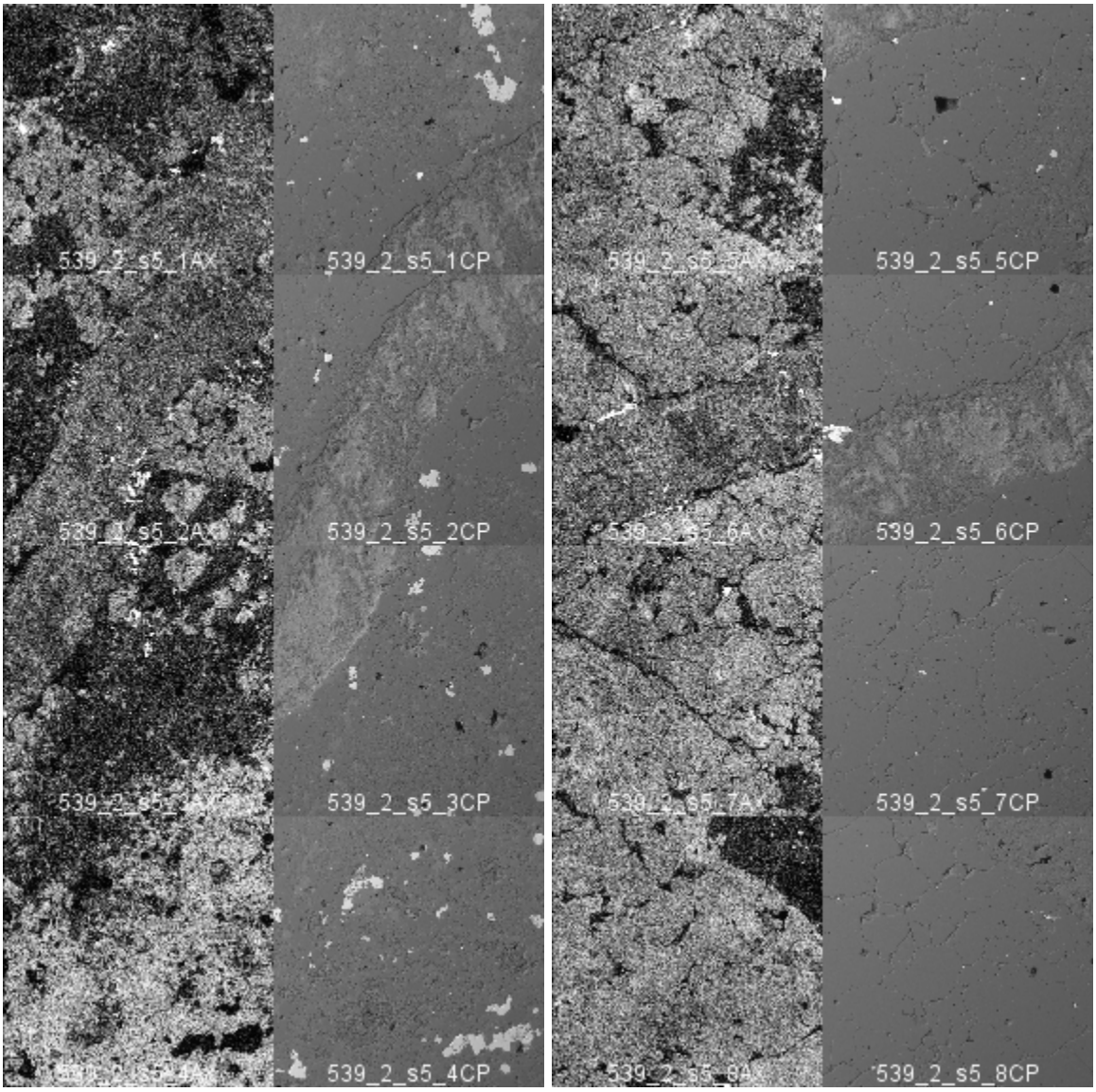

539_2 s5: EPMA images from sample 539_2, series 5. The suffix on the image name denotes the image in the series, and the image type, where AX are CL images and CP are back scattered electron images (BEI). CL images change grey intensity possibly owing to changes in the concentration of Al, Ti, K, or other elements causing shifts in the quartz lattice. CL activity in quartz may also be related to the conditions of formation, including temperature and pressure. Non-quartz phases appear either as black regions (sulfides) or as grey to bright white (CL active, non-quartz minerals). In BEI, more dense minerals appear brighter white, where quartz appears as a mid-grey and more dense minerals. Note the anhydrite vein marked by the shredded texture in both CL and BEI.

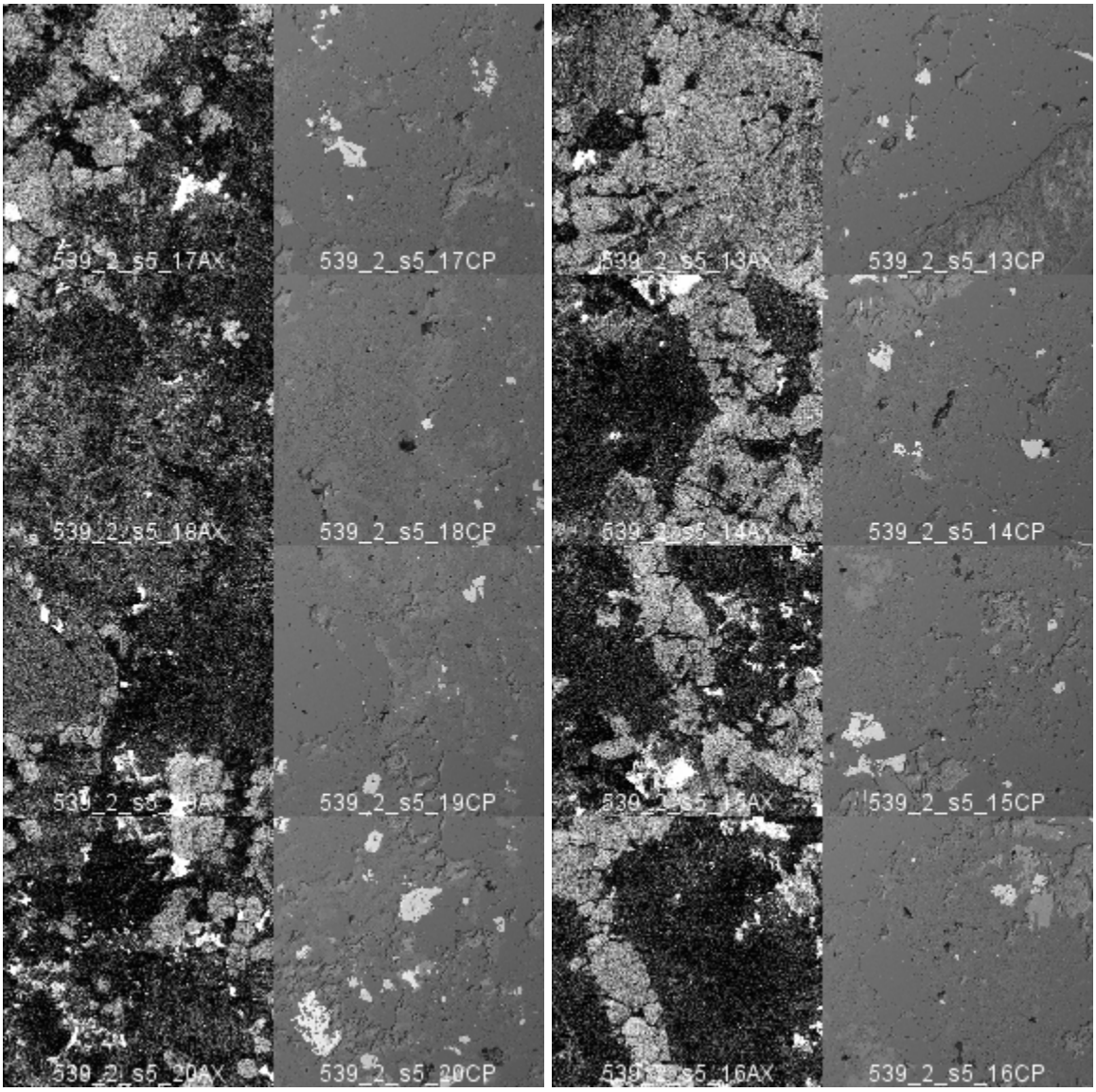
539_2_s5_17AX
539_2_s5_17CP
539_2_s5_13AX
539_2_s5_13CP
539_2_s5_18AX
539_2_s5_18CP
539_2_s5_14AX
539_2_s5_14CP
539_2_s5_19CP
539_2_s5_15CP
539_2_s5_20CP
539_2_s5_16AX
539_2_s5_16CP
1mm

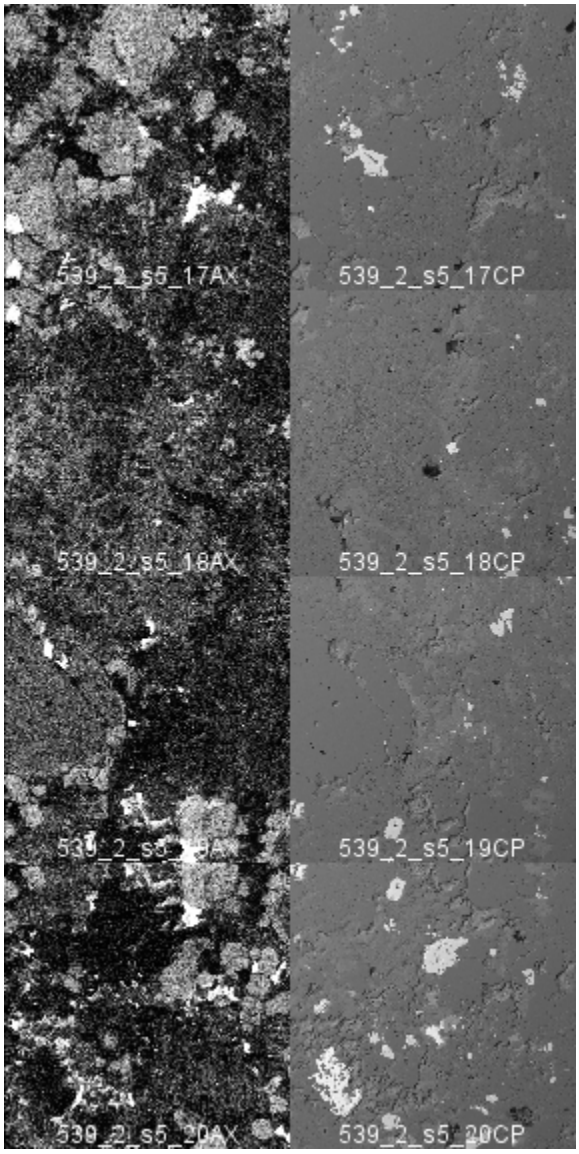
539_2_s5_17AX
539_2_s5_17CP
539_2_s5_18AX
539_2_s5_18CP
539_2_s5_19CP
539_2_s5_20CP
1mm

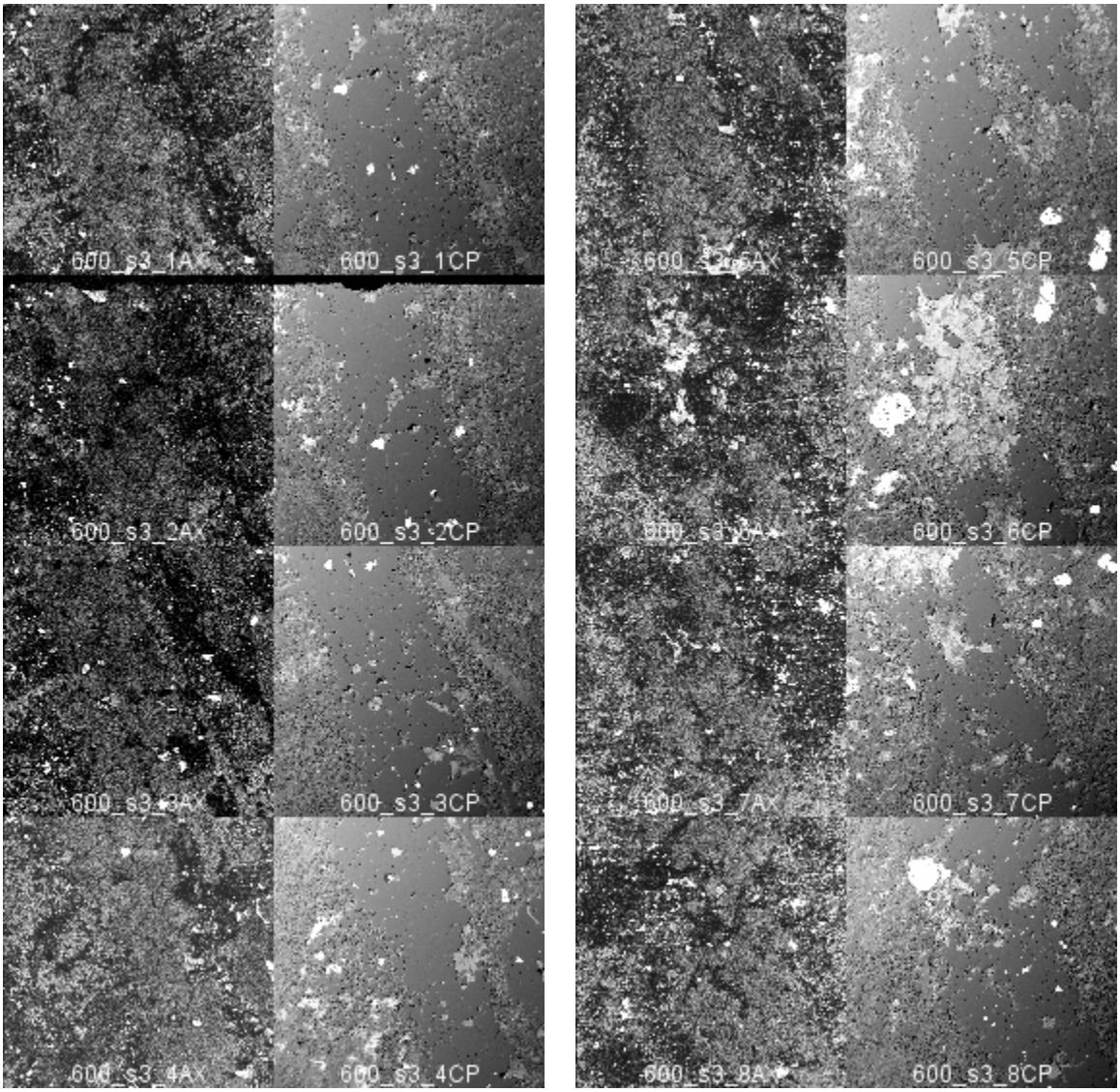

600 s3: EPMA images from sample 600, series 3. The suffix on the image name denotes the image in the series, and the image type, where AX are CL images and CP are back scattered electron images (BEI). CL images change grey intensity possibly owing to changes in the concentration of Al, Ti, K, or other elements causing shifts in the quartz lattice. CL activity in quartz may also be related to the conditions of formation, including temperature and pressure. Non-quartz phases appear either as black regions (sulfides) or as grey to bright white (CL active, non-quartz minerals). In BEI, more dense minerals appear brighter white, where quartz appears as a mid-grey and more dense minerals, e.g., sulfide minerals, appear as light grey or white.

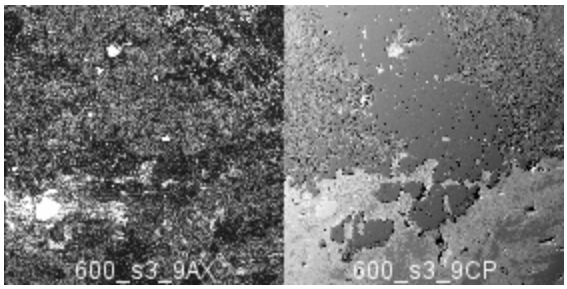
600_s3_9AX
600_s3_9CP
1mm

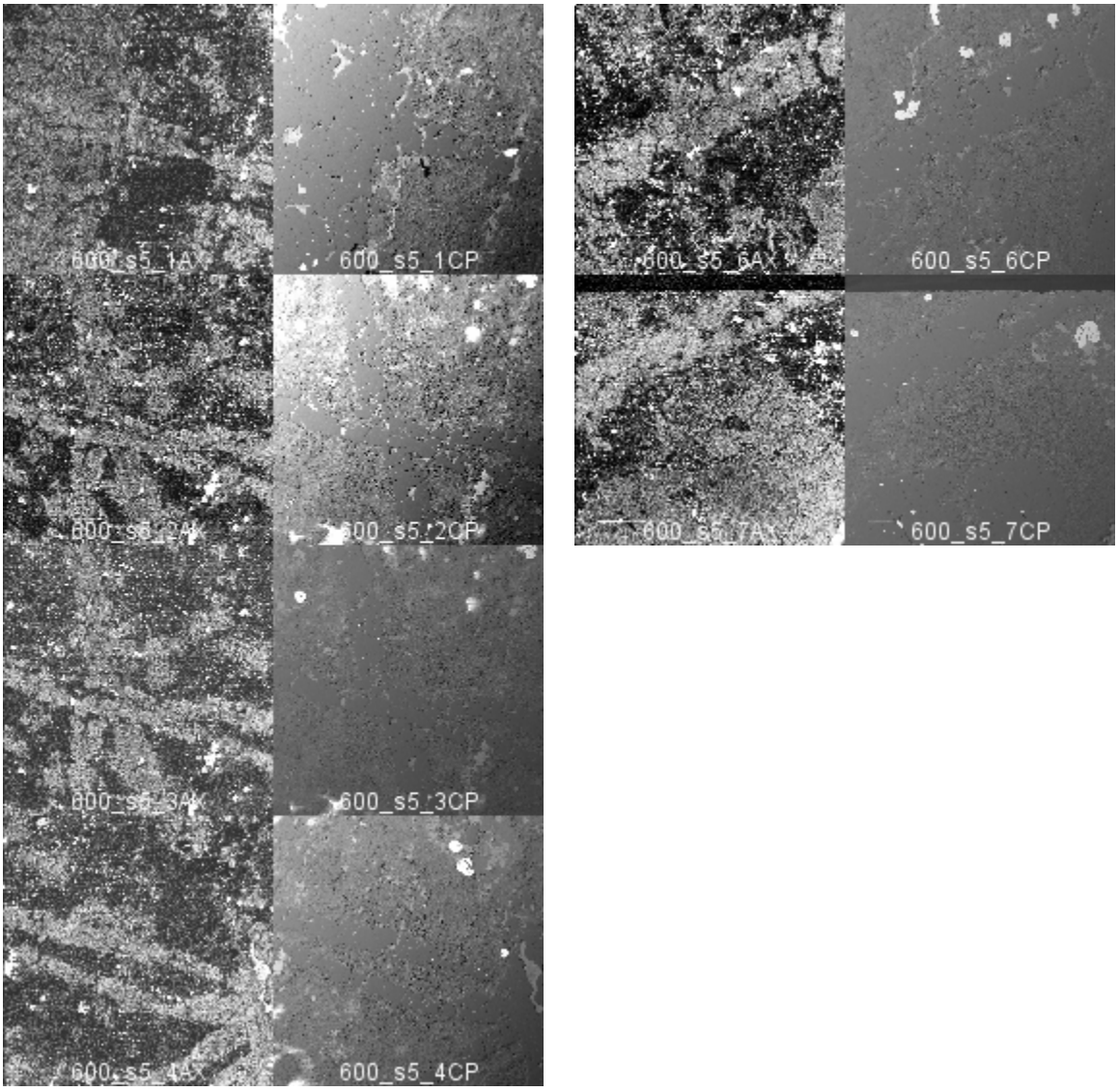

600 s5: EPMA images from sample 600, series 5. The suffix on the image name denotes the image in the series, and the image type, where AX are CL images and CP are back scattered electron images (BEI). CL images change grey intensity possibly owing to changes in the concentration of Al, Ti, K, or other elements causing shifts in the quartz lattice. CL activity in quartz may also be related to the conditions of formation, including temperature and pressure. Non-quartz phases appear either as black regions (sulfides) or as grey to bright white (CL active, non-quartz minerals). In BEI, more dense minerals appear brighter white, where quartz appears as a mid-grey and more dense minerals, e.g. sulfide minerals, appear as light grey or white.

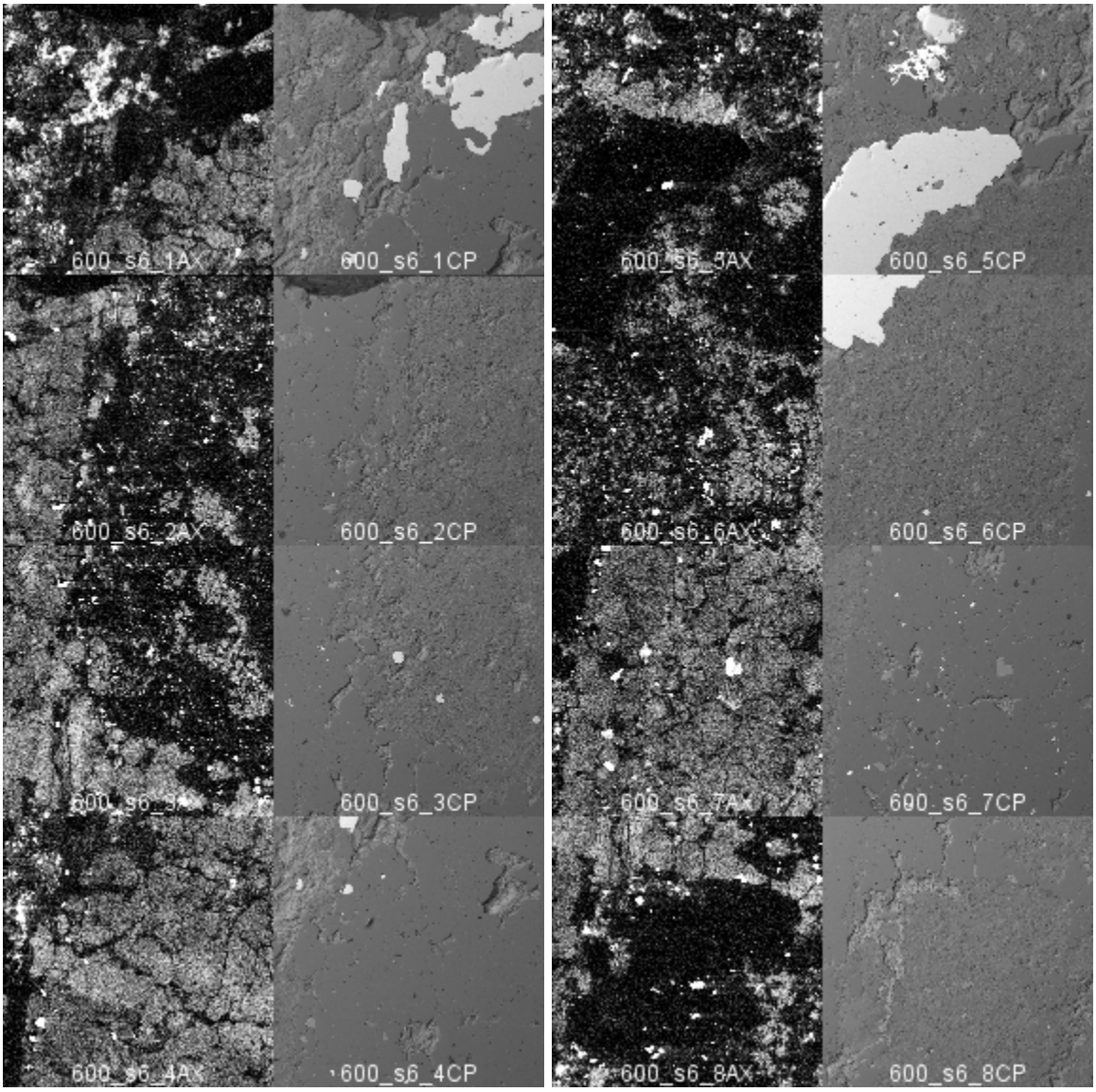

600 s6: EPMA images from sample 600, series 6. The suffix on the image name denotes the image in the series, and the image type, where AX are CL images and CP are back scattered electron images (BEI). CL images change grey intensity possibly owing to changes in the concentration of Al, Ti, K, or other elements causing shifts in the quartz lattice. CL activity in quartz may also be related to the conditions of formation, including temperature and pressure. Non-quartz phases appear either as black regions (sulfides) or as grey to bright white (CL active, non-quartz minerals). In BEI, more dense minerals appear brighter white, where quartz appears as a mid-grey and more dense minerals, e.g. sulfide minerals, appear as light grey or white.

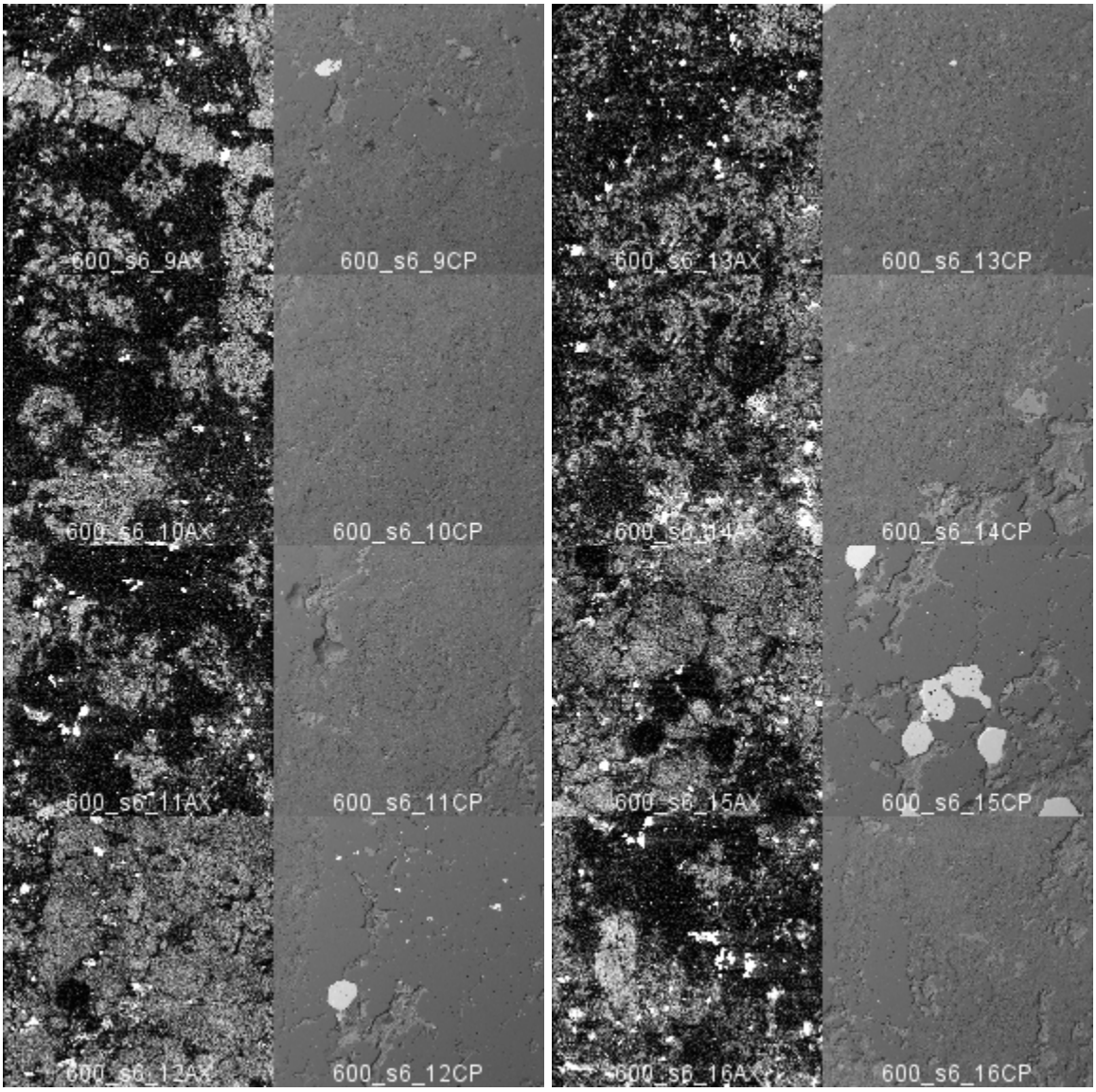
600_s6_9AX
600_s6_9CP
600_s6_13AX
600_s6_13CP
600_s6_10AX
600_s6_10CP
600_s6_14AX
600_s6_14CP
600_s6_11AX
600_s6_11CP
600_s6_15AX
600_s6_15CP
600_s6_12AX
600_s6_12CP
600_s6_16AX
600_s6_16CP
1mm

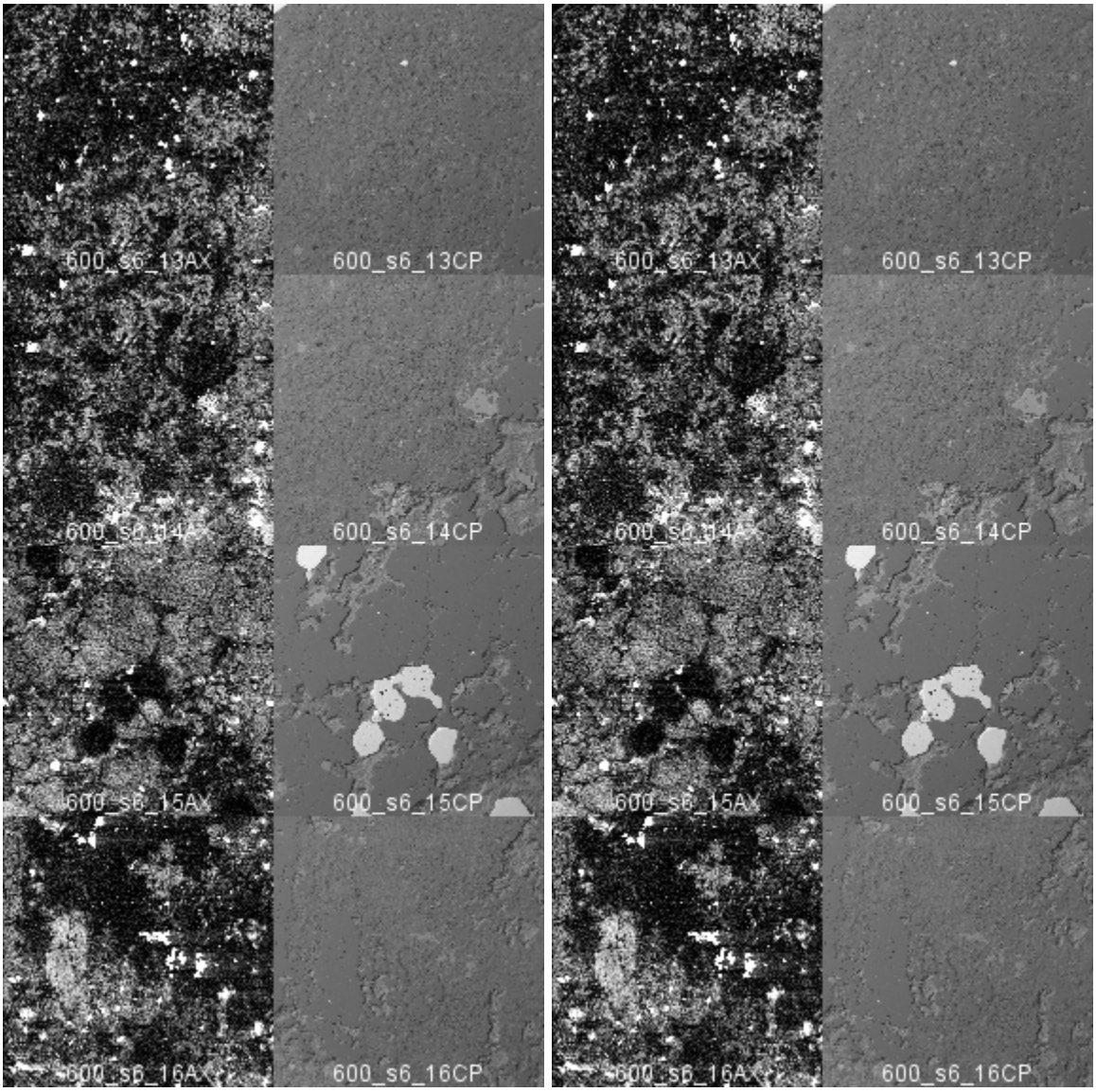
600_s6_13AX
600_s6_13CP
600_s6_14AX
600_s6_14CP
600_s6_15AX
600_s6_15CP
600_s6_16AX
600_s6_16CP
600_s6_13AX
600_s6_13CP
600_s6_14AX
600_s6_14CP
600_s6_15AX
600_s6_15CP
600_s6_16AX
600_s6_16CP
1mm

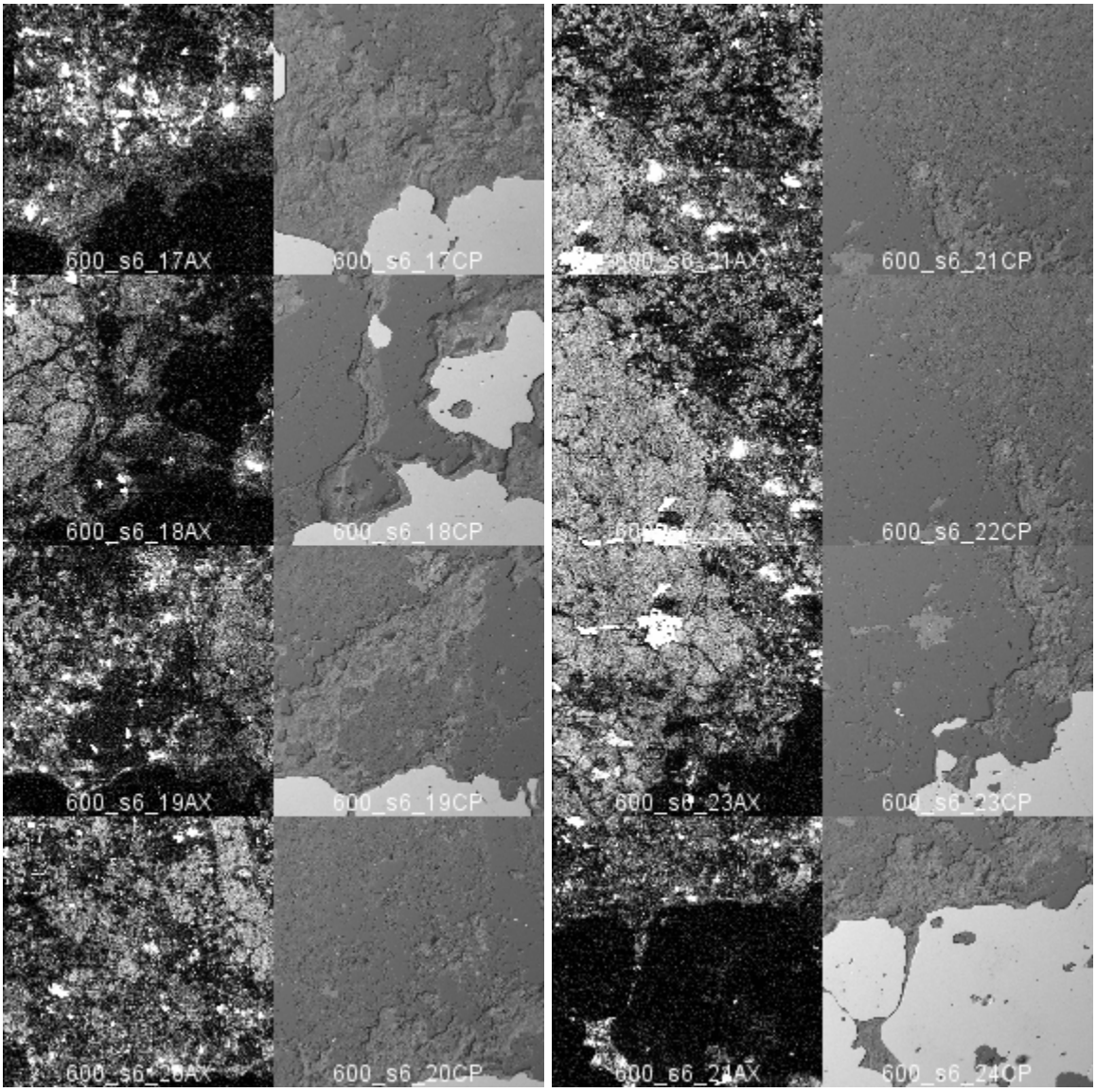
600_s6_17AX
600_s6_17CP
600_s6_21CP
600_s6_18AX
600_s6_18CP
600_s6_22CP
600_s6_19AX
600_s6_19CP
600_s6_23CP
600_s6_20CP
600_s6_24CP
1mm

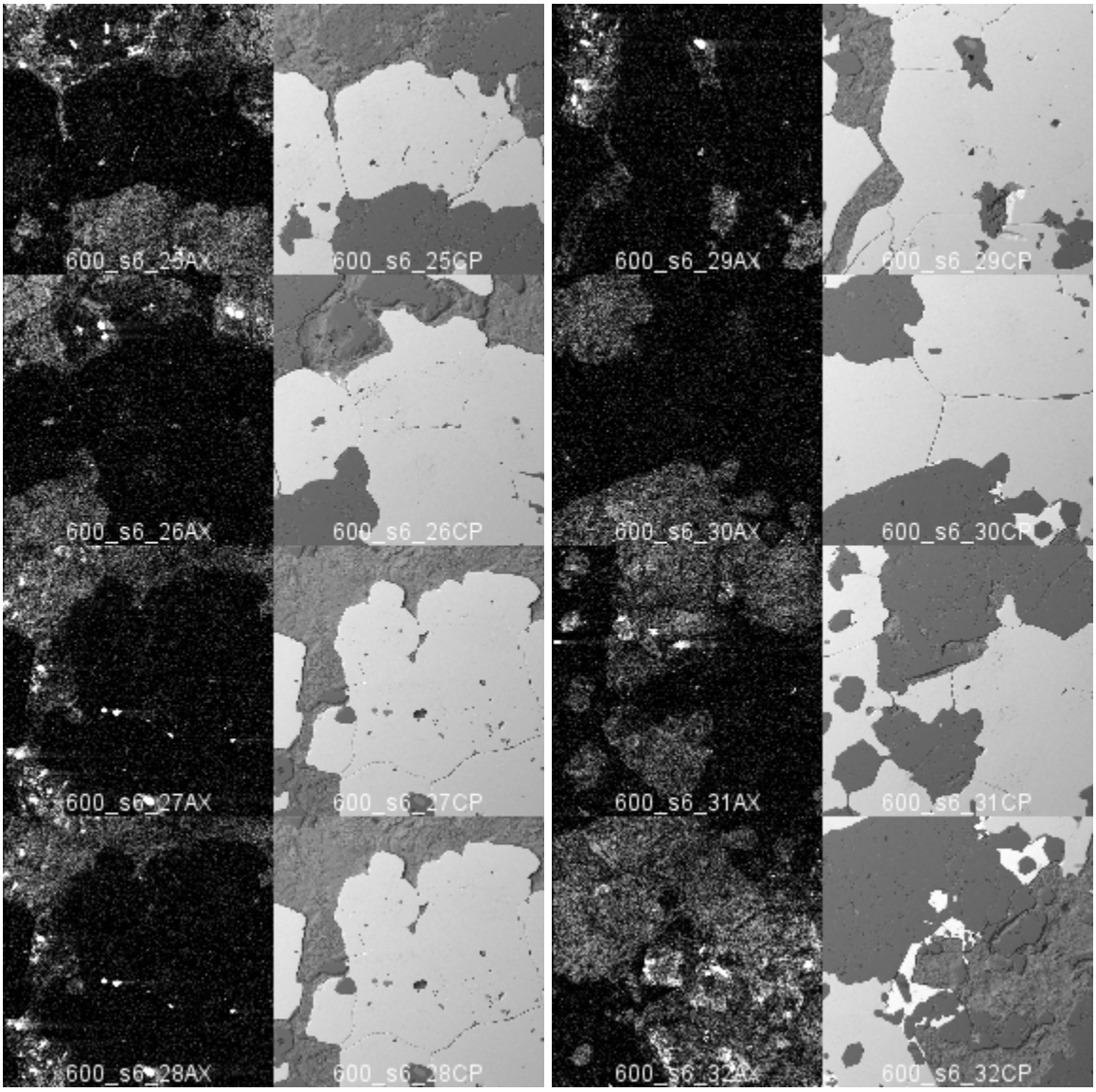
600_s6_25AX
600_s6_25CP
600_s6_29AX
600_s6_29CP
600_s6_26AX
600_s6_26CP
600_s6_30AX
600_s6_30CP
600_s6_27AX
600_s6_27CP
600_s6_31AX
600_s6_31CP
600_s6_28AX
600_s6_28CP
600_s6_32AX
600_s6_32CP
1mm

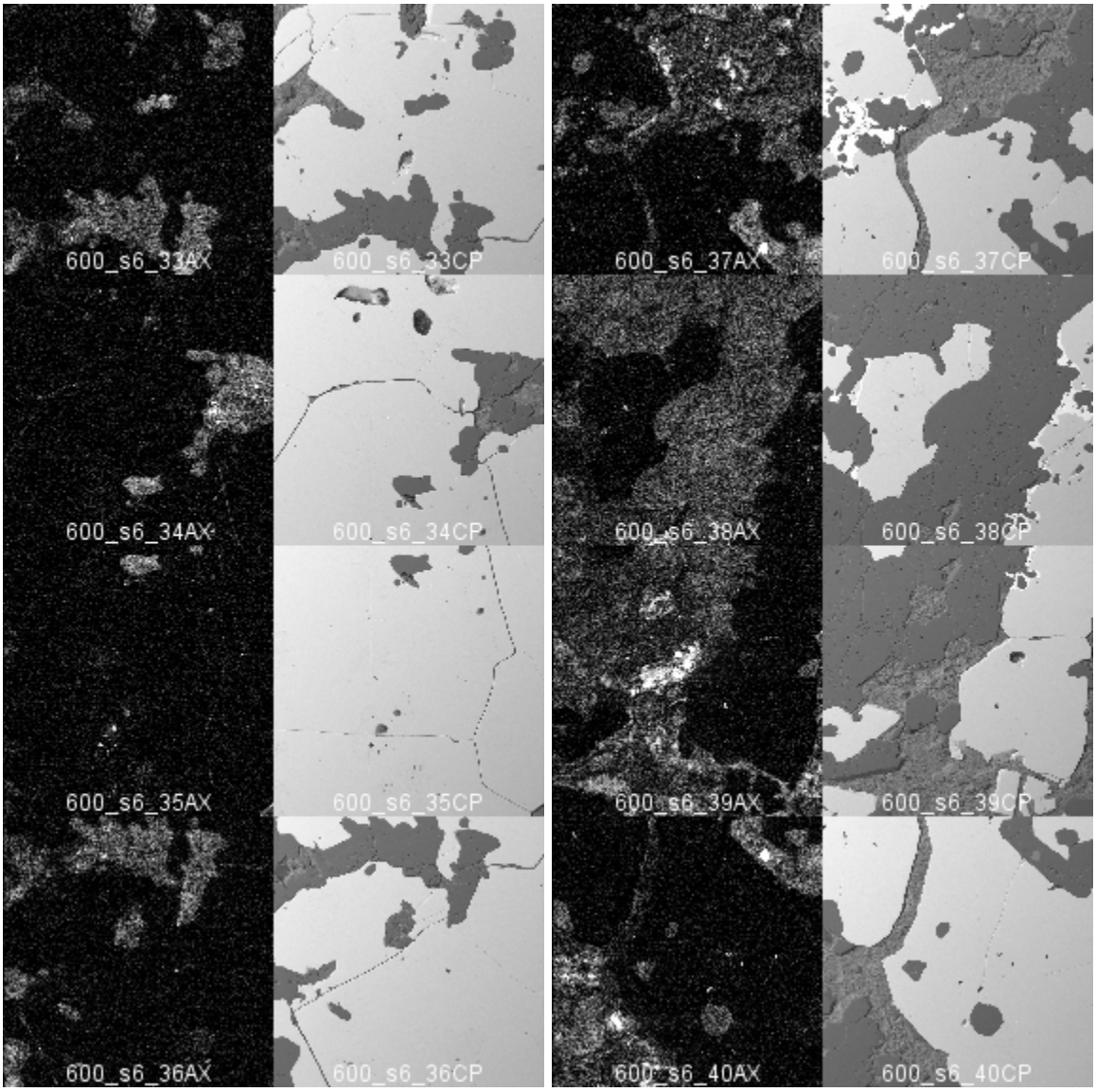
600_s6_33AX
600_s6_33CP
600_s6_37AX
600_s6_37CP
600_s6_34AX
600_s6_34CP
600_s6_38AX
600_s6_38CP
600_s6_35AX
600_s6_35CP
600_s6_39AX
600_s6_39CP
600_s6_36AX
600_s6_36CP
600_s6_40AX
600_s6_40CP
1mm

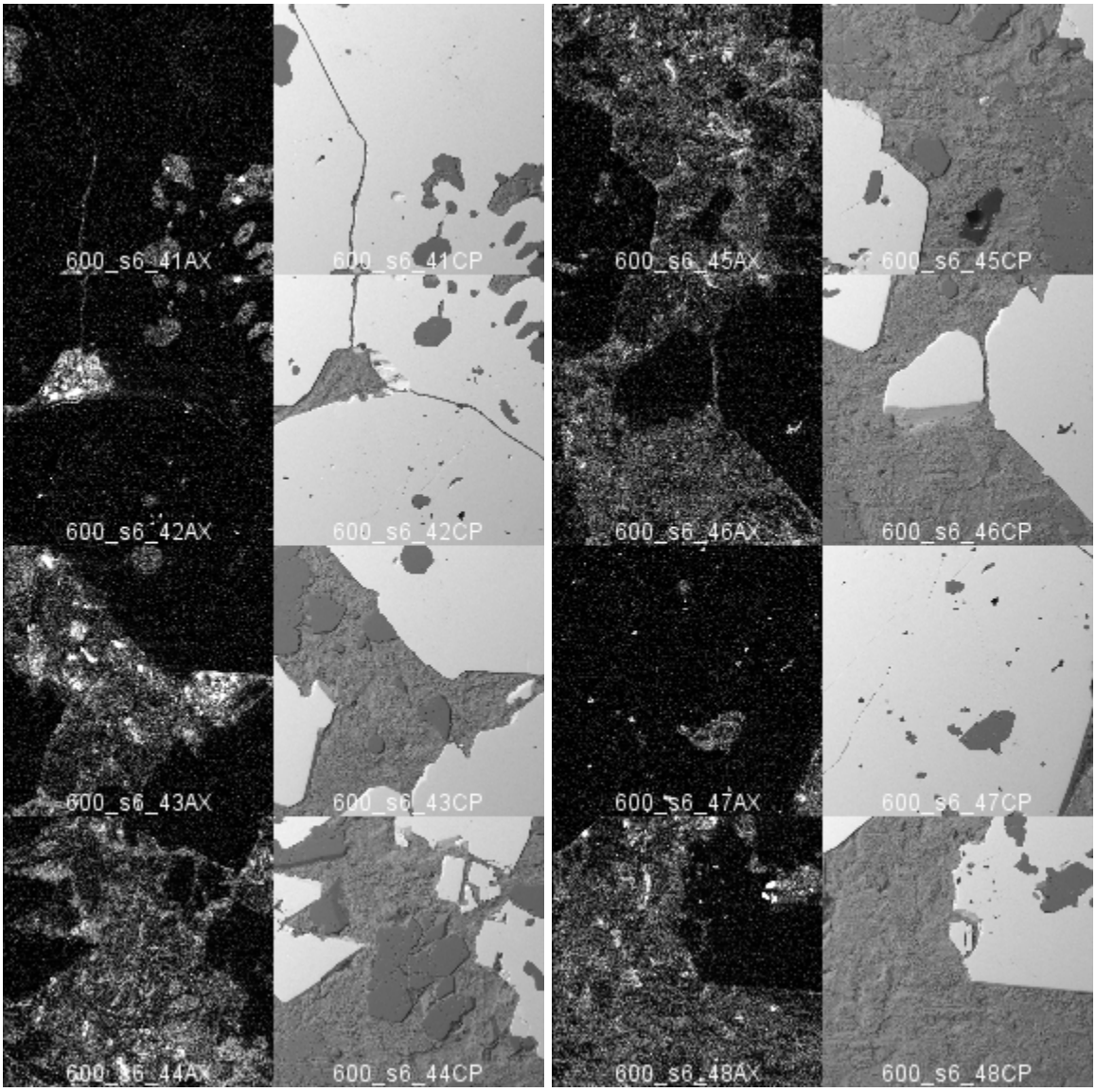
600_s6_41AX
600_s6_41CP
600_s6_45AX
600_s6_45CP
600_s6_42AX
600_s6_42CP
600_s6_46AX
600_s6_46CP
600_s6_43AX
600_s6_43CP
600_s6_47AX
600_s6_47CP
600_s6_44AX
600_s6_44CP
600_s6_48AX
600_s6_48CP
1mm

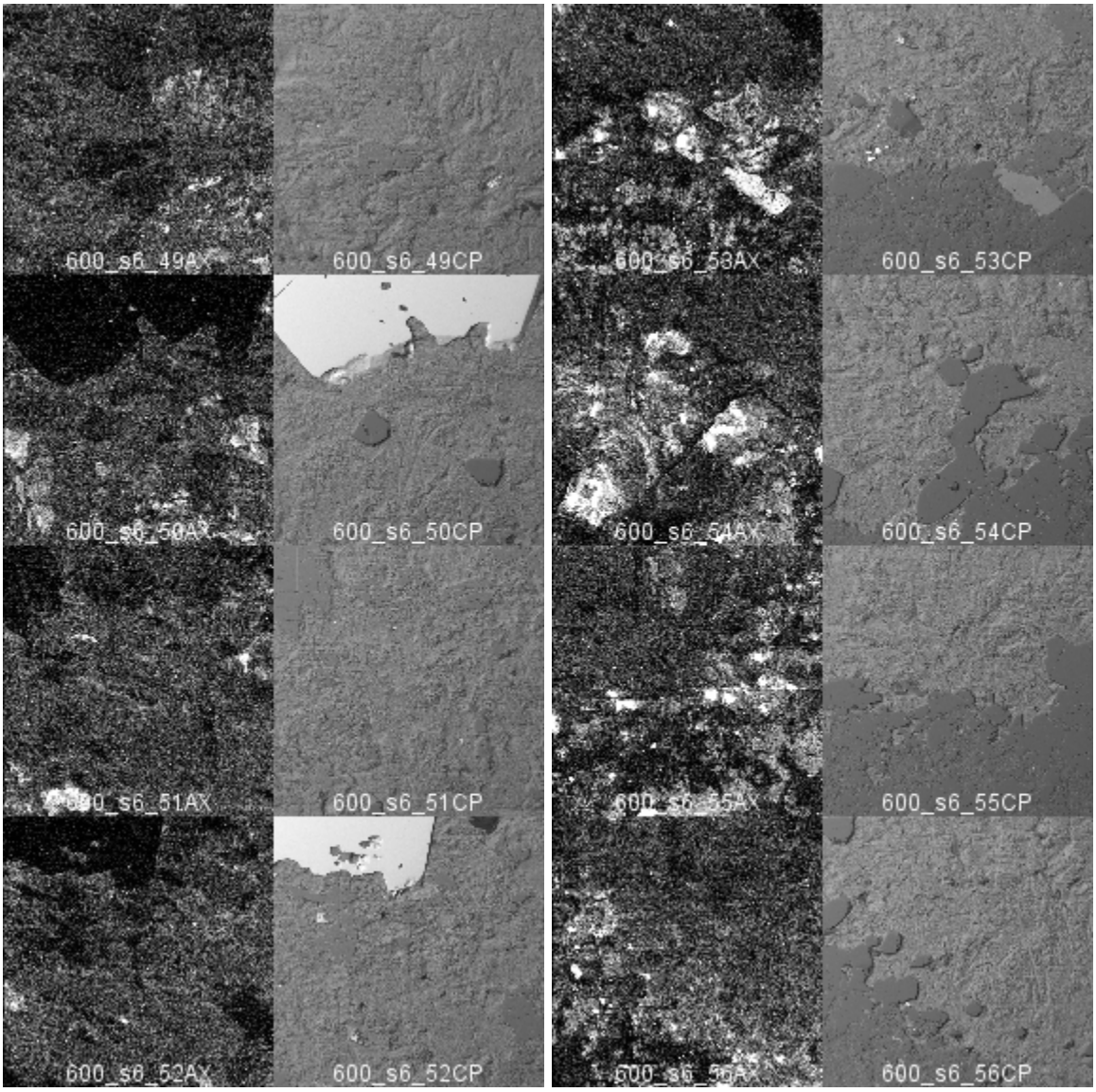
600_s6_49AX
600_s6_49CP
600_s6_50AX
600_s6_50CP
600_s6_51AX
600_s6_51CP
600_s6_52AX
600_s6_52CP
600_s6_53AX
600_s6_53CP
600_s6_54AX
600_s6_54CP
600_s6_55AX
600_s6_55CP
600_s6_56AX
600_s6_56CP
1mm

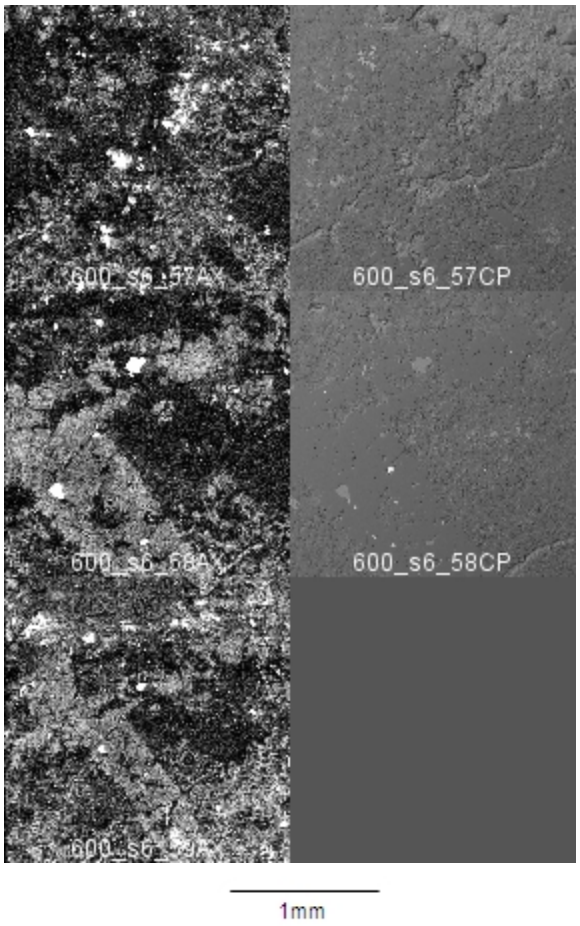
600_s6_57AX
600_s6_57CP
600_s6_58AX
600_s6_58CP
1mm

BIBLIOGRAPHY

Arribas, A., Jr., Hedenquist, J. W., Itaya, T., Okada, T., Concepcion, R. A., and Garcia, J. S., Jr., 1995, Contemporaneous formation of adjacent porphyry and epithermal Cu-Au deposits over 300 ka in northern Luzon, Philippines: Geology, v. 23, no. 4, p. 337-340.

Audetat, A., Pettke, T., Heinrich, C. A., and Bodnar, R. J., 2008, The composition of magmatic-hydrothermal fluids in barren and mineralized intrusions: Economic Geology, v. 103, no. 5, p. 877-908.

Bodnar, R.J., 1994, Philosophy of fluid inclusion analysis *in* Fluid Inclusions in Minerals, Methods and Applications, B. De Vivo and M. L. Frezzotti, eds., pub. by Virginia Tech,Blacksburg, VA, p. 1-6.

Bodnar, R.J., and Vityk, M.O., 1994, Interpretation of microthermometric data for H2O-NaCl fluid inclusions *in* Fluid Inclusions in Minerals,Methods and Applications, B. De Vivo and M. L. Frezzotti, eds., pub. by Virginia Tech, Blacksburg, VA, p. 117-130.

Burnham, C. W., 1979, Magmas and hydrothermal fluids in Geochemistry of hydrothermal ore deposits, H. L. Barnes (ed), John Wiley & Sons, NY, p. 71-136.

Candela, P.A., 1991, Physics of aqueous phase exsolution in plutonic environments: American Mineralogist, v. 76, p. 1081-1091

Drummond, S. E., and Ohmoto, H., 1985, Chemical evolution and mineral deposition in boiling hydrothermal systems: Economic Geology, v. 80, p. 126-147.

Gill, J. B., 1981, Orogenic Andesites and Plate Tectonics: Springer-Verlag, 390pp.

Goldstein, R. H., and Reynolds, T. J., 1994, Systematics of fluid inclusions in diagenetic

minerals: Tulsa, OK, Society for Sedimentary Geology.

Gustafson, L. B., and Hunt, J. P., 1975, The porphyry copper deposit at El Salvador, Chile: Economic Geology, v. 70, no. 5, p. 857-912.

Hattori, K. H. and Keith, J. D., 2001, Contribution of mafic melt to porphyry copper mineralization: evidence from Mount Pinatubo, Philippines, and Bingham Canyon, Utah, USA: Mineralium Deposita, v. 36, p. 799-806.

Hedenquist, J. W., and Lowenstern, J. B., 1994, The role of magmas in the formation of hydrothermal ore deposits: Nature, v. 370, p. 519-527.

Heinrich, C. A., 2005, The physical and chemical evolution of low-salinity magmatic fluids at the porphyry to epithermal transition: a thermodynamic study: Mineralium Deposita, v. 39, p. 864-889.

Heinrich, C. A., Gunther, D., Audeatat, A., Ulrich, T., and Frischknecht, R., 1999, Metal fractionation between magmatic brine and vapor, determined by microanalysis of fluid inclusions: Geology, v. 27, no. 8, p. 755-758.

Heinrich, C. A., Pettke, T., Halter, W. E., Aigner-Torres, M., Audetat, A., Gunther, D., Hattendorf, B., Bleiner, D., Guillong, M., and Horn, I., 2003, Quantitative multi-element analysis of minerals, fluid and melt inclusions by laser-ablation inductively-couple-plasma mass-spectrometry: Geochimica et Cosmochimica Acta, v. 67, no. 18, p. 3473-3496.

Henly, R. W., and Hughes, G. O., 2000, Underground fumaroles: "Excess heat" effects in vein formation: Economic Geology, v. 95, no. 3, p. 453-466.

Keppler, H., 1999, Experimental evidence for the source of excess sulfur in explosive volcanic eruptions: Science, v. 284, p. 1652-1654.

Kesler, S. E., Chryssoulis, S. L., and Simon, G., 2002, Gold in porphyry copper deposits: its abundance and fate:Ore Geology Reviews, v.21, p. 103-124.

Klemm, L. M., 2005, Cu-Mo-Au ratios in poerphyry-type ore deposits: constraints from fluid inclusion microanalysis [Dissertation thesis]: Swiss Federal Institue of Technology Zuerich.

Klemm, L. M., Pettke, T., and Heinrich, C. A., 2007, Hydrothermal Evolution of the El Teniente Deposit, Chile: Porphyry Cu-Mo ore deposition from low-salinity magmatic fluids: Economic Geology, v. 102, p. 1021-1045.

Landtwing, M. R., Pettke, T., Halter, W. E., Heinrich, C. A., Redmond, P. B., Einaudi, M. T., and Kunze, K., 2005, Copper deposition during quartz dissolution by cooling magmatic-hydrothermal fluids: The Bingham Porhphyry: Earth and Planetary Science Letters, v. 235, p. 229-243.

Marsh, B. D., 1996, Solidification fronts and magmatic evolution: Mineralogical Magazine, v. 60, p. 5-40.

Muntean, J. L., 1998, Magmatic-hydrothermal gold deposits of the Maricunga Belt, Nothern Chile [Dissertation thesis]: Stanford University.

Muntean, J. L., 2006, Unpublished Consulting Report.

Muntean, J. L., and Einaudi, M. T., 2000, Porphyry gold deposits of the Refugio District, Maricunga Belt, Northern Chile: Economic Geology, v. 95, p. 1445-1472.

Muntean, J. L., and Einaudi, M. T., 2001, Porphyry-epithermal transition: Maricunga Belt, Northern Chile: Economic Geology, v. 96, p. 743-772.

Murakami, H., Seo, J. H., and Heinrich, C. A., 2009, The relation between Cu/Au ratio and formation depth of porphyry-style Cu-Au±Mo deposits: Miner Deposita, DOI

10.1007/s00126-009-0255-1.

Nash, J.T., 1976, Fluid-inclusion petrology – data from porphyry copper deposits and applications to exploration: U.S. Geological Survey Professional Paper 907D, 16p.

Pudack, C., Halter, W. E., Heinrich, C. A., and Pettke, T., 2009, Evolution of magmatic vapor to gold-rich epithermal liquid: The porphyry to epithermal transition at Nevados de Famatina, Northwest Argentina: Economic Geology, v. 104, no. 4, p. 449-477.

Redmond, P. B., Einaudi, M. T., Inan, E. E., Landtwing, M. R., and Heinrich, C. A., 2004, Copper deposition by fluid cooling in intrusion-centered systems: new insights from the Bingham porphyry ore deposit, Utah: Geology, v. 32, no. 3, p. 217-220.

Richards, J. P., 2003, Tectono-magmatic precursors for the porphyry Cu-(Mo-Au) deposit formation: Economic Geology, v. 98, p. 1515-1533.

Richards, J. P., 2009, Postsubduction porphyry Cu-Au and epithermal Au deposits: Products of remelting of subduction-modified lithosphere: Geology, v. 37, p. 247-250.

Roedder, E. 1971, Fluid inclusion studies on the porphyry-type ore deposits at Bingham, Utah, Butte, Montana, and Climax, Colorado: Economic Geology, vol. 66, p. 98-120.

Roedder, E., 1984, Fluid inclusions, Reviews *i*n Mineralogy: Washington, D.C., Mineralogic Society of America.

Roedder, E. and Bodnar, R. J., 1980, Geologic pressure determinations from fluid inclusion studies: Annual Review of Earth and Planetary Sciences, v. 8, p. 263-

301.

Rusk, B. G., Reed, M. H., Dilles, J. H., Klemm, L. M., and Heinrich, C. A., 2004, Compositions of magmatic hydrothermal fluids determined by LA-ICP-MA of fluid inclusions from the porphyry copper-molybdenum deposit at Butte, MT: Chemical Geology, v. 210, p. 173-199.

Rusk, B. G., Reed, M. H., Dilles, J. H., and Kent, A. J. R., 2006, Intensity of quartz cathodoluminescence and trace-element content in quartz from the porphyry copper deposit at Butte, Montana: American Mineralogist, v. 91, p. 1300-1312.

Rusk, B. G., Lowers, H. A., Reed, M. H., 2008b, Trace elements in hydrothermal quartz: Relationships to cathodoluminescent textures and insights into vein formation: Geology, v. 36, no. 7, p. 547-550.

Rusk, B. G., Reed, M. H., and Dilles, J. H., 2008a, Fluid inclusion evidence for magmatic-hydrothermal fluid evolution in the porphyry copper-molybdenum deposit at Butte, Montana: Economic Geology, v. 10, no. 2, p. 307-334.

Seo, J. H., Guillong, M. and Heinrich, C. A., 2009, The role of sulfur in the formation of magmatic-hydrothermal copper-gold deposits: Earth and Planetary Science Letters, v. 282, p. 323-328.

Simon, A. C., Frank, M. R., Pettke, T., Candela, P. A., Piccoli, P. M., Heinrich, C. A. and Glascock, M., 2007, An evaluation of synthetic fluid inclusions for the purpose of trapping equilibrated, coexisting, immiscible fluid phases at magmatic conditions: American Mineralogist, v. 92, no. 1, p. 124-138.

Singer, D. A., 1995, World class base and precious metal deposits - A quantitative analysis: Economic Geology, v. 90, p. 88-104.

Vila, T. and Sillitoe, R. H., 1991, Gold-rich porphyry systems in the Maricunga Belt, Northern Chile: Economic Geology, v. 86, p. 1238-1260.

VITA

Graduate College
University of Nevada, Las Vegas

Brian Joshua Aillaud

Degree:
Bachelor of Science, Mineral Engineering, 2005
New Mexico Institute of Mining and Technology

Thesis Title: Using Fluid Inclusions to Trace Formative Fluid Evolution at the Verde and Pancho Porphyry Au Deposits of the Refugio District, Chile

Thesis Examination Committee:
Chairperson, Adam Simon, Ph.D.
Committee Member, John Muntean, Ph. D.
Committee Member, Jean Cline, Ph. D.
Committee Member, Rodney Metcalf, Ph. D.
Graduate Faculty Representative, Barbara Luke, Ph.D.